

**CENTRO DE INVESTIGACIÓN Y DE ESTUDIOS AVANZADOS  
DEL INSTITUTO POLITÉCNICO NACIONAL**

**UNIDAD ZACATENCO  
DEPARTAMENTO DE INGENIERÍA ELÉCTRICA  
SECCIÓN DE ELECTRÓNICA DEL ESTADO SÓLIDO**

**Título de la tesis:**

**“Estudio experimental de películas delgadas de CIGSe y CdS para aplicaciones  
fotovoltaicas y evaluación de sus propiedades mediante simulaciones SCAPS”**

**Tesis que presenta:**

**ASHOK ADHIKARI**

**Para obtener el grado de:**

**DOCTOR EN CIENCIAS**

**En la especialidad de:**

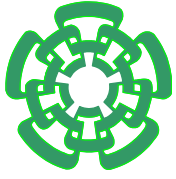
**INGENIERÍA ELÉCTRICA**

**Director de tesis:**

**DR. VELUMANI SUBRAMANIAM**

**Ciudad de México**

**Junio, 2022**



**CENTER FOR RESEARCH AND ADVANCED STUDIES OF THE  
NATIONAL POLYTECHNIC INSTITUTE**

**ZACATENCO UNIT  
DEPARTMENT OF ELECTRICAL ENGINEERING  
SECTION OF SOLID STATE ELECTRONICS**

**Thesis title:**

**“Experimental study of CIGSe and CdS thin films for photovoltaic applications and  
evaluation of their properties through SCAPS simulation”**

**Thesis presented by:**

**ASHOK ADHIKARI**

**To obtain the grade of:**

**DOCTOR OF SCIENCE**

**Specialty in:**

**ELECTRICAL ENGINEERING**

**Thesis director:**

**DR. VELUMANI SUBRAMANIAM**

## Resumen

Las celdas solares de película delgada  $\text{CuInSe}_2$  son el candidato más prometedor en el mercado fotovoltaico para la producción de energía debido a sus propiedades favorables. En este estudio se utiliza un nuevo método de depósito híbrido para sintetizar las películas delgadas de  $\text{CuInSe}_2$ . El método de depósito híbrido es similar al método de co-evaporación de tres etapas, pero en este se combina con la técnica de pirólisis por pulverización neumática para obtener ventajas de ambos métodos. La primera etapa consistió en el depósito de capas precursoras de  $\text{In}_2\text{Se}_3$  mediante la técnica de pirólisis por pulverización neumática. La segunda y tercera etapa del método de depósito híbrido se llevó a cabo por el método de co-evaporación seguido del proceso de selenización. En este trabajo de investigación, se prestó más atención a la variación de la temperatura del sustrato de la primera etapa, las temperaturas y tiempos de selenización ya que estos parámetros pueden afectar fuertemente las propiedades del material de las películas delgadas de  $\text{CuInSe}_2$ . A partir de los resultados se observó la estructura cristalina de calcopirita con la orientación preferencial de (112), las composiciones ligeramente pobres en Cu y ricas en Se, los granos compactos y más grandes con formas irregulares y la conductividad tipo p de las películas absorbentes de  $\text{CuInSe}_2$  depositadas. La segunda parte de este trabajo se enfocó sobre el crecimiento de películas delgadas de CdS por el método de depósito por baño químico, trabajando a diferentes proporciones de amoníacos, temperaturas y tiempos de depósito. Se obtuvo la estructura de cristal hexagonal, las películas uniformes y suaves, la alta transmitancia y la conductividad de tipo n en las películas delgadas de CdS que se pueden utilizar en las celdas solares como capa búfer.

Se simuló las celdas solares de película delgada  $\text{CuInSe}_2$  mediante el software SCAPS, que estudia principalmente el espesor y la concentración de portadores de cada semiconductor utilizado en las celdas solares. Se investigó la influencia de los defectos (en semiconductores y en la interfaz), la temperatura ambiente y las resistencias parásitas en el rendimiento del dispositivo. A partir de estos resultados, la eficiencia de la celda solar de película delgada  $\text{CuInSe}_2$  mejoró con un aumento en el espesor de la capa absorbente al mejorar la absorción de fotones. Los centros de recombinación para los portadores de carga generados aumentaron a mayores concentraciones de portadores de la capa absorbente. El espesor de CdS superior a 100 nanómetros reduce el rendimiento de la celda solar

aumentando la resistencia en serie y absorbiendo fotones en la capa de CdS. Las mayores concentraciones de portadores de CdS mejoró la recolección de portadores de carga generados al extender la región de carga espacial en la capa absorbente. Después de analizar estos resultados, la eficiencia optimizada para las celdas solares de película delgada CISE, CIGSe y CIGSe bicapa fue del 22.81, 27.32 y 27.99 %, respectivamente. Estos resultados demostraron que la celda solar de película delgada CIGSe bicapa obtuvo un mejor rendimiento que el uso de capas absorbentes individuales al mejorar la absorción de fotones. A partir de los resultados de eficiencia cuántica se observó que la eficiencia está directamente relacionada con el bandgap de la capa absorbente.

A través de la simulación se analizaron los resultados experimentales de los semiconductores CISE, CIGSe y CdS. La eficiencia de las celdas solares de película delgada CI(G)Se después de reemplazar los resultados experimentales en la simulación se redujo con poco margen que los resultados teóricos optimizados. Estos mostraron que las condiciones optimizadas experimentalmente tienen el potencial de lograr más del 20% de eficiencia para las celdas solares de película delgada CI(G)Se. La presencia de defectos en la capa absorbente, la capa amortiguadora y su interfaz redujo el rendimiento del dispositivo al aumentar las tasas de recombinación de los portadores de carga generados, disminuyendo la longitud de difusión de los portadores de carga minoritarios. La eficiencia de las celdas solares se reduce con el aumento de la temperatura ambiente, lo que se debe principalmente a la disminución del voltaje de circuito abierto al aumentar la corriente de saturación. El factor de llenado de la celda solar es muy sensible a las resistencias parásitas. El alto rendimiento de la celda solar se detectó en valores bajos de resistencia en serie y valores altos de resistencia en derivación. Este incremento del rendimiento de los dispositivos se debe a un mejor transporte por deriva de los portadores de carga libres hacia los electrodos con resistencias en serie más bajas y una tasa de recombinación más baja con resistencias en derivación más altas. El estudio teórico puede proporcionar información valiosa, orientando así el diseño del trabajo experimental.

**Palabras Clave:**  $\text{In}_2\text{Se}_3$ , CISE, CIGSe, CIGSe-bicapa, CdS, método de depósito híbrido, técnica de pirolisis por pulverización neumática, método de co-evaporación, proceso de selenización, método de depósito por baño químico, simulación SCAPS.



## Abstract

The  $\text{CI(G)Se}$  thin film solar cells are the most promising candidate in photovoltaic market for energy production due to their favorable material properties. In this study, a new hybrid deposition method is used to synthesize  $\text{CI(G)Se}$  thin films. The hybrid deposition method is similar to the three-stage co-evaporation method, but in this, it was combined with the pneumatic spray pyrolysis technique to get the advantages of both methods. The first stage involved the deposition of  $\text{In}_2\text{Se}_3$  precursor layers by the pneumatic spray pyrolysis technique. The second and third stages of the hybrid deposition method were carried out in the co-evaporation method followed by the selenization process. In this research work, more attention was given to the variation of the first stage substrate temperature, selenization temperatures and times because these parameters can strongly affect the material properties of  $\text{CI(G)Se}$  thin films. The chalcopyrite crystal structure with the preferential orientation of (112), the slightly Cu-poor and Se-rich compositions, the compact and larger grains with irregular shapes, and p-type conductivity of deposited  $\text{CI(G)Se}$  absorber films were observed from the results. The second part of this work was focused on the growth of CdS thin films by the chemical bath deposition method, working at different proportions of ammonia, deposition temperatures and times. The hexagonal crystal structure, uniform and smooth films, high transmittance as well as n-type conductivity were found for CdS thin films that can be utilized in solar cells as a buffer layer.

The  $\text{CI(G)Se}$  thin film solar cells were simulated through SCAPS software, which mainly studied the thickness and carrier concentration of each semiconductor used in solar cells. The influence of defects (in bulk semiconductors and at the interface), ambient temperature, and parasitic resistances on the device performance was also investigated. From these results, the efficiency of  $\text{CI(G)Se}$  thin film solar cell was enhanced with an increase in thickness of the absorber layer by improving the absorption of photons. The recombination centers for the generated charge carriers increased at higher carrier concentrations of the absorber layer. The thickness of CdS greater than 100 nanometers reduce the solar cell performance by increasing the series resistance and absorbing photons in the CdS layer. The higher carrier concentrations of CdS improved the collection of generated charge carriers by extending the space charge region in the absorber layer. After analyzing these results, the optimized efficiency for  $\text{CISE}$ ,  $\text{CIGSe}$ , and  $\text{CIGSe}$  bilayer thin film solar cells were 22.81,

27.32, and 27.99%, respectively. These results demonstrated that the CIGSe bilayer thin film solar cell obtained better performance than using single absorber layers by enhancing the absorption of photons. It was seen from quantum efficiency results that efficiency is directly related to the bandgap of the absorber layer.

The experimental results of the CISE, CIGSe and CdS semiconductors are also analyzed through this simulation. The efficiency of CI(G)Se thin film solar cells after replacing the experimental results in the simulation was decreased with little margin than optimized theoretical results. These results showed that the experimentally optimized conditions had the potential to achieve more than 20% of efficiency for CI(G)Se thin film solar cells. The presence of defects in the absorber layer, buffer layer, and their interface reduced the device performance by increasing the recombination rates of generated charge carriers, decreasing the diffusion length of the minority charge carriers. The efficiency of solar cells reduced with an increase in the ambient temperature, which is mainly due to the decrement of open circuit voltage by increasing the saturation current. The fill factor of the solar cell is very sensitive to parasitic resistances. The high solar cell performance was detected at low values of series resistance and high values of shunt resistance. This increment of the device performance is due to the better drift transport of free charge carriers towards the electrodes at lower series resistances and lower recombination rate at higher shunt resistances. The theoretical study can provide valuable information, thus guiding a design in the experimental work.

**Keywords:** In<sub>2</sub>Se<sub>3</sub>, CISE, CIGSe, CIGSe-bilayer, CdS, hybrid deposition method, pneumatic spray pyrolysis technique, co-evaporation method, selenization process, chemical bath deposition method, SCAPS simulation.

**Dedicated To**  
**“My Beloved Family”**

## **Acknowledgement**

First, I would like to express my gratitude to my thesis director Dr. Velumani Subramaniam for providing me an opportunity to work with his research team and for his continuous support, guidance, and motivation throughout my research. I am immensely appreciative of his profound knowledge, availability, and patience. It was a great experience and an overall growth of my personality.

I also want to express my thankfulness to my thesis committee members: Dra María de la Luz Olvera Amador, Dr. Arturo Maldonado Alvarez, Dr. Gabriel Romero Paredes Rubio from Solid State Electronic Section (SEES), Department of Electrical Engineering, CINVESTAV-IPN, and Dr. Jose Chavez Carvayar from IIM-UNAM, Mexico City for their valuable suggestions, help, encouragement and time to make my thesis perfect in all aspects. I would like to give special thanks to Dr. Homero Castaneda Lopez from Texas A&M University for accepting the internship program, which was helpful to broaden my skills and knowledge in scientific research work. I also want to acknowledge Dr. Fabián Andrés Pulgarín Agudelo from Departamento de Fisica, Instituto Politecnico Nacional, Mexico City, and Dr. Jorge Evaristo Conde Diaz from CONACYT-Institute for Research and innovation in Renewable Energies, University of Science and Arts of Chiapas, Chiapas for their collaboration in the research work. My sincere thanks to Dr. Iouri Koudriavtsev, Dr. Arturo Escobosa Echavarria, and other professors from the SEES for their help in professional work. I wish to thank the SEES secretaries, Monica Davar Ocegueda, Yesenia Cervantes Aguirre, Beatriz Urrutia Bohorquez, for their continuous support in many things.

I am grateful to the Consejo Nacional de Ciencia y Tecnología (CONACYT) for providing financial support and Centro de Investigación y de Estudios Avanzados del Instituto Politécnico Nacional (CINVESTAV- IPN) for providing a place to do research work. I would like to thank the Biblioteca-CINVESTAV for providing resources to improve my knowledge. I wish to express my acknowledgement to people from the department de Becas y Estímulos, especially Oscar Ivan Buendia Montano and Elvia Lomeli Cortés, to apply for financial support for conferences, internships, extra, etc. I want to express my special thanks to auxiliaries, technicians, and professors from various departments and institutes for their collaboration in technical support. I would like to thank Dr. Jaime Vega Pérez, Miguel Angel

Avendano Ibarra, Norma Iris Gonzalez Garcia, Miguel Luna Arias, Miguel Galvan Arellano, Adolfo Tavira Fuentes, Francisco Alvarado Cesar, Dr. Jorge Roque De la Puente, Jose Martin Jimenez Sarmiento, Daniel Benito Ramirez Gonzalez, Edmundo Rodriguez Ascencion, etc. I am thankful to the Department of Electronics and Information Systems (ELIS) researcher who developed the SCAPS-1D simulator and distributed it freely to the research community. I want to express special acknowledgement to Katia Gabriela Ocampo Reyna for helping to make immigration documents.

I would like to express my sincere gratitude to Mrs. Malathy Velumani for her care, motivation, encouragement and valuable suggestions. I also wish to thank our research group members: Dr Roberto Hernandez Maya, Dra. Myriam Solis López, Dra. Araceli Romero Nuñez, Dr. Jorge Sergio Narro Rios, Dr. Jose Jorge Rios Ramirez, Dra. Atzin Ferrel, Dr. Odin Reyes Vallejo, Dr. Ganesh Regmi, Dr. Kartick Sekar, Dra. Drisya Karathuparathottathil Damodharan, Dra. Christeena Theresa Thomas, Dra. Mercyrani Babudurai, Dr. Onyekachi Michael Nwakanma, Francisco Javier Gomez Cano, Javier Covarrubias Garcia, David Oswaldo Rocha Cadena, Hugo Cesar Ramos Lopez, Luis Dorian Valencia Ordonez, Cesar Carrillo, Alejandra, Fernanda, Josue, etc. for their valuable time, kind support and friendly atmosphere during my Ph. D. program. I am also grateful to my friends: Manmohan, Goban Kumar, Isaac Montes, Jair Antonio, Elvira Gomez, Agustin Cortes, Russell Abel, Lucia Ivonne, Leticia Romero, Juan Gabriel, Filiberto Javier, Igor Morett, Jesus Che Banuelos, Magaly Ramirez, Alma Isabel, Jordi Solis, Patricia Mendez, Maria Teresa, Celia Cesar, Francisco Alvarado, Veronica Alvarado, Gabriela Alvarado, Karla Hortensia, Alma Gabriela, Jose Guillermo, Guillermo Garcia, Maria de Lourdes, etc. for their support, time and encouragement during this academic journey.

Last but not least, I am very grateful to my grandparents (Thirbahadur and Vagabati), my parents (Ramkaji and Devimaya), my uncle (Hariraj), my aunt (Naumata), my brothers (Arjun, Sushil Bikram, Arun, Aprim), my sisters (Pragati, Prakriti), my sisters-in-law (Rekha, Mira, Jamuna), my nieces (Paridhi, Sushila, Priyansa), for their endless love, faith, support, encouragement during these years. Thank you all for believing in me and supporting me to fulfill my dreams

# Table of Contents

<b>Chapter 1 Introduction.....</b>	<b>1</b>
1.1 Introduction of energy sources.....	1
1.2 Semiconductor and solar cell physics.....	2
1.2.1 Semiconductors.....	2
1.2.2 p-n junction.....	4
1.2.2.1 Homojunction.....	4
1.2.2.2 Heterojunction.....	6
1.2.3 Working principle of solar cell.....	7
1.2.4 Basic characteristics of solar cell.....	9
1.2.5 Development of PV technology.....	12
1.3 Introduction of the numerical simulation.....	15
1.3.1 SCAPS simulation.....	16
1.4 Objectives of this research work.....	18
1.5 Organization of thesis.....	19
References:.....	20
<b>Chapter 2 CI(G)Se thin film solar cells technology.....</b>	<b>26</b>
2.1 Development of the CI(G)Se thin film solar cells.....	26
2.2 CIGSe thin film solar cell structure.....	27
2.2.1 Substrate.....	28
2.2.2 Back contact.....	28
2.2.3 CIGSe absorber layer.....	29
2.2.3.1 Structural properties.....	30
2.2.3.2 Phase diagram.....	31
2.2.3.3 Optical properties.....	32
2.2.3.4 Electrical properties.....	34
2.2.4 Window layer.....	35
2.2.5 Front contacts.....	36
2.3 Role of alkali element doping in CI(G)Se.....	37
2.4 Recombination mechanism in CI(G)Se thin film solar cells.....	39
2.5 Deposition methods for CI(G)Se thin films.....	40
2.5.1 Co-evaporation method.....	41
2.5.2 Sputter deposition.....	44
2.5.3 Selenization or sulfurization.....	45
2.5.4 Electrodeposition based methods.....	46
2.5.5 Particulate based methods.....	47
2.5.6 Solution based methods.....	48
2.6 Hybrid deposition method.....	51
References:.....	52
<b>Chapter 3 Experimental, simulation and characterization details.....</b>	<b>61</b>
3.1 Experimental details.....	61
3.1.1 Substrate preparation.....	61
3.1.2 CI(G)Se thin films by hybrid deposition method.....	62
3.1.3 CdS thin films by chemical bath deposition method.....	66
3.2 SCAPS simulation details.....	68
3.3 Device characterization.....	71
3.3.1 Material characterization.....	71
3.3.1.1 Film thickness measurement.....	71

3.3.1.2 XRD measurement .....	72
3.3.1.3 SEM analysis and EDS measurement.....	73
3.3.1.4 Raman spectroscopy.....	75
3.3.1.5 AFM measurement.....	76
3.3.1.6 UV-Vis spectroscopy.....	78
3.3.1.7 Electrical characterization techniques.....	80
3.3.1.7.1 Four-probe technique.....	80
3.3.1.7.2 Hall van der Pauw method.....	81
3.3.2 External-quantum efficiency (EQE) measurements.....	83
References: .....	84
<b>Chapter 4 Results and discussions for absorber layers .....</b>	<b>87</b>
4.1 Growth of the In <sub>2</sub> Se <sub>3</sub> thin films .....	87
4.1.1 Structural properties of In <sub>2</sub> Se <sub>3</sub> thin films.....	88
4.1.2 Morphological properties of In <sub>2</sub> Se <sub>3</sub> thin films.....	90
4.1.3 Compositional analysis of In <sub>2</sub> Se <sub>3</sub> thin films.....	91
4.1.4 Topographical analysis of In <sub>2</sub> Se <sub>3</sub> thin films.....	92
4.1.5 Optical properties of In <sub>2</sub> Se <sub>3</sub> thin films .....	93
4.2 Growth of the CISE absorber layer.....	94
4.2.1 Influence of selenization temperatures and times.....	94
4.2.1.1 Structural properties of CISE thin films.....	95
4.2.1.2 Morphological properties of CISE thin films .....	97
4.2.1.3 Compositional analysis of CISE thin films.....	98
4.2.2 Effect of first stage temperatures .....	99
4.2.2.1 Structural properties of CISE thin films.....	100
4.2.2.2 Morphological properties of CISE thin films .....	102
4.2.2.3 Compositional analysis of CISE thin films.....	103
4.2.2.4 Topographical analysis of CISE thin films .....	104
4.2.2.5 Electrical properties of CISE thin films .....	105
4.3 Growth of the CIGSe absorber layer.....	106
4.3.1 Structural properties of CIGSe thin films.....	106
4.3.2 Morphological properties of CIGSe thin films .....	109
4.3.3 Compositional analysis of CIGSe thin films.....	110
4.3.4 Topographical analysis of CIGSe thin films .....	111
4.3.5 Electrical properties of CIGSe thin films .....	113
4.4 Summary .....	114
References: .....	114
<b>Chapter 5 Study on CdS buffer layer for CI(G)Se thin film solar cells.....</b>	<b>119</b>
5.1 Introduction .....	119
5.2 Deposition methods .....	120
5.3 Chemical bath deposition method.....	120
5.3.1 Deposition mechanisms .....	122
5.3.1.1 Ion by ion deposition .....	122
5.3.1.2 Cluster by cluster deposition .....	123
5.3.2 Results and discussions.....	124
5.3.2.1 Effect of ammonia.....	124
5.3.2.2 Influence of temperatures and times .....	125
5.3.2.2.1 Growth rate .....	126
5.3.2.2.2 Structural properties of CdS thin films .....	127
5.3.2.2.3 Morphological properties of CdS thin films.....	129
5.3.2.2.4 Compositional analysis of CdS thin films.....	131
5.3.2.2.5 Topographical analysis of CdS thin films.....	132
5.3.2.2.6 Optical properties of CdS thin films .....	133
5.3.2.2.7 Electrical properties of CdS thin films .....	135

5.4 Summary .....	136
References: .....	137
<b>Chapter 6 Simulation study on CI(G)Se thin film solar cells.....</b>	<b>142</b>
6.1 Study on CISE thin film solar cells.....	142
6.1.1 Effect of thicknesses and carrier concentrations of CISE for CISE TFSC.....	142
6.1.2 Influence of thicknesses and carrier concentrations of CdS for CISE TFSC .....	145
6.1.3 Analysis of thicknesses and carrier concentrations of ZnO for CISE TFSC.....	147
6.1.4 Effect of thicknesses and carrier concentrations of ZnO:Al for CISE TFSC.....	149
6.1.5 Optimized conditions for CISE TFSC .....	151
6.2 Study on CIGSe thin film solar cells.....	151
6.2.1 Effect of thicknesses, bandgaps, and carrier concentrations of CIGSe for CIGSe TFSC ..	152
6.2.2 Analysis of thicknesses and carrier concentrations of CdS for CIGSe TFSC .....	156
6.2.3 Influence of thicknesses and carrier concentrations of ZnO for CIGSe TFSC .....	158
6.2.4 Effect of thicknesses and carrier concentrations of ZnO:Al for CIGSe TFSC.....	160
6.2.5 Optimized conditions for CIGSe TFSC .....	161
6.3 Study on CIGSe bilayer thin film solar cells.....	162
6.3.1 Influence of thicknesses and carrier concentrations of CISE for CIGSe bilayer TFSC.....	163
6.3.2 Effect of thicknesses, bandgaps, and carrier concentrations of CIGSe for CIGSe bilayer TFSC .....	165
6.3.3 Analysis of thicknesses, and carrier concentrations of CdS for CIGSe bilayer TFSC .....	169
6.3.4 Effect of thicknesses and carrier concentrations of ZnO for CIGSe bilayer TFSC.....	171
6.3.5 Influence of thicknesses and carrier concentrations of ZnO:Al for CIGSe bilayer TFSC .	173
6.3.6 Optimized conditions for CIGSe bilayer TFSC .....	175
6.4 Fitting experimental results in the simulation .....	176
6.4.1 Study on CISE thin film solar cells .....	176
6.4.2 Analysis on CIGSe thin film solar cells.....	177
6.4.3 Study on CIGSe bilayer thin film solar cells.....	179
6.5 Effect of the defects on the solar cell performance.....	181
6.5.1 Defects in the absorber layer .....	181
6.5.2 Defects in the CdS buffer layer.....	184
6.5.3 Defects at the interface .....	185
6.6 Effect of ambient temperatures on the solar cell performance .....	188
6.7 Influence of parasitic resistances on the solar cell performance.....	189
6.8 Summary .....	191
References: .....	192
<b>Chapter 7 Conclusions .....</b>	<b>197</b>
7.1 General conclusions.....	197
7.2 Future perspectives .....	198
7.3 Research publications and conference activities .....	199
7.3.1 Journal publications .....	199
7.3.2 Conference publications.....	199
7.3.3 Patent publication.....	200
7.3.4 Conference activities.....	201



## List of Figures

Figure No.	Caption	Page No.
Fig. 1.1	Band diagrams for a) an intrinsic semiconductor, b) p-type and c) n-type semiconductor	3
Fig. 1.2	Schematic of a) p-n junction at equilibrium, and b) energy band diagram of p-n homojunction	5
Fig. 1.3	Energy band diagram of p-n heterojunction	7
Fig. 1.4	Schematic diagram of working principle of solar cell	8
Fig. 1.5	The radiation spectrum for Black body, AM0 and AM1.5 global	9
Fig. 1.6	The equivalent circuit of solar cell in the presence of series and shunt resistances	11
Fig. 1.7	The J-V characteristics of solar cell performed on dark and light conditions	11
Fig. 1.8	The current voltage characteristics for ideal and non-ideal conditions	12
Fig. 1.9	Evolution of best laboratory efficiency for different generations of PV (source: National Renewable Energy Laboratory, 2021)	15
Fig. 2.1	Schematic of the structure of CI(G)Se thin film solar cell	27
Fig. 2.2	Chalcopyrite crystal structure of CIGSe unit cell	31
Fig. 2.3	Schematic diagram of a) phase diagram of quaternary elemental (Cu-In-Ga-Se) system, and b) pseudo-binary phase diagram along with the tie line between $\text{Cu}_2\text{Se}$ and $(\text{In,Ga})_2\text{Se}_3$ represented in terms of Cu composition	32
Fig. 2.4	Schematic of the band diagram and recombination mechanisms of CIGSe heterostructure TFSC, showing recombination at 1) back contact, 2) quasi-neutral region, 3) Space charge region, 4) CdS/CIGSe interface	40
Fig. 2.5	The classification of the CI(G)Se thin film deposition methods	41
Fig. 2.6	The schematic of co-evaporation method for CI(G)Se thin film synthesis	42
Fig. 2.7	Schematic of the sputtering systems	45
Fig. 2.8	Schematic of the Particulate-based methods for the deposition of CI(G)Se thin films	48
Fig. 2.9	Schematic of a) pneumatic spray pyrolysis, b) spin coating, and c) doctor blade techniques	51
Fig. 2.10	Schematic image of hybrid deposition method developed for the growth of CI(G)Se thin films	52
Fig. 3.1	Pneumatic spray pyrolysis technique for the deposition of $\text{In}_2\text{Se}_3$ thin films	63
Fig. 3.2	Schematic of a) co-evaporation process, b) deposition process of second and third stages	65
Fig. 3.3	Schematic of a) MTI vacuum oven and b) selenization process used for CI(G)Se thin films	66
Fig. 3.4	Experimental details of CBD method for CdS thin films	68
Fig. 3.5	Schematic diagram of the a) CIGSe TFSC structure, b) CIGSe TFSC structure, and c) CIGSe bilayer TFSC structure generated by SCAPS simulation	69
Fig. 3.6	Schematic representation of thickness monitor	72
Fig. 3.7	Fig. 3.7 Schematic of a) Bruker XRD-D2 phaser and b) an XRD measurement setup	73
Fig. 3.8	Fig. 3.8 Schematic of a) Tescan Vega-3 SEM and b) atomic structure with energy lines	75
Fig. 3.9	Schematic of a) energy level and b) experimental setup for Raman processes	76
Fig. 3.10	Schematic of the NTMDT Ntegra spectra	76
Fig. 3.11	Schematic of atomic force microscope and AFM imaging mode	78
Fig. 3.12	Block diagram of UV-Vis spectrophotometer	79

Fig. 3.13 Schematic of four-probe technique	81
Fig. 3.14 Schematic of Hall effect measurement system	82
Fig. 3.15 Representative test circuit for measuring van der Pauw specimens	82
Fig. 3.16 Example of quantum-efficiency curve and types of loss mechanisms	84
Fig. 4.1 XRD patterns of $\text{In}_2\text{Se}_3$ thin films deposited at three different substrate temperatures	89
Fig. 4.2 Raman spectroscopy of $\text{In}_2\text{Se}_3$ thin films prepared at three different substrate temperatures	90
Fig. 4.3 SEM images of $\text{In}_2\text{Se}_3$ thin films deposited (inserted with FESEM images) at three different substrate temperatures, a) 300, b) 320, and c) 340 °C	91
Fig. 4.4 Schematic diagram of a) EDS spectrum and b) EDS mapping for $\text{In}_2\text{Se}_3$ thin films	91
Fig. 4.5 Schematic of compositional details of $\text{In}_2\text{Se}_3$ thin films	92
Fig. 4.6 2D AFM images of $\text{In}_2\text{Se}_3$ thin films deposited (inserted with 3D images) at three different substrate temperatures, a) 300, b) 320, and c) 340 °C	92
Fig. 4.7 Transmittance of $\text{In}_2\text{Se}_3$ thin films (inserted with bandgap energy diagram) deposited at various substrate temperatures	94
Fig. 4.8 XRD patterns of CISE thin films selenized at different temperatures (i.e., 500, 525, and 550 °C) and times (i.e., 30 and 60 minutes)	95
Fig. 4.9 Raman spectroscopy of CISE thin films selenized at different temperatures (i.e., 500, 525, and 550 °C) and times (i.e., 30 and 60 minutes)	97
Fig. 4.10 SEM images of CISE thin films selenized at different temperatures and times a) 500 °C 30 minutes, b) 525 °C 30 minutes, c) 550 °C 30 minutes, d) 500 °C 60 minutes, e) 525 °C 60 minutes, f) 550 °C 60 minutes	98
Fig. 4.11 EDS spectrum of selenized CISE thin films (at 550 °C for 60 minutes)	99
Fig. 4.12 XRD patterns of CISE thin films deposited at different first stage substrate temperatures of 300, 320, and 340 °C	100
Fig. 4.13 Raman spectroscopy of CISE thin films deposited at three different first stage substrate temperatures of 300, 320, and 340 °C	102
Fig. 4.14 SEM images of CISE thin films deposited at different first stage substrate temperatures a) 300 °C, b) 320 °C, and c) 340 °C	103
Fig. 4.15 Schematic of the a) EDS spectrum and b) EDS mapping of CISE thin films deposited at first stage substrate temperature of 320 °C	104
Fig. 4.16 AFM images of CISE thin films deposited at different first stage substrate temperatures a) 300 °C, b) 320 °C, and c) 340 °C	105
Fig. 4.17 XRD patterns of CIGSe thin films deposited at three different first stage substrate temperatures a) before selenization, and b) after selenization	107
Fig. 4.18 Raman spectroscopy of CIGSe thin films deposited at three different first stage substrate temperatures a) before selenization, and b) after selenization	109
Fig. 4.19 SEM images of the CIGSe thin films (abc) before selenization, (def) after selenization at three different first stage substrate temperatures of 300, 320, and 340 °C	110
Fig. 4.20 Schematic of the EDS spectrum (inserted with EDS mapping) of the CIGSe thin films a) before selenization, b) after selenization	111

Fig. 4.21 AFM images of the CIGSe thin films abc) before selenization, def) after selenization at three different first stage substrate temperatures of 300, 320, and 340 °C	112
Fig. 5.1 Ion by ion mechanism for cadmium sulfide thin film formation on the substrate: i) diffusion of ions, ii) attach of ions on the substrate, iii) nucleation of the ions on the substrate forming CdS nuclei, iv) growth of the CdS film	122
Fig. 5.2 Cluster by cluster mechanism for cadmium sulfide thin film formation on the substrate: i) diffusion of Cd(OH) <sub>2</sub> molecule and sulfur ions, ii) exchange reaction, iii) nucleation of the ions forming CdS nuclei, iv) growth of the CdS film	123
Fig. 5.3 XRD of CdS thin films deposited at various ammonia quantity (from 1:2 to 1:4)	125
Fig. 5.4 SEM of CdS thin film deposited at different ammonia quantity (from 1:2 to 1:4)	125
Fig. 5.5 Graphical representation of growth rate of CdS thin films deposited at different a) deposition temperatures (i.e., 70, 75, 80, 85°C) and b) deposition times (20, 30, 40, 50, 60 minutes)	126
Fig. 5.6 XRD patterns of CdS thin films deposited at different a) deposition temperatures (i.e., 70, 75, 80, 85°C), and b) deposition times (i.e., 20, 30, 40, 50, 60 minutes)	128
Fig. 5.7 Raman spectra of CdS thin films deposited at different a) deposition temperatures (i.e., 70, 75, 80, 85°C) and b) deposition times (i.e., 20, 30, 40, 50, 60 minutes)	129
Fig. 5.8 SEM images of CdS thin films deposited at different a-d) deposition temperatures (i.e., 70, 75, 80, 85°C) and i-v) deposition times (i.e., 20, 30, 40, 50, 60 minutes)	130
Fig. 5.9 Schematic of a) EDS spectrum and b) EDS Mapping of CdS thin films deposited at 80 °C for 30 min	131
Fig. 5.10 AFM images (2D images with area of 2x2 μm <sup>2</sup> ) of CdS thin films deposited at different deposition a-d) temperatures (i.e., 70, 75, 80, 85°C) and i-v) times (i.e., 20, 30, 40, 50, 60 minutes)	132
Fig. 5.11 Transmittance of CdS thin films (inserted with bandgap energy diagram) deposited at different a) deposition temperatures (i.e., 70, 75, 80, 85°C) and b) deposition times (i.e., 20, 30, 40, 50, 60 minutes)	134
Fig. 5.12 The PL spectra of CdS thin films deposited at different a) deposition temperatures (i.e., 70, 75, 80, 85°C) and b) deposition times (i.e., 20, 30, 40, 50, 60 minutes)	135
Fig. 6.1 Schematic of a) J-V curve of CIGSe TFSC inserted with QE curve, b) the solar cell parameter curve at different CIGSe thickness	143
Fig. 6.2 Schematic of a) J-V curve of CIGSe TFSC inserted with QE curve, b) the solar cell parameter curve at different carrier concentration of CIGSe absorber layer	145
Fig. 6.3 Schematic of a) J-V curve of CIGSe TFSC inserted with QE curve, b) the solar cell parameter curve at different CdS thickness	146
Fig. 6.4 Schematic of a) J-V curve of CIGSe TFSC inserted with QE curve, b) the solar cell parameter curve at different carrier concentration of CdS buffer layer	147
Fig. 6.5 Schematic of a) J-V curve of CIGSe TFSC inserted with QE curve, b) the solar cell parameter curve at different ZnO window layer thickness	148
Fig. 6.6 Schematic of a) J-V curve of CIGSe TFSC inserted with QE curve, b) the solar cell parameter curve at different carrier concentration of ZnO window layer	149
Fig. 6.7 Schematic of a) J-V curve of CIGSe TFSC inserted with QE curve, b) the solar cell	

parameter curve at different thickness of ZnO:Al TCO	150
Fig. 6.8 Schematic of a) J-V curve of CIGSe TFSC inserted with QE curve, b) the solar cell	
parameter curve at different carrier concentration of ZnO:Al TCO	150
Fig. 6.9 Schematic of the J-V characteristics curve for optimized CIGSe TFSC inserted with QE curve	151
Fig. 6.10 Schematic of a) J-V curve of CIGSe TFSC inserted with QE curve, b) the solar cell	
parameter curve at different CIGSe thicknesses	153
Fig. 6.11 Schematic of a) J-V curve of CIGSe TFSC inserted with QE curve, b) the solar cell	
parameter curve at different CIGSe bandgaps	154
Fig. 6.12 Schematic of a) J-V curve of CIGSe TFSC inserted with QE curve, b) the solar cell	
parameter curve at different CIGSe carrier concentrations	155
Fig. 6.13 Schematic of a) J-V curve of CIGSe TFSC inserted with QE curve, b) the solar cell	
parameter curve at different CdS thicknesses	157
Fig. 6.14 Schematic of a) J-V curve of CIGSe TFSC inserted with QE curve, b) the solar cell	
parameter curve at different CdS carrier concentrations	158
Fig. 6.15 Schematic of a) J-V curve of CIGSe TFSC inserted with QE curve, b) the solar cell	
parameter curve at different ZnO thicknesses	159
Fig. 6.16 Schematic of a) J-V curve of CIGSe TFSC inserted with QE curve, b) the solar cell	
parameter curve at different ZnO carrier concentrations	159
Fig. 6.17 Schematic of a) J-V curve of CIGSe TFSC inserted with QE curve, b) the solar cell	
parameter curve at different ZnO:Al thicknesses	161
Fig. 6.18 Schematic of a) J-V curve of CIGSe TFSC inserted with QE curve, b) the solar cell	
parameter curve at different ZnO:Al carrier concentrations	161
Fig. 6.19 Schematic of the J-V curve of optimized CIGSe TFSC inserted with QE curve	162
Fig. 6.20 Schematic of a) J-V curve of CIGSe bilayer TFSC inserted with QE curve, b) the solar cell	
parameter curve at different CIGSe thicknesses	164
Fig. 6.21 Schematic of a) J-V curve of CIGSe bilayer TFSC inserted with QE curve, b) the solar cell	
parameter curve at different CIGSe carrier concentrations	165
Fig. 6.22 Schematic of a) J-V curve of CIGSe bilayer TFSC inserted with QE curve, b) the solar cell	
parameter curve at different CIGSe thicknesses	166
Fig. 6.23 Schematic of a) J-V curve of CIGSe bilayer TFSC inserted with QE curve, b) the solar cell	
parameter curve at different CIGSe bandgaps	167
Fig. 6.24 Schematic of a) J-V curve of CIGSe bilayer TFSC inserted with QE curve, b) the solar cell	
parameter curve at different CIGSe carrier concentrations	168
Fig. 6.25 Schematic of a) J-V curve of CIGSe bilayer TFSC inserted with QE curve, b) the solar cell	
parameter curve at different CdS thicknesses	170
Fig. 6.26 Schematic of a) J-V curve of CIGSe bilayer TFSC inserted with QE curve, b) the solar cell	
parameter curve at different CdS concentrations	171
Fig. 6.27 Schematic of a) J-V curve of the CIGSe bilayer TFSC inserted with QE curve, b) the	
solar cell parameter curve at different ZnO thicknesses	172
Fig. 6.28 Schematic of a) J-V curve of CIGSe bilayer TFSC inserted with QE curve, b) the solar cell	

parameter curve at different ZnO carrier concentrations	173
Fig. 6.29 Schematic of a) J-V curve of CIGSe bilayer TFSC inserted with QE curve, b) the solar cell parameter curve at different ZnO:Al thicknesses	174
Fig. 6.30 Schematic of a) J-V curve of the CIGSe bilayer TFSC inserted with QE curve, b) the solar cell parameter curve at different ZnO:Al carrier concentrations	174
Fig. 6.31 Schematic of the J-V curve of the optimized CIGSe bilayer TFSC inserted with QE curve	175
Fig. 6.32 Schematic of a) J-V curves of CIGSe TFSC b) solar cell parameter curve after analyzing the experimental results of CIGSe absorber layer and CdS buffer layer	177
Fig. 6.33 Schematic of a) J-V curves of CIGSe TFSC b) solar cell parameter curve after analyzing the experimental results of CIGSe absorber layer and CdS buffer layer	179
Fig. 6.34 Schematic of a) J-V curves of the CIGSe bilayer TFSC b) solar cell parameter curve after analyzing the experimental results of CIGSe, CIGSe, and CdS thin films	180
Fig. 6.35 J-V curves for a) CIGSe TFSC, b) CIGSe TFSC and c) CIGSe bilayer TFSC, and solar cell parameter curves for i) CIGSe TFSC, ii) CIGSe TFSC and c) CIGSe bilayer TFSC at different defect densities in absorber layer	182
Fig. 6.36 J-V curves for a) CIGSe TFSC, b) CIGSe TFSC and c) CIGSe bilayer TFSC, and solar cell parameter curves for i) CIGSe TFSC, ii) CIGSe TFSC and c) CIGSe bilayer TFSC at different CCCS in absorber layer	183
Fig. 6.37 J-V curves for a) CIGSe TFSC, b) CIGSe TFSC and c) CIGSe bilayer TFSC, and solar cell parameter curves for i) CIGSe TFSC, ii) CIGSe TFSC and c) CIGSe bilayer TFSC at different defect densities in CdS buffer layer	184
Fig. 6.38 J-V curves for a) CIGSe TFSC, b) CIGSe TFSC and c) CIGSe bilayer TFSC, and solar cell parameter curves for i) CIGSe TFSC, ii) CIGSe TFSC and c) CIGSe bilayer TFSC at different CCCS in CdS buffer layer	185
Fig. 6.39 J-V curves for a) CIGSe TFSC, b) CIGSe TFSC and c) CIGSe bilayer TFSC, and solar cell parameter curves for i) CIGSe TFSC, ii) CIGSe TFSC and c) CIGSe bilayer TFSC at different defect densities in the interface	187
Fig. 6.40 J-V curves for a) CIGSe TFSC, b) CIGSe TFSC and c) CIGSe bilayer TFSC, and solar cell parameter curves for i) CIGSe TFSC, ii) CIGSe TFSC and c) CIGSe bilayer TFSC at different CCCS in the interface	187
Fig. 6.41 J-V curves for a) CIGSe TFSC, b) CIGSe TFSC and c) CIGSe bilayer TFSC, and solar cell parameter curves for i) CIGSe TFSC, ii) CIGSe TFSC, and iii) CIGSe bilayer TFSC at different ambient temperatures	189
Fig. 6.42 J-V curves for a) CIGSe TFSC, b) CIGSe TFSC, and c) CIGSe bilayer TFSC, and solar cell parameter curves for i) CIGSe TFSC, ii) CIGSe TFSC and iii) CIGSe bilayer TFSC at different series resistances	190
Fig. 6.43 J-V curves for a) CIGSe TFSC, b) CIGSe TFSC, and c) CIGSe bilayer TFSC, and solar cell parameter curves for i) CIGSe TFSC, ii) CIGSe TFSC and iii) CIGSe bilayer TFSC at different shunt resistances	191

## List of Tables

Table No.	Caption	Page No.
Table 3.1	Parameters used in SCAPS software for analyzing the CISE TFSC	69
Table 3.2	Parameters used in SCAPS software for analyzing the CIGSe TFSC	70
Table 3.3	Parameters used in SCAPS software for analyzing the CIGSe-bilayer TFSC	70
Table 4.1	Structural parameters for In <sub>2</sub> Se <sub>3</sub> thin films deposited by PSP technique	89
Table 4.2	Topographical parameters for In <sub>2</sub> Se <sub>3</sub> thin films measured from AFM	93
Table 4.3	Structural parameters for CISE thin films selenized at different temperatures, and times	96
Table 4.4	Compositional analysis for CISE thin films selenized at different temperatures, and times	99
Table 4.5	Structural parameters for CISE thin films deposited at different first stage substrate temperatures	101
Table 4.6	Compositional analysis for CISE thin films deposited at different first stage substrate temperatures	104
Table 4.7	Topographical parameters for CISE thin films deposited at different first stage substrate temperatures	105
Table 4.8	Electrical parameters for CISE thin films deposited at different first stage substrate temperatures	106
Table 4.9	Structural parameters for CIGSe thin films before and after selenization at different first stage substrate temperatures	108
Table 4.10	Compositional analysis for CIGSe thin films before and after selenization at different first stage substrate temperatures	111
Table 4.11	Topographical parameters for CIGSe thin films before and after selenization at different first stage substrate temperatures	113
Table 4.12	Electrical properties for CIGSe thin films before and after selenization at different first stage substrate temperatures	114
Table 5.1	Calculated structural parameters of CdS thin films deposited different times and temperatures	128
Table 5.2	Compositional analysis of CdS thin films	131
Table 5.3	Parameters such as average grain size, average roughness, RMS roughness, skewness, kurtosis calculated from AFM	133
Table 5.4	Electrical properties of CdS thin films prepared by CBD method	136
Table 6.1	Parameters used in CISE TFSC at different CISE thicknesses	143
Table 6.2	Parameters used in CISE TFSC at different carrier concentrations of CISE	144
Table 6.3	Parameters used in CISE TFSC at different CdS thicknesses	146
Table 6.4	Parameters used in CISE TFSC at different carrier concentrations of CdS	147
Table 6.5	Parameters used in CISE TFSC at different thicknesses and carrier concentrations of ZnO	148
Table 6.6	Parameters used in CISE TFSC at different thicknesses and carrier concentrations	

of ZnO:Al	150
Table 6.7 Parameters used in CIGSe TFSC at different CIGSe thicknesses	153
Table 6.8 Parameters used in CIGSe TFSC at different bandgaps of CIGSe	154
Table 6.9 Parameters used in CIGSe TFSC at different carrier concentrations of CIGSe	155
Table 6.10 Parameters used in CIGSe TFSC at different CdS thicknesses	156
Table 6.11 Parameters used in CIGSe TFSC at different carrier concentrations of CdS	158
Table 6.12 Parameters used in CIGSe TFSC at different thicknesses and carrier concentrations of ZnO	160
Table 6.13 Parameters used in CIGSe TFSC at different thicknesses and carrier concentrations of ZnO:Al	161
Table 6.14 Parameters used in CIGSe bilayer TFSC at different CIGSe thicknesses	163
Table 6.15 Parameters used in CIGSe bilayer TFSC at different carrier concentrations of CIGSe	164
Table 6.16 Parameters used in CIGSe bilayer TFSC at different CIGSe thicknesses	166
Table 6.17 Parameters used in CIGSe bilayer TFSC at different bandgaps of CIGSe	167
Table 6.18 Parameters used in CIGSe bilayer TFSC at different carrier concentrations of CIGSe	168
Table 6.19 Parameters used in CIGSe bilayer TFSC at different CdS thicknesses	169
Table 6.20 Parameters used in CIGSe bilayer TFSC at different carrier concentrations of CdS	171
Table 6.21 Parameters used in CIGSe bilayer TFSC at different thicknesses and carrier concentrations of ZnO	172
Table 6.22 Parameters used in CIGSe bilayer TFSC at different thicknesses and carrier concentrations of ZnO:Al	174
Table 6.23 Experimental results of CIGSe and CdS materials	177
Table 6.24 Experimental results of CIGSe and CdS materials	178
Table 6.25 Experimental results of CIGSe, CIGSe and CdS materials	180

## List of Acronyms/Abbreviations

Acronym	Definition of Acronym
PV	Photovoltaic
$E_v$	Valence band
$E_c$	Conduction band
Si	Silicon
C60	Buckminsterfullerene
GaAs	Gallium arsenide
CdTe	Cadmium telluride
InGaAs	Indium gallium arsenide
Cu(In,Ga)Se <sub>2</sub> (CIGSe)	Copper indium gallium diselenide
CuInSe <sub>2</sub> (CISe)	Copper indium diselenide
CI(G)Se	CIGSe-based
$E_f$	Fermi energy
SCR	Space charge region
CdS	Cadmium sulfide
$\Delta E_c$	Conduction band offset
$\Delta E_v$	Valence band discontinuity
AM	Air mass
AM0	Air mass zero
AM1.5G	Air mass 1.5 global
$J_{sc}$	Short circuit current density
$V_{oc}$	Open circuit voltage
FF	Fill factor
PCE	Photovoltaic cell efficiency
$R_s$	Series resistance
$R_{sh}$	Parallel (or shunt) resistance
$P_{max}$	Maximum power density
$P_o$	Ideal power density
a-Si	Amorphous silicon
SCAPS	Solar cell capacitance simulator
$E_g$	Bandgap
$\chi$	Electron affinity
$\epsilon$	Dielectric permittivity
$V_{th}$	Thermal velocity
$\mu$	Mobility
$N_D$	Donor density
$N_A$	Acceptor density
$N_t$	Defect density



$\sigma$	Capture cross-section
ZnO	Zinc oxide
ZnO:Al	Aluminum doped zinc oxide
SLG	Soda lime glass
Cu	Copper
In	Indium
Ga	Gallium
Se	Selenium
In <sub>2</sub> Se <sub>3</sub>	Indium selenide
InCl <sub>3</sub>	Indium Chloride
NH <sub>2</sub> (CH <sub>3</sub> ) <sub>2</sub> NCSe	N, N-dimethyl-selenourea
Mo	Molybdenum
MoSe <sub>2</sub>	Molybdenum diselenide
TFSC(s)	Thin film solar cell(s)
TCO	Transparent conducting oxide
DC sputtering	Direct current sputtering
RF sputtering	Radio frequency sputtering
NHE	Normal hydrogen electrode
pH	Potential of hydrogen
XRD	X-ray diffraction
SEM	Scanning electron microscopy
EDS	Energy dispersive X-ray spectroscopy
AFM	Atomic force microscopy
UV-Vis	Ultraviolet-visible
PSP	Pneumatic spray pyrolysis
CBD	Chemical bath deposition
$\tau_{n, p}$	Carrier lifetime
$D_{n, p}$	Diffusion coefficient
$L_{Diff}$	Diffusion length
FWHM	Full width half maximum
EM	Electromagnetic
$\alpha$	Absorption coefficient
$h\nu$	Photon energy
$\rho$	Resistivity
$R_H$	Hall coefficient
QE	Quantum efficiency
ICDD	International center for diffraction data
PL	Photoluminescence
CCCS	Carrier capture cross-section

# Chapter 1 Introduction

## 1.1 Introduction of energy sources

Energy is required for a wide range of applications such as transportation, industries, agriculture, household applications, etc. The use of energy plays an essential role in individual and nation development, including quality of life index, life expectancy, water access, literacy rates, per capita income [1, 2], etc. The world energy demand is ever-growing and expects to grow further in the future due to the growth in the world's population, the development of human civilization, and the industrial revolution [3]. The worldwide energy supply is currently based on non-renewable fossil fuels such as coal, oil, gas, etc. But these energy sources have raised concern due to their limited quantity and environmental impact. Generally, these energy sources are combusted to derive useful energy that drives the emissions of greenhouse gases like nitrous oxide ( $\text{N}_2\text{O}$ ), carbon dioxide ( $\text{CO}_2$ ), methane ( $\text{CH}_4$ ), and other pollutants [4, 5]. The average global temperature rises with an increase in greenhouse gas emissions and finally affects the ecological system. Non-renewable energy sources are not uniformly available worldwide, increasing the cost of energy sources to use in all parts of the world. The formation of non-renewable fossil fuels takes a long time. So that it is challenging to recover in time once they are gone, this problem could result in conflicts and unstable pricing of these fossil fuels. Hence, there is essential for alternative energy sources that should be secure, sustainable, economical, environmentally friendly, and socially acceptable.

Renewable energy comes from the natural flow of wind, sunlight, water, or biological material around the world. These energy sources are abundantly, everlastingly, uniformly, and freely available on the earth, providing security for future development and growth. All renewable energy sources such as hydropower, wind energy, geothermal, biomass, solar energy, etc., are not equivalent in terms of the energy scale. Solar energy is the most promising clean, safe, and abundant energy source among different renewable energy sources, which can meet global energy demands [7, 8]. The main motivation to use solar energy for energy production is its huge energy (i.e., around 14 TWyr) reaching the earth's surface every day, which is the world's present energy consumption in one year. Apart from sunlight and heat, the sun's energy has the advantage of forming other types of sources,

including biomass, wind energy, hydroelectric energy, and conventional energy sources indirectly. Solar energy can be harnessed directly in electrical energy, which is the most convenient and versatile form of energy, by using photovoltaic devices or solar cells containing semiconductors. A solar cell is a p-n junction semiconductor device. For understanding the design and operation of solar cells, it is necessary to review the fundamentals of semiconductors and the crucial principles of solar cells.

## 1.2 Semiconductor and solar cell physics

### 1.2.1 Semiconductors

The elements can be classified into three sections: a conductor, an insulator, and a semiconductor. A conductor contains a large number of free electrons and has high conductivity. An insulator has no free electrons, a huge forbidden energy gap, and low conductivity. The semiconductor is a material whose electrical conductivity magnitude lies between that of a conductor and an insulator. Semiconductors are considered the foundation of the modern electronics industry. There are mainly two types of semiconductors: elemental semiconductor (such as Si, Ge, Se, C60, etc.) and the other is a compound semiconductor (i.e., GaAs, CdTe, InGaAs, ClSe, ClGSe, etc.) [9, 10]. Semiconductor materials at 0 K have completely filled valence bands and completely empty conduction bands (i.e., behave like an insulator), which is not suitable to carry current. At higher temperatures ( $T > 0$ ), electrons are excited from the valence band to the conduction band by breaking the bond. The presence of free electrons in a conduction band at higher temperatures conducts current and behaves as a conductor. The electrons' occupation in the conduction band and valence band states vary with ambient temperature, which is determined by the Fermi-Dirac distribution function and is given by [11, 12],

$$f(E) = \frac{1}{1 + \exp\left(\frac{E - E_f}{KT}\right)} \quad (\text{eq. 1.1})$$

where  $K$  is the Boltzmann constant ( $8.62 \times 10^{-5}$  eV/K),  $T$  is an absolute temperature in kelvin,  $E_f$  is the Fermi energy, and  $f(E)$  is the Fermi-Dirac function, which determines the probability of electron occupancy at energy level 'E' at absolute temperature. The above-mentioned Fermi-Dirac distribution function is valid only under equilibrium conditions, and

its value can vary between 0 and 1. The unity value of  $f(E)$  at energy level  $E$  suggests the probability that an electron occupying that energy level is 100%. On the other hand, the zero percent probability of an electron will occupy in the energy level  $E$  is found for the zero value of  $f(E)$ . The probability that a hole will occupy at energy level  $E$  is given by  $[1 - f(E)]$ . The Fermi level is the energy level at which the 50% probability of an electron occupying that level. The band diagram of intrinsic, n-type, and p-type semiconductors is shown in Fig. 1.1. The  $E_f$  lies almost in the middle between the conduction band and valence band for an intrinsic semiconductor. At  $T=0$  K, the value of  $f(E)$  is nonzero for all energy levels below the  $E_f$  and zero for all energy levels above  $E_f$ . At  $T>0$  K, the probability of an electron occupying a conduction band edge energy level is nonzero because some electrons will get enough energy to get excited to the conduction band. In a p-type semiconductor, there are more holes than electrons as compared to an intrinsic semiconductor. The higher probability of an electron occupying an energy state  $E$  is in the valence band, shifting the  $f(E)$  towards the valence band. Therefore, the  $E_f$  lies near to valence band. More electrons than holes are found in an n-type semiconductor compared to an intrinsic semiconductor. The  $f(E)$  shifts towards the conduction band due to the higher probability of an electron occupying an energy level in the conduction band. As a result of this, the  $E_f$  lies closer to the conduction band [12].

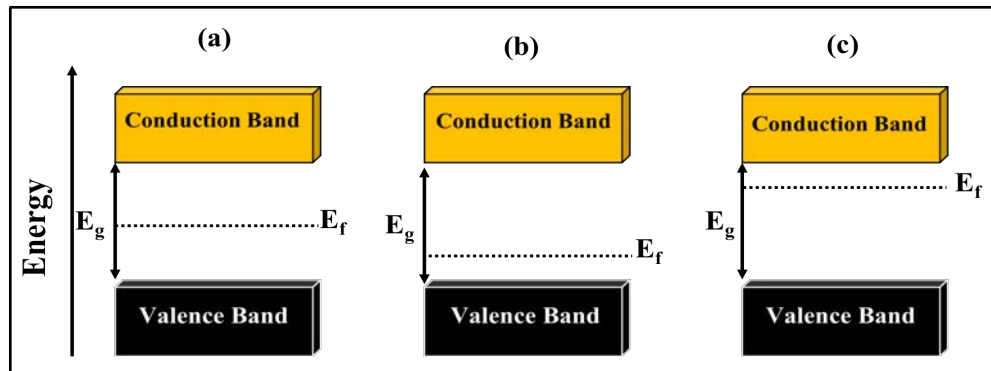


Fig. 1.1 Band diagrams for a) an intrinsic semiconductor, b) p-type and c) n-type semiconductor

The forbidden energy is the minimum energy required to excite an electron from the valence band's top level or lower energy band ( $E_v$ ) to the bottom of the conduction band or higher energy band ( $E_c$ ). There are two types of bandgap for semiconductors depending on the electronic band structure, indirect and direct bandgap. In the indirect bandgap semiconductor, the excitation of an electron from the valence band to the conduction band requires absorption of the photon and absorption of a phonon (i.e., high momentum). The

only absorption of a photon is sufficient for an electron transition from the valence to the conduction band in the direct bandgap semiconductor. A semiconductor can divide into two parts, intrinsic and extrinsic semiconductors. An intrinsic semiconductor is an ideal semiconductor with no lattice defects and no impurities, whose both bands contain an equal number of electrons and holes after thermal excitation. An extrinsic semiconductor is formed by adding impurities into the semiconductor that causes the different value of the electrons and holes in both conduction and valence bands. Both type semiconductors, n-type and p-type, are made by doping a semiconductor with donor and acceptor impurities, respectively. The impurities atoms that create free electrons (or holes) are called donors (or acceptors). The conductivity of a semiconductor can vary by adding impurities in it through the variation of the concentration of charge carriers.

### **1.2.2 p-n junction**

A p-n junction is formed by sandwiching the p-type semiconductor and n-type semiconductor. In isolation, a p-type semiconductor has more holes than electrons and vice versa. Thus, electrons and holes act as mobile charge carriers in the n- and p-type semiconductor materials. Once these two semiconductors come in contact with each other, the thermal equilibrium of each system is lost. Depending on the types of semiconductor materials used in the p-n junction formation, the p-n junction structure divides into homojunction and heterojunction. A thorough understanding of the p-n junction is necessary to understand the solar cell's behavior and its operation.

#### **1.2.2.1 Homojunction**

A p-n homojunction is formed using the same semiconductor materials with a different type of doping (e.g., p-type silicon with n-type silicon). A p-type and n-type semiconductors are produced by doping acceptor and donor impurities into an intrinsic semiconductor, respectively. After sandwiching p-type and n-type semiconductors, free electrons diffuse from the n-side to the p-side, and holes diffuse from the p-side to the n-side. As an electron crosses, it leaves behind a fixed positive charge in the form of ionized donor impurities. Similarly, holes diffuse from p-side to n-side and leave behind fixed negative charges in the form of ionized acceptor impurities. The region with a layer of positive charges and a layer

of negative charges is known as the space charge region (SCR) or depletion region. The region outside the SCR also called the quasi-neutral region, is electrically neutral at both the n-side and p-side.

The separation of negative and positive charges across the junction results in an electric field built-up, pointed from the n-side to the p-side. An electric field in the SCR creates a potential barrier between the two semiconductors called voltage drop or built-in potential [7, 14]. Finally, an equilibrium is established in the depletion region and hence stops the further diffusion of electrons from the n-region and holes from the p region. The schematic diagram of the p-n junction at equilibrium is presented in Fig. 1.2. Once the magnitudes of diffusion and drift currents equal one another, it results in no net flow. The Fermi level at equilibrium is constant throughout the entire system. If the charge carriers are created inside the SCR, these charge carriers (electron and hole) will drift in the electric field and cause holes to move into the p-region and electrons into the n-region. The recombination probability of charge carriers is low at SCR. Therefore, the generated charge carriers outside the SCR need to be transported to the SCR to prevent the recombination process. This transportation or diffusion process of charge carriers from quasi-neutral region to SCR represents a high recombination probability. The parameters such as diffusion length and lifetime of charge carrier are vital for reducing the recombination rate and improving the device's performance. Diffusion length is the average distance a charge carrier can travel before it recombines with another carrier, and lifetime is the amount of time the charge carriers generated away from the electric field remain active.

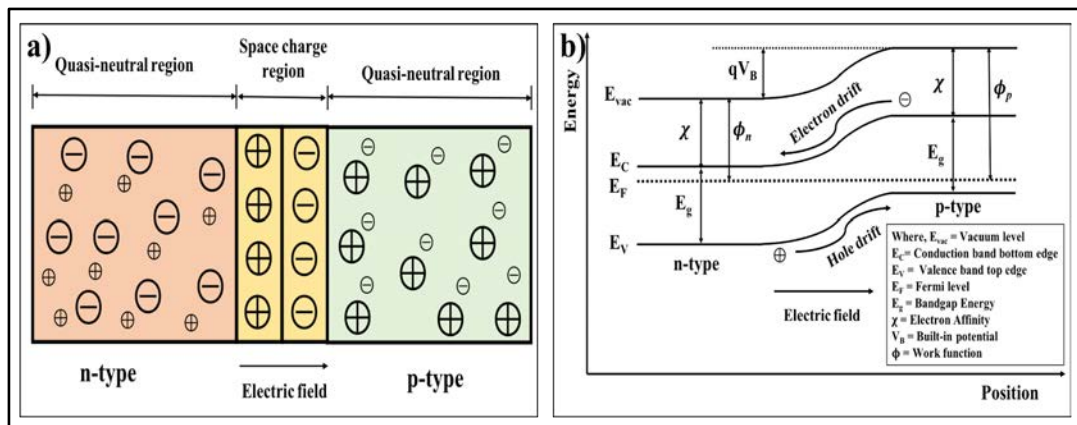


Fig. 1.2 Schematic of a) p-n junction at equilibrium, and b) energy band diagram of p-n homojunction

### 1.2.2.2 Heterojunction

A p-n heterojunction is a junction that combines two different types of semiconductor materials (e.g., CuInGaSe<sub>2</sub>/CdS, CdTe/CdS). This p-n heterojunction is classified into an isotype and an anisotype heterojunctions. An isotype heterojunction is formed when two semiconductors with similar conductivity, different bandgaps and lattice constants are brought together. In contrast, an anisotype heterojunction is formed by sandwiching two semiconductors with different conductivities. The band bending of heterojunction is not smoother than that of homojunction. This different band bending in heterojunction is mainly due to the difference in other electronic properties, remarkably different bandgaps, electron affinities, work functions, etc. This difference causes interface states or discontinuities in the valence band and conduction band that affect the flow of electrons (holes) by presenting a barrier in the junction and can form the recombination centers. The junction's stability, chemical compatibility between materials, and the reproducibility of the physical and chemical interface are also affected. The formation of a buried junction (i.e., n-type layer creation into the p-type material) and the inversion of the interface by forming an n<sup>+</sup>p interface in the absorber layer are two main approaches to reduce the defects found in heterojunction.

There are several advantages of using heterojunction over homojunction in solar cells. Heterojunction solar cells use the semiconductors with an unequal bandgap, normally a wider bandgap of the window layer than the absorber layer. This combination can overcome the surface recombination problems faced in homojunction solar cells. Heterojunction can also improve the efficiency by enhancing the absorption of more photons along with short-wavelength photons in the absorber layer. The semiconductors used in this combination have special properties such as direct bandgap and high absorption coefficient that can absorb solar energy in a few micrometers of semiconductor's thicknesses, reducing the device cost. Furthermore, the defect levels at the interface can reduce in the heterojunction by the formation of buried junction as well as inversion of the junction [14–16]. Fig.1.3 shows the energy band diagram of heterojunction. When the electronic affinity of the p-type absorber layer ( $\chi_p$ ) is greater than the electronic affinity of the n-type window layer ( $\chi_n$ ), a spike (also called conduction band offset) forms in the conduction band. This spike acts as a potential barrier that controls the motion of the minority charge carriers through the p-n junction itself.

at illumination. On the other hand, another discontinuity called cliff is formed in the valence band if the  $\chi_n$  value is bigger than the  $\chi_p$  value. The cliff limits the diffusion of charge carriers through the junction by creating the built-in junction potential. This built-in potential weakens the junction's electric field and reduces the space charge region, which negatively affects the device's performance. By choosing an appropriate junction partner to the absorber layer, the spike and cliff can be minimized and improve the current flow in a solar cell. The magnitude of conduction band offset ( $\Delta E_c$ ), and valence band discontinuity ( $\Delta E_v$ ) is described below [12].

$$\Delta E_c = \chi_p - \chi_n \quad (\text{eq. 1.2})$$

$$\Delta E_v = E_{gn} - E_{gp} - \Delta E_c \quad (\text{eq. 1.3})$$

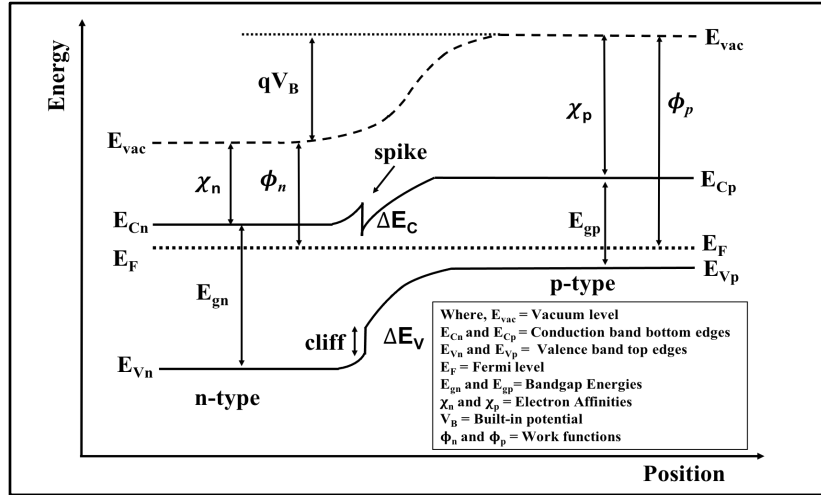


Fig. 1.3 Energy band diagram of p-n heterojunction

### 1.2.3 Working principle of solar cell

Since a solar cell is a p-n junction diode, it is used to convert solar energy directly into electricity. The solar cell's working principle is mainly based on the photovoltaic effect (or photoelectric effect), where sunlight with energy greater than the material's bandgap is absorbed by generating electrons in the conduction band. This effect can be explained by assuming that the sunlight consists of energy quanta, called photons. Depending on their wavelength values, each photon carries a specific amount of energy. The energy of such a photon is expressed by the following equation [16],



$$E_p = \frac{hc}{\lambda} \approx \frac{1.24 \text{ eV} \cdot \mu\text{m}}{\lambda(\mu\text{m})} \quad (\text{eq. 1.4})$$

where,  $E_p$  is the photon energy in electron volts,  $h$  is the Planck's constant ( $6.626 \times 10^{-34}$  Js),  $c$  is the speed of light in vacuum ( $3.0 \times 10^8 \text{ ms}^{-1}$ ), and  $\lambda$  is the wavelength of photon. When the p-n junction is illuminated, the photons whose energy is greater than the bandgap of the semiconductor material are absorbed, and electrons are excited to the semiconductor's conduction band. If the energy of the photon is smaller than the semiconductor bandgap, it will not be absorbed but will traverse the material without interaction. The basic operation of the solar cell (see Fig. 1.4) involves the following steps [9, 10, 18]:

- i. Absorption of photons
- ii. Generation of charge carriers (i.e., creation of electron-hole pairs)
- iii. Separation of generated charge carriers with the help of built electric field at depletion region or recombination of these charge carriers
- iv. Finally, collection of those separated charge carriers by an external circuit

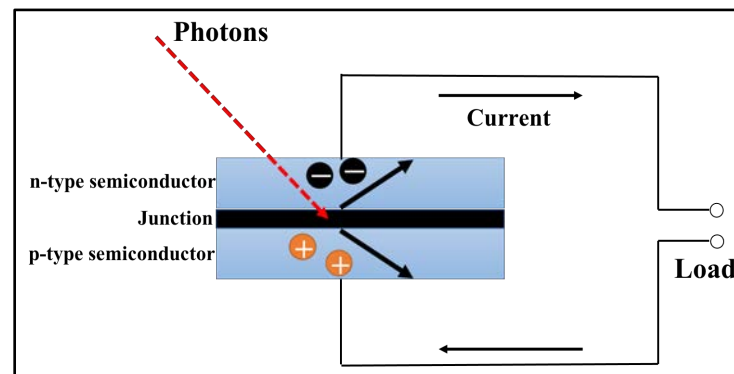


Fig. 1.4 Schematic diagram of working principle of solar cell

The spectral nature of sunlight has to be considered in choosing the semiconductor material for solar cells. Sunlight is a polychromatic light; its spectrum is much like the black body spectrum at 5762 K. Solar constant is the intensity of sunlight in the free space at the earth's average distance from the sun. Air mass (AM) measures how the atmosphere affects the solar spectrum entering the earth's surface. The spectral distribution air mass zero (AM0) describes the solar irradiance in space corresponding to the solar constant of  $1353 \text{ Wm}^{-2}$ . The value of AM0 is unaffected by the earth's atmosphere. The spectrum air mass 1.5 global (AM1.5G) is the solar spectrum falling on the earth's surface. AM1.5G is generally used to

evaluate solar cell performance, which contains incident powers of  $1000 \text{ Wm}^{-2}$ . This change in the radiation intensity is due to the absorption or scattering of the radiation by air molecules, clouds, and particles present in the earth's atmosphere. Fig. 1.5 displays the radiation spectrum for the black body, AM0, and AM1.5G. It is observed from Fig. 1.5 that the maximum sunlight radiation is between 250 and 1000 nm (i.e., photon energy in the range of 1.24 to 4.96 eV). The wavelength of ultraviolet (UV) region, visible region, and near-infrared region corresponds in the range from 10 to 400 nm, 400 to 700 nm, and 750 to 2500 nm. Understanding this spectrum makes it possible to select a suitable semiconductor and design a high-efficiency solar cell.

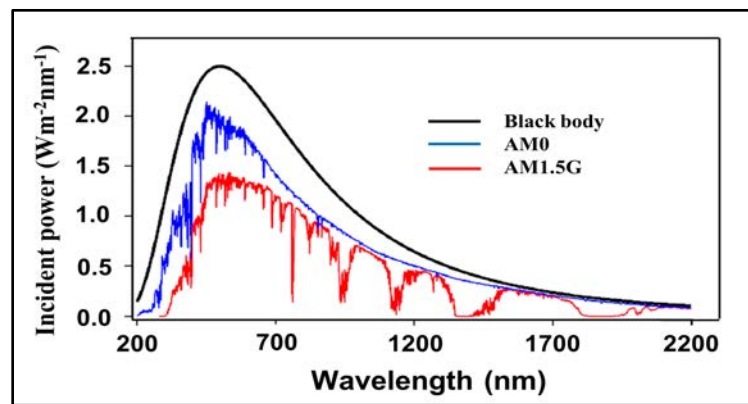


Fig. 1.5 The radiation spectrum for Black body, AM0 and AM1.5 global [8]

#### 1.2.4 Basic characteristics of solar cell

Solar cells are characterized and compared with each other with four parameters: short circuit current density ( $J_{sc}$ ), open circuit voltage ( $V_{oc}$ ), fill factor (FF), photovoltaic cell efficiency (PCE). The equivalent circuit of solar cells in the presence of series and shunt resistances is presented in Fig. 1.6. Two different currents are considered for a single-diode model: reverse photocurrent and a forward current corresponding to the diode. The performance of solar cell devices is mainly limited by series resistance ( $R_s$ ) and parallel (or shunt) resistance ( $R_{sh}$ ) of the solar cell. The  $R_s$  in a solar cell combines the resistances of the semiconductor materials, electrical contacts, and connecting wires. The shunt resistance is reduced due to pin-holes present in a solar cell or the crystal defects or precipitates of impurities in the junction resulting in alternative paths and recombination centers for generated charge carriers. The  $R_s$  and  $R_{sh}$  values are respectively considered to be zero and infinity in an ideal solar cell. The current density is the ratio between current ( $I$ ) and the

surface area of the solar cell (A). In an ideal case, the current density-voltage (J-V) curve of a solar cell equals a p-n junction diode shifted by the photogenerated current. Fig. 1.7 shows the J-V characteristics of solar cells performed in dark and light conditions. The total current density for an ideal solar cell is expressed as the sum of the dark current density and light current density and is given by the following equation [14],

$$J = J_{\text{dark}} + J_{\text{light}} = J_0 \left[ \exp \left( \frac{qV}{nKT} \right) - 1 \right] - J_L \quad (\text{eq. 1.5})$$

where, J is the current density of the diode, n is the ideality factor (n = 1 for ideal case), KT is the product of Boltzmann constant and absolute temperature, and V is the applied voltage. The  $J_{\text{sc}}$  is the maximum current density in a solar cell when no load or resistance is applied. The  $J_{\text{sc}}$  value usually depends on the absorption coefficient of the absorber materials, the range of photons (their number and energy), band gap of the material, recombination in the material. The  $V_{\text{oc}}$  is the maximum voltage generated across the solar cell when equivalent circuit of solar cell kept open (i.e., at zero current). The  $V_{\text{oc}}$  depends on the light-generated current and reverse saturation current. It is mainly limited by the absorber material's bandgap, ambient temperature, built-in voltage and shunt resistance of the solar cell. Another parameter to describe the quality of solar cells is the FF. FF is the ratio of maximum power density ( $P_{\text{max}} = V_{\text{max}} \times J_{\text{max}}$ ) that can extract from solar cell to the ideal power density ( $P_0 = V_{\text{oc}} \times J_{\text{sc}}$ ). FF measures the perfect shape or squareness of the current-voltage curve of solar cells and is mainly related to the resistive losses in a solar cell. The PCE of solar cell is defined as the ratio of the output power by the solar cell to the input power. The PCE changes on the spectrum and intensity of the incident sunlight and the temperature of the solar cell. These solar cell parameters can be determined and expressed as follows [9, 15]:

$$V_{\text{oc}} = \left( \frac{nKT}{q} \right) \ln [(J_L/J_0) + 1] \quad (\text{eq. 1.6})$$

$$J_{\text{sc}} = -J_L = J_0 \left[ \exp \left( \frac{qV_{\text{oc}}}{nKT} \right) - 1 \right] \quad (\text{eq. 1.7})$$

$$\text{FF} = \left( \frac{P_{\text{max}}}{V_{\text{oc}} J_{\text{sc}}} \right) = \left( \frac{V_{\text{max}} J_{\text{max}}}{V_{\text{oc}} J_{\text{sc}}} \right) \quad (\text{eq. 1.8})$$

$$\text{PCE} = \frac{\text{maximum power delivered}}{\text{input power}} = \frac{P_{\text{max}}}{P_{\text{in}}} = \frac{V_{\text{oc}} J_{\text{sc}} \text{FF}}{P_{\text{in}}} \quad (\text{eq. 1.9})$$

where,  $J_o$  is the reverse saturation current density of the diode,  $P_{in}$  is the input power (generally  $1000 \text{ W/m}^2$ ),  $J_{max}$  and  $V_{max}$  are current density and voltage at maximum-power conditions, respectively. In non-ideal case, the series and shunt resistances mainly affect the FF of the solar cells, which affects the PCE of the solar cell [8]. It is desirable to have the value of  $R_s$  as low as possible and the value of  $R_{sh}$  as high as possible. The effect can be observed by noticing the change in the squareness of the current-voltage curves shown in Fig. 1.8. For a very high value of  $R_s$ , the value of  $J_{sc}$  reduces, but  $V_{oc}$  remains the same. The value of  $V_{oc}$  is affected and declined at a lower value of  $R_{sh}$ , but it does not affect the  $J_{sc}$  value. These parasitic ( $R_s$  and  $R_{sh}$ ) resistances can be graphically determined from the J-V curve. The  $R_s$  value is calculated from the reciprocal of the slope of the J-V curve under forward bias. And the reciprocal of the slope of the J-V curve in the reverse bias condition gives  $R_{sh}$  value. The J-V equation of equivalent circuit containing non-ideal series and shunt resistances of a solar cell is written in the following form [8]:

$$J(V) = J_o \left[ \exp \left( \frac{q(V - R_s J)}{nKT} \right) - 1 \right] - J_L + \frac{V - R_s J}{R_{sh}} \quad (\text{eq. 1.10})$$

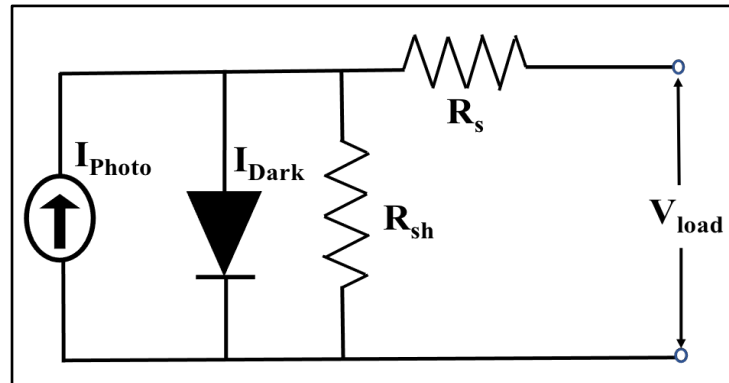


Fig. 1.6 The equivalent circuit of solar cell in the presence of series and shunt resistances

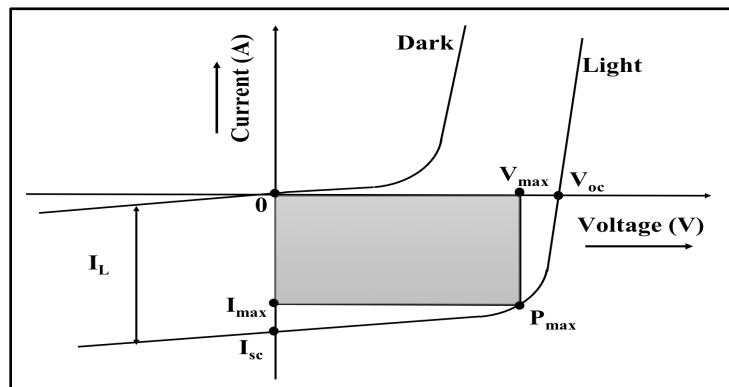


Fig. 1.7 The J-V characteristics of solar cell performed on dark and light conditions

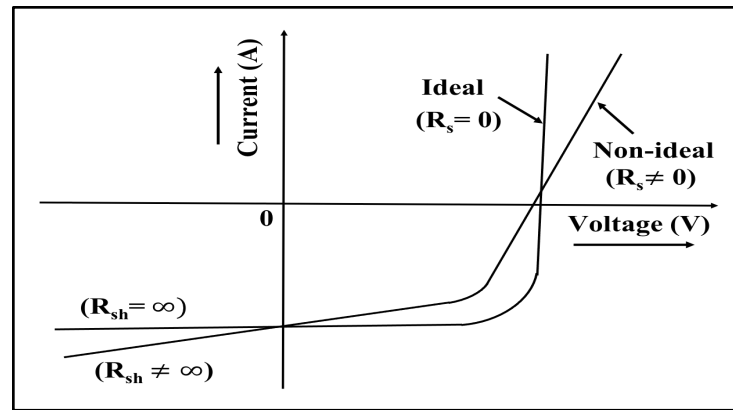


Fig. 1.8 The current voltage characteristics for ideal and non-ideal conditions

### 1.2.5 Development of PV technology

Photovoltaic devices can convert solar energy directly into electricity based on the photoelectric effect. Edmund Becquerel, a French scientist, discovered the photoelectric effect in 1839 [8]. He observed that a current was produced when two plates of silver chloride and counter metal electrodes were immersed in an electrolyte solution upon illumination with sunlight. A large area solar cell based on Se film was fabricated for the first time in 1883. But the performance of this solar cell was limited. A real breakthrough in photovoltaics was reported in 1954 with the first 6% efficient solar cells: silicon solar cell (Bell Lab, USA) and  $\text{Cu}_2\text{S}/\text{CdS}$  heterojunction solar cell (Air force, USA) [18]. After that, many improvements (i.e., use of different semiconductors and structures in solar cell technology) have been seen in the photovoltaic technology for being commercially available. Various types of solar cell technology have been introduced to improve efficiency, durability, technical/economic feasibility, payback time, etc., of the solar cells [9, 14, 20]. The solar cells need to be cheaper to take an essential share in energy production. To date, PV technologies are classified into three generations, namely first, second, and third depending on the type of semiconductors used in solar cell fabrication [18, 19]. Fig. 1.9 presents the evolution of the best reported solar cell efficiency to date for different PV technologies (Best research-cell efficiency chart, NREL, 2021).

The first generation of PV devices is made of monocrystalline and polycrystalline Si wafers [9, 18]. Wafer-based silicon solar cells have dominated the market with a share of more than 85% in the global annual production due to their good photovoltaic properties, their excellent

stability and reliability, and its earth abundance. However, wafer-based silicon solar cell is the most mature technology with a record efficiency of 26.7% [20]; its production cost is high. The high device cost is the disadvantage of silicon-based solar cells for converting solar energy into electrical energy. Silicon is an indirect bandgap semiconductor with a bandgap of 1.12 eV; silicon poorly absorbs solar energy. And therefore, a larger thickness of around 200-300  $\mu\text{m}$  is required to efficiently absorb the incident solar energy. Subsequently, the highly pure material is needed to assure the collection of the generated carriers and avoid the recombination process, which further increases the manufacturing cost of the device. The p-n homojunction is generally found in silicon solar cells where p-type and n-type semiconductors are made by doping acceptor and donor impurities into the intrinsic semiconductor, respectively. This disadvantage has led the PV market to explore alternate technologies that are efficient as well as cost-effective.

The second generation of PV (also called thin film solar cell (TFSC) technologies) is employed in the PV market to reduce the solar cell's production cost compared to wafer-based silicon solar cells. The semiconductors used in this technology have specific properties such as direct bandgap and high absorption coefficient ( $>10^5 \text{ cm}^{-1}$ ), which absorb solar energy effectively within a few microns of the semiconductor thickness. And the utilization of cheaper growth methods and low-cost substrates can help in faster manufacturing that reduces the production cost of the device. Commercially, thin film solar cells (TFSCs) are primarily divided into three types: amorphous silicon (a-Si), cadmium telluride (CdTe), and copper-indium-gallium-diselenide (CIGSe) [14], [17]. These TFSCs rely on a p-n heterojunction design having a top layer called the window layer and a bottom layer called the absorber layer. The photons are absorbed in an absorber layer with a comparatively lower bandgap value than the window layer. To date, the record efficiencies of a-Si, CdTe, CIGSe TFSCs are 14, 22.1, and 23.4%, respectively [21]. The a-Si semiconductor has a direct bandgap of around 1.7 to 1.8 eV, but its conduction and valence band edges are not well specified. The CdTe semiconductor has a direct bandgap of 1.45 eV and an absorption coefficient of  $10^5 \text{ cm}^{-1}$ . And the CIGSe is a semiconductor made from quaternary compounds whose bandgap value can be tuned from 1.04 to 1.68 eV with increasing gallium content. Although the TFSCs have the advantages of low cost, low payback time, monolithic integrations etc., they contain some drawbacks. The major problems associated with the thin solar cells are the presence of grain boundaries and the complex defect chemistry due to

polycrystalline nature, which reduces the efficiency of solar cells. They also contain the problems of adhesion of the film to the substrate, use of rare and more expensive (indium and gallium), and use of toxic (cadmium) materials. The different generations of the solar cell are being inspired to resolve the problems mentioned earlier.

All the emerging approaches in PV are also known as the third generation of solar cells. The reasons for developing this new generation are to improve solar cell efficiency, use less expensive and less toxic material, and make it accessible to the public. In the third generation, various types of solar cell technologies, including dye-sensitized solar cells (DSSC), nanostructured solar cells (NSC), organic polymer solar cells (OPSC), multi-junction solar cells (MJSC), and perovskite solar cells (PSC), are studied [9, 18]. The first and second generations rely on the p-n junction design, and photons whose energy is equal to or greater than the absorber material's bandgap can be absorbed in the solar cell. Therefore, the thermodynamic Schokley-Queisser limit for these two generations lays only around 31%. The third-generation solar cells have the potential to surpass the Schokley-Queisser limit and lower the production cost. NSC is made up of inexpensive materials, including quantum dot (record cell efficiency of 16.6%), nanowires and mesoscopic. These materials can also use for transforming solar energy into chemical fuels. OPSC, with a record efficiency of 18.2%, exhibits excellent flexibility and is composed of organic or polymer materials. DSSC demonstrates attractive properties such as low cost, simple, non-toxic, flexible, transparency, good plasticity, etc., for commercially viable. Record efficiency of 12.3% has been found for dye-sensitized solar cells [18]. The MJSC, also known as tandem solar cells, are designed to absorb a maximum number of photons from the broad solar spectrum by stacking semiconductor material with increasing bandgaps on top of each other. The highest solar cell conversion efficiency of 47.1% has been reported in PV history using multijunction solar cells [21]. PSC is made from organic-inorganic halide materials defined by the formula  $ABX_3$  (where A and B are cations and X is an anion). For perovskite solar cells, the recently reported photovoltaic cell efficiency is 25.5 % [22].

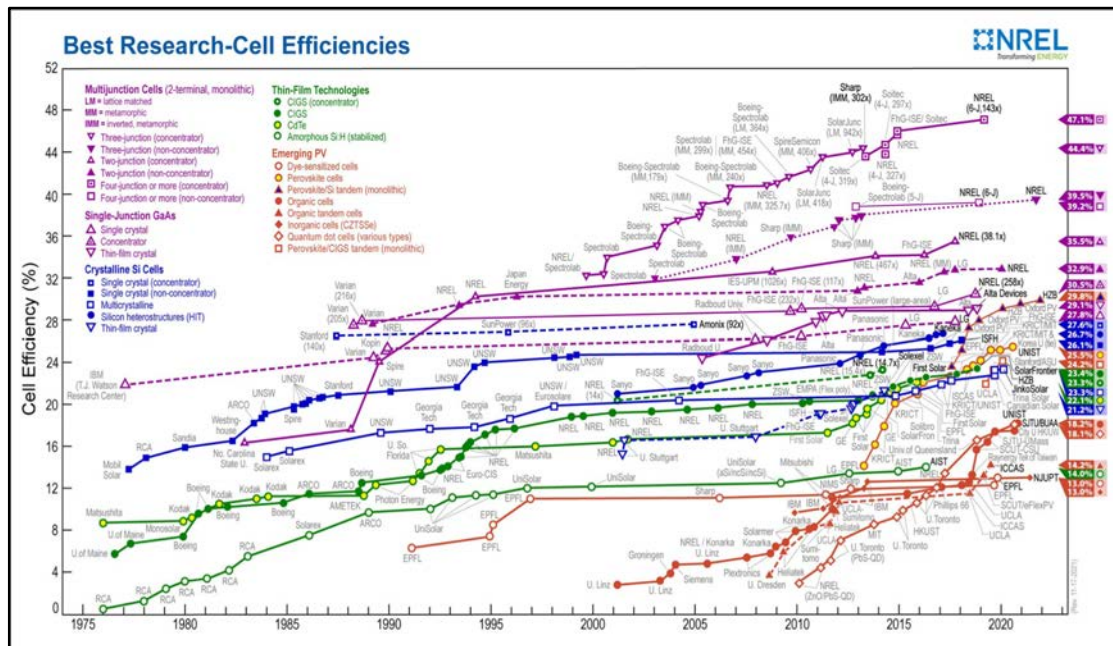


Fig. 1.9 Evolution of best laboratory efficiency for different generations of PV devices (source: National Renewable Energy Laboratory, 2021)

### 1.3 Introduction of the numerical simulation

Numerical simulations are a high-priority job that helps to integrate real-life problems into a virtual machine environment like a computer. Incorporating computers in numerical problem solving has led the researcher to find an optimum way of efficiently performing complex problem-solving. Numerical simulation in a computer can save research time and resources. It is also easy to optimize any real-time design problem without physically implementing it in real test environments. Because of this reason, computer-based learning is emphasized over worldwide universities. Computer-based learning systems have helped researchers in the field of semiconductor devices. Today, most of the world's market is dominated by semiconductor devices like mobile phones, laptops, computers, streetlights, and solar panels. In the field of semiconductor devices, one of the most prominent areas is solar cells. A semiconductor device can convert solar energy into electrical energy. Due to the excessive demand of electric power by consumers, the photovoltaic cell is an excellent alternative to meet user demands. The photovoltaic cell has been developing rapidly and has been reaching maximum efficiency of 29% [23]. But there are still some issues, including high cost, low efficiency, and environmental issue available for these solar cells that prevent commercial development [25–27].



The numerical simulation can play a vital role in dealing with those issues of the solar cell. Numerical simulation can interpret semiconductor devices' physical phenomena and behaviors because well-controlled device parameters are available in simulators. The simulators are designed to solve the basic semiconductor equations (i.e., Poisson's equation and Continuity equations) for charge carriers and produce non-linear equations for modeling the solar cells. The simulated study is cheaper and quicker than experimental work. The numerical simulation predicts the outcome of changes in material properties and tests the practicability of the proposed physical explanation. From the above discussion, it is evident that for rapid improvement in design and efficiency, numerical analysis of photovoltaic solar cells is imperative to assess the proposed physical structure's practicability and performance.

Many simulators are available for theoretical modeling of solar cells that solve basic semiconductor equations [27]. The different types of simulators commercially available for modeling various types of solar cells are found in groups of literature [28–64]. These simulators can analyze the device with three different dimensions (i.e., 1D, 2D, and 3D). Some software is freely available online. Most of the software is supported on Windows computers, while some software can also work on MacBook and Linux. A solar cell capacitance simulator (SCAPS) has remained one of the favored simulators to analyze the device performance and optimize the parameters for achieving high-efficiency solar cells. SCAPS software is selected in this study for modeling CIGSe based TFSCs because this can provide better information about thin film solar cells than other simulations.

### **1.3.1 SCAPS simulation**

A SCAPS is a one-dimensional solar cell simulator software available freely to the research community. This software is a Windows-oriented program and user-friendly. It uses a Gummel iteration scheme with Newton-Raphson substeps [64]. Several researchers from the Department of Electronics and Information Systems (ELIS) of the University of Gent, namely Alex Niemegeers, Marc Burgelman, Koen Decock, Stefaan Degraeve, Johan Verschraegen, have contributed to its development [66–70]. SCAPS was initially developed for simulating solar cell structures of the CI(G)Se and the CdTe family. Recently, SCAPS has improved its study area to various types of solar cells, including crystalline solar cells (Si and GaAs family) and amorphous solar cells (a-Si), perovskite solar cells, tandem solar

cells, multijunction solar cells, and many other solar cells [58, 70–73]. This progress shows that SCAPS software can have a remarkable promise for designing and optimizing solar cells. An overview of its main features is explained below [70, 74].

1. Can introduce up to 7 semiconductor layers
2. The main semiconductor's parameters such as thickness, bandgap ( $E_g$ ), electron affinity ( $\chi$ ), dielectric permittivity ( $\epsilon$ ), conduction band and valence band effective density of states (CB, VB), electron and hole thermal velocity ( $V_{thn}$ ,  $V_{thp}$ ), electron and hole mobility ( $\mu_n$ ,  $\mu_p$ ), shallow uniform donor and acceptor density ( $N_A$ ,  $N_D$ ), all traps (defect density ( $N_t$ ), electron and hole capture cross section ( $\sigma_n$ ,  $\sigma_p$ ), etc. can be varied.
3. Recombination profiles in the solar cells: band-to-band (direct), Auger, Shockley-Read-Hall type.
4. Defect density in bulk semiconductors and at interface.
5. Defect levels with charge type: no charge, monovalent (single donor, acceptor), divalent (double donor, double acceptor, amphoteric), multivalent (user-defined).
6. Defect with different energy distribution: uniform distribution, single level distribution, Gaussian distribution, and band tails.
7. Defect levels with optical property and metastable transitions between defects
8. Metal contacts: work function or flat band; optical property.
9. Tunneling mechanism: intra-band tunneling (within a conduction band or within a valence band); tunneling to and from interface states.
10. Illumination of a working structure with a variety of standard and other spectra included (AM0, AM1.5D, AM1.5G, monochromatic, etc.).
11. Illumination from either the p-side or the n-side; spectrum cut-off and attenuation
12. Working point for calculations: Energy band diagram, concentrations and currents at a given working point, J-V characteristics, ac characteristics (C and G, as a function of V and/or f), quantum efficiency, recombination profile, etc.
13. Batch calculations: presentation of results and settings as a function of batch parameters.

14. Loading and saving of all settings; start-up of SCAPS in a personalized configuration; a script language including a free user function and very intuitive user interface.
15. Friendly user interface and a built-in curve fitting facility a panel for the interpretation of admittance measurements.

#### **1.4 Objectives of this research work**

This study is focused on the CI(G)Se TFSCs, which is the most promising candidate in the PV market due to its long-term thermal stability, high radiation tolerance on electrons and holes, high yield per weight, low energy payback time, and flexibility in the device design. The efficiency, lifetime, and production cost of solar cells determine their commercial applications. For this, various strategies such as improving the solar cell performance by understanding the physio-chemical process of CI(G)Se and recombination process, developing low-cost deposition methods without compromising the conversion efficiency, using less semiconductor material and simplifying the processing steps, reducing the waste of materials during the deposition, utilization of optical concentrators, use of less pure precursor material and improve the material-utilization efficiency, etc., could apply in the CI(G)Se TFSCs to improve efficiency and reduce cost.

Here, the novel hybrid deposition method is introduced for the synthesis of CI(G)Se thin films. Understanding the mechanism of the photovoltaic phenomenon in a hybrid deposited CIGSe absorber layer is the primary goal of this study. This hybrid deposition method combines the non-vacuum pneumatic spray pyrolysis technique and the vacuum co-evaporation method. The idea of combining these two methods is to improve the efficiency-to-cost ratio value by increasing material utilization efficiency and reducing the waste of highly pure materials in solar cells. The material properties of semiconductors used in the CI(G)Se TFSCs are also studied through SCAPS software. This simulation study can help to optimize the material properties as well as design the solar cells without doing experimental work, which is helpful to reduce the cost and research time. The general objectives of this research work are:

1. Develop the novel hybrid deposition method for CI(G)Se absorber films synthesis.

2. Optimize the growth parameters of the hybrid deposition method for CI(G)Se thin films to use as an absorber layer in a solar cell.
3. Deposition and optimization of CdS buffer film by chemical bath deposition method.
4. Investigate the influence of the material properties such as thicknesses and carrier concentration of each material used in CI(G)Se TFSCs using SCAPS software.
5. Simulate the experimentally obtained results of CISE, CIGSe, and CdS thin films and analyze the results of CI(G)Se TFSCs.
6. Study the effect of defects, ambient temperature, and parasitic resistances on the solar cell performance by SCAPS software.

## **1.5 Organization of thesis**

This thesis is partitioned into seven sections or chapters.

Chapter one deals with introducing energy sources, semiconductor and solar cell physics, the introduction of numerical simulation, the objective of this thesis, and the organization of the complete thesis.

Chapter two describes the development of the CIGSe thin film solar cells, the structure of the CI(G)Se TFSCs, the role of alkali elements doping in CI(G)Se, recombination mechanism present in CI(G)Se TFSCs, deposition methods for CI(G)Se thin films synthesis, and finally describes the novel hybrid deposition method for the synthesis of CI(G)Se thin films.

Chapter three illustrates the details of experimental work for deposition of the CI(G)Se thin films and CdS thin films, details of SCAPS software, and characterization, including material and device characterizations.

Chapter four deals with the results of  $\text{In}_2\text{Se}_3$  thin films by pneumatic spray pyrolysis technique and results of CI(G)Se thin films by the hybrid deposition method.

Chapter five describes the introduction of the buffer window layer for the CIGSe device, CdS thin film deposition techniques, and results of the CdS thin films by chemical bath deposition methods.

Chapter six deals with the optimization of the CI(G)Se TFSCs by analyzing the material properties of semiconductor materials, theoretical study of the experimental results of CIGSe, CdS thin films, the effect of defects, ambient temperatures, and parasitic resistances on the performance of CI(G)Se TFSCs.

Finally, chapter 7 describes the general conclusion of this thesis work, future perspectives to improve the device performance, and details of publications and conference presentations.

## References:

- [1] O. Makarova, T. Kalashnikova, and I. Novak, "The impact of energy consumption on quality of life in the world: Methodological aspects of evaluation," *Econ. Ann.*, vol. 184, no. 7–8, pp. 29–37, 2020.
- [2] C. Pasten and J. C. Santamarina, "Energy and quality of life," *Energy Policy*, vol. 49, pp. 468–476, 2012.
- [3] B. Gilland, "Population , Economic Growth , and Energy Demand, 1985-2020," vol. 14, no. 2, pp. 233–244, 2020.
- [4] R. R. . J. and M. K. . S. William Fulkerson, "Energy from Fossil Fuels," vol. 263, no. 3, pp. 128–135, 1990.
- [5] V. M. Fthenakis and P. D. Moskowitz, "Photovoltaics: Environmental, health and safety issues and perspectives," *Prog. Photovoltaics Res. Appl.*, vol. 8, no. 1, pp. 27–38, 2000.
- [6] V. Chandrasekaran, "Effect of heat treatments and reduced absorber layer thickness on cu ( in , ga ) se<sub>2</sub> thin film solar cells," 2005.
- [7] T. LU, "Thin Film Solar Cells With Light Trapping Transparent," no. May, 2011.
- [8] I. M. Dharmadasa, *Advanced in Thin-film solar cells*. 2012.
- [9] A. Luque and S. Hegedus, *Handbook of Photovoltaic Science and Engineering*. 2011.
- [10] A. Rockett, *The materials science of semiconductor*. Springer US, 2008.
- [11] K. L. Chopra and S. R. Das, *Thin Film Solar Cells*. 1983.

- [12] A. A. Kadam, "Preparation of efficient  $\text{CuIn}_{1-x}\text{Ga}_x\text{Se}_2\text{-ySy}/\text{CdS}$  thin film solar cells by optimizing the molybdenum back contact and using diethylselenide as selenium precursor," University of Central Florida, 2006.
- [13] V. Hadagali, "Study of The Effects of Sodium and Absorber Microstructure for the Development of  $\text{CuIn}_{1-x}\text{Ga}_x\text{Se}_2\text{-Ysy}$  Thin Film Solar Cell Using an Alternative Selenium Precursor," 2009.
- [14] P. I. R. Figueroa, "Deposition and characterization of  $\text{Cu}(\text{In}_{1-x}\text{Ga}_x)\text{Se}_2$  films by multiple deposition techniques," CINVESTAV-IPN, 2016.
- [15] D. Vaccarello, Fabricating and Characterizing Chalcogenide Thin Films as Light Absorbing Layers in Solar Cells Thesis, no. October. 2016.
- [16] J. Bisquert, The physics of solar cells: Perovskites, organics, and photovoltaic fundamentals. 2017.
- [17] M. A. Hassan, "Spray Pyrolysis Synthesized  $\text{Cu}(\text{In,Ga/Al})(\text{S,Se})_2$  Thin Films for Photovoltaic Applications By Spray Pyrolysis Synthesized  $\text{Cu}(\text{In,Ga/Al})(\text{S,Se})_2$  Thin Films for Photovoltaic Applications," National University of Sciences & Technology (NUST), Pakistan, 2018.
- [18] K. Ranabhat, L. Patrikeev, A. A. evna Revina, K. Andrianov, V. Lapshinsky, and E. Sofronova, "An introduction to solar cell technology," J. Appl. Eng. Sci., vol. 14, no. 4, pp. 481–491, 2016.
- [19] Soteris A. Kalogirou, Solar Energy Engineering Processes and Systems. 2009.
- [20] K. Yoshikawa et al., "Silicon heterojunction solar cell with interdigitated back contacts for a photoconversion efficiency over 26%," Nat. Energy, vol. 2, no. 5, 2017.
- [21] M. A. Green, E. D. Dunlop, J. Hohl-Ebinger, M. Yoshita, N. Kopidakis, and X. Hao, "Solar cell efficiency tables (Version 58)," Prog. Photovoltaics Res. Appl., vol. 29, no. 7, pp. 657–667, 2021.
- [22] H. A. Dewi et al., "Highly Efficient Semitransparent Perovskite Solar Cells for Four Terminal Perovskite-Silicon Tandems," ACS Appl. Mater. Interfaces, vol. 11, no. 37, pp. 34178–34187, 2019.
- [23] M. Green, E. Dunlop, J. Hohl-Ebinger, M. Yoshita, N. Kopidakis, and X. Hao, "Solar cell efficiency tables (version 57)," Prog. Photovoltaics Res. Appl., vol. 29, no. 1, pp. 3–15, 2021.
- [24] A. Matsuda, "Thin-film silicon - Growth process and solar cell application," Japanese J. Appl. Physics, Part 1 Regul. Pap. Short Notes Rev. Pap., vol. 43, no. 12, pp. 7909–

7920, 2004.

- [25] X. Zhao and N. G. Park, “Stability issues on perovskite solar cells,” *Photonics*, vol. 2, no. 4, pp. 1139–1151, 2015.
- [26] A. Morales-Acevedo, “Thin film CdS/CdTe solar cells: Research perspectives,” *Sol. Energy*, vol. 80, no. 6, pp. 675–681, 2006.
- [27] A. Kowsar, M. Billah, S. Dey, S. C. Debnath, S. Yeakin, and S. F. Uddin Farhad, “Comparative Study on Solar Cell Simulators,” *ICIET 2019 - 2nd Int. Conf. Innov. Eng. Technol.*, pp. 23–24, 2019.
- [28] C. Jiang, T. Li, X. Zhang, and L. Hou, “Simulation of silicon solar cell using PC1D,” *Adv. Mater. Res.*, vol. 383–390, no. 1, pp. 7032–7036, 2012.
- [29] M. Sittirak, J. Ponrat, K. Thubthong, P. Kumnorkaew, J. Lek-Uthai, and Y. Infahsaeng, “The effects of layer thickness and charge mobility on performance of FAI:MABr:PbI<sub>2</sub>:PbBr<sub>2</sub> perovskite solar cells: GPVDM simulation approach,” *J. Phys. Conf. Ser.*, vol. 1380, no. 1, 2019.
- [30] B. C. R. Borges et al., “Incomplete adherence to the ASA difficult airway algorithm is unchanged after a high-fidelity simulation session,” *Can. J. Anesth.*, vol. 57, no. 7, pp. 644–649, 2010.
- [31] K. L. Damena, “Investigation of Organic Solar Cell at different Active Layer Thickness and Suns using GPVDM,” pp. 1615–1626, 2019.
- [32] R. Stangl and C. Leendertz, “General Principles of Solar Cell Simulation and Introduction to AFORS-HET,” pp. 445–458, 2012.
- [33] R. Stangl, C. Leendertz, and J. Haschke, *Numerical Simulation of Solar Cells and Solar Cell Characterization Methods: the Open-Source on Demand Program AFORS-HET*, no. February. 2010.
- [34] W. Lisheng, C. Fengxiang, and A. Yu, “Simulation of high efficiency heterojunction solar cells with AFORS-HET,” *J. Phys. Conf. Ser.*, vol. 276, no. 1, 2011.
- [35] F. Smole, M. Topič, and J. Furlan, “Analysis of TCO/p(a-Si:C:H) heterojunction and its influence on p-i-n a-Si:H solar cell performance,” *J. Non. Cryst. Solids*, vol. 194, no. 3, pp. 312–318, 1996.
- [36] J. Krc et al., “Optical and electrical modeling of Cu(In,Ga)Se<sub>2</sub> solar cells,” *Opt. Quantum Electron.*, vol. 38, no. 12–14, pp. 1115–1123, 2006.
- [37] M. Topic, F. Smole, and J. Furlan, “Computer model for simulation of amorphous silicon solar cell structures,” *Mediterr. Electrotech. Conf. - MELECON*, vol. 2, pp.

18–21, 1994.

- [38] S. Lorenzo, D. El Escorial, C. Gabriel, C. Arviset, D. Ponz, and E. Solano, “Edited by European Space Agency ( ESA ) - Madrid , Spain European Space Agency ( ESA ) - Madrid , Spain,” vol. 351, 2005.
- [39] S. Sepeai et al., “Design optimisation of bifacial solar cells by PC1D simulation,” *J. Energy Technol. Policy*, vol. 3, no. 5, pp. 1–11, 2013.
- [40] M. Magdeldin, T. Kohl, and M. Järvinen, “Techno-economic assessment of the by-products contribution from non-catalytic hydrothermal liquefaction of lignocellulose residues,” *Energy*, vol. 137, pp. 679–695, 2017.
- [41] M. B. Hosen, A. N. Bahar, M. K. Ali, and M. Asaduzzaman, “Modeling and performance analysis dataset of a CIGS solar cell with ZnS buffer layer,” *Data Br.*, vol. 14, pp. 246–250, 2017.
- [42] K. A. S. M. Ehetshamul Haque, T. N. Bin Quddus, M. T. Ferdaous, and M. A. Hoque, “An analysis of efficiency variation in an  $\text{Al}_{0.7}\text{Ga}_{0.3}\text{As}/\text{Al}_{0.48}\text{In}_{0.52}\text{As}$  heterojunction solar cell with change in device parameters using adept 1D software,” *Electron. Mater. Lett.*, vol. 9, no. 1, pp. 47–52, 2013.
- [43] M. S. Salem et al., “Physically Based Analytical Model of Heavily Doped Silicon Wafers Based Proposed Solar Cell Microstructure,” *IEEE Access*, vol. 8, pp. 138898–138906, 2020.
- [44] M. Belarbi, M. Beghdad, and A. Mekemeche, “Simulation and optimization of n-type interdigitated back contact silicon heterojunction (IBC-SiHJ) solar cell structure using Silvaco Tcad Atlas,” *Sol. Energy*, vol. 127, pp. 206–215, 2016.
- [45] M. Turowski et al., “Simulating the radiation response of GaAs solar cells using a defect-based TCAD model,” *IEEE Trans. Nucl. Sci.*, vol. 60, no. 4, pp. 2477–2485, 2013.
- [46] S. Michael and A. Bates, “The design and optimization of advanced multijunction solar cells using the Silvaco ATLAS software package,” *Sol. Energy Mater. Sol. Cells*, vol. 87, no. 1–4, pp. 785–794, 2005.
- [47] Y. Marouf, L. Dehimi, F. Bouzid, F. Pezzimenti, and F. G. D. Corte, “Theoretical design and performance of  $\text{In}_x\text{Ga}_{1-x}\text{N}$  single junction solar cell,” *Optik (Stuttg.)*, vol. 163, pp. 22–32, 2018.
- [48] A. Kowsar et al., “A novel simulator of multijunction solar cells-MSCS-1D,” *Int. J. Renew. Energy Res.*, vol. 10, no. 3, pp. 1369–1375, 2020.



- [49] M. B. Hosen, M. K. Ali, M. Asaduzzaman, A. Kowsar, and A. N. Bahar, "Performance Optimization of ZnS/CIGS Solar Cell With Over 25% Efficiency Enabled by Using a CuIn<sub>3</sub>Se<sub>5</sub> OVC Layer," *Int. J. Renew. Energy Res.*, vol. 10, no. 4, pp. 2000–2005, 2020.
- [50] U. Mandadapu, "Simulation and Analysis of Lead based Perovskite Solar Cell using SCAPS-1D," *Indian J. Sci. Technol.*, vol. 10, no. 1, pp. 1–8, 2017.
- [51] M. Arnela and O. Guasch, "Finite element simulation of /asa/ in a three-dimensional vocal tract using a simplified aeroacoustic source model," *Proc. Int. Congr. Acoust.*, vol. 2019-Sept, no. 1, pp. 1802–1809, 2019.
- [52] D. A. Clugston and P. A. Basore, "PC1D version 5: 32-bit solar cell modeling on personal computers," *Conf. Rec. IEEE Photovolt. Spec. Conf.*, pp. 207–210, 1997.
- [53] H. Zhu, A. K. Kalkan, J. Hou, and S. J. Fonash, "Applications of AMPS-1D for solar cell simulation," vol. 309, no. March 2008, pp. 309–314, 2009.
- [54] Y. Liu, Y. Sun, and A. Rockett, "A new simulation software of solar cells - WxAMPS," *Sol. Energy Mater. Sol. Cells*, vol. 98, pp. 124–128, 2012.
- [55] Y. Liu, D. Heinzl, and A. Rockett, "A new solar cell simulator: WxAMPS," *Conf. Rec. IEEE Photovolt. Spec. Conf.*, pp. 002753–002756, 2011.
- [56] A. Bouloufa, K. Djessas, and A. Zegadi, "Numerical simulation of CuIn<sub>x</sub>Ga<sub>1-x</sub>Se<sub>2</sub> solar cells by AMPS-1D," *Thin Solid Films*, vol. 515, no. 15 SPEC. ISS., pp. 6285–6287, 2007.
- [57] N. Hernández-Como and A. Morales-Acevedo, "Simulation of hetero-junction silicon solar cells with AMPS-1D," *Sol. Energy Mater. Sol. Cells*, vol. 94, no. 1, pp. 62–67, 2010.
- [58] M. Mostefaoui, H. Mazari, S. Khelifi, A. Bouraiou, and R. Dabou, "Simulation of High Efficiency CIGS Solar Cells with SCAPS-1D Software," *Energy Procedia*, vol. 74, pp. 736–744, 2015.
- [59] A. D. Adewoyin, M. A. Olopade, O. O. Oyebola, and M. A. Chendo, "Development of CZTGS/CZTS tandem thin film solar cell using SCAPS-1D," *Optik (Stuttg.)*, vol. 176, no. March 2018, pp. 132–142, 2019.
- [60] M. T. Neukom, S. Züfle, and B. Ruhstaller, "Reliable extraction of organic solar cell parameters by combining steady-state and transient techniques," *Org. Electron.*, vol. 13, no. 12, pp. 2910–2916, 2012.
- [61] V. Steinmann et al., "An efficient merocyanine/zinc phthalocyanine tandem solar

- cell,” *Org. Electron.*, vol. 14, no. 8, pp. 2029–2033, 2013.
- [62] B. Ruhstaller et al., “Comprehensive simulation of light-emitting and light-harvesting organic devices,” *Org. Light Emit. Mater. Devices XII*, vol. 7051, p. 70510J, 2008.
  - [63] A. Kumar Mishra and R. K. Shukla, “Electrical and optical simulation of typical perovskite solar cell by GPVDM software,” *Mater. Today Proc.*, no. xxxx, 2020.
  - [64] A. Haddout, A. Raidou, and M. Fahoume, “A review on the numerical modeling of CdS/CZTS-based solar cells,” *Appl. Phys. A Mater. Sci. Process.*, vol. 125, no. 2, pp. 1–16, 2019.
  - [65] M. Burgelman, P. Nollet, and S. Degrave, “Modelling polycrystalline semiconductor solar cells,” *Thin Solid Films*, vol. 361, pp. 527–532, 2000.
  - [66] M. Burgelman, K. Decock, S. Khelifi, and A. Abass, “Advanced electrical simulation of thin film solar cells,” *Thin Solid Films*, vol. 535, no. 1, pp. 296–301, 2013.
  - [67] J. Verschraegen and M. Burgelman, “Numerical modeling of intra-band tunneling for heterojunction solar cells in scaps,” *Thin Solid Films*, vol. 515, no. 15 SPEC. ISS., pp. 6276–6279, 2007.
  - [68] K. Decock, S. Khelifi, and M. Burgelman, “Modelling multivalent defects in thin film solar cells,” *Thin Solid Films*, vol. 519, no. 21, pp. 7481–7484, 2011.
  - [69] M. Burgelman, J. Verschraegen, S. Degrave, and P. Nollet, “Modeling thin-film PV devices,” *Prog. Photovoltaics Res. Appl.*, vol. 12, no. 2–3, pp. 143–153, 2004.
  - [70] J. V. Marc Burgelman, Koen Decock, Alex Niemegeers, “SCAPS manual,” *SCAPS Man.*, no. December, 2016.
  - [71] J. M. Marc Burgelman, “Analysis of Graded Band Gap Solar Cells With SCAPS,” *23rd Eur. Photovolt. Sol. Energy Conf.*, 2008.
  - [72] S. Karthick, S. Velumani, and J. Bouclé, “Experimental and SCAPS simulated formamidinium perovskite solar cells: A comparison of device performance,” *Sol. Energy*, vol. 205, no. March, pp. 349–357, 2020.
  - [73] O. K. Simya, A. Mahaboobbatcha, and K. Balachander, “A comparative study on the performance of Kesterite based thin film solar cells using SCAPS simulation program,” *Superlattices Microstruct.*, vol. 82, pp. 248–261, 2015.
  - [74] M. Burgelman, J. Verschraegen, B. Minnaert, and J. Marlein, “Numerical simulation of thin film solar cells : practical exercises with SCAPS,” *Numos Work.*, pp. 357–366, 2007.

## **Chapter 2 CI(G)Se thin film solar cells technology**

This chapter describes an overview of the CI(G)Se TFSCs. The first part discusses the trend in the development of the CI(G)Se TFSCs and a brief review of a CI(G)Se thin film solar cell's structure. The material properties such as structural, optical, and electrical properties of CIGSe semiconductors are reviewed in detail. Moreover, the role of alkali elements doping in the CI(G)Se TFSCs, the different recombination mechanisms involved in the CI(G)Se TFSCs and a brief review of deposition methods for the synthesis of the CI(G)Se thin films are explained. Finally, the novel hybrid deposition method for CI(G)Se thin films is introduced in this study. Understanding all this information helps to improve the performance of CI(G)Se TFSCs.

### **2.1 Development of the CI(G)Se thin film solar cells**

The CIGSe has been considered promising for solar cell technologies due to its favorable electronic and optical properties, including its direct bandgap with high absorption coefficient and inherent p-type semiconductor. Moreover, it contains the advantages for cost-effective, potential to obtain high device performance, high deposition rate over a large area, long-term stability, high radiation resistance, and fabrication of monolithically interconnected modules [1]. The CIGSe TFSC can be used in various applications such as terrestrial applications, the building integrates portable applications and space applications. In solar cell application, CI(G)Se semiconductor material received significant attention for the first time in 1974, in which Wagner et al. reported 5% conversion efficiency for CdS/CiSe heterojunction [2]. Afterward, Shay et al. optimized the CiSe solar cell and achieved 12% conversion efficiency in 1975 [3]. Kazmerski et al. has grown the CiSe thin films by evaporation with excess of Se and fabricated CdS/CiSe solar cells with an efficiency of 5.7% in 1976 [4]. In 1981, Boeing produced the CiSe TFSC with an efficiency of 9.4%, in which the CiSe absorber layer was deposited over Mo back contact by the evaporation method [1]. ARCO Solar used a precursor layer of Cu and In deposition at a low temperature followed by annealing at a high temperature in the Se atmosphere [1]. In 2000, the conversion efficiency for CI(G)Se TFSC was then increased to 18.2% by NREL [5]. NREL improved the CI(G)Se TFSC efficiency from 18.2 to 19.4% in 2010 [6]. Solar Frontier fabricated the CI(G)Se TFSC with a maximum conversion efficiency of 21.7% in 2017 [7].

In the present scenario, the CI(G)Se TFSC with the conversion efficiency of 23.35% for 1 cm<sup>2</sup> total area by Solar Frontier and 23.30% for 0.1 cm<sup>2</sup> total area by NREL are observed [8, 9]. Many solar cell research groups have fabricated the CI(G)Se TFSC with an efficiency of 20% or greater. All of these groups employed various processing technologies to improve solar cell device performance. Almost all the solar cell groups used the same basic solar cell structure (i.e., stack layer of a substrate, Mo layer as a back contact, CI(G)Se thin films as an absorber layer, n-type window layer, and transparent conducting oxide) [1].

## 2.2 CIGSe thin film solar cell structure

The basic concept of designing the solar cells is based on combining a p-type absorber layer and a wide bandgap n-type window layer. Since CI(G)Se TFSC contain several materials as stack films, the solar cell structure is quite complex. Those stacked materials may react with each other, depending on the ambient temperature. The materials such as back contact, absorber layer, buffer layer, window layer, transparent conducting oxide (TCO) layer and front contact are generally used in a typical CIGSe TFSC, as shown in Fig. 2.1. Most of the CI(G)Se TFSCs have the similar solar cell structure mentioned above [1]. The Mo is employed in a CIGSe TFSC as a back contact. The CdS is mainly used as a buffer layer in the CI(G)Se TFSCs, However, some groups have studied CdS free buffer layers in the CI(G)Se TFSC due to toxic nature of cadmium. The ZnO and ZnO:Al are generally used as window layer and TCO layer.

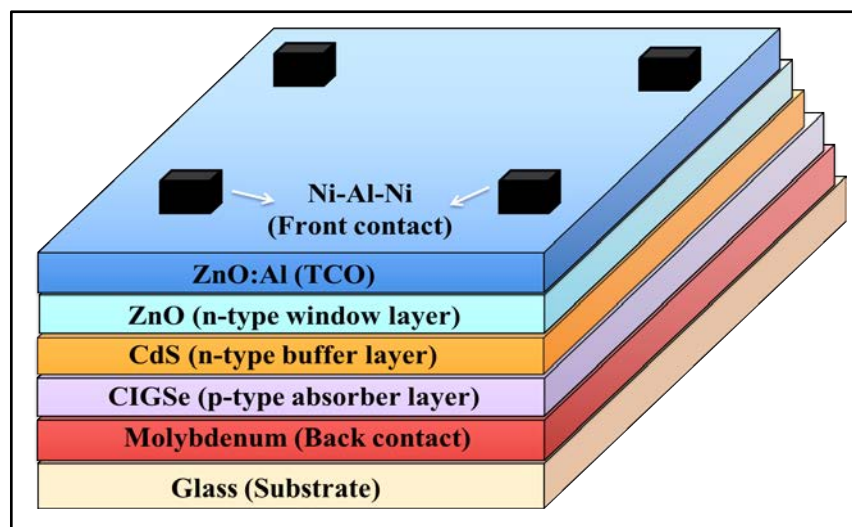


Fig. 2.1 Schematic of the structure of CI(G)Se thin film solar cell

### 2.2.1 Substrate

Generally, two configurations are used for designing the thin film solar cells, namely substrate and superstrate structure. In superstrate configuration, the transparent substrate with the contact made by conducting metal oxide coating is employed. While in the substrate configurations, metal or conducting metal oxide is applied for contact. Since the substrate is used as the base of the solar cells, it can affect the properties of deposited materials based on its thermal coefficient value, mechanical and chemical state, and nature of the surface. The substrate should have a perfectly smooth and clean surface to improve the nucleation of films. The thermal coefficient of the substrate and the deposited materials must match to prevent unnecessary defects (i.e., voids, cracks, adhesion failure, etc.) in the deposited film. Moreover, the substrate should be mechanically and chemically stable at the operating conditions of the deposited films and relatively low in price for reducing the device cost. The suitable substrate is chosen in the solar cells based on these criteria. The soda-lime glass (SLG) substrate fulfills the abovementioned requirements and is mostly used in CIGSe TFSCs. The CIGSe TFSC has achieved a high record efficiency of 23.35% using SLG substrate [10]. The thermal expansion coefficient for SLG substrate is closely matched with the thermal expansion coefficient of the CIGSe (i.e.,  $9 \times 10^{-6} \text{ K}^{-1}$ ) [11]. This feature leads to the formation of fewer defects in the CIGSe thin films. The SLG substrate contains various metal oxides, such as  $\text{SiO}_2$ ,  $\text{Na}_2\text{O}$ ,  $\text{K}_2\text{O}$ ,  $\text{MgO}$ ,  $\text{CaO}$ ,  $\text{ZnO}$ , etc. Sodium from substrates can be diffused through the molybdenum back contact and reach the CIGSe thin film [12]. Sodium incorporation into CIGSe material varies the material properties (mainly structural and electrical properties) of the CIGSe [13, 14]. The effect of sodium on the properties of the CIGSe will discuss briefly later in this chapter. Various diffusion barriers, such as  $\text{SiO}_x$ ,  $\text{Al}_2\text{O}_3$ ,  $\text{SiN}$ , etc., can control the supply of sodium from the substrate to the CIGSe [15]. The SLG substrate is limited to work at high temperatures because of its low softening temperature of around  $700^\circ\text{C}$  [16]. But the CIGSe thin film deposition requires the operating temperature in the range of  $500\text{-}550^\circ\text{C}$  for high device performance. Therefore, SLG substrate is primarily preferred for CIGSe TFSC fabrication.

### 2.2.2 Back contact

The back contact is the first layer made of metallic materials deposited on the substrate, which is used to collect charge carriers from the CIGSe absorber layer. The suitable metallic materials for back contact of the CIGSe TFSCs should require various characteristics. The metallic materials should have good adhesion, matching thermal expansion coefficient to both the substrate and CIGSe absorber layer, high conductivity to minimize the recombination of the generated charge carriers, an excellent reflectivity to improve the absorption of long-wavelength photons, high chemical and mechanical stability with elements of CIGSe (i.e., Cu, In, Ga, and Se), lower work function than that of CIGSe semiconductor to form an ohmic contact, and relatively low-cost [11, 17]. The material should also possess a suitable transportation medium for alkali metals (especially sodium) from the SLG substrate into the CIGSe absorber layer that can help to improve the material properties of CIGSe. Various metallic materials such as tungsten (W), gold (Au), tantalum (Ta), chromium (Cr), niobium (Nb), titanium (Ti), manganese (Mn), vanadium (V), nickel (Ni), molybdenum (Mo), etc. have been studied as a possible back contact for CIGSe TFSCs [17, 18]. Among these metallic materials, Mo can fulfill all the requirements mentioned above and is considered a suitable back contact for CIGSe TFSCs. The formation of an intermediate MoSe<sub>2</sub> layer could be produced during the synthesis of the CIGSe thin films at high operating temperatures. This MoSe<sub>2</sub> layer promotes the formation of an ohmic contact instead of Schottky contact that improves the collection of charge carriers [19]. But a very thick MoSe<sub>2</sub> layer can deteriorate the device performance by providing mechanical problems in the solar cells [19]. Although Mo contains some issues, namely its corrosion and slightly poor optical reflection, the maximum efficiency of 23.35% is observed for the CIGSe TFSC by using Mo back contact [10]. Hence, Mo is favorable back contact in CIGSe TFSC technology, which is primarily deposited by magnetron direct current sputtering.

### **2.2.3 CIGSe absorber layer**

One of the most promising semiconducting materials for the absorber layer of thin film solar cells is CIGSe. The CIGSe semiconductor belongs to the I-III-IV<sub>2</sub> material family, normally used as an absorber layer in solar cells. The CIGSe material has various properties, such as direct bandgap, high absorption coefficient (greater than 10<sup>5</sup> cm<sup>-1</sup>), tunable bandgap (i.e., 1.0-1.7 eV), long-term thermal stability, high radiation hardness on electrons and holes, high yield per weight, low energy pay-back time, flexibility in the device design [20], etc.

Because of these features, the CI(G)Se semiconductors have attracted thin film solar cells as an absorber layer for cost-effective power generation. Understanding material properties of CIGSe semiconductors can enhance the performance of CI(G)Se TFSCs, which are described following.

### 2.2.3.1 Structural properties

The Cu(In,Ga)Se<sub>2</sub> quaternary system is usually formed by combining CuInSe<sub>2</sub> and CuGaSe<sub>2</sub> ternary systems. Fig. 2.2 displays the chalcopyrite crystal structure of the CIGSe material. The chalcopyrite crystal structure of CIGSe resembles the cubic zinc blende structure of group II-IV materials (ZnS), which is obtained through ordered substitution of group II elements (Zn) by group I elements (Cu) and group III elements (In or/and Ga). The chalcopyrite structure is visualized in two interpenetrating face-centered cubic lattices: first anion lattice composed of group VI atoms (Se<sup>2-</sup>) and second cation lattice consisting of group I atoms (Cu<sup>+</sup>) and group III atoms (In<sup>3+</sup> or/and Ga<sup>3+</sup>) [1]. Each Se atom is coordinated to two Cu atoms and two In or/and Ga atoms in a tetrahedral way, while Cu atoms and In or/and Ga atoms are bonded to four Se atoms also in a tetrahedral manner. This tetrahedral coordination in CIGSe implies a covalent bonding between the elements of I, III, and IV groups with SP<sup>3</sup> hybridization [21]. However, the ionic bonding character is also present along with covalent bonding. A tetragonal unit cell's lattice constant ratio ( $c/a$ ) is close to 2 for an undistorted crystal structure [1]. Any deviation in the lattice structure is known as tetragonal distortion ( $=2-c/a$ ), which is mainly due to the different strengths of Cu-Se, In-Se, and Ga-Se bonds. The tetragonal distortion linearly depends on the Ga-content ( $x=\text{Ga}/(\text{In}+\text{Ga})$ ) [11, 22, 23]. The atomic radii of Ga atoms are smaller than the atomic radii of In atoms. Therefore, the lattice parameters of CIGSe decrease with an increase in gallium content in the CIGSe. The tetragonal distortion is negative for  $x<0.23$  and positive for  $x>0.23$  [11]. Various material properties of CIGSe such as structural, morphological, compositional, optical, electrical properties, etc., can also influence tetragonal distortion conditions.

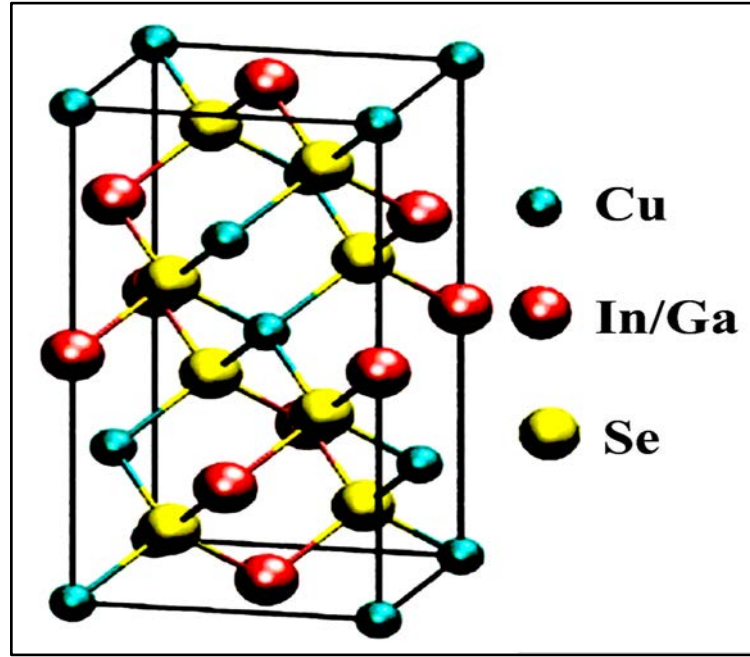


Fig. 2.2 Chalcopyrite crystal structure of CIGSe unit cell

### 2.2.3.2 Phase diagram

The phase diagram can provide information about alloy composition and process temperature for producing a different phase of semiconducting material. The chalcopyrite CIGSe phase normally lays on the  $\text{Cu}_2\text{Se}-(\text{In,Ga})_2\text{Se}_3$  tie line, as shown in Fig. 2.3a [1]. The ordered vacancy compound (OVC) or ordered defect compound (ODC) phases, namely  $\text{Cu}_3(\text{In,Ga})_5\text{Se}_9$ ,  $\text{Cu}(\text{In,Ga})_3\text{Se}_5$ , and  $\text{Cu}_2(\text{In,Ga})_4\text{Se}_7$  are also laid on the same tie line and have the same chalcopyrite structure. These OVC phases are formed from the point defects in the regular arrangement of chalcopyrite crystal structure [24]. Fig. 2.3b shows the pseudo-binary phase diagram of CIGSe along with the tie-line between  $\text{Cu}_2\text{Se}$  and  $(\text{In,Ga})_2\text{Se}_3$  represented in terms of Cu composition, where the formation of different phases at various temperatures are demonstrated. Various phases (namely  $\alpha$ ,  $\beta$ ,  $\gamma$ ,  $\delta$  phases) exist in the CIGSe material, depending on the process temperature and Cu compositions in the CIGSe thin film [25–27]. The  $\alpha$ -phase, the desired phase in the CIGSe TFSC, is the most stable compound that exists in the range from 22 to 24.5 at% of Cu. The  $\text{Cu}_{2-x}\text{Se}$  phase is formed when the CIGSe thin film is grown in Cu-rich composition. The slight Cu-poor composition (from 16 to 22 at%) comprises the  $\beta$ -phase, also called  $\text{Cu}(\text{In,Ga})_3\text{Se}_5$  OVC phase, which is attributed to the regular arrangement of the vacancies sites. These OVC phases typically have a higher bandgap than the bulk CIGSe material. Moreover, the  $\beta$ -phase is weakly n-type that forms a



buried p-n junction with p-type bulk material and helps to reduce the recombination at the interface [28]. The  $\gamma$ -CIGSe phase is observed at a copper concentration of less than 16 at%. The  $\delta$ -phase has a sphalerite crystal structure, which exists at high process temperature and is unstable at room temperature [27]. The chalcopyrite phase differs from the sphalerite phase in the random distribution of Cu, In, Ga, and Se.

A transition from the precursor  $(\text{In,Ga})_2\text{Se}_3$  to complete absorber  $\text{Cu}(\text{In,Ga})\text{Se}_2$  is by the addition of  $\text{Cu}_{2-x}\text{Se}$  phase on it, which is due to the in-diffusion of Cu-atoms and out-diffusion of In-atoms. The stoichiometric composition of CIGSe semiconductor consists of 25 at% for Cu, 25 at% for In+Ga, and 50 at% for Se [11]. The slight deviations from the stoichiometric composition of CIGSe can cause drastic changes in the electronic properties of CIGSe (i.e., 1% non-stoichiometric composition can provide a defect concentration of around  $10^{21} \text{ cm}^{-3}$ , which is higher than the effective carrier concentration of CIGSe and acts as recombination centers for the generated charge carriers.

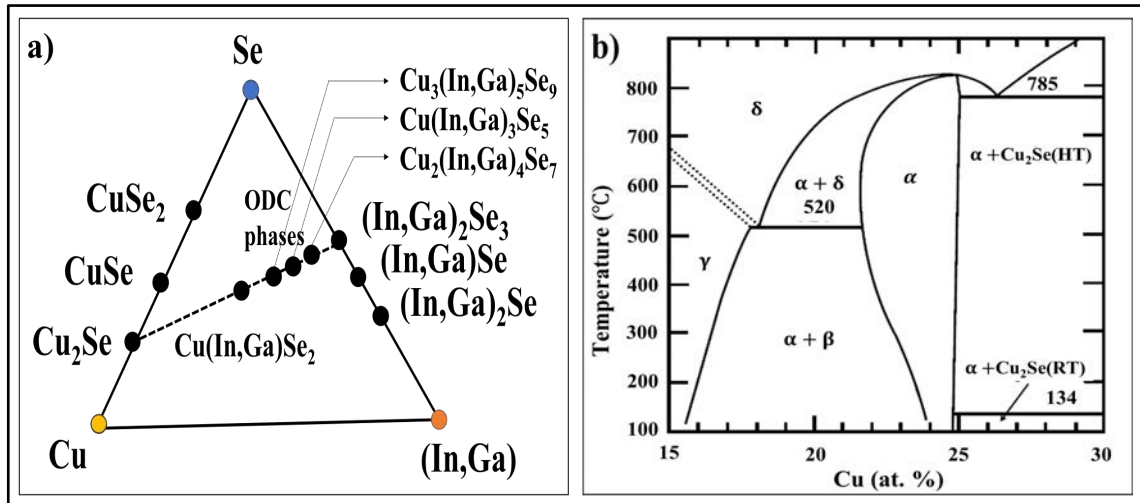


Fig. 2.3 Schematic diagram of a) phase diagram of quaternary elemental (Cu-In-Ga-Se) system, and b) pseudo-binary phase diagram along with the tie line between  $\text{Cu}_2\text{Se}$  and  $(\text{In,Ga})_2\text{Se}_3$  represented in terms of Cu composition [1]

### 2.2.3.3 Optical properties

Different semiconducting materials have different absorption coefficients, which determines how far sunlight of a particular wavelength can penetrate into a material before it is absorbed. The material thickness is adjusted in a solar cell to complete the absorption of sunlight

depending on its absorption coefficient. The semiconductor material with high absorption coefficient can absorb around 95% of incident photons in 1  $\mu\text{m}$  of its thickness. In a variety of semiconductor materials, the absorption coefficient is related to the function of extinction coefficient ( $k$ ) and wavelength of light ( $\lambda$ ) by the following formula [29],

$$\alpha = \frac{4\pi k}{\lambda} \quad (\text{eq. 2.1})$$

The absorption coefficient is also defined in the function of the incident photon energy ( $h\nu$ ) and bandgap of the semiconductor ( $E_g$ ) [1, 29, 30], which is described by,

$$\alpha = A(h\nu)^{-1}(h\nu - E_g)^{1/n} \quad (\text{eq. 2.2})$$

where  $A$  is the constant that depends on the density of states,  $n$  defines the types of bandgap (i.e.,  $n=2$  for direct bandgap semiconductor and  $n=1/2$  for indirect bandgap semiconductor). Since CIGSe semiconducting material has variable bandgaps, its absorption coefficient varies with its bandgap value. The CIGSe has the potential to obtain high efficiency due to its characteristic of a direct and tunable bandgap. The bandgap of CIGSe can be tuned from 1.04 to 1.7 eV with increased gallium content, which is governed by the following equation [31, 32]:

$$E_g = (1 - x)E_g^{\text{CISE}} + xE_g^{\text{CGSe}} - bx(1 - x) \quad (\text{eq. 2.3})$$

where  $x$  is the gallium ( $\text{Ga}/(\text{In}+\text{Ga})$ ) ratio,  $E_g^{\text{CISE}}$  is the bandgap for CISE (1.04 eV),  $E_g^{\text{CGSe}}$  is the bandgap for CGSe (1.7 eV), and  $b$  is the bowing coefficient that lays in the range of 0.15-0.24 for CIGSe material [33].

Gallium incorporation in CIGSe creates a graded bandgap in the absorber layer, which improves the collection of charge carriers. Gallium tends to diffuse towards the back contact and helps make better adhesion between the CIGSe absorber layer and back contact. Gallium forms an electric field, also called back surface field, near to back contact that helps electrons move towards the space charge region and enhances the probability of charge carrier collection [19]. The absorber material's bandgap range of 1.1-1.5 eV normally provides the maximum theoretical efficiencies for single-junction solar cells. At a higher gallium ratio

(greater than 0.3), the number of defects in the CIGSe film, such as mid-gap defects, band discontinuities at the interface, etc., increases and finally reduces the solar cell performance [19, 33, 34]. Furthermore, the bandgap of CIGSe can also be influenced by the copper content in the CIGSe film. The  $\beta$ -Cu(In,Ga)<sub>3</sub>Se<sub>5</sub> phase has a greater (around 0.2-0.3 eV) bandgap than the  $\alpha$ -Cu(In,Ga)Se<sub>2</sub> phase [11, 35]. Therefore, CIGSe is a suitable absorber layer in photovoltaic applications due to its flexible characteristics and favorable optical properties.

#### 2.2.3.4 Electrical properties

The electrical properties such as conductivity type and carrier density of the CIGSe are mainly affected by the doping types (intrinsic or extrinsic dopants) and doping density. Intrinsic defects control the doping of the CIGSe. There are twelve intrinsic defects (i.e., three vacancies, three interstitials, and six antisites) in the CIGSe semiconductor, depending on the elemental compositions in the CIGSe thin films [1]. The defects, which contain the lowest formation energy, will exist in the semiconductor material. In CIGSe, the defects such as copper vacancy ( $V_{Cu}$ ), selenium vacancy ( $V_{Se}$ ), indium on copper or gallium on copper antisites ( $In_{Cu}$  or  $Ga_{Cu}$ ), copper on indium or copper on gallium antisites ( $Cu_{In}$  or  $Cu_{Ga}$ ), etc., contain lower formation energy than other defects [33]. The defects  $V_{Cu}$ ,  $V_{III}$ , and  $V_{Se}$  are created due to the sub-stoichiometry in copper, group III, and selenium compositions, respectively. The defects  $Cu_{In}$  or  $Cu_{Ga}$  antisites and In-vacancy ( $V_{In}$ ) are observed in the case of Cu-rich CIGSe, where both of the defects are shallow acceptors and contribute p-type CIGSe material [11]. The observed  $V_{Cu}$  acts as the dominant acceptor in Cu-poor composition and  $In_{Cu}$  represents a compensating donor. Therefore, Cu-poor CIGSe can be p-type or n-type semiconductor nature [36]. The types of CIGSe material can also define by the selenium content (i.e.,  $Se/(Cu+In+Ga)$ ) in the film. A p-type and n-type CIGSe are obtained at high (greater than or equal to 1) and low (less than 1) selenium content in CIGSe thin film, respectively. The selenium vacancy ( $V_{Se}$ ) is formed at lower Se content in CIGSe thin film that acts as a compensating donor [11, 36–38]. The di-vacancy complex defects (i.e.,  $V_{Se}-V_{Cu}$  or  $V_{Se}-V_{In}$ ) are also observed in the sub-stoichiometry of Se atoms, considering the origin of metastable defects in CIGSe TFSC. These di-vacancy complex defects can shift from a donor into an acceptor configuration in p-type CIGSe, which increases the hole concentration and acts as a recombination center for minority charge

carriers [38], [39]. Since vacancy and antisite have opposite charges, the  $2V_{Cu}+In_{Cu}$  defect pair shows a neutral electrical property [40]. The defect cluster  $2V_{Cu}+In_{Cu}$  has lower formation energy than  $2V_{Cu}+Ga_{Cu}$  defect pair, reducing the formation of OVC phases and increasing the growth of the  $\alpha$ -CIGSe phase [35]. The copper ratio ( $Cu/(In+Ga)$ ) from 0.85 to 0.95 and gallium ratio from 0.2 to 0.3 is the best compositions to achieve highly efficient CIGSe TFSC.

#### 2.2.4 Window layer

The window layer could be an n-type or intrinsic semiconductor used in the CI(G)Se TFSCs. The primary function of the window layer is to form a p-n junction with the absorber layer in a heterojunction thin film solar cell. Moreover, it helps to reach the photons into the absorber layer. The window layer must have a higher bandgap than the absorber layer and be as thin as possible to allow more photons into the junction and absorber layer. A thin window layer with no defects can minimize the resistive loss by maintaining the low series resistance and improving device performance [17]. The higher carrier concentration of the window layer than the absorber layer helps extend the space charge region wider into the absorber layer, improving the collection of the generated charge carriers. The window layer materials should have fewer defects and good coverage in the absorber layer to prevent the undesirable shunt path [19].

The CdS is the II-VI n-type semiconductor, mainly used as a buffer window layer in CI(G)Se TFSCs because of its many advantageous features. The CdS has a direct bandgap ranging from 2.38 eV (for cubic crystal structure) to 2.58 eV (for wurtzite crystal structure) [41, 42]. The bandgap of CdS is higher than the bandgap of the CIGSe absorber layer (i.e., 1.04-1.68 eV), which allows more photons reaching into the junction and absorber layer. The CdS can involve the passivation of the absorber surface by removing the surface impurities (i.e., oxides, selenides, etc.) and protecting the CIGSe absorber layer's surface during the deposition of upper layers of the CIGSe TFSCs [11, 19, 41]. The diffusion of metallic atoms from the upper layers can impact the space charge region of solar cells by shunting at the junction. The CdS can prevent the diffusion of metallic atoms from the upper layers to the junction during its deposition or/and heat treatment. The CdS intermixes both the CIGSe absorber layer and ZnO window layer with better lattice mismatch that minimizes the

interfacial defects [42]. The CdS also provides a good band alignment in the solar cell structure, reducing the recombination center for charge carriers in the space charge region [43]. The Cd can diffuse from the CdS buffer layer to the surface of the absorber layer at higher temperatures than 200°C. This diffusion of Cd promotes the formation of pseudo-buried-homojunction (i.e., p-CIGSe/n-CIGSe), which helps to reduce the recombination at the CdS/CIGSe interface. All these above characteristics prove that the CdS is the best choice as a buffer window layer for CIGSe TFSCs. The thickness and deposition methods of the CdS buffer window layer are the main parameters that can strongly impact solar cell performance. The chemical bath deposition for CdS thin films deposition is the best method for achieving high CIGSe TFSC performance [42]. Various alternative window materials include ZnS, In(OH)<sub>3</sub>, In<sub>2</sub>S<sub>3</sub>, ZnSe, ZnInSe<sub>x</sub>, In<sub>x</sub>Se<sub>y</sub>, ZnMgO, ZnO, SnO<sub>2</sub>, etc. have been investigated by different research groups because of the toxic nature of Cd [19, 41].

Another window layer employed in the CIGSe TFSC is undoped zinc oxide (ZnO), an n-type semiconductor with a bandgap of 3.3 eV [11]. Generally, a thin ZnO layer is suitable in solar cells due to its relatively high conductivity, excellent electron mobility, high stability against photo-corrosion, and availability at a low cost. The ZnO effectively blocks the short-circuit pathways through the voids in the CdS and consecutively improves the FF and  $V_{oc}$  by increasing the shunt resistance of a solar cell. Therefore, the ZnO along with the CdS can prevent the electric losses by limiting the defective parts (i.e., shunt paths) in the CIGSe TFSCs. Moreover, ZnO can also avoid the diffusion of Al from the aluminum-doped zinc oxide that protects the CdS buffer window layer against chemical reactions and mechanical damage [43, 44]. The material properties of ZnO are strongly dependent on the oxygen composition of the material. The good optical properties of ZnO can be observed at high oxygen content. Radio-frequency (RF) sputtering has mostly deposited the ZnO thin films for high-efficiency CI(G)Se TFSCs [45].

### **2.2.5 Front contacts**

The front contact transports the generated charge carriers (i.e., electrons) from the absorber layer or p-n junction to the external circuit. The front contact of the solar cell has to be highly transparent to allow reaching the incident photons into the absorber layer for improving the generation of charge carriers. The front contact should also be highly conductive to improve

the device performance by preventing resistance losses while transporting the charge carriers into the external circuit [45, 46]. In CIGSe TFSC, the aluminum-doped zinc oxide (ZnO:Al) is used as a TCO layer due to its highly transparent, excellent conductive nature, and high bandgap of 3.6 eV [47, 48]. The ZnO:Al thickness ranging from 50 to 300 nm is usually employed in CIGSe TFSC. Its conductivity primarily depends on carrier concentration and mobility, which increases with an increase in doping rate [49]. The carrier concentration and mobility can be improved by enhancing the crystallinity of the material. The RF sputtering is also utilized to deposit the ZnO:Al thin films [49, 50]. Finally, the front contact is deposited over the ZnO:Al TCO to reduce the series resistance of the solar cells. The grid formed by trimetallic contacts consists of stacked nickel, aluminum, and nickel (Ni/Al/Ni) layers. These trimetallic contacts are normally deposited by the thermal evaporation method. Therefore, the quality of trimetallic grid depends on the spacing between these metals [46, 51]. The minimum shadow of the front contact is applied to allow the maximum penetration of sunlight into the absorber layer. The aluminum metal represents the ohmic contact of the solar cells, and nickel metal protects against the oxidation of the aluminum metal and connects solar cells into electronic devices.

### **2.3 Role of alkali element doping in CI(G)Se**

The doping of small amounts of alkali elements in the CIGSe absorber film tends to have a favorable effect on the properties of CIGSe film and CIGSe TFSC performance. Many studies based on the CIGSe material doped with alkali metals have been published. The beneficial effect of the alkali elements on the CIGSe material was first observed in 1993, where CIGSe TFSCs were grown on the soda-lime glass substrate containing sodium (Na) atoms [52]. The properties of the CIGSe absorber layer and solar cell device efficiency are mainly dependent on the methods of incorporation and types of alkali elements. The alkali elements consist of two types: light alkali elements (i.e., Li, Na, K) and heavy alkali elements (i.e., Rb, Cs), depending on the atomic mass of elements. The doping of alkali elements into the CIGSe material is mainly divided into three methods: pre-deposition, co-evaporation, and post-deposition incorporations [52–54]. The pre-deposition and co-evaporation incorporations mostly dope light alkali elements to the CIGSe absorber film, while post-deposition methods were used to incorporate both light and heavy alkali elements to the CIGSe. The pre-deposition incorporation is commonly recognized for diffusing alkali atoms

from the alkali elements containing substrate during the growth of CIGSe thin films [54]. The soda-lime glass substrate is usually used in pre-deposition incorporation, which contains sodium and some potassium atoms. In pre-deposition incorporation, alkali elements are also distributed into CIGSe thin films by sputtering alkali-containing Mo back contact and deposition of an alkali-halide layer on Mo. The alkali elements are evaporated during the absorber layer deposition in co-evaporation incorporation [52]. The post-deposition incorporation commonly involves the depositing alkali halide thin layers on the CIGSe absorber layer and then annealed with Se atmosphere at high temperature [55]. The migration mechanisms of alkali atoms in the CIGSe thin film are different, depending on the types of alkali atoms. The light alkali atoms tend to diffuse into the bulk CIGSe layer and create little surface effects, while heavy alkali atoms mostly exhibit surface effects. The post-deposition incorporation serves for desired deposition thicknesses and combines two or more alkali atoms.

It has been reported that the incorporation of alkali atoms into the CIGSe absorber film promotes an increase in the acceptor concentration by reducing the number of electrically active donors. This increment enhances the p-type carrier concentration and built-in voltage, promoting higher  $V_{oc}$  and FF values of solar cells [52, 53, 55–57]. It is also beneficial for the passivation of the defects at the CIGSe surface or/and at grain boundaries through activation of oxygen atoms that can improve the current density and FF by reducing the recombination centers of charge carriers [18]. Alkali elements react with Se to form an alkali polyselenide compound, which acts as a Se source during the growth of CIGSe absorber film [11, 52, 53]. This alkali polyselenide helps to reduce the formation of undesirable donor selenium vacancies. Moreover, alkali elements replace the copper vacancies, thereby reducing the formation of OVC phases of CIGSe and increasing the formation of desired  $\alpha$ -CIGSe phase. Alkali elements in the CIGSe TFSC promote the formation of alkali on copper antisites that supports the formation of (112) preferred orientation of CIGSe, growth of beneficial  $MoSe_2$  layer between Mo and CIGSe, improvement of the grain size, and crystallinity of CIGSe absorber film, formation of smoother surface and increasing the charge carrier mobility [46, 52, 53, 58, 59], etc. These favorable properties improve the collection of charge carriers. Although various hypotheses have been formulated regarding the effect of alkali metals by different groups, the actual mechanisms for improving the solar cell device performance in the presence of alkali elements are still controversial.

## 2.4 Recombination mechanism in CI(G)Se thin film solar cells

The recombination phenomenon brings the solar cell back to equilibrium by recombining excited electrons and holes before collecting these charge carriers. An excited electron relaxes back to the lower state (valence band) and recombines to the hole by losing its energy in the form of photon or/and phonon. A semiconductor's recombination mechanism is mainly divided into radiative recombination, Auger recombination, and Shockley-Read-Hall (SRH) recombination [11, 60, 61]. Radiative recombination refers to a direct band-to-band recombination. An electron falls from conduction band minima to the valence band maxima by emitting a photon with an energy equivalent to the semiconductor's bandgap. In Auger recombination, the energy of an electron is transferred to another electron, exciting it into higher energy states within the same band instead of giving off photons. The new excited electron then thermalizes and recombines to the hole of the valence band. The Auger recombination process involves a carrier-phonon interaction. The probability of Auger recombination increases at a higher concentration of charge carriers [61]. The SRH recombination, also known as trap-assisted recombination, includes the transition of electrons between bands with the emission of one or several phonons. The SRH recombination involves typically the presence of defects (i.e., point defects, grain boundaries, impurities, etc.) at the surface or bulk of the semiconductor material [62, 63]. The SRH recombination is considered a dominant recombination mechanism due to the existence of defects in the CIGSe absorber film. The following equation describes the general expression of recombination rate for SRH recombination [61, 64]:

$$R_{SRH} = (np - n_i^2) / (\tau_p(n + n^1) + \tau_n(p + p^1)) \quad (\text{eq. 2.4})$$

where the  $n$  and  $p$  are electron and hole densities, respectively, the  $n_i$  denotes the intrinsic carrier concentration. The  $\tau_n$  is the minimum lifetime of the electron and  $\tau_p$  is the minimum lifetime of the hole. The  $n^1$  and  $p^1$  are respective electron and hole densities when the Fermi level lies at the energetic position of the defect. Depending on the region in CIGSe TFSC, the recombination mechanism is categorized into four types: recombination at the back contact, recombination in the quasi-neutral region of the absorber, recombination in the space charge region of the absorber, and recombination at the absorber/buffer interface [63–



65], as shown in Fig. 2.4. The recombination of charge carriers is commonly observed maximum in the region other than the space charge region [64]. The back-contact recombination is found in the solar cell having a thin absorber layer where the electrons diffuse to the back contact and recombine to the holes of the back-contact material. The quasi-neutral region of the absorber comprises the area outside the space charge region and extends up to the back contact. Therefore, the generated charge carriers in the quasi-neutral region of the absorber will either recombine or diffuse to the space charge region. The recombination in the quasi-neutral and space charge regions can be enhanced by shallow and deep defect levels, a linear defect distribution, and exponential defect distribution in the absorber layer [64]. At the buffer/absorber interface, many interface states containing the defects (i.e., an exponential defect distribution and Fermi level position) can lead to an interface recombination path. The recombination at the buffer/absorber interface depends on the symmetry of material properties such as bandgap, electron affinity, etc., between the absorber and buffer materials.

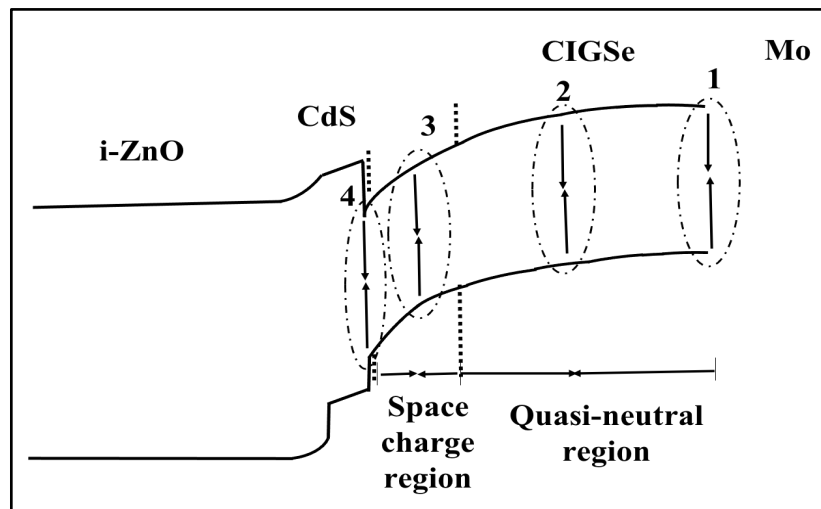


Fig. 2.4 Schematic of the band diagram and recombination mechanisms of CIGSe heterostructure TFSC, showing recombination at 1) back contact, 2) quasi-neutral region, 3) Space charge region, 4) CdS/CIGSe interface [66]

## 2.5 Deposition methods for CI(G)Se thin films

Since the CI(G)Se thin films are an essential layer in the CI(G)Se TFSC, their deposition methods are crucial factors for commercial manufacturing. The high conversion efficiency and affordable solar cells are preferred for commercialization. Many deposition methods are utilized for CIGSe thin films synthesis. These deposition methods can impact the material

properties and production costs. The deposition methods (see Fig. 2.5) are mainly divided into two types, namely vacuum-based methods and non-vacuum-based methods, depending primarily on the material quality and production cost [11, 19, 67–69]. Vacuum-based methods such as co-evaporation, sputter deposition, selenization or sulfurization of precursor layers, etc., are more reliable and reproducible, yielding high-quality thin films with fewer impurities [70, 71]. Although vacuum-based methods provide high device performance, the device cost is very high using expensive equipment and high purity precursor materials. The non-vacuum techniques are generally divided into three parts: electrodeposition, particulate and solution-based methods [19, 72–74]. These non-vacuum methods possess cost-effective devices due to their simplicity of the deposition process, require less energy usage, have better material utilization, and use of potentially low energetic incentives (i.e., low substrate temperatures, atmospheric environment, etc.). However, the non-vacuum methods have the disadvantage of low-quality film deposition, making it less efficient. The choice of the particular deposition method for CIGSe thin films depends on various features such as source materials, nature of substrate, required film thickness, specific application of film, film purity, film stability, repeatability, uniformity, and flexibility of the deposition method, etc. Various steps such as generation of the atoms/molecules from the source, transport of the source atoms/molecules to the substrate, deposition of atoms/molecules on the substrate, and post-growth treatment and analysis are involved in any deposition methods for the growth of the thin films. A few deposition methods that are in practice for CIGSe thin films are described here in detail.

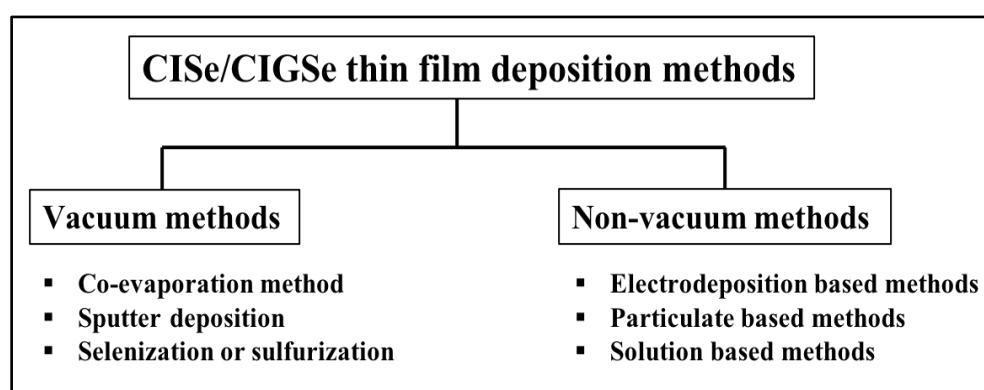


Fig. 2.5 The classification of the CI(G)Se thin film deposition methods

### 2.5.1 Co-evaporation method

One of the most used vacuum techniques for the deposition of CIGSe thin films is the co-evaporation method. This method involves the simultaneous deposition of various materials on the substrate from the evaporation sources. In this technique, the vapors of the materials are produced by boiling or sublimation and then transported from the elemental source region to the substrate region, and finally, condensed the materials on the substrate [19, 33, 70, 71]. The parameters such as elemental source temperatures, the pressure of deposition chamber, substrate temperature, sticking nature of materials, and distance between elemental sources and substrates, are important factors in the co-evaporation method that can control the growth rate of deposited thin films. Generally, a very low base pressure deposition chamber removes all potential residual and contaminated gases. Therefore, the vapors of materials can reach the substrate very easily and enhance the growth rate of the required materials. The source elements, namely Cu, In, Ga, and Se, are utilized in the co-evaporation method to deposit the CIGSe thin films. Typical ranges of source temperatures of elements used in the co-evaporation method are 1000-1400°C for Cu, 800-1100°C for In, 900-1200°C for Ga, and 250-350°C for Se evaporation. The co-evaporation method for CIGSe thin films consists of multiple steps or stages: one-stage process, two-stage process, and three-stage process [11, 19, 46]. These stages of the co-evaporation process are investigated to improve the quality of the CIGSe absorber layer for CIGSe TFSC application. The schematic diagram of the co-evaporation method is shown in Fig. 2.6.

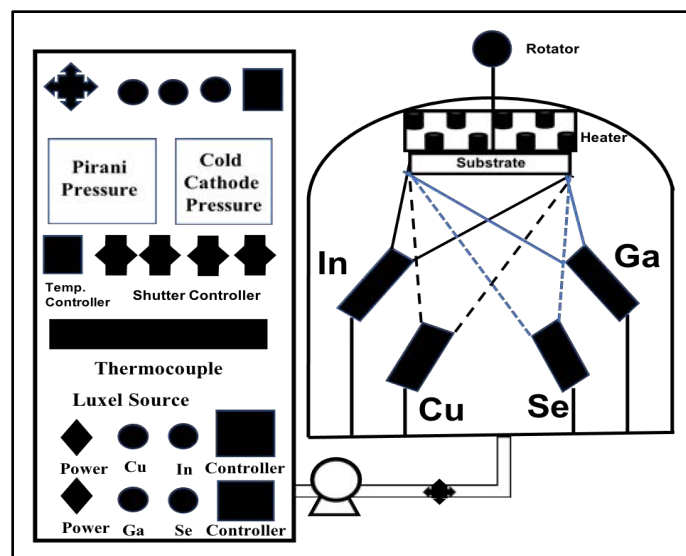


Fig. 2.6 The schematic of co-evaporation method for CI(G)Se thin film synthesis

The one-stage process is the simple deposition process. All the required materials are simultaneously evaporated and condensed on the substrate in a one-stage process [11, 75]. The substrate temperature is kept at a constant value throughout the deposition process. The slightly copper-poor film composition is preferred due to the favorable electronic properties in the CI(G)Se thin film, obtained by varying evaporation rates of each material. Record efficiency of 16.4% has been observed so far for CIGSe TFSCs by using a one-stage process [76].

The two-stages processes are introduced to improve the quality of the CIGSe thin films and CIGSe TFSC performance. The two-stage techniques provide larger grain sizes of the CIGSe thin films than the one-stage process, attributed to the formation of a  $\text{Cu}_x\text{Se}$  phase during the Cu-rich first stage. This  $\text{Cu}_x\text{Se}$  phase improves the grain size through the diffusion of group III atoms during film growth [77]. The two-stages processes are classified into three types: bilayer or Boeing process, CURO (Cu-rich/off) process, and inverted process [19]. In the Boeing process [78], the Cu-rich CIGSe thin films are formed in the first stage at low substrate temperature (i.e., 350-450°C), and then In-rich CIGSe thin films are obtained in the final stage at a high substrate temperature (i.e., 550-600°C). To date, the maximum conversion efficiency of 13-14% has been found for CIGSe TFSC using the bilayer process in CIGSe thin film synthesis [79]. The CURO process is related to the bilayer process, where all the elements (i.e., Cu, In, Ga, Se) are evaporated at constant substrate temperature [80]. After a certain deposition time, the copper flux is stopped to obtain slightly Cu-poor CIGSe thin films. The presence of the Cu-rich phase in the CIGSe thin films at the first stage can help to enhance the grain size of CIGSe thin films. The CURO process has achieved a maximum conversion efficiency of 14-16% for CIGSe TFSC [80]. The inverted process is an inverse Boeing process for the growth of the CIGSe thin films. This inverted process consists of the deposition of Cu-free precursor layer at low substrate temperature followed by the deposition of  $\text{Cu}_x\text{Se}$  at the same substrate temperature. And finally, the complete CIGSe absorber layer is formed by evaporating Se over the incomplete CIGSe thin films at high substrate temperature (i.e., 550-600°C) [81]. The deposition time of each element is chosen so that the final composition of CIGSe thin films becomes slightly Cu-poor. The maximum conversion efficiency of 13-17% has been observed for CI(G)Se thin films prepared by an inverted process [80, 81].

The three-stage process is the most used technique for fabricating the CIGSe absorber layer. This method consists of three steps: deposition of precursor layer (co-evaporation In and Se for CIGSe or In, Ga, and Se for CIGSe), co-evaporation of Cu and Se over the precursor layer deposited in the first stage, and finally co-evaporation of In and Se (for CIGSe) or In, Ga, and Se (for CIGSe) [19, 82]. The first stage is carried out at low substrate temperature (i.e., 300-400°C), whereas the second and third stages are performed at high substrate temperature (i.e., 500-600°C). The deposited CI(G)Se thin films from the three-stage process are initially In-rich composition, which is changed to Cu-rich composition in the second stage and finally made In-rich or slightly Cu-poor composition. In the second stage, a transition from the Cu-poor to the Cu-rich CIGSe phase occurs in the atomic composition. This phenomenon is called the recrystallization phenomenon, forming CuSe (liquid) and Cu<sub>2</sub>Se (Solid) phases. These phases encourage the film's growth through the mechanism of diffusion, transport, and reaction kinetics [11]. The material properties of CIGSe, namely structural, morphological, electrical, etc., are improved in the recrystallization phenomenon by minimizing crystalline defects in the grains. A solid-state interdiffusion of Cu, In, Ga, and Se atoms is necessary to have a uniform distribution of atoms in the CIGSe thin films. The interdiffusion of atoms is classified into three steps: atom-atom replacement, interstitial migration, and vacant lattice sites [11, 82]. The diffusion rate of Cu, In, Ga, and Se are respectively around  $10^{-13}$  m<sup>2</sup>/s (at 400°C),  $10^{-17}$  to  $10^{-16}$  m<sup>2</sup>/s (at 400°C),  $10^{-17}$  to  $10^{-16}$  m<sup>2</sup>/s (at 400°C), and  $10^{-16}$  m<sup>2</sup>/s (at 300°C) [19]. A slightly Cu-poor phase and excess selenium in the third stage allow the formation of a p-type CIGSe absorber layer as well as that is required to achieve higher CIGSe TFSC performance. Various groups have used different selenium content (Se/(Cu+In+Se)) in the CIGSe thin films to improve CIGSe TFSC performance. Till date, it has obtained a maximum CIGSe TFSC efficiency of around 23% by using a three-stage co-evaporation process [19].

### **2.5.2 Sputter deposition**

Another commercially available vacuum deposition technique for the growth of the CIGSe absorber layer is sputter deposition or sputtering [68, 83]. In the sputtering, the atoms of required materials are ejected from the target material by bombarding with an energetic particle on it. These ejected atoms are condensed and deposited on the substrate, forming a thin material film. The sputtering technique can deposit uniform CIGSe thin films with high

deposition rates over large areas. The sequential deposition of copper, indium, and gallium as a precursor layer is carried out on the substrate in the sputtering [19, 69]. This precursor material is then annealed in the presence of selenium or sulfur. The annealing temperatures between 400 to 500°C is the condition to achieve high-quality material. At the industrial scale, this method is used mainly by Solar frontier, Avancis, Sulfurcell, etc. The highest CIGSe TFSC efficiency of 23.35% is achieved by the Solar frontier [10]. In practice, several types of sputtering systems are used: DC sputtering, RF sputtering, magnetron sputtering, and ion beam sputtering [21]. Fig. 2.7 shows the schematic diagram of sputtering systems. Argon gas is typically bombarded into the target material for ejecting the required material from the target material towards the substrate.

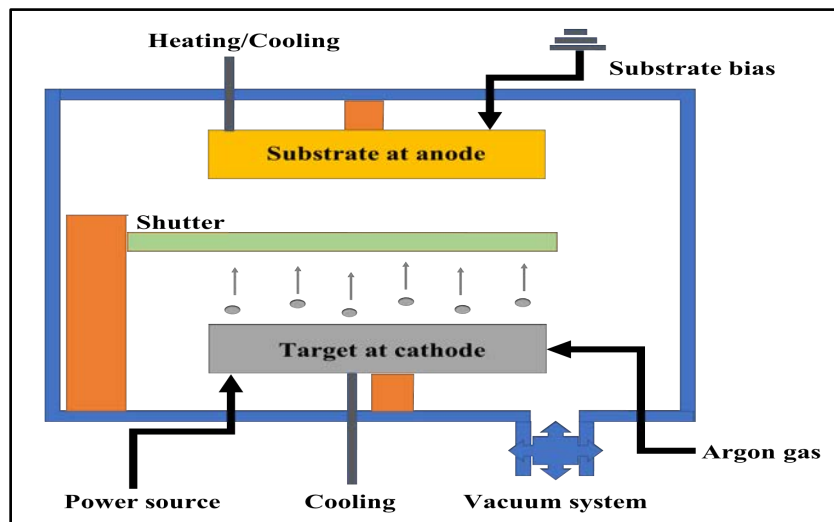


Fig. 2.7 Schematic of the sputtering systems

### 2.5.3 Selenization or sulfurization

The selenization or sulfurization of precursor materials is another vacuum process to get high-quality thin films [84]. This process also helps to get uniform thin films over a large area. The precursor materials for CIGSe thin films can be deposited by various methods, including vacuum methods (i.e., co-evaporation, sputtering) and non-vacuum methods (i.e., electrodeposition, spray pyrolysis, etc.). The precursor materials consist of layers of single elements, layers of binary materials, layers of ternary materials, and layers of mixed materials for the deposition of the CIGSe absorber layer [19, 70]. The growth of the CIGSe thin films by selenization process is mostly a two-steps process, consisting of an initial lower-temperature selenization (i.e., 300-400°C) followed by a higher temperature

selenization (i.e., 500-600°C) in an inert gas atmosphere [84, 85]. Apart from grain growth and the uniform composition of CIGSe thin films, high reaction temperatures can facilitate the formation of MoSe<sub>2</sub> at the CIGSe/Mo interface [86]. The MoSe<sub>2</sub> forms an ohmic contact between the CIGSe absorber layer and molybdenum back contact, reducing the recombination rate of generated charge carriers. Generally, the elemental Se or/and H<sub>2</sub>Se are used as selenium sources in the selenization process, and H<sub>2</sub>S is used as a sulfur source in the sulfurization process. The main parameters of this process, such as selenization or sulfurization time, temperature, chamber pressure, the quantity of selenium or sulfur source, can affect the properties of CIGSe. These parameters vary depending on the precursor materials' thickness and the required elemental composition of the final material. The maximum conversion efficiency of 22.3% has been achieved for the CIGSe TFSC using the selenization process [87].

#### **2.5.4 Electrodeposition based methods**

The electrodeposition method is intensely studied for depositing chalcopyrite-based semiconducting materials [19, 37, 83]. This method has the characteristics of simple, large-area deposition, cost-effective, time-saving, adequate for safety concerns, low-temperature deposition and use of soft processing materials, etc. Generally, a three-electrode system, namely working electrode (substrate material for film deposition), counter electrode (inert electrode often Pt wire or plate), reference electrode (SCE or Ag/AgCl), is applied in the electrodeposition process [19, 33]. Electrodeposition for CIGSe thin films is mainly divided into one-step and two-step processes. Bhattacharya et al. published the paper for the first time on one-step electrodeposition to deposit CIGSe thin films [88]. The CIGSe based thin films are deposited on the substrate from the aqueous solution containing a single electrolyte (often compounds containing sulfates or chlorides). The electrode potentials over normal hydrogen electrode (NHE) for Cu, In, Ga, and Se are +0.337 V, -0.342 V, -0.529 V, and +0.741 V, respectively [89]. The elements Cu and Se can be easily electrodeposited by reduction. But it is challenging for electrodeposition of In and Ga due to their negative potential values and reduction reaction of the proton. Therefore, special efforts in the electrodeposition process such as adjusting the concentration of elements (Cu, In, Ga, and Se), varying the pH of the solution, adding complexing agents, etc., can make the electrode potential of all the elements closer to each other. The two-step electrodeposition process

involves depositing the stacked layers of metals or alloys or binary selenides, followed by selenization or sulfurization treatment [89]. In the electrodeposition process, the reaction rate increases when the potential of the working electrode is made more negative. Several deposition parameters, namely deposition potential, the conductivity of a solution, the surface area of a working electrode, electrolyte temperature, complexing agent, concentration of elements, electrode materials, pH of electrolyte, deposition time, can affect the properties of deposited films. Many strategies have been developed to the deposition of  $\text{Cl(G)Se}$  thin films by electrodeposition process for improving the quality of deposited thin films and overcoming the thermodynamic and chemical difficulties [33, 37, 88]. The electrodeposition using an aqueous electrolyte, non-aqueous electrolyte, electrochemical mechanism, electroless, and chemical bath deposition is developed strategies so far for the  $\text{Cl(G)Se}$  thin films. The electrodeposited  $\text{Cl(G)Se}$  TFSC results are reported in many publications. The maximum efficiency of 17.3% has been observed for  $\text{ClGSe}$  TFSC using the electrodeposition process [90].

### **2.5.5 Particulate based methods**

Particulate-based methods offer an efficient method for depositing chalcopyrite thin film precursor materials [19, 73, 90]. The inks of the particulate precursor materials are deposited onto the substrates, followed by the necessary thermal treatment under a chalcogen atmosphere to achieve the desired phase. The particulate-based methods have the advantages of uniform film deposition, large-area film preparation, fewer pinhole defects, low deposition temperature ( $<400^\circ\text{C}$ ), easy to control the composition of elements, etc. Particulate precursor materials are sub-micron powders or nanoparticles of metals, metal alloys, metal oxides, or chalcogenides [33, 90]. The process of obtaining  $\text{Cl(G)Se}$  thin films by particulate-based methods is presented in Fig. 2.8. First, various techniques are synthesized  $\text{ClGSe}$  nanoparticles, typically ball milling, hot injection, and solvothermal methods. The ball milling is used to grind a fine powder through an internal cascading effect [91]. Nanoparticles with an extremely large surface area can also be obtained from the ball milling process, which might be more reactive than ordinary materials.

A multi-necked flask is mounted on a heating mantle in the hot injection method. This flask is filled with solvents that can be degassed by inert gas. The reagents are injected into the



flask after heating the solvents at a certain temperature, and then the reaction between solvents and reagent starts. The CIGSe nanoparticles are separated by centrifuging the mixture and redispersed in non-polar solvents for more purification [88, 92]. A solvothermal process is a solution-based approach where autoclaves are used to provide relatively high pressure over the reactants [93]. The precursor materials (i.e., metals or metal salts) are added to autoclaves with solvents and surfactants. The sealed autoclaves are sintered at a temperature less than 200°C and then cooled to room temperature. Similarly, CIGSe nanoparticles are collected by centrifuging process and then redispersed in non-polar solvents. Next, the CIGSe nanoparticles are dispersed in a compatible solvent (or additives) and then mixed adequately through ultrasonication. The mixture of nanoparticles and solvents are deposited on the substrate as inks, suspensions, or pastes by numerous synthesis methods such as spin-coating, dip-coating, doctor-blading, Ink-printing, etc. The solvent materials in particulate-based methods should be volatile with low temperatures to prevent the formation of complex phases with nanoparticles. Finally, the CIGSe thin films are obtained by annealing the deposited inks annealed at high temperature in the presence of Se or S. Nano solar has been working to develop particulate-based methods and has reported the maximum conversion efficiency of 17.1% for CIGSe [19].

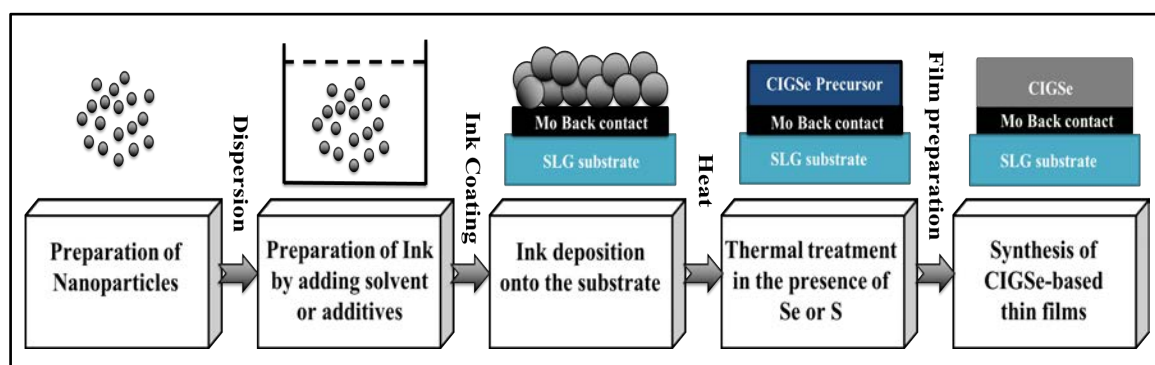


Fig. 2.8 Schematic of the Particulate-based methods for the deposition of CI(G)Se thin films

## 2.5.6 Solution based methods

The solution-based methods have been attracted in the deposition of CI(G)Se thin films due to their several advantageous properties, such as simplicity, easy scale-up, uniform film deposition, high material utilization, operation at moderate temperature (i.e., 100-500°C), use of low-cost equipment [72, 73], etc. The precursor materials are generally dissolved in the solvent in the solution-based methods, forming a true solution with the required

materials. The solvents are chosen in the solution-based methods due to their polarity, reactivity, and toxicity [19]. Many precursor materials are used in solution-based processes to deposit materials needed on the substrate. These precursor materials can broadly be classified into three sections: metal salts-based precursors, organometallic-based precursors, and hydrazine-based precursors [19, 46]. The metal salts (i.e., chlorides and nitrates) offer good solubility in water and alcohol, considered the most intuitive and the easiest ways to make precursor solutions. These precursor solutions possess low viscosity without adding any binding agent. The spray pyrolysis deposition system is typically utilized for the solution containing low viscosity. The spray pyrolysis is based on the pyrolytic decomposition of tiny droplets of precursor solution onto a heated substrate under atmospheric pressure [21, 93]. Using this technique, the deposition of thin films involves three main steps: the atomization of precursor solutions, transportation of the resultant aerosol, and decomposition of the precursor on the substrate. Understanding these three steps of the spray pyrolysis technique can improve the quality of the deposited films. The spray pyrolysis technique is mainly classified into pneumatic, ultrasonic, electrostatic depending on the atomizer used in the atomization process [21]. Fig. 2.9a displays the pneumatic spray pyrolysis technique, consisting of an atomizer, a solution container, temperature controller, a substrate heater, gas, and liquid flow meter. Precursor materials such as metal chlorides or nitrides (for copper, indium, gallium sources), thiourea (for sulfur source), and N, N-dimethyl selenourea (for selenium source), and water/alcohol mixed solvents are used in the deposition of Cl(G)Se thin films. The maximum 10.5% conversion efficiency is obtained for Cl(G)Se TFSC by spray pyrolysis technique [94].

The deposition techniques other than spray pyrolysis, such as doctor blading, spin coating, etc., can be applied for viscous solutions [19, 90]. The precursor solutions become highly viscous by adding binders or chelating agents. The spin coating technique (see Fig. 2.9b) involves the application of inks to the rotating substrate at a certain angular velocity. The deposited thin films are annealed at high temperatures in the presence of selenium or sulfur atmosphere. The spin coating technique normally utilizes nitrate salts and PVA as a binder. The thickness of deposited films over the substrate depends on the rotation speed and viscosity of solutions. Multiple depositions in the spin coating are required to build up the necessary film thickness (typically, 4/5 times deposition is needed to obtain 1.2  $\mu\text{m}$  of film thickness) [22, 73]. To date, the maximum ClGSe TFSC efficiency of 15.2% has been

observed by using the spin coating technique [95]. The doctor blading technique is also employed to deposit thin films by moving the blade over the substrate containing highly viscous precursor solutions, as shown in Fig. 2.9c. Afterward, the deposited films over the substrate are annealed in a selenium or sulfur environment. In the doctor blading technique, various binders (i.e., methanol, ethyl cellulose, polymethyl methacrylate, etc.) are combined with metal nitrates to make precursor inks. The record efficiency of 15% has been observed for CIGSe TFSC using the doctor blading technique [96].

Organometallic-based precursors are different than metal salts precursors, where the components of CIGSe material are mixed with the solution at a molecular level [19, 72, 73]. These precursors are classified into two types: single-source (e.g.,  $(\text{Ph}_3\text{P})_2\text{Cu}(\mu\text{-SEt})_2\text{In}(\text{SEt})_2$ ) and multi-source (metal naphthenate). The single-source precursors prevent the binary phase formation during the deposition of CIGSe based thin films that could negatively affect the device performance. Various techniques such as spin coating, spray pyrolysis, spray chemical vapor deposition, etc., are used to deposit CI(G)Se thin films from the organometallic precursors. The maximum efficiency obtained for CIGSe based TFSC using a single-source organometallic precursor is of 6.7% [97].

Hydrazine-based precursors are introduced to address the issues of film purity and quality [98]. Hydrazine is an extremely polar liquid with similar physical properties to water. Hydrazine possesses the unique reducing nature to dissolve metal chalcogenides at high concentrations. First, the metal chalcogenides ( $\text{Cu}_2\text{S}/\text{Cu}_2\text{Se}$ ,  $\text{Ga}_2\text{S}/\text{Ga}_2\text{Se}$ ,  $\text{In}_2\text{S}_3/\text{In}_2\text{Se}_3$ ,  $\text{S}/\text{Se}$ ) are dissolved separately into the hydrazine through stirring at room temperature. Afterward, all precursor solutions are mixed to form precursor inks of CIGSe. These obtained precursor inks can be deposited onto the substrates by different deposition techniques (such as spin coating, drop-casting, etc.) followed by annealing treatment [72, 73]. Upon heating, the hydrazine decomposes into various compounds that show volatile nature and leaves from the system and finally forms CI(G)Se thin films directly on the substrate. To date, the maximum conversion efficiency of 15.2% has been observed for CI(G)Se TFSC using hydrazine precursor solutions [95]. Since hydrazine is a highly toxic and reactive material, safety precautions must be required to prepare precursor inks and the deposition of films on the substrate. Because of that, many alternative solvents have been developed to replace

hydrazine solvents. But the emerging solvents have not found good results on CI(G)Se TFSC so far.

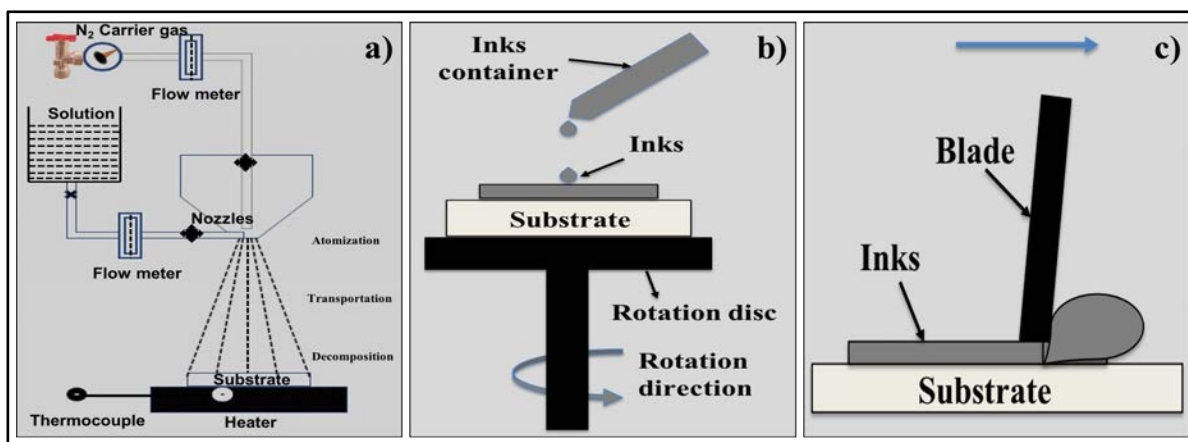


Fig. 2.9 Schematic of a) pneumatic spray pyrolysis, b) spin coating, and c) doctor blade techniques

## 2.6 Hybrid deposition method

The solar cell performance can be improved by increasing the solar cell efficiency and reducing the manufacturing cost. The efficiency of solar cell depends on the quality of the semiconducting material used in the solar cells, while the cost can be reduced by using low-cost materials and growth methods. The growth methods of semiconductors can also alter the material properties and qualities. Vacuum-based methods yield high-quality thin films with fewer impurities. On the other hand, non-vacuum methods possess cost-effective devices by utilizing low-cost growth processes and cheaper precursor materials. But the high fabrication cost in vacuum-based methods and low PCE in non-vacuum-based techniques are the main concerns in thin film solar cells. A new approach for synthesis of CI(G)Se thin films is required to get high efficiency-to-cost ratio of the device. The novel hybrid deposition method is employed in this study for CI(G)Se thin films synthesis to address the challenges associated with either of those methods.

This hybrid deposition method resembles the three-stage co-evaporation method that combines the non-vacuum spray pyrolysis technique and vacuum co-evaporation method [34], as shown in Fig. 2.10. The purpose of combining vacuum and non-vacuum methods in the hybrid method is to utilize their advantages for improving the efficiency-to-cost ratio of a photovoltaic cell. The first stage of the hybrid deposition method involves the indium

selenide ( $\text{In}_2\text{Se}_3$ ) precursor layer deposition using the pneumatic spray pyrolysis technique [99]. The 2<sup>nd</sup> and 3<sup>rd</sup> stages of the hybrid deposition method are performed in the co-evaporation method. In the 2<sup>nd</sup> stage, the co-evaporation of copper and selenium over the  $\text{In}_2\text{Se}_3$  precursor layer deposited in the first stage is carried out. This idea aims to obtain a transition from Cu-poor to the Cu-rich CIGSe phase in the atomic composition, a phenomenon called the recrystallization phenomenon and associated with an increase in the grain sizes and subsequent improvement in absorber layer quality. The 3<sup>rd</sup> stage consists of the co-evaporation of indium and selenium (for CIGSe) or indium, gallium, and selenium (for CIGSe) until the nominal composition returns to the slightly Cu-poor composition to achieve the requirement of Cu-poor composition for the CI(G)Se absorber layer. The slightly Cu-poor composition can form buried homojunction, which helps to reduce the recombination of charge carriers at the interface. Finally, the CI(G)Se thin films deposited by hybrid methods are annealed in a selenium environment at high temperatures. The post-annealing treatment aims to get uniform distribution of elements inside the films and improve the grain size of the CI(G)Se thin films. The larger grains in the CI(G)Se thin films decrease the number of grain boundaries, which eventually reduces the recombination centers and then improves device performance.

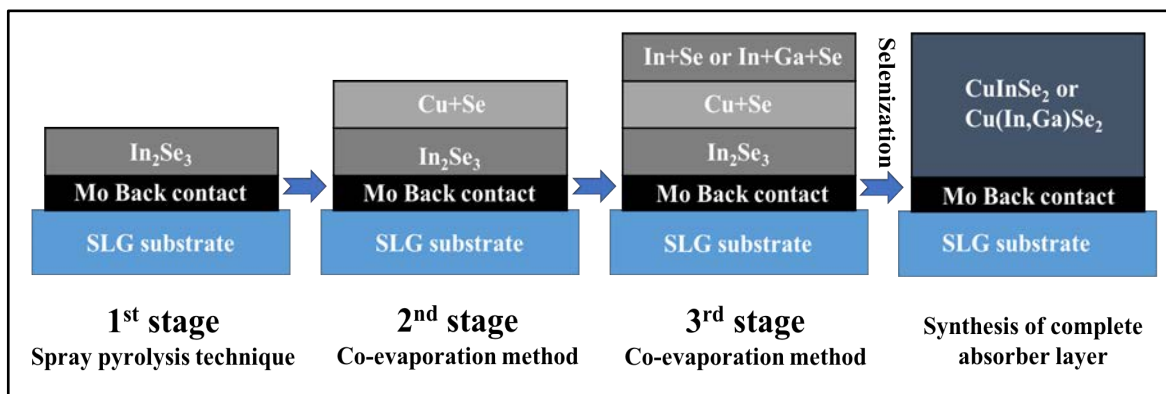


Fig. 2.10 Schematic image of hybrid deposition method developed for the growth of CI(G)Se thin films

## References:

- [1] S. H. Antonio Luque, Handbook of Photovoltaic Science and Engineering, Second. John Wiley & Sons, 2011.
- [2] B. Telephone, L. Murray, and H. New, "CuInSe<sub>2</sub>/CdS heterojunction photovoltaic detectors," vol. 25, no. 8, pp. 434–435, 1974.

- [3] J. Shay and S. Wagner, “Efficient CuInSe<sub>2</sub>/CdS solar cells,” *Appl. Phys.*, vol. 89, no. Table I, pp. 89–90, 1975.
- [4] F. R. W. and G. K. M. L. L. Kazmerski, “Thin-film CuInSe<sub>2</sub>/CdS heterojunction solar cells,” vol. 29, p. 268, 1976.
- [5] M. A. Green, K. Emery, D. L. King, S. Igari, and W. Warta, “Solar cell efficiency tables (Version 15),” *Prog. Photovoltaics Res. Appl.*, vol. 8, no. 4, pp. 377–383, 2000.
- [6] M. A. Green, K. Emery, Y. Hishikawa, and W. Warta, “Solar cell efficiency tables (version 35),” *Prog. Photovoltaics Res. Appl.*, vol. 18, no. 2, pp. 144–150, 2010.
- [7] M. A. Green et al., “Solar cell efficiency tables (version 50),” *Prog. Photovoltaics Res. Appl.*, vol. 25, no. 7, pp. 668–676, 2017.
- [8] M. Green, E. Dunlop, J. Hohl-Ebinger, M. Yoshita, N. Kopidakis, and X. Hao, “Solar cell efficiency tables (version 57),” *Prog. Photovoltaics Res. Appl.*, vol. 29, no. 1, pp. 3–15, 2021.
- [9] M. A. Green, E. D. Dunlop, J. Hohl-Ebinger, M. Yoshita, N. Kopidakis, and X. Hao, “Solar cell efficiency tables (Version 58),” *Prog. Photovoltaics Res. Appl.*, vol. 29, no. 7, pp. 657–667, 2021.
- [10] M. Nakamura, K. Yamaguchi, Y. Kimoto, Y. Yasaki, T. Kato, and H. Sugimoto, “Cd-Free Cu(In,Ga)(Se,S)<sub>2</sub> thin-film solar cell with record efficiency of 23.35%,” *IEEE J. Photovoltaics*, vol. 9, no. 6, pp. 1863–1867, 2019.
- [11] Pablo Itzam Reyes Figueroa, “Deposition and characterization of Cu(In<sub>1-x</sub>Ga<sub>x</sub>)Se<sub>2</sub> films by multiple deposition techniques,” 2016.
- [12] J. Nam, Y. Kang, D. Kim, D. Baek, D. Lee, and J. Yang, “The oxidation effect of a Mo back contact on Cu(In,Ga)(Se,S)<sub>2</sub> thin-film solar modules,” *Sol. Energy Mater. Sol. Cells*, vol. 144, pp. 445–450, 2016.
- [13] L. Kronik, D. Cahen, and H. W. Schock, “Effects of sodium on polycrystalline Cu(In,Ga)Se<sub>2</sub> and its solar cell performance,” *Adv. Mater.*, vol. 10, no. 1, pp. 31–36, 1998.
- [14] S. H. Wei, S. B. Zhang, and A. Zunger, “Effects of Na on the electrical and structural properties of CuInSe<sub>2</sub>,” *J. Appl. Phys.*, vol. 85, no. 10, pp. 7214–7218, 1999.
- [15] K. Herz, A. Eicke, F. Kessler, R. Wächter, and M. Powalla, “Diffusion barriers for CIGS solar cells on metallic substrates,” *Thin Solid Films*, vol. 431–432, no. 03, pp. 392–397, 2003.
- [16] J. Martin, *Materials for engineering*, vol. 21, no. 5. 2013.

- [17] A. A. Kadam, "Preparation of efficient  $\text{CuIn}_{1-x}\text{Ga}_x\text{Se}_2\text{-ySy}/\text{CdS}$  thin film solar cells by optimizing the molybdenum back contact and using diethylselenide as selenium precursor," University of Central Florida, 2006.
- [18] S. A. Pethe, "Optimization Of Process Parameters For Reduced Thickness CIGS Thin Film Solar Cells STARS Citation," 2010.
- [19] G. Regmi et al., "Perspectives of chalcopyrite-based CIGSe thin-film solar cell: a review," *J. Mater. Sci. Mater. Electron.*, vol. 31, no. 10, pp. 7286–7314, 2020.
- [20] J. Kaneshiro, N. Gaillard, R. Rocheleau, and E. Miller, "Advances in copper-chalcopyrite thin films for solar energy conversion," *Sol. Energy Mater. Sol. Cells*, vol. 94, no. 1, pp. 12–16, 2010.
- [21] M. A. Hassan, "Spray Pyrolysis Synthesized  $\text{Cu}(\text{In,Ga/Al})(\text{S,Se})_2$  Thin Films for Photovoltaic Applications By Spray Pyrolysis Synthesized  $\text{Cu}(\text{In,Ga/Al})(\text{S,Se})_2$  Thin Films for Photovoltaic Applications," National University of Sciences & Technology (NUST), Pakistan, 2018.
- [22] J. Ramanujam and U. P. Singh, "Copper indium gallium selenide based solar cells - A review," *Energy Environ. Sci.*, vol. 10, no. 6, pp. 1306–1319, 2017.
- [23] S. C. Abrahams and J. L. Bernstein, "Piezoelectric nonlinear optic  $\text{CuGaSe}_2$  and  $\text{CdGeAs}_2$ : Crystal structure, chalcopyrite microhardness, and sublattice distortion," *J. Chem. Phys.*, vol. 61, no. 3, pp. 1140–1146, 1974.
- [24] D. Rudmann, "Effects of sodium on growth and properties of  $\text{Cu}(\text{In,Ga})\text{Se}_2$  thin films and solar cells," University of Basel \_\_, 2004.
- [25] J. C. Mikkelsen, "Ternary Phase Relations of the Chalcopyrite Compound  $\text{CuGaSe}_2$ ," vol. 10, no. 3, pp. 541–558, 1981.
- [26] B. J. Stanbery, "Copper indium selenides and related materials for photovoltaic devices," *Crit. Rev. Solid State Mater. Sci.*, vol. 27, no. 2, 2002.
- [27] S. Kulkarni, "Effect of Composition, Morphology and Semiconducting properties on the Efficiency of  $\text{CuIn}_{1-x}\text{Ga}_x\text{Se}_2\text{-ySy}$  Thin-Film Solar Cells Prepared by Rapid Thermal Processing," 2008.
- [28] Y. Tamm and S. Fiechter, "Crystal growth of materials for photovoltaics," *J. Ceram. Process. Res.*, vol. 6, no. 2, pp. 141–145, 2005.
- [29] A. Dahshan and K. A. Aly, "Determination of the thickness and optical constants of amorphous Ge-Se-Bi thin films," *Philos. Mag.*, vol. 89, no. 12, pp. 1005–1016, 2009.
- [30] H. Kafashan, "Optoelectronic properties of In-doped SnS thin films," *Ceram. Int.*, vol.

45, no. 1, pp. 334–345, 2019.

- [31] A. Morales-Acevedo, “Effective absorption coefficient for graded band-gap semiconductors and the expected photocurrent density in solar cells,” *Sol. Energy Mater. Sol. Cells*, vol. 93, no. 1, pp. 41–44, 2009.
- [32] S. H. Wei and A. Zunger, “Band offsets and optical bowings of chalcopyrites and Zn-based II-VI alloys,” *J. Appl. Phys.*, vol. 78, no. 6, pp. 3846–3856, 1995.
- [33] S. H. Wei, S. B. Zhang, and A. Zunger, “Effects of Ga addition to CuInSe<sub>2</sub> on its electronic, structural, and defect properties,” *Appl. Phys. Lett.*, vol. 72, no. 24, pp. 3199–3201, 1998.
- [34] D. Valencia, J. Conde, A. Ashok, and S. Velumani, “Optimization of Cu(In, Ga)Se<sub>2</sub> (CIGSe) thin film solar cells parameters through numerical simulation and experimental study,” *Sol. Energy*, 2021.
- [35] M. Kemell, M. Ritala, and M. Leskelä, “Thin film deposition methods for CuInSe<sub>2</sub> solar cells,” *Crit. Rev. Solid State Mater. Sci.*, vol. 30, no. 1, pp. 1–31, 2005.
- [36] A. R. and R. W. Birkmire, “CuInSe<sub>2</sub> for photovoltaic applications,” vol. 81, no. August, 1998.
- [37] R. Noufi, R. Axton, C. Herrington, and S. K. Deb, “Electronic properties versus composition of thin films of CuInSe<sub>2</sub>,” *Appl. Phys. Lett.*, vol. 45, no. 6, pp. 668–670, 1984.
- [38] R. Chandran, S. K. Panda, and A. Mallik, “A short review on the advancements in electroplating of CuInGaSe<sub>2</sub> thin films,” *Mater. Renew. Sustain. Energy*, vol. 7, no. 2, pp. 1–20, 2018.
- [39] U. Rau and H. W. Schock, “Electronic properties of Cu(In,Ga)Se<sub>2</sub> heterojunction solar cells-recent achievements, current understanding, and future challenges,” *Appl. Phys. A Mater. Sci. Process.*, vol. 69, no. 2, pp. 131–147, 1999.
- [40] S. B. Zhang, S. H. Wei, and A. Zunger, “Stabilization of ternary compounds via ordered arrays of defect pairs,” *Phys. Rev. Lett.*, vol. 78, no. 21, pp. 4059–4062, 1997.
- [41] G. A. W. M. Cardona, M. Weinstein, “Ultraviolet Reflection Spectroscopy of Cubic CdS,” vol. 140, no. 1964, 1965.
- [42] A. Ashok, G. Regmi, A. Romero-Núñez, M. Solis-López, S. Velumani, and H. Castaneda, “Comparative studies of CdS thin films by chemical bath deposition techniques as a buffer layer for solar cell applications,” *J. Mater. Sci. Mater. Electron.*, vol. 31, no. 10, pp. 7499–7518, 2020.



- [43] R. Hunger et al., “Junction formation of CuInSe<sub>2</sub> with CdS: A comparative study of ‘dry’ and ‘wet’ interfaces,” *Thin Solid Films*, vol. 515, no. 15 SPEC. ISS., pp. 6112–6118, 2007.
- [44] M. Nichterwitz, R. Caballero, C. A. Kaufmann, H. W. Schock, and T. Unold, “Generation-dependent charge carrier transport in Cu(In,Ga)Se<sub>2</sub>/CdS/ZnO thin-film solar-cells,” *J. Appl. Phys.*, vol. 113, no. 4, 2013.
- [45] G. Regmi, M. Rohini, P. Reyes-Figueroa, A. Maldonado, M. de la Luz Olvera, and S. Velumani, “Deposition and characterization of ultrathin intrinsic zinc oxide (i-ZnO) films by radio frequency (RF) sputtering for propane gas sensing application,” *J. Mater. Sci. Mater. Electron.*, vol. 29, no. 18, pp. 15682–15692, 2018.
- [46] P. Pushkaraj, “Copper Gallium Diselenide Solar Cells: Processing, Characterization and Simulation Studies,” 2003.
- [47] U. P. Singh and S. P. Patra, “Progress in polycrystalline thin-film Cu(In,Ga) Se<sub>2</sub> solar cells,” *Int. J. Photoenergy*, vol. 2010, 2010.
- [48] T. D. C. Nguyen Duy Phuong and N. H. V. Nguyen Nguyen Ngoc Long, “Preparation of Transparent Conducting ZnO:Al Films On Glass Substrates By R.F. Magnetron Sputtering,” *J. Sci. Math. - Phys.*, 2002.
- [49] K. L. Chopra, P. D. Paulson, and V. Dutta, “Thin-film solar cells: An overview,” *Prog. Photovoltaics Res. Appl.*, vol. 12, no. 2–3, pp. 69–92, 2004.
- [50] O. Nwakanma, V. Subramaniam, and A. Morales-Acevedo, “Properties of Ultra-Thin Radio-frequency Sputtered Aluminum Doped Zinc Oxide Thin Films for Solar Cell Applications,” 2020 17th Int. Conf. Electr. Eng. Comput. Sci. Autom. Control. CCE 2020, no. 2947, 2020.
- [51] H. Park, S. Qamar Hussain, and S. Velumani, “Influence of working pressure on the structural, optical and electrical properties of sputter deposited AZO thin films,” *Mater. Sci. Semicond. Process.*, vol. 37, pp. 29–36, 2015.
- [52] L. Stolt et al., “ZnO / CdS / CuInSe<sub>2</sub> thin-film solar cells with improved performance performance,” vol. 597, no. June 1992, pp. 4–7, 1993.
- [53] O. Nwakanma, S. Velumani, and A. Morales-Acevedo, “Review on the effects due to alkali metals on copper–indium–gallium–selenide solar cells,” *Mater. Today Energy*, vol. 20, p. 100617, 2021.
- [54] Y. Sun et al., “Review on Alkali Element Doping in Cu(In,Ga)Se<sub>2</sub> Thin Films and Solar Cells,” *Engineering*, vol. 3, no. 4, pp. 452–459, 2017.

- [55] F. Werner et al., “Alkali treatments of Cu(In,Ga)Se<sub>2</sub> thin-film absorbers and their impact on transport barriers,” *Prog. Photovoltaics Res. Appl.*, vol. 26, no. 11, pp. 911–923, 2018.
- [56] S. Siebentritt et al., “Heavy Alkali Treatment of Cu(In,Ga)Se<sub>2</sub> Solar Cells: Surface versus Bulk Effects,” *Adv. Energy Mater.*, vol. 10, no. 8, 2020.
- [57] D. Rudmann, G. Bilger, M. Kaelin, F. J. Haug, H. Zogg, and A. N. Tiwari, “Effects of NaF coevaporation on structural properties of Cu(In,Ga)Se<sub>2</sub> thin films,” *Thin Solid Films*, vol. 431–432, no. 03, pp. 37–40, 2003.
- [58] D. Braunger, D. Hariskos, G. Bilger, U. Rau, and H. W. Schock, “Influence of sodium on the growth of polycrystalline Cu(In,Ga)Se<sub>2</sub> thin films,” *Thin Solid Films*, vol. 361, pp. 161–166, 2000.
- [59] M. A. Contreras and R. Noufi, “Chalcopyrite Cu ( In , Ga ) Se<sub>2</sub> and defect-chalcopyrite Cu ( In , Ga ) 3Se<sub>5</sub> materials in photovoltaic P-N junctions,” vol. 174, pp. 283–288, 1997.
- [60] A. Rockett et al., “Na in selenized Cu(In,Ga)Se<sub>2</sub> on Na-containing and Na-free glasses: Distribution, grain structure, and device performances,” *Thin Solid Films*, vol. 372, no. 1, pp. 212–217, 2000.
- [61] R. Scheer and H.-W. Schock, *Chalcogenide Photovoltaics*. 2011.
- [62] N. Khoshsirat and N. A. M. Yunus, “Copper-Indium-Gallium-diSelenide (CIGS) Nanocrystalline Bulk Semiconductor as the Absorber Layer and Its Current Technological Trend and Optimization,” *Nanoelectron. Mater. Dev.*, 2016.
- [63] W. Shockley and W. T. Read, “Statistics of the recombinations of holes and electrons,” *Phys. Rev.*, vol. 87, no. 5, pp. 835–842, 1952.
- [64] U. Malm, J. Malmström, C. Platzer-Björkman, and L. Stolt, “Determination of dominant recombination paths in Cu(In,Ga)Se<sub>2</sub> thin-film solar cells with ALD-ZnO buffer layers,” *Thin Solid Films*, vol. 480–481, pp. 208–212, 2005.
- [65] A. V. Tovar, “Analysis of Current Transport and Recombination Mechanisms in Chalcopyrite-Based Thin-Film Solar Cells with RbF Treatment.”
- [66] F. Baig, “Numerical Analysis for Efficiency Enhancement of Thin Film Solar Cells,” 2019.
- [67] V. Nadenau, U. Rau, A. Jasenek, and H. W. Schock, “Electronic properties of CuGaSe<sub>2</sub>-based heterojunction solar cells. Part I. Transport analysis,” *J. Appl. Phys.*, vol. 87, no. 1, pp. 584–593, 2000.

- [68] X. Lyu et al., “Influences of sulfurization on performances of Cu(In,Ga)(Se,S)<sub>2</sub> cells fabricated based on the method of sputtering CIGSe quaternary target,” *J. Alloys Compd.*, vol. 791, pp. 1193–1199, 2019.
- [69] J. Liu, D. Zhuang, H. Luan, M. Cao, M. Xie, and X. Li, “Preparation of Cu(In,Ga)Se<sub>2</sub> thin film by sputtering from Cu(In,Ga)Se<sub>2</sub> quaternary target,” *Prog. Nat. Sci. Mater. Int.*, vol. 23, no. 2, pp. 133–138, 2013.
- [70] S. Ahn et al., “Cu(In,Ga)Se<sub>2</sub> thin films without Ga segregation prepared by the single-step selenization of sputter deposited Cu-In-Ga-Se precursor layers,” *Energy Environ. Sci.*, vol. 5, no. 12, pp. 9914–9921, 2012.
- [71] M. Powalla, G. Voorwinden, D. Hariskos, P. Jackson, and R. Kniese, “Highly efficient CIS solar cells and modules made by the co-evaporation process,” *Thin Solid Films*, vol. 517, no. 7, pp. 2111–2114, 2009.
- [72] S. T. Kim, K. Kim, J. H. Yun, and B. T. Ahn, “A new simple route to grow Cu(In,Ga)Se<sub>2</sub> thin films with large grains in the co-evaporation process,” *Curr. Appl. Phys.*, vol. 18, no. 8, pp. 912–918, 2018.
- [73] D. Lee and K. Yong, “Non-vacuum deposition of CIGS absorber films for low-cost thin film solar cells,” *Korean J. Chem. Eng.*, vol. 30, no. 7, pp. 1347–1358, 2013.
- [74] C. J. Hibberd, E. Chassaing, W. Liu, D. B. Mitzi, D. Lincot, and A. N. Tiwari, “Non-vacuum methods for formation of Cu(In, Ga)(Se, S)<sub>2</sub> thin film photovoltaic absorbers,” *Prog. Photovoltaics Res. Appl.*, vol. 18, no. 6, pp. 434–452, 2010.
- [75] T. Todorov et al., “Solution-based synthesis of kesterite thin film semiconductors,” *JPhys Energy*, vol. 2, no. 1, 2020.
- [76] W. N. Shafarman and J. Zhu, “Effect of substrate temperature and deposition profile on evaporated Cu(InGa)Se<sub>2</sub> films and devices,” *Thin Solid Films*, vol. 361, pp. 473–477, 2000.
- [77] H. Rau and A. Rabenau, “Vapour pressure measurements in the copper-selenium system,” *J. Solid State Chem.*, vol. 1, no. 3–4, pp. 515–518, 1970.
- [78] R. A. M. and W. S. Chen, “High photocurrent polycrystalline thin-film CdS / CuInSe<sub>2</sub> solar cell a,” vol. 371, pp. 3–6, 1980.
- [79] and D. C. Reiner Klenk, Thornus Wulter, Hans- Werner Schock, “A Model for the Successful Growth of Poly- crystalline Films of CuInSe, by Multisource Physical Vacuum Evaporation,” *Adv. Mater.*, vol. 5, 1993.
- [80] J. Kessler, J. Scholdstrom, and L. Stolt, “Rapid Cu(In,Ga)Se/sub 2/ growth using ‘end

point detection,” 2000.

- [81] S. Nishiwaki et al., “Preparation of Cu ( In , Ga ) Se thin " lms from Cu } Se / In } Ga } Se precursors for high-e \$ ciency solar cells,” *Sol. Energy Mater. Sol. Cells*, vol. 67, pp. 217–223, 2001.
- [82] D. S. A. Andrew M. Gabor, John R. Tuttle, “High efficiency polycrystalline Cu(In,Ga)Se<sub>2</sub>-based solar cells,” vol. 59, p. 306, 1994.
- [83] B. Kim and B. K. Min, “Strategies toward highly efficient CIGSe thin-film solar cells fabricated by sequential process,” *Sustain. Energy Fuels*, vol. 2, no. 8, pp. 1671–1685, 2018.
- [84] Y. Huang, A. Han, X. Wang, X. Liu, Z. Liu, and F. Meng, “Tuning the band gap of Cu(In,Ga)Se<sub>2</sub> thin films by simultaneous selenization/sulfurization,” *Mater. Lett.*, vol. 182, pp. 114–117, 2016.
- [85] G. M. Albalawneh, M. M. Ramli, M. Z. M. Zain, and Z. Sauli, “The influence of selenium amount added into the graphite box during the selenization of solution deposited CIGSe thin films,” *J. Phys. Conf. Ser.*, vol. 2053, no. 1, 2021.
- [86] D. Abou-Ras et al., “Formation and characterisation of MoSe<sub>2</sub> for Cu(In,Ga)Se<sub>2</sub> based solar cells,” *Thin Solid Films*, vol. 480–481, pp. 433–438, 2005.
- [87] B. Kim and B. K. Min, “Strategies toward highly efficient CIGSe thin-film solar cells fabricated by sequential process,” *Sustain. Energy Fuels*, vol. 2, no. 8, pp. 1671–1685, 2018.
- [88] R. N. Bhattacharya, “Solution Growth and Electrodeposited CuInSe<sub>2</sub>Thin Films,” *J. Electrochem. Soc.*, vol. 130, 1983.
- [89] D. Lincot et al., “Chalcopyrite thin film solar cells by electrodeposition,” *Sol. Energy*, vol. 77, no. 6, pp. 725–737, 2004.
- [90] C. Broussillou et al., “Statistical Process Control for Cu(In,Ga)(S,Se)<sub>2</sub> electrodeposition-based manufacturing process of 60×120cm<sup>2</sup> modules up to 14,0% efficiency,” 2015 IEEE 42nd Photovolt. Spec. Conf. PVSC 2015, pp. 1–5, 2015.
- [91] V. Bermudez, “An overview on electrodeposited Cu(In,Ga)(Se,S)<sub>2</sub> thin films for photovoltaic devices,” *Sol. Energy*, vol. 175, no. February, pp. 2–8, 2018.
- [92] Q. Guo et al., “Development of CuInSe<sub>2</sub> nanocrystal and nanoring inks for low-cost solar cells,” *Nano Lett.*, vol. 8, no. 9, pp. 2982–2987, 2008.
- [93] B. Li, Y. Xie, J. Huang, and Y. Qian, “Synthesis by a solvothermal route and characterization of CuInSe<sub>2</sub> nanowhiskers and nanoparticles,” *Adv. Mater.*, vol. 11,

no. 17, pp. 1456–1459, 1999.

- [94] S. K. Hossain, M. A., Tianliang, Z., Keat, L. K., Xianglin, L., Prabhakar, R. R., Batabyal, “Synthesis of  $\text{Cu(In,Ga)(S,Se)}_2$  thin films using an aqueous spray-pyrolysis approach, and their solar cell efficiency of 10.5%,” *J. Mater. Chem. A*, no. 3, pp. 4147–4154, 2015.
- [95] D. B. Todorov, T. K., Gunawan, O., Gokmen, T., & Mitzi, “Solution-processed Cu (In, Ga)(S, Se)  $_2$  absorber yielding a 15.2% efficient solar cell,” *Prog. Photovoltaics Res. Appl.*, vol. 21, no. 1, pp. 82–87, 2013.
- [96] R. McLeod, S.M., Hages, C.J., Carter, N.J. and Agrawal, “Synthesis and characterization of 15% efficient CIGS<sub>Se</sub> solar cells from nanoparticle inks,” *Prog. Photovoltaics Res. Appl.*, vol. 23, no. 1, pp. 1550–1556, 2015.
- [97] M. Jin, K. Banger, C. Kelly, and J. Scofield, “Solar Cells Fabricated With  $\text{CuInS}_2$  Films Deposited Using Single Source Precursors,” *Sol. Cells*, pp. 3–6, 2008.
- [98] H. Azimi, Y. Hou, and C. J. Brabec, “Towards low-cost, environmentally friendly printed chalcopyrite and kesterite solar cells,” *Energy Environ. Sci.*, vol. 7, no. 6, pp. 1829–1849, 2014.
- [99] A. Ashok, G. Regmi, and S. Velumani, “Growth of  $\text{In}_2\text{Se}_3$  Thin Films Prepared by the Pneumatic Spray Pyrolysis Method for Thin Film Solar Cells Applications,” 2020 17th Int. Conf. Electr. Eng. Comput. Sci. Autom. Control. CCE 2020, pp. 2–7, 2020.

## **Chapter 3 Experimental, simulation and characterization details**

This chapter mainly describes experimental details, SCAPS simulation details, and characterization techniques used for the experimental and simulation study. In the experimental work section, a brief information of substrate preparation, hybrid deposition method for CI(G)Se absorber layer synthesis and chemical bath deposition method for CdS buffer layer are explained. This chapter also introduces the SCAPS simulation details, containing solar cell structures for CIGSe based TFSCs as well as details of material parameters used in the solar cells. The characterization techniques namely X-ray diffraction (XRD), Raman spectroscopy, scanning electron microscopy (SEM), energy dispersive X-ray spectroscopy (EDS), atomic force microscopy (AFM), ultraviolet-visible (UV-Vis), four-probe method, and Hall van der Pauw method, are briefly described here for studying the structural, morphological, compositional, topographical, optical, electrical properties of the thin films. Finally, the external-quantum efficiency measurement is also introduced to estimate the individual losses responsible for reducing the current in the CI(G)Se TFSCs.

### **3.1 Experimental details**

#### **3.1.1 Substrate preparation**

The selection of the best substrate in the deposition process is typically based on various characteristics, such as temperature stability, thermal expansion coefficient, and chemical stability. Soda-lime glass (SLG) substrate has all the qualities mentioned above for fabricating CIGSe based TFSCs. Here, thin film materials are grown over SLG substrate (corning No 2947,  $75 \times 25 \times 1 \text{ mm}^2$ ). The deposited films should adhere effectively to the substrate for better growth of the thin films. Therefore, the substrates must be cleaned properly before using in the solar cell fabrication. For this, the substrates are cleaned by using various steps that are explained as follows.

- i. First, substrates are ultrasonically cleaned with de-ionized water for 10 minutes. Shock waves created in the solvent rendered the possible removal of residues.
- ii. Then, substrates are subjected to ultrasonic agitation in Extran solution for 10 minutes, followed by ultrasonic agitation in de-ionized water for 10 minutes.

- iii. Subsequently, substrates are washed in NaOH aqueous solution (2.5M) for 60 minutes, followed by ultrasonic agitation in de-ionized water for 10 minutes.
- iv. After that, substrates are rinsed with HCl (0.1M) solution in an ultrasonic bath for 5 minutes, followed by ultrasonic agitation in de-ionized water for 10 minutes.
- v. Then, substrates are cleaned with methanol (98 %, pure) for 10 minutes, followed by ultrasonic agitation in de-ionized water for 10 minutes.
- vi. Finally, substrates are dried by nitrogen gas and directly put in the deposition of thin films or preserved in a vacuum for future use.

### 3.1.2 CI(G)Se thin films by hybrid deposition method

The CI(G)Se absorber materials are deposited using the novel hybrid deposition method. This proposed hybrid deposition method resembles with 3-stages co-evaporation process, that combines the pneumatic spray pyrolysis (PSP) technique and the co-evaporation method. The hybrid deposition method helps to obtain the material with high quality, better growth rate and low-cost by utilizing less pure precursor materials as well as reducing the waste of pure materials (especially in the co-evaporation method). These advantages can improve the efficiency and reduce the cost for CIGSe TFSC. The first stage of the hybrid deposition method involves depositing indium selenide thin films through the PSP technique [1]. The second and third stages were carried out in the vacuum co-evaporation method [2, 3]. The copper and selenium are co-evaporated in the second stage. Finally, the third stage consists of the co-evaporation of indium and selenium for CIGSe thin films or indium, gallium, and selenium for CIGSe thin films, respectively.

PSP technique, also called solution process, is based on a pyrolytic decomposition of tiny droplets of precursor solution on a heated substrate. Fig. 3.1 displays the PSP technique for the deposition of indium selenide ( $\text{In}_2\text{Se}_3$ ) thin films. The  $\text{In}_2\text{Se}_3$  films are deposited on the SLG substrates, heated by a heater containing a molten tin bath because of its better heat transfer property to a solid surface. All the precursor materials for thin film deposition are chosen in such a way that the product compounds other than the  $\text{In}_2\text{Se}_3$  compound will be volatile with substrate temperature. The precursor materials, namely indium chloride ( $\text{InCl}_3$ , the concentration of 0.0015 M) and N, N-dimethyl-selenourea ( $\text{NH}_2(\text{CH}_3)_2\text{NCSe}$ , the concentration of 0.005 M) are dissolved in a solution containing ethanol (20 vol%), and

water (80 vol%). These precursor materials should be completely soluble with ethanol solution for getting uniform growth of the thin films on the heated substrate. Ethanol is suitable solvent material in the PSP technique because it can dissolve the precursor materials completely in 20 vol% and contains nonflammable nature with temperature. As selenium showed volatile nature with temperature, a higher amount of N, N-dimethyl-selenourea is applied than indium chloride in the solution to maintain high selenium content within the film. The excess selenium content in the film allows the formation of the gamma-In<sub>2</sub>Se<sub>3</sub> ( $\gamma$ -In<sub>2</sub>Se<sub>3</sub>) phase, which is more stable phase than others. Various parameters such as substrate temperature, deposition time, nozzle-to-substrate distances, gas flow rate, solution flow rate, etc., are adjusted and optimized to deposit indium selenide thin films. The optimized deposition parameters for In<sub>2</sub>Se<sub>3</sub> thin films by PSP technique such as the solution flow rate, gas flow rate, the substrate temperature, deposition time, and the distance between the nozzle to substrate are 5mL/min, 4000 mL/min, 300-340°C, 90 minutes and 26 cm, respectively. A thickness of around 1  $\mu$ m for In<sub>2</sub>Se<sub>3</sub> thin film is found. The chemical reaction mechanisms occurred in the PSP technique for indium selenide deposition are explained below [4].

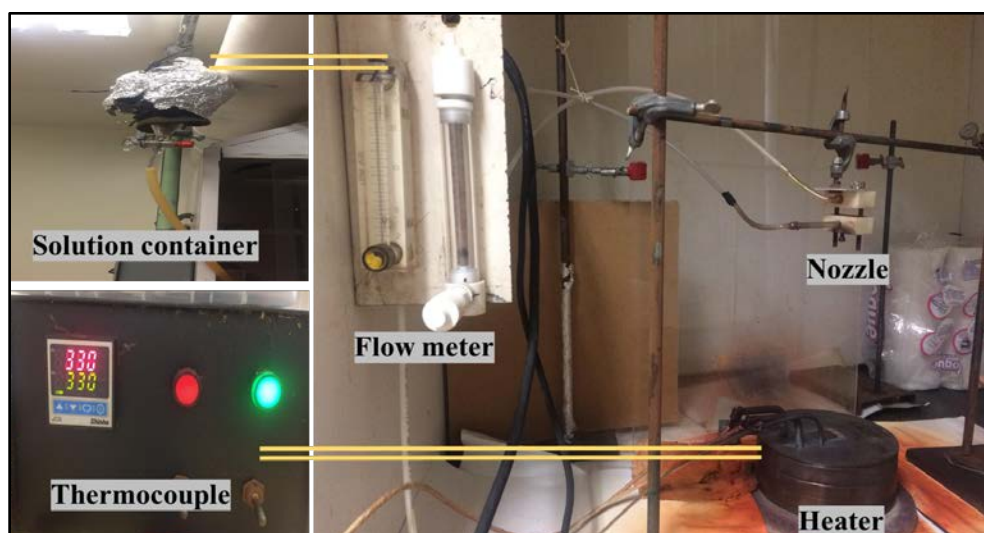
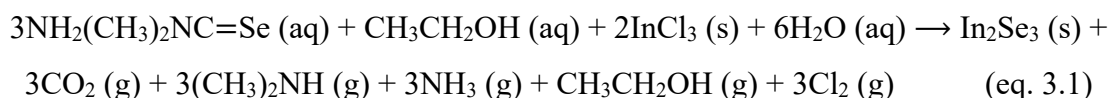


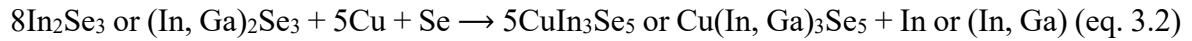
Fig. 3.1 Pneumatic spray pyrolysis system used for the deposition of In<sub>2</sub>Se<sub>3</sub> thin films

The co-evaporation method is a vacuum process where elements are evaporated and condensed on the substrate at a certain distance from the evaporation source. In the second stage, copper and selenium are co-evaporated over the In<sub>2</sub>Se<sub>3</sub> precursor layer deposited in

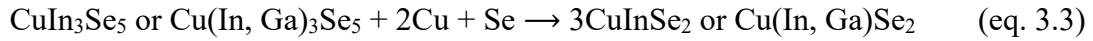


the first stage. The base pressure of the chamber is maintained at  $5 \times 10^{-6}$  Torr for depositing the precursor materials without any disturbance. The substrate temperature is kept at  $500^\circ\text{C}$  to diffuse copper inside the films and to have chemical reactions of the compounds to form a single compound. Source temperature for copper of  $1300^\circ\text{C}$  was used in the evaporation process. Excess selenium is employed due to its low sticking coefficient than other elements (i.e., copper, gallium, indium). Moreover, selenium acts as a volatile nature at higher substrate temperature, so that deposited selenium on the substrate can be ejected out and contain a low proportion of selenium in the film. Therefore, excess selenium must be used to prevent selenium deficiency in the film. This idea aims to obtain a transition from Cu-poor to Cu-rich CIGSe phase of its atomic composition. This phenomenon is called the recrystallization phenomenon, where the grain size of the layer increases and subsequently improves material quality. During this stage, deposition is aiming to reach a stoichiometry ( $y = [\text{Cu}]/([\text{In}] + [\text{Ga}])$  or  $([\text{Cu}]/[\text{In}]) = 1$ ) or off-stoichiometry Cu-rich ( $y > 1$ ). Then, copper evaporation is promptly suspended with the completion of the deposition time of 60 minutes. The chemical reaction mechanisms during the second stage are mentioned below [5].

At the beginning of second stage,



At the mid of second stage,

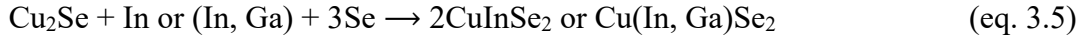


At the end of the second stage,



Finally, the third stage involves completing the absorber layer (CIGSe) by the co-evaporation of In+Se (for CIGSe) or In+Ga+Se (for CIGSe) until the nominal composition returns to the slightly Cu-poor composition. Slightly sub-stoichiometric ( $y < 1$ ) values (i.e., 0.85 to 0.95) and excess selenium allow the formation of p-type CIGSe material, which is the requirements of the thin film solar cells. The indium is evaporated at a source temperature of  $850^\circ\text{C}$  for 15 minutes, and gallium is evaporated at a source temperature of  $950^\circ\text{C}$  for 5 minutes. A brief description of the co-evaporation process is shown in Figure 3.2. The chemical reaction mechanisms during the third stage are shown below [5].

At the beginning of the third stage,



At the end of the third stage,

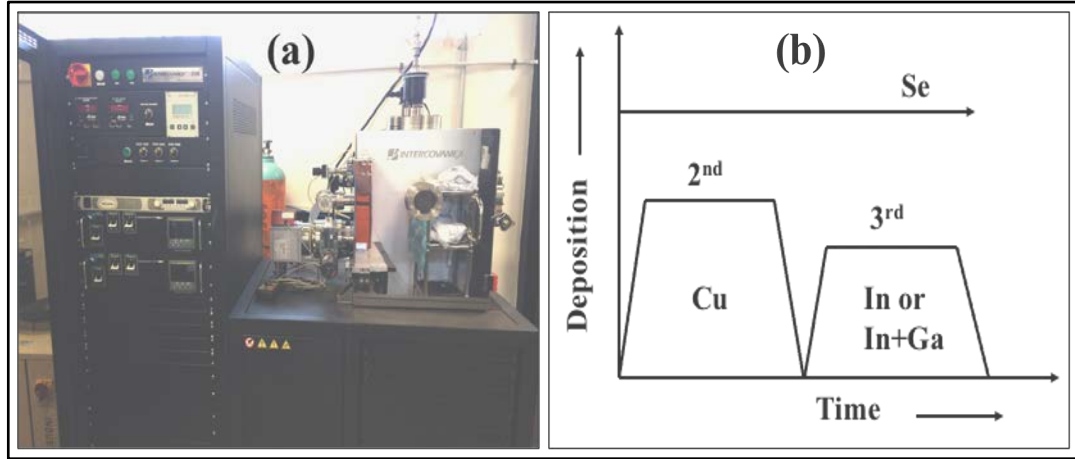
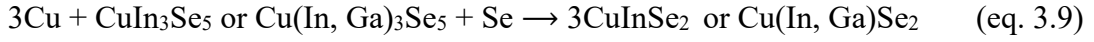
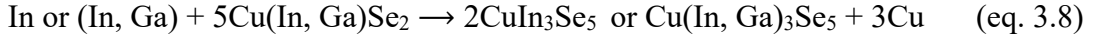


Fig. 3.2 schematic of a) co-evaporation process, b) deposition process of second and third stages

The absorber materials obtained by the hybrid deposition method are selenized to complete  $\text{CI(G)Se}$  absorber layer's synthesis. The main purpose of doing the selenization process is to make uniform distribution of elements inside the film and improve the grain size of films. Larger the grain size of films, lower the number of grain boundaries where the generated charge carriers recombine and reduce the solar cell efficiency. Here, the two-steps selenization process was performed in the MTI vacuum oven at atmospheric pressure with argon gas [6]. The first step consists of selenization at a lower temperature of  $300^\circ\text{C}$  for 30 minutes and the last step involves selenization at the higher temperature (i.e., reaction temperature) of  $500\text{--}550^\circ\text{C}$  for 60 minutes. Subsequently, the selenized samples were cooled in the chamber for several hours to stabilize the selenized film. The complete selenization process is shown graphically in Figure 3.3.

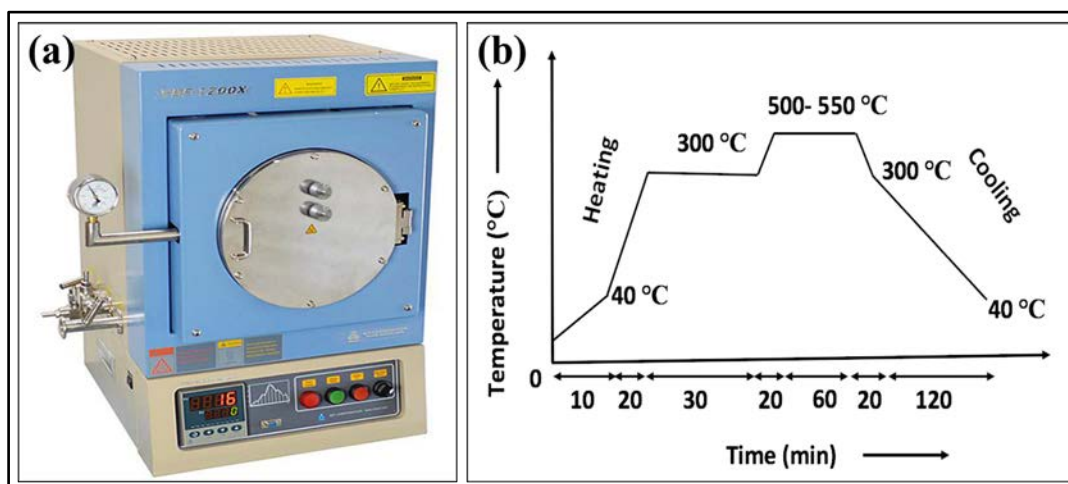


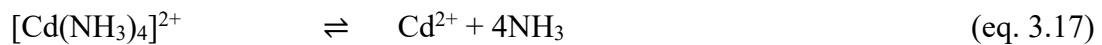
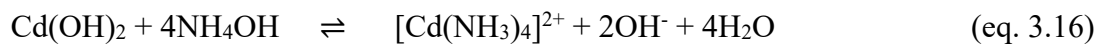
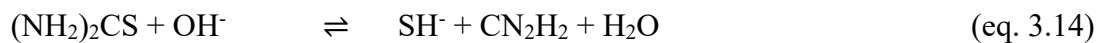
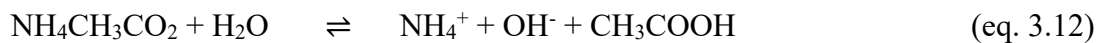
Fig. 3.3 Schematic of a) MTI vacuum oven and b) selenization process used for CI(G)Se thin films

### 3.1.3 CdS thin films by chemical bath deposition method

The CdS thin films used as a buffer layer in the CIGSe TFSCs is deposited by the chemical bath deposition (CBD) method [7]. In this research work, various deposition parameters of CBD method such as type of precursor material and their concentration, time, temperature, etc. are applied to analyze growth process mechanism as well as optimize the CdS material as buffer layer in the CI(G)Se TFSCs. A systematic investigation on the effect of ammonia content, deposition temperature and deposition time on the physical properties of CdS thin films are carried out. Various precursor materials such as cadmium acetate (cadmium source), thiourea (sulfur source), ammonium hydroxide (complexing agent), and ammonium acetate (catalytic reagent) are used for the deposition of the CdS film. The schematic diagram of the CBD method for CdS thin films deposition is shown in Fig. 3.4. First of all, CdS thin films are deposited at several proportions of ammonium hydroxide from 1:1 to 5:1 compared with the quantity of cadmium acetate and thiourea. After that, CdS thin films are fabricated on different bath temperatures (70, 75, 80, and 85°C) at a constant time of 30 min and different timings (20, 30, 40, 50, and 60 min) at constant bath temperature of 80°C. The substrates are mounted vertically with the help of Teflon holders inside the solution. Precursor solution is prepared by dissolving 0.033 M of cadmium acetate (as cation ( $\text{Cd}^{2+}$ ) source), 0.07 M of thiourea (as anion ( $\text{S}^{2-}$ ) source), 3 M of ammonium hydroxide, and 1 M of ammonium acetate on 200 mL of de-ionized water. The stirring action inside the bath helps to interact between substrate and reactants that is also significant for uniform deposition. When all the precursor solutions are mixed, the chemical reactions between

cadmium ions and sulfur ions begin and the color of the solution changes into a yellow color that signifies the formation of CdS material. After the deposition, the substrates are taken out from the solution and then ultrasonically rinsed with de-ionized water for 2–3 min to remove loosely bonded CdS particles. Finally, the films are washed with running de-ionized water and dried with nitrogen gas to get rid of moisture. The rear side film of the substrate is removed with the help of the HCl solution in order to characterize the film.

The ammonia is used as a complexing agent which controls the free cadmium metal ion concentration and produces free cadmium ions ( $\text{Cd}^{2+}$ ) through dissociation reaction. Ammonium acetate is applied as a buffer solution to control the cadmium concentration as well as reaction rate. Ammonia and ammonium acetate combined with water liberate the hydroxyl ions ( $\text{OH}^-$ ) that reacts with cadmium acetate giving cadmium hydroxide and with thiourea providing free sulfur ions. The cadmium hydroxide in the presence of ammonium hydroxide produces cadmium tetraamine complex ions and hydroxyl ions. The produced hydroxyl ions serve to maintain a constant pH value ( $\text{pH} = 10$ ) of the bath. Furthermore, an increase in  $\text{OH}^-$  tends to accelerate the growth process, favoring the hydrolysis reaction and consequently decreasing the formation time of the desired layer. Finally, the complex ions mixed with sulfur ions form cadmium sulfide compound. The chemical reaction mechanisms that occur in this growth process are shown in following equations [7–9].



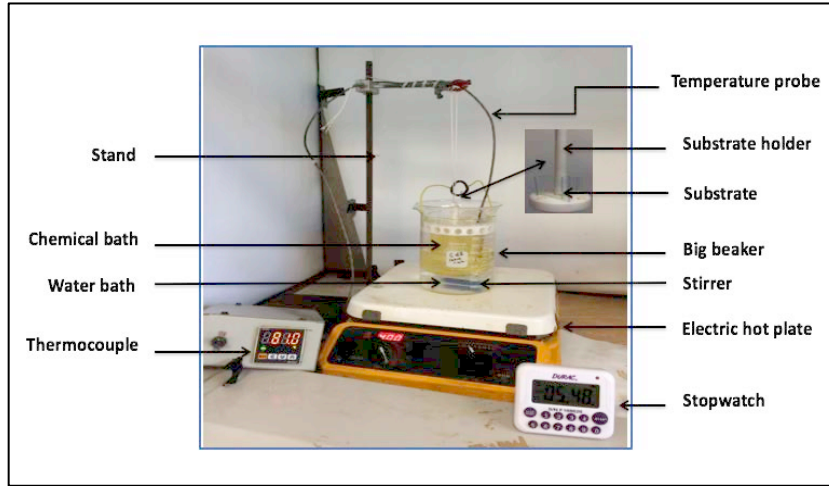


Fig. 3.4 Experimental details of CBD method for CdS thin films

### 3.2 SCAPS simulation details

SCAPS can study the effect of the different parameters, namely thickness, bandgap, electron affinity, dielectric permittivity, electron and hole mobilities, shallow uniform donor, and acceptor densities on the solar cell's performance, etc. Fig. 3.5 displays the schematic of the CISE, CIGSe and CIGSe bilayer TFSC structures generated in the SCAPS software process. This simulation employed the solar spectrum of AM 1.5G and ambient temperature of 300 K. The parameters of different layers used in CISE, CIGSe, and CIGSe bilayer TFSC are summarized in Table 3.1, Table 3.2, and Table 3.3, respectively. In this simulation study, the thickness and carrier concentration of each material used in CISE, CIGSe and CIGSe bilayer TFSC are primarily focused and graded. These two parameters are linked to understand the device cost and efficiency. The output parameters, such as  $J_{sc}$ ,  $V_{oc}$ , FF, and PCE, for every graded condition are calculated from the SCAPS simulator. The CISE, CIGSe, and CIGSe bilayer TFSCs are optimized for getting device performance as high as possible. The simulation study is also focused on the effect of the defects, ambient temperatures, and parasitic resistances on the solar cell performance. Analyzing these parameters will be helpful to understand their influence on the solar cell parameters. This simulation study is designed to solve the basic semiconductor equations (i.e., Poisson's equation and Continuity equations) for charge carriers and produce non-linear equations for modeling solar cells, which play a key role in analyzing photovoltaic cell performance and its possible output [11]. There are mainly two effects responsible for the change in charge carrier collection efficiency. The first one is narrowing the space charge region upon

light soaking, and the second is reducing minority carrier diffusion length. The diffusion length ( $L_{Diff}$ ) of the minority charge carriers is related to the carrier lifetime ( $\tau_{n, p}$ ) and diffusion coefficient ( $D_{n, p}$ ) of the minority charge carriers. These parameters are calculated from the following equations [29, 43, 45]:

$$L_{Diff} = \sqrt{D(n, p) \tau(n, p)} \quad (\text{eq. 3.19})$$

$$D_{n, p} = \mu_{n, p} \frac{kT}{q} \quad (\text{eq. 3.20})$$

$$\tau_{n, p} = (\sigma_{(n, p)} V_{(thn, thp)} N_t)^{-1} \quad (\text{eq. 3.21})$$

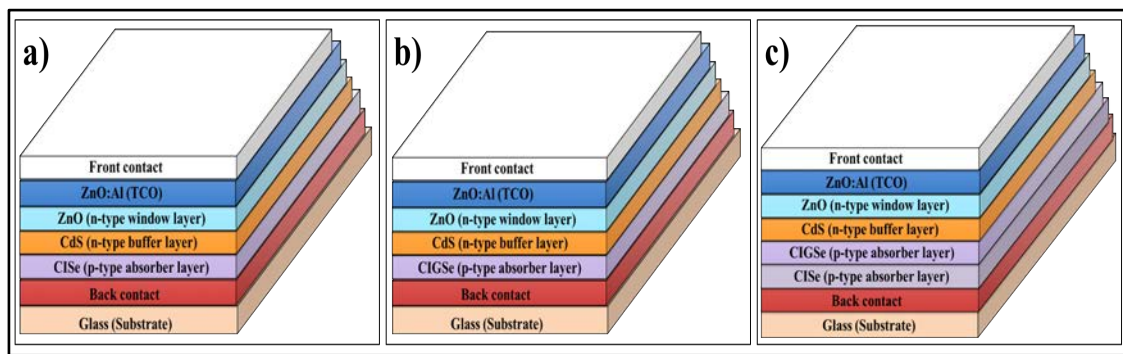


Fig. 3.5 Schematic diagram of the a) CISe TFSC structure, b) CIGSe TFSC structure, and c) CIGSe bilayer TFSC structure generated by SCAPS software

Table 3.1 Parameters used in SCAPS software for analyzing the CISe TFSC

Materials	CISe	CdS	ZnO	ZnO:Al
Parameters				
Thickness (nm)	1000-10000	20-100	20-100	50-350
Bandgap (eV)	1.04	2.45	3.25	3.5
Electron affinity (eV)	4.5	4.2	4.55	4.5
Dielectric permittivity	13.6	10	9	9
CB density of states ( $\text{cm}^{-3}$ )	$2.2 \times 10^{18}$	$2.2 \times 10^{18}$	$2.2 \times 10^{18}$	$2.2 \times 10^{18}$
VB density of states ( $\text{cm}^{-3}$ )	$1.8 \times 10^{19}$	$1.8 \times 10^{19}$	$1.8 \times 10^{19}$	$1.8 \times 10^{19}$
Electron thermal velocity (cm/s)	$1 \times 10^7$	$1 \times 10^7$	$1 \times 10^7$	$1 \times 10^7$
Hole thermal velocity (cm/s)	$1 \times 10^7$	$1 \times 10^7$	$1 \times 10^7$	$1 \times 10^7$
Electron mobility ( $\text{cm}^2/\text{Vs}$ )	100	100	100	100
Hole mobility ( $\text{cm}^2/\text{Vs}$ )	25	25	25	25
Donor density ( $\text{cm}^{-3}$ )	0	$1 \times 10^{14}$ - $1 \times 10^{19}$	$1 \times 10^{14}$ - $1 \times 10^{20}$	$1 \times 10^{14}$ - $1 \times 10^{21}$
Acceptor density ( $\text{cm}^{-3}$ )	$1 \times 10^{14}$ - $1 \times 10^{18}$	0	0	0
Defect density ( $\text{cm}^{-3}$ )	$1 \times 10^{12}$ - $1 \times 10^{19}$	$1 \times 10^{12}$ - $1 \times 10^{18}$	-	-
Capture cross section ( $\text{cm}^2$ )	$1 \times 10^{-18}$ - $1 \times 10^{-12}$	$1 \times 10^{-18}$ - $1 \times 10^{-12}$	-	-

Table 3.2 Parameters used in SCAPS software for analyzing the CIGSe TFSC

Parameters \ Materials	CIGSe	CdS	ZnO	ZnO:Al
Thickness (nm)	1000-10000	20-100	20-80	50-400
Bandgap (eV)	1.0-1.7	2.45	3.25	3.5
Electron affinity (eV)	4.5	4.2	4.55	4.5
Dielectric permittivity	13.6	10	9	9
CB density of states (cm <sup>-3</sup> )	$2.2 \times 10^{18}$	$2.2 \times 10^{18}$	$2.2 \times 10^{18}$	$2.2 \times 10^{18}$
VB density of states (cm <sup>-3</sup> )	$1.8 \times 10^{19}$	$1.8 \times 10^{19}$	$1.8 \times 10^{19}$	$1.8 \times 10^{19}$
Electron thermal velocity (cm/s)	$1 \times 10^7$	$1 \times 10^7$	$1 \times 10^7$	$1 \times 10^7$
Hole thermal velocity (cm/s)	$1 \times 10^7$	$1 \times 10^7$	$1 \times 10^7$	$1 \times 10^7$
Electron mobility (cm <sup>2</sup> /Vs)	100	100	100	100
Hole mobility (cm <sup>2</sup> /Vs)	25	25	25	25
Donor density (cm <sup>-3</sup> )	0	$1 \times 10^{13}$ - $1 \times 10^{20}$	$1 \times 10^{13}$ - $1 \times 10^{20}$	$1 \times 10^{13}$ - $1 \times 10^{21}$
Acceptor density (cm <sup>-3</sup> )	$1 \times 10^{14}$ - $5 \times 10^{17}$	0	0	0
Defect density (cm <sup>-3</sup> )	$1 \times 10^{12}$ - $1 \times 10^{20}$	$1 \times 10^{12}$ - $1 \times 10^{19}$	-	-
Capture cross section (cm <sup>2</sup> )	$1 \times 10^{-20}$ - $1 \times 10^{-12}$	$1 \times 10^{-19}$ - $1 \times 10^{-12}$	-	-

Table 3.3 Parameters used in SCAPS software for analyzing the CIGSe bilayer TFSC

Parameters \ Materials	CIGSe	CIGSe	CdS	ZnO	ZnO:Al
Thickness (nm)	1000-9000	1000-9000	20-90	20-80	50-400
Bandgap (eV)	1.04	1.1-1.7	2.45	3.25	3.5
Electron affinity (eV)	4.5	4.5	4.2	4.55	4.5
Dielectric permittivity	13.6	13.6	10	9	9
CB density of states (cm <sup>-3</sup> )	$2.2 \times 10^{18}$	$2.2 \times 10^{18}$	$2.2 \times 10^{18}$	$2.2 \times 10^{18}$	$2.2 \times 10^{18}$
VB density of states (cm <sup>-3</sup> )	$1.8 \times 10^{19}$	$1.8 \times 10^{19}$	$1.8 \times 10^{19}$	$1.8 \times 10^{19}$	$1.8 \times 10^{19}$
Electron thermal velocity	$1 \times 10^7$	$1 \times 10^7$	$1 \times 10^7$	$1 \times 10^7$	$1 \times 10^7$
Hole thermal velocity	$1 \times 10^7$	$1 \times 10^7$	$1 \times 10^7$	$1 \times 10^7$	$1 \times 10^7$
Electron mobility (cm <sup>2</sup> /Vs)	100	100	100	100	100
Hole mobility (cm <sup>2</sup> /Vs)	25	25	25	25	25
Donor density (cm <sup>-3</sup> )	0	0	$1 \times 10^{13}$ - $1 \times 10^{20}$	$1 \times 10^{13}$ - $1 \times 10^{20}$	$1 \times 10^{13}$ - $1 \times 10^{20}$
Acceptor density (cm <sup>-3</sup> )	$1 \times 10^{13}$ - $1 \times 10^{20}$	$1 \times 10^{13}$ - $1 \times 10^{20}$	0	0	0
Defect density (cm <sup>-3</sup> )	-	$1 \times 10^{12}$ - $5 \times 10^{19}$	$1 \times 10^{12}$ - $5 \times 10^{19}$	-	-
Capture cross section (cm <sup>2</sup> )	-	$1 \times 10^{-17}$ - $1 \times 10^{-10}$	$1 \times 10^{-17}$ - $1 \times 10^{-10}$	-	-

### **3.3 Device characterization**

#### **3.3.1 Material characterization**

Characterization is a vital step in the development of materials for technological applications. The basic properties of material like structural, morphological, compositional, optical, electrical, etc., are essential material information because the material can use in different areas based on these properties. Material characterization allows optimizing the growth parameters of the deposition method for semiconducting material. This section introduces a brief description of the techniques such as film thickness measurement, X-ray diffraction (XRD), Raman spectroscopy, scanning electron microscopy (SEM), energy-dispersive X-ray spectroscopy (EDS), atomic force microscopy (AFM), optical properties, electrical properties measurement.

##### **3.3.1.1 Film thickness measurement**

The thickness of thin film material is one of the most crucial factors in the photovoltaic application, which can mainly affect the cost of the solar cell device. Moreover, the basic properties of thin film material, namely microstructure, morphological, optical, and electrical properties, are dependent on its thickness. Film thickness can be measured either by in-situ monitoring of deposition or after the film deposition. Measuring the thickness of the film is also vital in coating over any substance. Various techniques such as the Gravimetric method, Ellipsometry, profilometry, optical interference method, etc., are available for estimating the film thickness. In this study, the thickness of deposited films is measured by Bruker's DektakXT stylus profiler. A piece of aluminum foil was placed at the one edge of a substrate before the film deposition, leaving a step after removing it. The thickness of the film is measured (i.e., the height of the step) using that step. A diamond tip of the profilometer travels across the specimen along its length, and its vertical downward movement provides a step height or film thickness (see in Fig. 3.6).



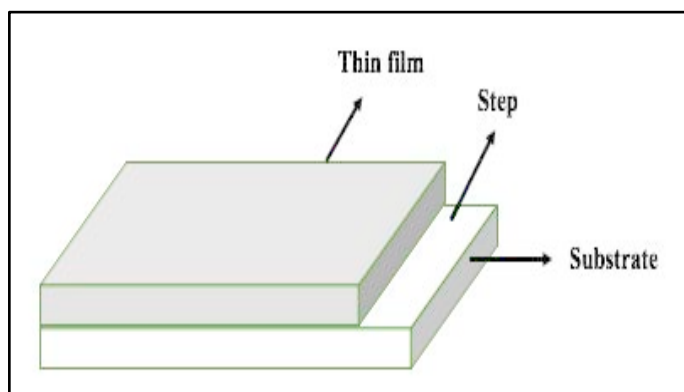


Fig. 3.6 Schematic representation of thickness monitor

### 3.3.1.2 XRD measurement

The crystallographic structures, phases, lattice constants, particle size, and crystalline quality of the films are assessed from XRD data collected using a Bruker XRD-D2 phaser with Cu-K $\alpha$  radiation ( $\lambda=1.5406 \text{ \AA}$ ) at a step size of  $0.02^\circ$ . The atomic and molecular structure of a crystal can be determined by X-ray crystallography, where the crystalline atoms cause a beam of X-rays to diffract into many directions. A crystallographer can make a three-dimensional picture of the density of electrons within the crystal by determining the angles and intensities of diffracted X-ray beams. It can estimate the mean positions of the atoms in the crystal, their chemical bonds, and disorder. Interaction of X-rays with a crystalline phase results in a diffraction pattern that is a material fingerprint. The regular arrangement of atoms in crystals can be calculated by the constructive interference of X-rays scattered at different parallel planes of electron densities [15]. The condition of constructive interference is described by Bragg's law [16]:

$$2d\sin\theta = n\lambda \quad (\text{eq. 3.22})$$

where,  $\theta$  is the Bragg angle,  $d$  is the distance between the parallel planes (i.e., lattice spacing),  $\lambda$  is the wavelength of X-rays and  $n$  is an integer called the order of diffraction. Crystals containing different lattice planes consist of a large number of crystallites with different orientations. The lattice spacing of the crystals is related to the miller indices ( $hkl$ ) of the planes and dimensions of unit cells that can determine by the angle of diffraction accordingly. The diffraction pattern is measured by an X-ray diffractometer that is composed of an X-ray source, goniometer, detector, and automatic recorder. Fig. 3.7 displays the

schematic diagram of Bruker XRD-D2 phaser and the XRD measurement setup. The peak width, infinitely narrow in an ideal XRD spectrum, is limited by several effects such as line width of the used X-ray source, detector area, accuracy in focus, and nature of crystal structure. The crystallite size, strain ( $\epsilon$ ), dislocation density ( $\delta$ ), and crystallite number per unit surface ( $N$ ) are calculated from the following equations [17]:

$$D = \frac{0.9 \times \lambda}{\beta \cos \theta} \text{ (Scherrer formula)} \quad (\text{eq. 3.23})$$

$$\epsilon = \frac{\beta \cot \theta}{4} \quad (\text{eq. 3.24})$$

$$\delta = 1/D^2 \quad (\text{eq. 3.25})$$

$$N = t/D^3 \quad (\text{eq. 3.26})$$

where,  $\beta$  is the full width at half maximum (FWHM) value (in radians) of the peak,  $\lambda$  is the wavelength of X-rays,  $\theta$  is the diffraction angle, and  $t$  is the thickness of the films.

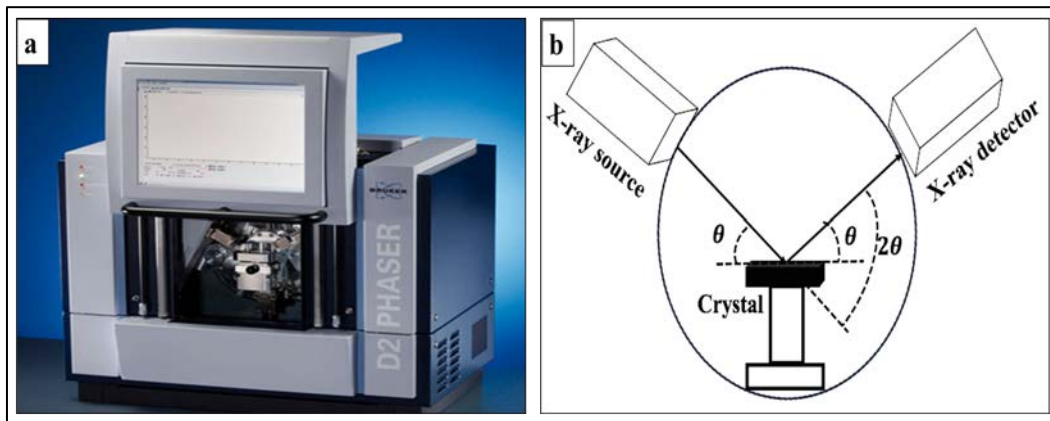


Fig. 3.7 Schematic of a) Bruker XRD-D2 phaser and b) an XRD measurement setup

### 3.3.1.3 SEM analysis and EDS measurement

SEM is another widely used characterization technique in research areas due to higher magnification, high depth of focus, excellent resolution, and ease of sample observation. The scanning electron microscope uses electrons rather than light to get information about the sample's surface morphology. A source of an electron beam, series of lenses, series of apertures, position and orientation of specimen, an area of beam/specimen interaction, and a high vacuum system are primary components of SEM that collect a variety of information from a sample of interest. The electron beams are produced by a field emission gun and are

accelerated towards the specimen through a potential difference. A series of lenses (i.e., condenser and objective) are used to control the diameter of the beam and focus the electron beam on the specimen. A series of apertures, micro-scale holes in metal plates, modify the characteristics of the electron beam. Position and orientation (tilt, rotation) of specimen and area of beam/specimen interaction generate several types of signal that can be detected and processed to produce an image or spectra. A high vacuum system is employed to avoid contamination from any other elements in the chamber while imaging the specimen. When electron beam strikes on the specimen, various signals, namely secondary electrons, backscattered electrons, Auger electrons, X-rays, and photons of different energies, are produced. The secondary electrons are collected by a secondary detector which is converted to a voltage and amplified. This amplified voltage causes the formation of many spots of varying intensity that correspond to the specimen's morphology. The resolution of the specimen image is based on beam accelerating voltage (kV), probe (beam electron) convergence angle, probe current, and probe diameter (spot size) [18].

EDS analysis comprises the generation of an X-ray spectrum from the entire scan area of the SEM. The characteristic X-rays, when the beam electrons eject inner shell electrons of specimen atoms, are used for elemental identification rather than continuum X-rays (when the beam electrons interact with the nucleus of the specimen atoms). These characteristic X-rays are named according to the shell where the initial vacancy occurs and the shell from which an electron drops to fill that vacancy (see Fig. 3.8b). The energy of a particular X-ray is equal to the energy difference between the two inner-core electron states corresponding to the transition. For example, the  $K\alpha$ ,  $K\beta$ , and  $K\gamma$  X-rays are produced when the vacancy occurs in the K shell, and the vacancy filling electron drops from the L-shell (adjacent shell), M shell (two shells away), N shell (three shells away), respectively. The energy of  $K\alpha$  X-ray will be lower than the energy of  $K\beta$  and  $K\gamma$  X-rays and higher than the energy of  $L\alpha$  and  $M\alpha$  X-rays. Moseley's law is the basis for elemental analysis with EDS. If the energy of a given K, L, or M line is measured, then the atomic number of the element can be determined using Moseley's law [18]:

$$E = C_1(Z-C_2)^2 \quad (\text{eq. 3.27})$$

where,  $E$  is the energy of the emission line for a given X-ray series,  $Z$  is the atomic number,  $C_1$  and  $C_2$  are constants. The surface and cross-sectional morphology and chemical compositions of films were carried out using Tescan Vega-3 SEM equipped with an energy dispersive X-ray spectrometer at an operating voltage of 15 kV, as shown in Fig. 3.8a.

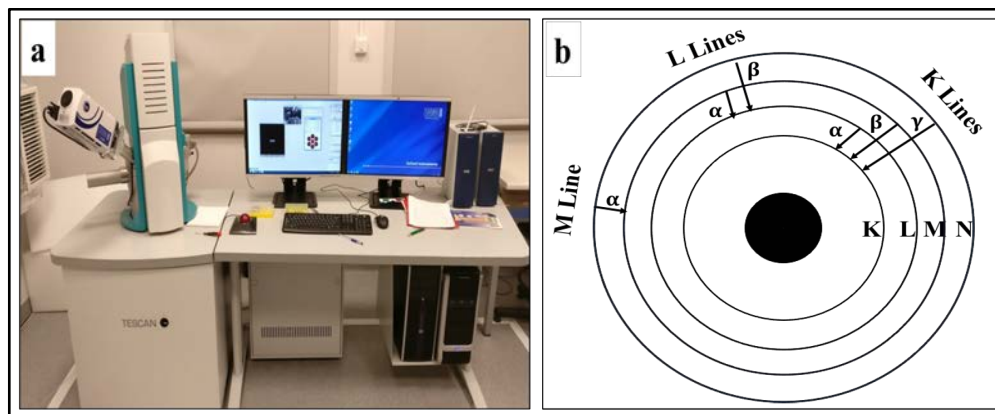


Fig. 3.8 Schematic of a) Tescan Vega-3 SEM and b) atomic structure with energy lines

#### 3.3.1.4 Raman spectroscopy

Raman spectroscopy is a powerful characterization technique for chemical identification, characterization of molecular structure, effects of bonding, lattice defect, the concentration of dopant, etc. Raman spectroscopy is based on inelastic scattering of monochromatic light interaction with a specimen, which means the energy of the emitted photons changes upon interaction with the specimen [19]. Photons of the laser light are absorbed by the specimen and then re-emitted. The magnitude of the Raman effect correlates with the polarizability of the electron in a molecule. The shift in the frequency of the emitted photons helps to get the information about vibrational, rotational, and other low-frequency modes in a system and determines single or poly-type structures and secondary phases of the sample. The component with a smaller frequency than the incident light is called Stokes Raman scattering, and with a larger frequency than the incident light is called anti-Stokes Raman scattering (see Fig. 3.9a). The light that keeps the same frequency as the incident light is known as Rayleigh scattering or elastically scattered light and provides no information on the sample's composition. The light source of a Raman spectrometer is generally a laser with a specific wavelength that can range from Ultraviolet to the near-Infrared depending on the area of application. The light beam is focused on a Notch filter. This filter reflects the radiation to the specimen at the right angle and removes Rayleigh scattering. The Raman

scattered light can only pass the filter unaltered. Then the light is redirected by mirrors into a monochromator where diffraction grating diffracts the beam into a narrow band of wavelengths. After that, a charge-coupled device detector is used to generate the spectrum. Finally, the measured data are saved and evaluated on a computer, as shown in Fig. 3.9b. The spectrum gives information about molecular bonding. The Raman spectra of the films are studied by the NT-MDT Ntegra spectra (see Fig. 3.10) with green laser with a probe area of around  $1\ \mu\text{m}^2$  for an acquisition time of 10 min.

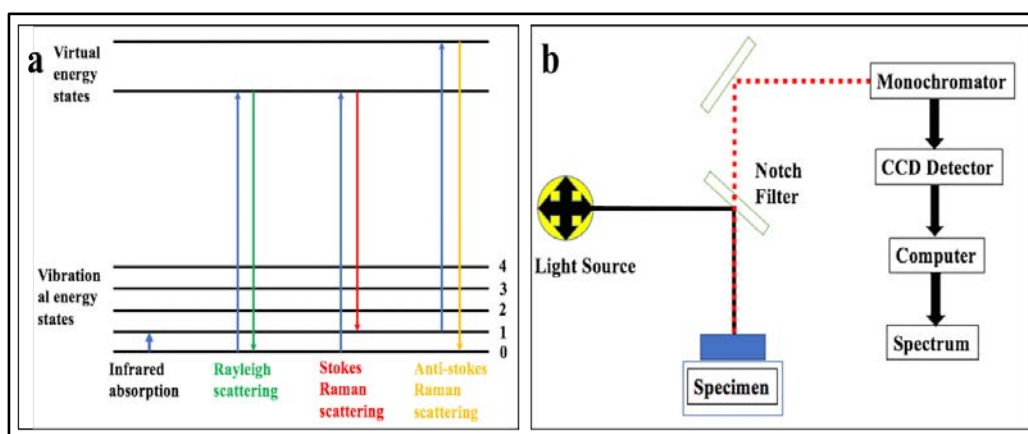


Fig. 3.9 Schematic of a) energy levels and b) experimental setup for Raman processes



Fig. 3.10 Schematic of the NTMDT Ntegra spectra

### 3.3.1.5 AFM measurement

AFM is a technique that helps to characterize topography (surface) of the specimen at a high resolution [20]. A tiny probe, also called a cantilever, is employed to measure the force or potential energy between a small tip and a specimen. The topographic height of the specimen, as well as the interacting force between the tip and the specimen can be measured

by pushing and pulling the cantilever to the specimen, respectively. The interacting forces can be classified into attractive (long-range) and repulsive (short-range) forces. The attractive force decreases the resonant frequency, while the repulsive force causes an increase in resonant frequency. If a tip is brought into close proximity of the surface, then the existing interacting forces are superposed. A tip and the specimen are then moved relative to each other in a raster fashion and surface parameters are measured in a serial pattern at a distinct location. There are two modes of operation of AFM: contact mode and non-contact mode based on experimental needs. The contact mode, also called static mode, is the easiest and simplest AFM mode to understand the collection of measurements. The static mode is carried out in contact with the scanned surface, where very high lateral resolution can be observed. But the deformation of both tips of the cantilever and surface of the specimen occurs during a collision. Therefore, soft cantilevers for contact mode are preferred for drawing the image.

In non-contact mode, the cantilever is levitated above the specimen surface during the scan process. An oscillating cantilever at constant amplitude will tap on the specimen surface. The amplitude signal was fed into the feedback signal and the shift was recorded to create an image. The non-contact mode is capable of doing materials discrimination by the variations in the phase of the oscillation. The large amplitude values compared to atomic distances influence the imaging process that leads to qualitative results, while low amplitudes influence the sensing process. The non-contact mode helps to get the surface information of the specimen by protecting the specimen surface. NT-MDT Ntegra AFM with the non-contact mode is used to characterize 2D and 3D topographies as well as to get quantitative information of surface (i.e., Roughness, Skewness, Kurtosis, etc.). Fig. 3.11 shows the schematic of the atomic force microscope and AFM imaging mode. In non-contact mode, the cantilever oscillates with the resonance frequency ( $f_0$ ), which is determined by the spring constant ( $k$ ) of the cantilever and its effective mass ( $m^*$ ) [20].

$$f_0 = \frac{1}{2\pi} \sqrt{\frac{k}{m^*}} \quad (\text{eq. 3.28})$$

The cantilever's spring constant and resonance frequency are changed due to external force ( $F_{\text{ex}}$ ) between tip and specimen and expressed as a first-order approximation for small oscillation amplitudes.

$$k' = k - \text{force gradient} = k - \frac{\partial F_{ex}}{\partial z} \quad (\text{eq. 3.29})$$

$$f_o' = f_o \sqrt{1 - \frac{1}{k} \frac{\partial F_{ex}}{\partial z}} \quad (\text{eq. 3.30})$$

since  $\frac{\partial F_{ex}}{\partial z}$  is small compare to spring constant (k), using Taylor expansion:

$$f_o' \approx f_o \left(1 - \frac{1}{2k} \frac{\partial F_{ex}}{\partial z}\right) \quad (\text{eq. 3.31})$$

Therefore, the shift ( $\Delta f$ ) of the resonance frequency of the cantilever is determined by

$$\Delta f = f_o' - f_o \approx -f_o \frac{1}{2k} \frac{\partial F_{ex}}{\partial z} \quad (\text{eq. 3.32})$$

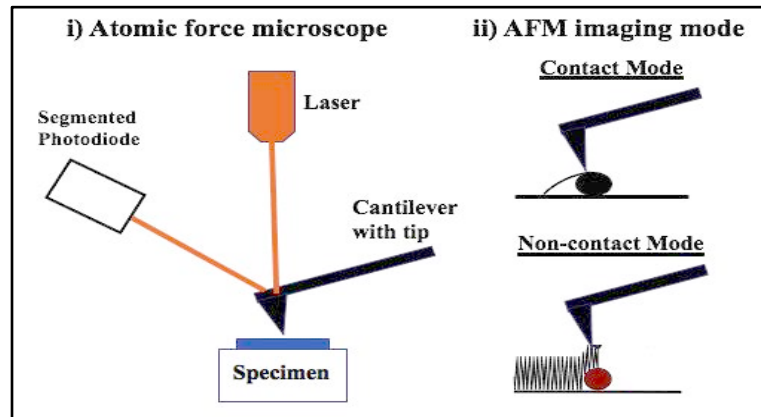


Fig. 3.11 Schematic of atomic force microscope and AFM imaging mode

### 3.3.1.6 UV-Vis spectroscopy

Ultraviolet-visible (UV-Vis) spectrophotometry refers to transmittance or reflectance spectroscopy in the UV-Vis spectral region. UV-Vis spectrophotometer measures the response of a specimen to the ultraviolet and visible range of electromagnetic (EM) radiation. It compares the intensity of light passing through a specimen with the intensity of the incident beams. Atoms and molecules undergo electronic transitions, while most solids have an interband transition in the region of the EM spectrum. The block diagram of a UV-Vis spectrophotometer is presented in Fig. 3.12. The UV-Vis spectrophotometer uses two

light sources, a deuterium lamp for UV light and a tungsten lamp for visible light. The light beam passes through a slit and hits a dispersive medium like prism or diffraction grating to separate the different wavelengths of light. The diffraction grating is rotated to allow monochromatic light can pass through a slit on an individual basis. A filter is employed to remove unwanted higher order of diffraction. The light beam splits into two halves after hitting a mirror (i.e., one half of the light beam is reflected, and the other half passes through). Between these two halves of the light, one half of the light beam is allowed to pass a reference substrate and the other half passes through the substrate containing the specimen. Finally, the intensities of the light beam are measured to study the optical properties.

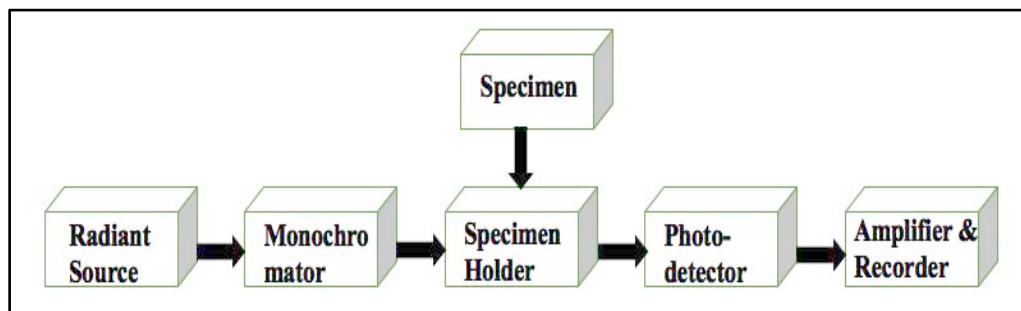


Fig. 3.12 Block diagram of UV-Vis spectrophotometer

According to the Beer-Lambert equation, the intensity of light is attenuated when the light enters a medium (absorbed) and the absorption coefficient ( $\alpha$ ) of semiconducting material can be derived from the absorption (or transmission) spectrum [16, 20]:

$$I = I_0 \exp\{-\alpha t\} \quad (\text{eq. 3.33})$$

$$\alpha = \frac{1}{t} \ln \left( \frac{1}{T} \right) \quad (\text{eq. 3.34})$$

where,  $I_0$  is the intensity of incident light beams,  $I$  is the intensity of light after passing through the film,  $t$  is the film thickness, and  $T$  is the transmittance. The bandgap energy of material can be determined by using the following equation [21, 22]:

$$(\alpha h\nu) = A(h\nu - E_g)^n \quad (\text{eq. 3.35})$$

where,  $h\nu$  is the photon energy,  $A$  is a constant,  $E_g$  is the optical bandgap of semiconductor and the magnitude of  $n$  determines whether the semiconductor is direct or indirect bandgap



where  $n = 2$  for indirect bandgap semiconductor and  $n = \frac{1}{2}$  for direct bandgap semiconductor [23].

The bandgap of semiconducting material is calculated by extrapolating the straight-line part of the plot  $(\alpha h\nu)^{1/n}$  versus photon energy ( $h\nu$ ) to the energy axis (i.e.  $(\alpha h\nu)^{1/n} = 0$ ). This calculation is based on the density of states in the valence and conduction bands of the semiconductor. In our study, the optical properties of the films were carried out by a Jasco V-670 spectrophotometer.

### 3.3.1.7 Electrical characterization techniques

#### 3.3.1.7.1 Four-probe technique

The four-probe (FP) technique is the most extensively used technique for electrical resistivity measurement of the material. The probes are arranged linearly in a straight line and connected to the ohmic contacts on the specimen. These probes are labeled with 1, 2, 3, and 4, as shown in Fig. 3.13. The ohmic contacts are made up of metallic substances like silver paste, gold, etc. The FP technique injects a current ( $I$ ) into the external probes and measures the potential difference ( $V$ ) through the internal probes. The effect of any contact resistance between the specimen and probes is canceled out in the FP technique. The injected electric current will flow over the surface of the specimen so that measured surface resistance is defined as sheet resistance and is calculated using the following formula [24]:

$$R_{\text{sheet}} = F \left( \frac{\Delta V}{I} \right) \quad (\text{eq. 3.36})$$

where,  $F$  is the geometric correction factor that depends on the separation between the tips and thickness of the specimen,  $\Delta V$  is the difference in electrical potential measured when an electric current  $I$  is injected. The resistivity ( $\rho$ ) of the film with thickness is estimated by using the following equation:

$$\rho = R_{\text{sheet}} \times t \quad (\text{eq. 3.37})$$

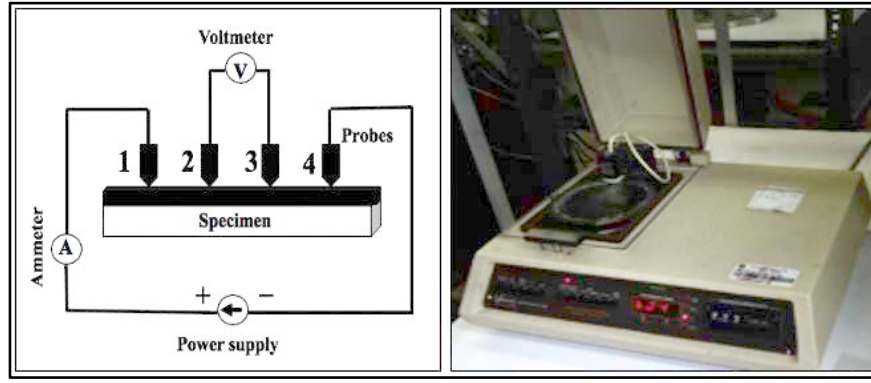


Fig. 3.13 Schematic of four-probe technique

### 3.3.1.7.2 Hall van der Pauw method

The Hall effect measurement is fundamental to solid-state physics and important to semiconductor material characterization. Several material parameters such as Hall coefficient ( $R_H$ ), Hall mobility ( $\mu_H$ ), type of semiconductor (n or p), carrier concentration of carriers, the Hall voltage ( $V_H$ ), and resistivity ( $\rho$ ) of material can all be determined from the Hall effect measurement (see Fig. 3.14). The specimens with irregular shapes and non-uniform thickness can also be analyzed using the van der Pauw method. The Hall voltage is measured as a result of applying voltage (or current) in the presence of a magnetic field. The magnetic Lorentz force builds a charge imbalance that produces a vertical electrical field, reaching a steady-state situation. The vertical electrical field can be measured as a transverse potential difference on the voltmeter. The positive or negative voltage in the voltmeter depends on the accumulation of electrons or holes. Material parameters are measured and analyzed using the van der Pauw method (see Fig. 3.15). The parameters such as  $Q_A$ ,  $Q_B$ , a correction factor ( $f$ ),  $\rho$  (unit of  $\Omega \text{ cm}$ ),  $R_H$  (unit of  $\text{cm}^3\text{C}^{-1}$ ),  $V_H$  (unit of V),  $\mu_H$  (unit of  $\text{cm}^2\text{V}^{-1}\text{s}^{-1}$ ), and concentration of carriers (unit of  $\text{cm}^{-3}$ ) are determined from the following equations [22, 23]:

$$Q_A = \frac{(V_1 - V_2)}{(V_3 - V_4)} \quad (\text{eq. 3.38})$$

$$Q_B = \frac{(V_5 - V_6)}{(V_7 - V_8)} \quad (\text{eq. 3.39})$$

$$\frac{(Q-1)}{(Q+1)} = \left(\frac{f}{0.693}\right) \cdot \text{arccosh} \left(\frac{\exp\left(\frac{0.693}{f}\right)}{2}\right) \quad (\text{eq. 3.40})$$

$$\rho_A = \left(\frac{\pi f B t S}{\ln 2}\right) \cdot \left(\frac{V_1 - V_2 + V_3 - V_4}{4I}\right) \quad (\text{eq. 3.41})$$

$$\rho_B = \left( \frac{\pi f B t S}{\ln 2} \right) \cdot \left( \frac{V_5 - V_6 + V_7 - V_8}{4I} \right) \quad (\text{eq. 3.42})$$

$$\rho = \frac{(\rho_A + \rho_B)}{2} \quad (\text{eq. 3.43})$$

$$R_{HC} = \left( \frac{t}{4BI} \right) (V_{a1} - V_{a2} + V_{a3} - V_{a4}) \quad (\text{eq. 3.44})$$

$$R_{HD} = \left( \frac{t}{4BI} \right) (V_{b1} - V_{b2} + V_{b3} - V_{b4}) \quad (\text{eq. 3.45})$$

$$R_H = \frac{(R_{HC} + R_{HD})}{2} \quad (\text{eq. 3.46})$$

$$V_H = \frac{(R_H \times B \times I)}{t} \quad (\text{eq. 3.47})$$

$$\mu_H = \frac{|R_H|}{\rho} \quad (\text{eq. 3.48})$$

$$n \text{ (or } p) = \frac{1}{q \cdot |R_H|} \quad (\text{eq. 3.49})$$

where, B is the magnetic field (unit of T or gauss), t is the thickness of specimen (unit of cm), S is the surface area of the specimen (unit of cm<sup>2</sup>), q is the electron (or hole) charge (unit of C), V<sub>1-8</sub> are the voltages without magnetic field, and V<sub>a1-a4</sub> and V<sub>b1-b4</sub> are voltages in the presence of magnetic field.

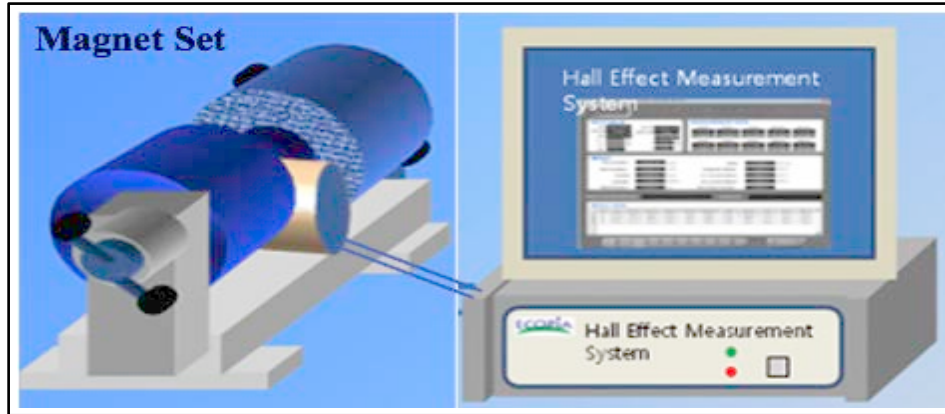


Fig. 3.14 Schematic of Hall effect measurement system

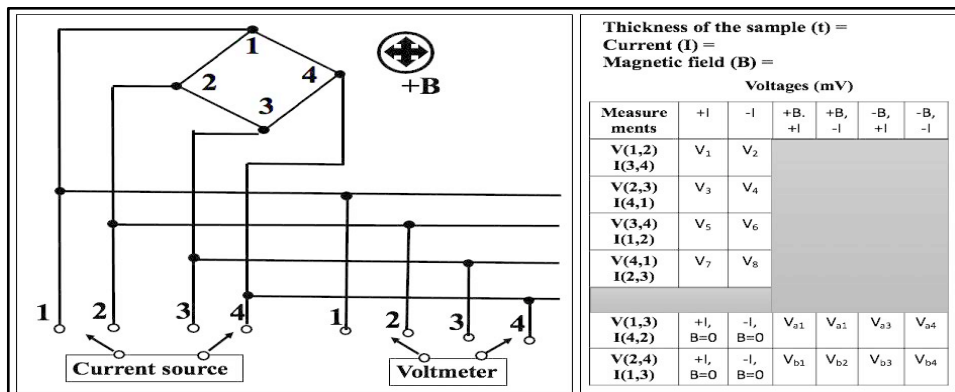


Fig. 3.15 Representative test circuit for measuring van der Pauw specimens

The type of semiconductor (n or p) is based on the sign of the Hall coefficient (i.e., for n-type semiconductors, the Hall coefficient is negative and for p-type semiconductors, it is positive). It is necessary to have good ohmic contacts, sensitive current measurement, good symmetry, and specimen homogeneity to get a good accuracy of obtained parameters.

### 3.3.2 External-quantum efficiency (EQE) measurements

Quantum efficiency (QE) measurements are helpful to determine the output current of the solar cell under illumination as well as estimate the individual losses responsible for reducing the current. QE is defined as the ratio of the number of electron-hole pairs generated by the solar cell to the number of incident photons at a specific wavelength range, which is expressed mathematically by the following equations [25, 26]:

$$QE(\lambda) = \frac{\text{The number of collected electron-holes pairs}}{\text{The number of incident photons}} = \frac{\Delta J/q}{\Phi(\lambda)} \quad (\text{eq. 3.50})$$

where,  $\Delta J$  is the photocurrent density,  $q$  is the elementary charge, and  $\Phi(\lambda)$  is the incident photon flux (number of photons per unit area per unit time) at a specific wavelength range. Therefore, the current density of the device ( $J$ ) is calculated by integrating quantum efficiency and the photon flux over the wavelength.

$$J = q \int QE(\lambda) \Phi(\lambda) d\lambda \quad (\text{eq. 3.51})$$

An example of the QE curve and types of loss mechanisms are shown in Fig. 3.17. Generally, the experimental QE curve is different from the ideal QE curve due to the various losses found in experimental work. The losses in solar cells are primarily due to the reflection losses (losses introduced by partial coverage of non-transparent front contacts), window layer absorption (is negligible due to high bandgap energy of this material), buffer layer absorption (due to thickness of this material), recombination losses (due to the quality of materials), deep penetration of carriers (photon energy less than the bandgap of the semiconductor is not absorbed), etc. Spectral response (SR), or EQE, is the quotient of the number of electron-hole pairs generated from the solar cell when conditions of short-circuiting are applied and

the number of photons incident on solar cell for each wavelength. The EQE measurements are carried out using a light monochromator having two sources of light with a Xenon lamp. The other equipment such as amplifier lock-in, Keithley power source, Chopper, Optical reference elements, Connection box, and Computer are also used to get results to form QE curves.

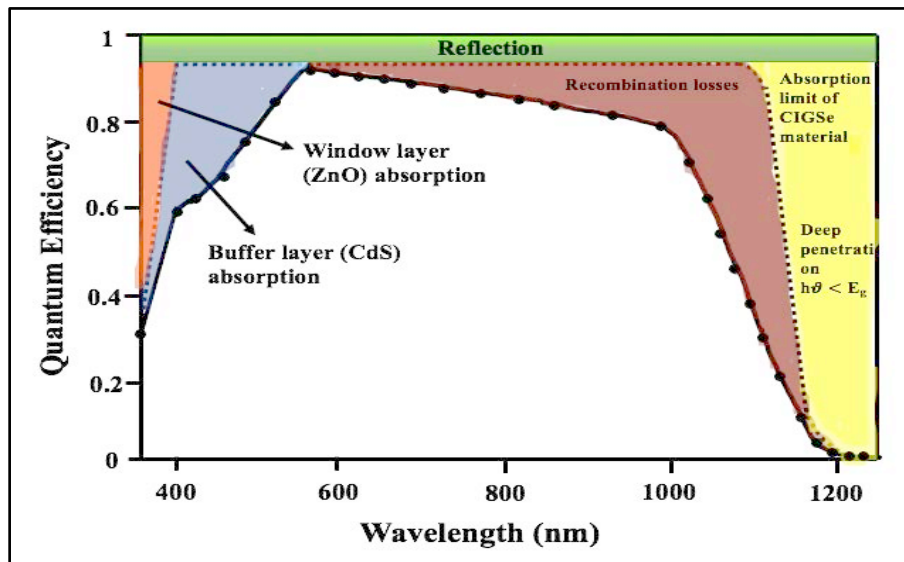


Fig. 3.16 Example of quantum-efficiency curve and types of loss mechanisms

## References:

- [1] A. Ashok, G. Regmi, and S. Velumani, "Growth of  $\text{In}_2\text{Se}_3$  Thin Films Prepared by the Pneumatic Spray Pyrolysis Method for Thin Film Solar Cells Applications," 2020 17th Int. Conf. Electr. Eng. Comput. Sci. Autom. Control. CCE 2020, pp. 2–7, 2020.
- [2] D. Valencia, J. Conde, A. Ashok, and S. Velumani, "Optimization of  $\text{Cu}(\text{In}, \text{Ga})\text{Se}_2$  (CIGSe) thin film solar cells parameters through numerical simulation and experimental study," Sol. Energy, 2021.
- [3] T. Klinkert, "Comprehension and optimisation of the co-evaporation deposition of  $\text{Cu}(\text{In}, \text{Ga})\text{Se}_2$  absorber layers for very high efficiency thin film solar cells Torben Klinkert To cite this version: cellules solaires en couches minces à très haut rendement Présentée," 2015.
- [4] A. Ashok, G. Regmi, and S. Velumani, "Growth of  $\text{In}_2\text{Se}_3$  Thin Films Prepared by the Pneumatic Spray Pyrolysis Method for Thin Film Solar Cells Applications," 17th Int. Conf. Electr. Eng. Comput. Sci. Autom. Control. CCE 2020.
- [5] H. Rodriguez-Alvarez, R. Mainz, and S. Sadewasser, "A one-dimensional Fickian

- model to predict the Ga depth profiles in three-stage Cu(In,Ga)Se<sub>2</sub>,” J. Appl. Phys., vol. 115, no. 20, 2014.
- [6] G. Regmi and S. Velumani, “Impact of selenization temperature on the performance of sequentially evaporated CuInSe<sub>2</sub> thin film solar cells,” Mater. Sci. Semicond. Process., vol. 137, no. May 2021, p. 106215, 2022.
  - [7] A. Ashok, G. Regmi, A. Romero-Núñez, M. Solis-López, S. Velumani, and H. Castaneda, “Comparative studies of CdS thin films by chemical bath deposition techniques as a buffer layer for solar cell applications,” J. Mater. Sci. Mater. Electron., vol. 31, no. 10, pp. 7499–7518, 2020.
  - [8] H. Moualkia, S. Hariech, M. S. Aida, N. Attaf, and E. L. Laifa, “Growth and physical properties of CdS thin films prepared by chemical bath deposition,” J. Phys. D. Appl. Phys., vol. 42, no. 13, 2009.
  - [9] F. Ouachtari, A. Rmili, B. Elidrissi, A. Bouaoud, H. Erguig, and P. Elies, “Influence of Bath Temperature, Deposition Time and S/Cd Ratio on the Structure, Surface Morphology, Chemical Composition and Optical Properties of CdS Thin Films Elaborated by Chemical Bath Deposition,” J. Mod. Phys., vol. 02, no. 09, pp. 1073–1082, 2011.
  - [10] G. Hodes, Chemical Solution Deposition Of Semiconductor Films. 2002.
  - [11] S. Selberherr, Analysis and simulation of semiconductor devices. 2019.
  - [12] J. V. Marc Burgelman, Koen Decock, Alex Niemegeers, “SCAPS manual,” SCAPS Man., no. December, 2016.
  - [13] C. O. Lawani et al., “Sciences Numerical Simulation of Copper Indium Gallium Diselenide Solar Cells Using One Dimensional SCAPS Software,” vol. 3, pp. 48–58, 2021.
  - [14] M. S. Chowdhury et al., “Effect of deep-level defect density of the absorber layer and n/i interface in perovskite solar cells by SCAPS-1D,” Results Phys., vol. 16, no. July 2019, p. 102839, 2020.
  - [15] J. D. Rachwal, “X-ray diffraction applications in thin films and ( 100 ) silicon substrate stress analysis,” 2010.
  - [16] U. Welzel, J. Ligot, P. Lamparter, A. C. Vermeulen, and E. J. Mittemeijer, “Stress analysis of polycrystalline thin films and surface regions by X-ray diffraction,” J. Appl. Crystallogr., vol. 38, no. 1, pp. 1–29, 2005.
  - [17] E. Muchuweni, T. S. Sathiaraj, and H. Nyakotyo, “Synthesis and characterization of

- zinc oxide thin films for optoelectronic applications,” *Heliyon*, vol. 3, no. 4, p. e00285, 2017.
- [18] B. Hafner, “Scanning electron microscopy primer,” *Handb. Adhes.* Second Ed., pp. 1–29, 2007.
  - [19] D. W. Mayo, F. A. Miller, and R. W. Hannah, *Course Notes on the Interpretation of Infrared and Raman spectra.* 2003.
  - [20] Y. Martin, C. C. Williams, and H. K. Wickramasinghe, “Atomic force microscope-force mapping and profiling on a sub 100-Å scale,” *J. Appl. Phys.*, vol. 61, no. 10, pp. 4723–4729, 1987.
  - [21] S. Kahraman, H. M. Çakmak, S. Çetinkaya, H. A. Çetinkara, and H. S. Güder, “The effects of coumarin additive on the properties of ZnO nanostructures,” *J. Phys. Chem. Solids*, vol. 74, no. 4, pp. 565–569, 2013.
  - [22] S. H. Antonio Luque, *Handbook of Photovoltaic Science and Engineering*, Second. John Wiley & Sons, 2011.
  - [23] J. Bisquert, *The physics of solar cells: Perovskites, organics, and photovoltaic fundamentals.* 2017.
  - [24] L. M. Vikhor, L. I. Anatychuk, and P. V. Gorskyi, “Electrical resistance of metal contact to Bi<sub>2</sub>Te<sub>3</sub> based thermoelectric legs,” *J. Appl. Phys.*, vol. 126, no. 16, 2019.
  - [25] ASTM F76-08, “Standard Test Methods for Measuring Resistivity and Hall Coefficient and Determining Hall Mobility in Single-Crystal Semiconductors,” *Annu. Books ASTM Stand.*, 2016.
  - [26] G. B. Armen, “Hall Effect Experiment,” in *Building*, 2007.
  - [27] D. Abou-ras and T. Kirchartz, Edited by *Physics of Solar Cells Thin Film Solar Cells Handbook of Photovoltaic Science and Engineering.* 2011.
  - [28] P. I. R. Figueroa, “Deposition and characterization of Cu(In<sub>1-x</sub>Ga<sub>x</sub>)Se<sub>2</sub> films by multiple deposition techniques,” *CINVESTAV-IPN*, 2016.
  - [29] R. H. Bube, *Photoelectronic Properties of Semiconductors.* Cambridge University Press, 1992.

## Chapter 4 Results and discussions for absorber layers

As mentioned earlier, the novel hybrid deposition method is employed for CI(G)Se absorber layer preparation, which combines the non-vacuum spray pyrolysis and vacuum co-evaporation methods. This chapter first describes the growth of indium selenide thin films by the PSP technique. The effect of substrate temperature on the material properties of indium selenide thin films is also studied. Afterward, the growth of CI(G)Se absorber layers using the hybrid deposition method is described. The best selenization condition and the first stage temperature for CI(G)Se absorber layers are optimized by analyzing their structural, morphological, compositional, topographical, and electrical properties.

### 4.1 Growth of the $\text{In}_2\text{Se}_3$ thin films

This work aims to deposit  $\text{In}_2\text{Se}_3$  thin films using the PSP technique, which is used as a precursor layer for the CI(G)Se synthesis process and optimize the best deposition condition for indium selenide thin films. The  $\text{In}_2\text{Se}_3$  belongs to the  $\text{III}_2\text{-VI}_3$  family group, which is one of the most vital compounds of the indium-selenium system. It can use in various applications [1], namely optoelectronic devices, diodes, solid solution electrodes, transistors, photodetectors, electro and photo memory devices, photovoltaics, etc. There exist five different phases (i.e.,  $\alpha$ ,  $\beta$ ,  $\gamma$ ,  $\delta$ ,  $\kappa$ ) of  $\text{In}_2\text{Se}_3$  depending on the synthesis temperature and elemental composition [2]. These different phases of  $\text{In}_2\text{Se}_3$  have different bandgap energy values, which can be used for various roles in photovoltaics. The  $\gamma$ -phase of the  $\text{In}_2\text{Se}_3$  has a wide bandgap of 1.8 eV, which is exploited as a window layer in the CI(G)Se TFSCs. Besides,  $\alpha$ - and  $\beta$ - phases of  $\text{In}_2\text{Se}_3$  are used as an absorber layer due to their absorbing nature and lower bandgap values (i.e., 1.45 eV for  $\alpha$ -phase and 1.55 eV for  $\beta$ -phase). Furthermore,  $\beta$ - and  $\gamma$ - phases of  $\text{In}_2\text{Se}_3$  can also be utilized as a precursor layer for the synthesis of CI(G)Se absorber material, which exhibits rhombohedral and defect wurtzite (hexagonal) crystal structure, respectively [1].

The nucleation and growth rate of  $\text{In}_2\text{Se}_3$  films by PSP technique vary with the deposition parameters such as substrate temperature, the concentration of precursor materials, nozzle to substrate distance, solution, and gas flow rate [1, 3], etc. The temperature is an essential parameter for the nucleation of thin films where the diffusion of impinging adatoms



increases with an increase in temperature that promotes the crystals to grow. When droplets approach the substrate, the solvent starts to vaporize, and then diffused vapors undergo a heterogeneous reaction for the growth of film by the PSP method. The temperature of the front surface is lower (around 15-20°C) than the temperature of the back surface of the substrate, which is due to the presence of droplets of precursor solution at the front surface [4]. From the deposited films, it is observed that the growth rate of the films falls gradually with a rise in deposition temperature. This result is mainly due to the volatile nature of selenium at a higher temperature. While studying the growth of  $\text{In}_2\text{Se}_3$  thin films, the substrate temperature is varied from 280 to 400°C. It was seen from the deposited samples that the poor quality (i.e., dry precipitate or powdery deposit) at the substrate temperatures lower than 300°C and higher than 340°C. The solvent vaporizes long before reaching the substrate (i.e., the chemical reaction takes place in the vapor phase) at the substrate temperature greater than 340°C, resulting in the deposition of a lower quantity and quality film on the substrate. The energy required to vaporize the droplets of precursor solutions is insufficient at the substrate temperature lower than 300°C, depositing the poor quality film on the substrate. Therefore, the deposition temperature for indium selenide is narrowed in this study from 300 to 340°C with a step of 20°C. A brief description of experimental procedures of the indium selenide thin films by PSP technique is seen in section 3.1.2. The growth rates for  $\text{In}_2\text{Se}_3$  thin films at different temperatures such as 300, 320, and 340°C were found around 13, 11, and 10 nanometers per minute (nm/min), respectively. The effect of the substrate temperatures on the material properties is studied and explained below.

#### 4.1.1 Structural properties of $\text{In}_2\text{Se}_3$ thin films

In Fig. 4.1, XRD patterns are shown for  $\text{In}_2\text{Se}_3$  thin films grown by the PSP method at various substrate temperatures ranging from 300 to 340°C. From XRD results, the dominant peak (006) and minor peaks (110), (300), and (314) exhibit that the films crystallize completely in the  $\gamma\text{-In}_2\text{Se}_3$  structure [5, 6]. After matching the position of the X-ray reflections with the reported phases of  $\text{In}_2\text{Se}_3$ , the film shows a defect wurtzite structure ( $\gamma\text{-In}_2\text{Se}_3$ ) described by the international center for diffraction data (ICDD) number 01-089-0658. The crystallite size, strain, and dislocation density are estimated using the Williamson-Hall equation [7]. X-ray diffraction data, such as two thetas ( $2\theta$ ), full width half maximum (FWHM), crystallite size, strain, and dislocation density, are presented in Table 4.1. It is

clear from the data that the films grown at higher substrate temperature shows better crystalline quality than at lower substrate temperature.

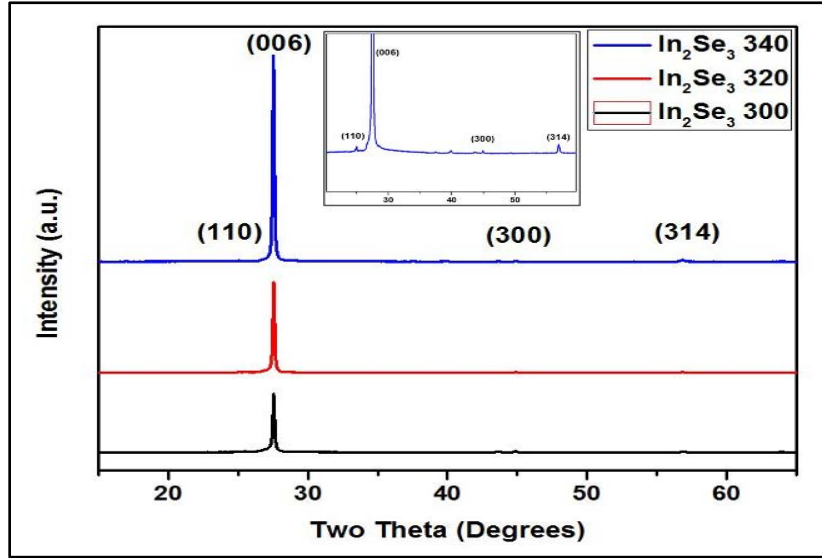


Fig. 4.1 XRD patterns of  $\text{In}_2\text{Se}_3$  thin films deposited at three different substrate temperatures

Table 4.1 Structural parameters for  $\text{In}_2\text{Se}_3$  thin films deposited by PSP technique

Samples	$\text{In}_2\text{Se}_3$ 300	$\text{In}_2\text{Se}_3$ 320	$\text{In}_2\text{Se}_3$ 340
Parameters			
$2\theta$ (degrees)	27.530	27.527	27.525
FWHM ( $\beta$ ) ( $\times 10^{-3}$ Rad)	9.050	8.100	7.450
Crystallite Size (D) (nm)	$16 \pm 1$	$18 \pm 1$	$19 \pm 1$
Strain ( $\epsilon$ ) ( $\times 10^{-3}$ Rad)	9.276	8.302	7.636
Dislocation density ( $\delta$ ) ( $\times 10^{-3}$ lines/ $\text{nm}^2$ )	4.016	3.217	2.722

Next, the Raman spectroscopy of  $\text{In}_2\text{Se}_3$  thin films is also studied. Fig. 4.2 displays the Raman spectroscopy of  $\text{In}_2\text{Se}_3$  samples deposited at various substrate temperatures, which helps to identify the phase of  $\text{In}_2\text{Se}_3$  through the presence of distinct vibrational modes. These results show that the characteristics peak at Raman shift of  $150 \text{ cm}^{-1}$  of samples are related to the  $\gamma\text{-In}_2\text{Se}_3$  phase and polycrystalline films [1]. The less intense peaks located at Raman shift of  $203$  and  $227 \text{ cm}^{-1}$  are also compatible with the  $\gamma\text{-In}_2\text{Se}_3$  phase, which is due to the transverse and longitudinal optical (TO-LO) phonon modes [8]. The peak at  $203 \text{ cm}^{-1}$  is related to the  $\beta\text{-In}_2\text{Se}_3$  phase, too [9]. The full width at half maximum (FWHM) value reflects the structural distribution of the material. The FWHM values for the predominant

peak at  $150\text{ cm}^{-1}$  of  $\text{In}_2\text{Se}_3$  thin films grown at  $300$ ,  $320$ , and  $340^\circ\text{C}$  are  $12.92$ ,  $12.60$ , and  $13.11\text{ cm}^{-1}$ , respectively. These results showed that the sharper Raman line is observed for  $\text{In}_2\text{Se}_3$  thin films grown at  $340^\circ\text{C}$ , indicating the high crystalline quality of  $\text{In}_2\text{Se}_3$  thin films.

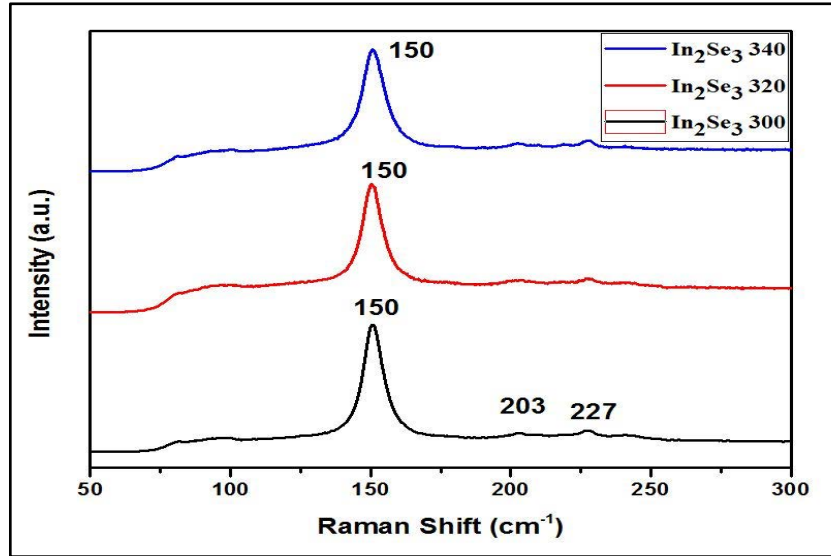


Fig. 4.2 Raman spectroscopy of  $\text{In}_2\text{Se}_3$  thin films prepared at three different substrate temperatures

#### 4.1.2 Morphological properties of $\text{In}_2\text{Se}_3$ thin films

The SEM images for  $\text{In}_2\text{Se}_3$  thin films grown at different substrate temperatures ( $300$ ,  $320$ ,  $340^\circ\text{C}$ ) are shown in Fig. 4.3. It is seen from the SEM images that the grains are composed of rectangular-like structures lying in different directions. The grain size of films is composed of both smaller ( $\sim 100\text{ nm}$ ) and larger ( $\sim 500\text{ nm}$ ) grains, is calculated by EVA software (is the software attached with Tescan Vega-3 SEM, which helps to calculate grain size directly from the SEM image of the film). The rise in mobility and migration (i.e., coalescence of neighboring grains) of grains cause to increase in the grain size of films. The number of grain boundaries, which impact the performance of the solar cell devices by recombining generated charge carriers, decreases when the size of the grains is increased. Since these  $\text{In}_2\text{Se}_3$  thin films are used as a precursor layer for the synthesis of  $\text{Cl(G)Se}$  absorber layers, the morphology of  $\text{In}_2\text{Se}_3$  thin films can impact the structural, morphological, and electrical properties of  $\text{Cl(G)Se}$ .

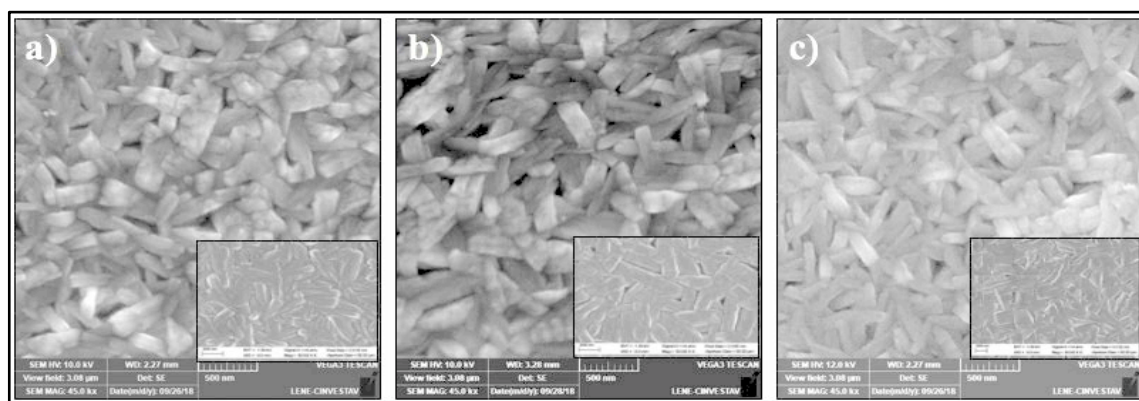


Fig. 4.3 SEM images of  $\text{In}_2\text{Se}_3$  thin films deposited (inserted with FESEM images) at three different substrate temperatures, a) 300, b) 320, and c) 340 °C

#### 4.1.3 Compositional analysis of $\text{In}_2\text{Se}_3$ thin films

Fig. 4.4(a) is the EDS spectrum of the  $\text{In}_2\text{Se}_3$  thin films confirming the presence of the indium and selenium elements through the spectrum, and Fig. 4.4(b) is the EDS mapping demonstrating the distribution of those elements in the films. The average elemental compositions (i.e., In and Se) of  $\text{In}_2\text{Se}_3$  films are acquired from 10 different random points of the samples.  $\text{In}_2\text{Se}_3$  phases depend mainly on the selenium content within the film (i.e., the  $\gamma$ -phase contains  $\geq 60$  at% of selenium and  $\beta$ -phase comprises selenium deficient ( $< 60$  at%)) [1, 10]. In an excess selenium condition, an atomic arrangement of constituents in the films is similar to  $\gamma$ -phase rather than other phases. From Fig. 4.5, the average selenium contents for  $\text{In}_2\text{Se}_3$  thin films deposited at three different substrate temperatures are observed more than 60 %, indicating the formation of  $\gamma$ - $\text{In}_2\text{Se}_3$ .

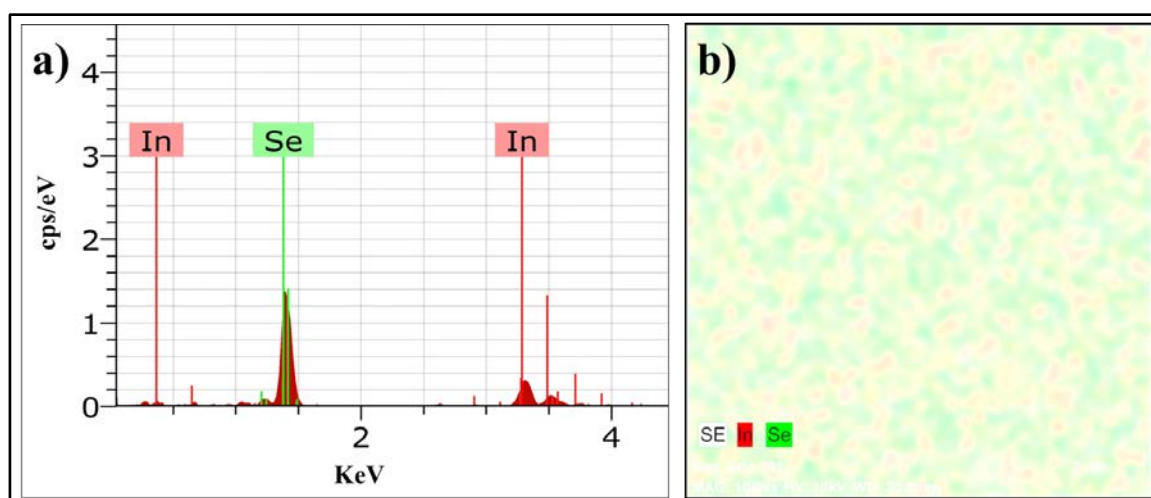


Fig. 4.4 Schematic diagram of a) EDS spectrum and b) EDS mapping for  $\text{In}_2\text{Se}_3$  thin films

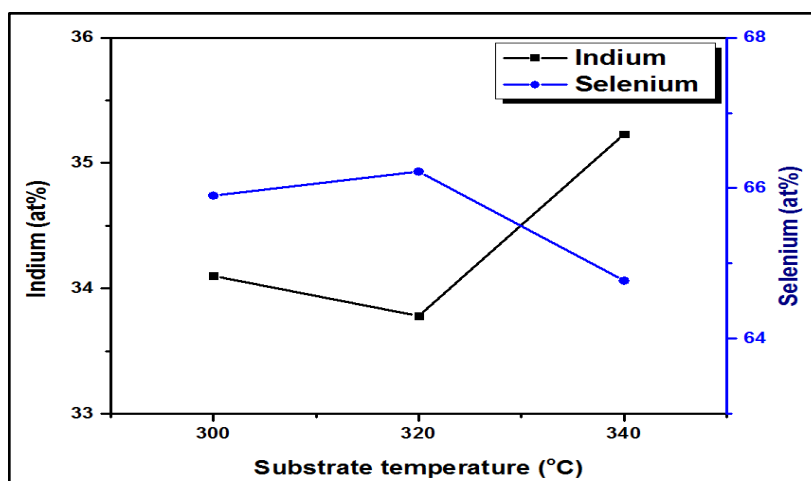


Fig. 4.5 Schematic of compositional details of  $\text{In}_2\text{Se}_3$  thin films

#### 4.1.4 Topographical analysis of $\text{In}_2\text{Se}_3$ thin films

Fig. 4.6 shows the 2D AFM images for  $\text{In}_2\text{Se}_3$  thin films deposited at three different substrate temperatures, with a surface area of  $2 \times 2 \mu\text{m}^2$ . From AFM images, it is seen that the grains are composed of closely packed and uniformly distributed in the film. The formation of the regular shape of grains infers that the kinetic energy is adequate to coalesce the grains [11]. Table 2 presents the values of parameters such as average grain size, average roughness, root mean square (RMS) roughness, skewness, and kurtosis. The average roughness is measured by the vertical spacing of the real surface from its ideal form, which is less than 10 nm for deposited samples indicating the smooth surface of the film. The positive values (near to zero) of skewness generalize that the height distribution is near to symmetrical [1]. And kurtosis values (greater than 3) suggest that the difference between the number of the peaks and valleys is a positive value (i.e., +1 because the peak must follow by a valley) [1].

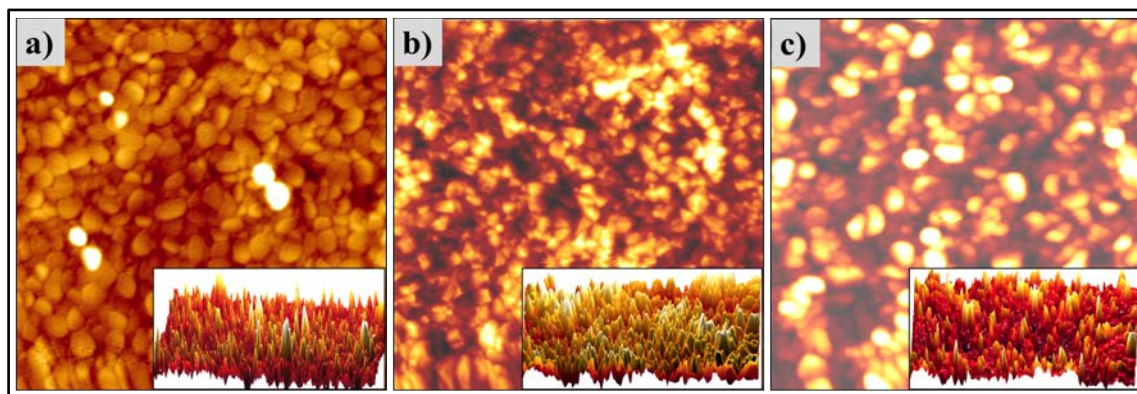


Fig. 4.6 2D AFM images of In<sub>2</sub>Se<sub>3</sub> thin films deposited (inserted with 3D images) at three different substrate temperatures, a) 300, b) 320, and c) 340°C

Table 4.2 Topographical parameters for In<sub>2</sub>Se<sub>3</sub> thin films measured from AFM

Parameters \ Samples	In <sub>2</sub> Se <sub>3</sub> 300	In <sub>2</sub> Se <sub>3</sub> 320	In <sub>2</sub> Se <sub>3</sub> 340
Average grain size (nm)	122	112	114
Average roughness (nm)	8.38	5.94	7.95
RMS roughness (nm)	10.72	7.40	10.23
Skewness (S <sub>sk</sub> )	0.711	0.603	0.819
Kurtosis (S <sub>ka</sub> )	3.856	3.248	4.132

#### 4.1.5 Optical properties of In<sub>2</sub>Se<sub>3</sub> thin films

In photovoltaic technology, the important parameter is the material's bandgap, which provides information about the fundamental absorption properties. Since the In<sub>2</sub>Se<sub>3</sub> is a direct bandgap semiconductor, the bandgap of this material is calculated using the Tauc relation. The optical bandgap of the material was computed by extrapolating the straight line of plot  $(\alpha h\nu)^2$  versus energy ( $h\nu$ ) to the energy axis [12]. The estimated bandgap for In<sub>2</sub>Se<sub>3</sub> thin films grown at 300, 320, and 340 °C substrate temperatures are 2.22, 2.34, and 2.55 eV, respectively. It is found that computed bandgap values were closer to the bandgap value for  $\gamma$ -phase by comparing these calculated bandgap values with the reported values for various In<sub>2</sub>Se<sub>3</sub> phases. This result indicates the formation of a stable compound [7]. The optical transmission for two In<sub>2</sub>Se<sub>3</sub> films grown at 320 and 340°C) were identical at around 50% at the visible region (see Fig. 4.7). The slightly lower transmission value for In<sub>2</sub>Se<sub>3</sub> at 300 °C is due to its high thickness value than others.

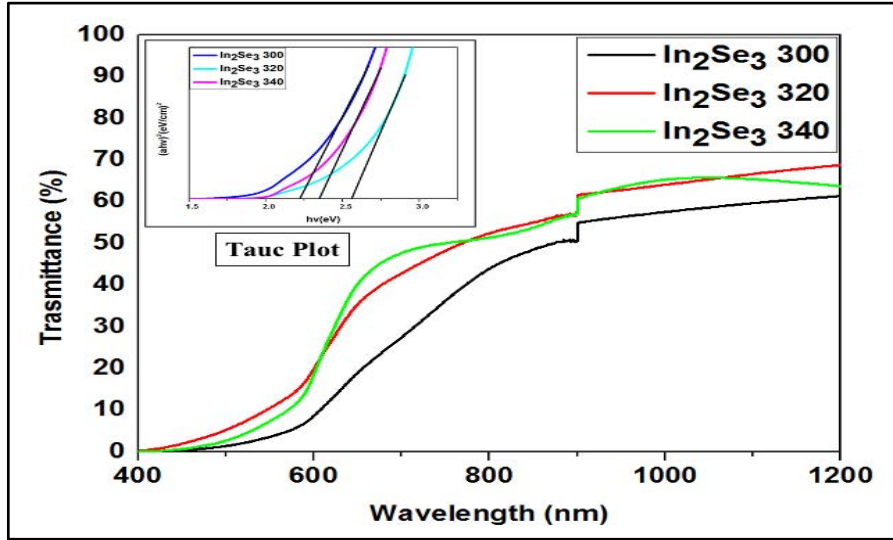


Fig. 4.7 Transmittance of  $\text{In}_2\text{Se}_3$  thin films (inserted with bandgap energy diagram) deposited at various substrate temperatures

## 4.2 Growth of the CISE absorber layer

The CISE thin films are used as absorber layers in CISE TFSCs. The material properties of the absorber layer, namely structural, morphological, compositional, electrical properties, etc., affect the solar cell performance. These material properties are dependent on their growth conditions. Therefore, optimizing the material properties can provide high-efficient solar cells. At the first stage of the hybrid deposition method, the  $\text{In}_2\text{Se}_3$  precursor layers are deposited by the PSP technique. The second and third stages consist of the respective co-evaporation of Cu+Se and In+Se at a constant substrate temperature of  $500^\circ\text{C}$ . Finally, the selenization of the complete CISE thin films by the hybrid deposition method is carried out.

### 4.2.1 Influence of selenization temperatures and times

In this study, the CISE thin films are prepared by hybrid deposition method followed by selenization process, giving particular attention to the selenization temperatures (i.e., 500, 525, and  $550^\circ\text{C}$ ) and times (i.e., 30 and 60 minutes). More than  $500^\circ\text{C}$  of selenization temperature was used to improve the homogeneity of the CISE thin films. The first, second, and third stage substrate temperatures were kept constant to optimize the selenization condition that helps to get the high-quality CISE absorber layer. The influence of the selenization temperatures and times on the structural, morphological, compositional properties are investigated below.



#### 4.2.1.1 Structural properties of CISE thin films

Fig. 4.8 displays the XRD pattern of the CISE thin films selenized at different temperatures, namely 500, 525, and 550°C, for 30 and 60 minutes. The different peaks with varying crystallite sizes and orientations in the XRD patterns indicate the polycrystalline nature of deposited films [12, 13]. The intense reflections (112), (204)/(220), and (312)/(116) from the XRD results confirm the chalcopyrite crystal structure of CISE [14–16]. The polycrystalline and chalcopyrite nature of CISE is matched with the international center for diffraction data (ICDD, PDF file number = 01-070-3358). The diffractogram also illustrates the presence of binary materials. The presence of the CuSe phase helps to enhance the films' grain size through the recrystallization phenomenon. The CISE samples other than sample selenized at 550 °C for 60 minutes have a low degree of crystallinity because temperature and time might not be sufficient for binary compounds (indium selenide, copper selenide, etc.) to get involved in the chemical reaction for the formation of ternary CISE compound. The structural parameters of CISE thin films (for (112) plane) deposited at different selenization conditions were calculated by the Scherrer equation and presented in Table 4.3. The results showed that the crystallite size of the film increases with an increasing selenization temperature and time.

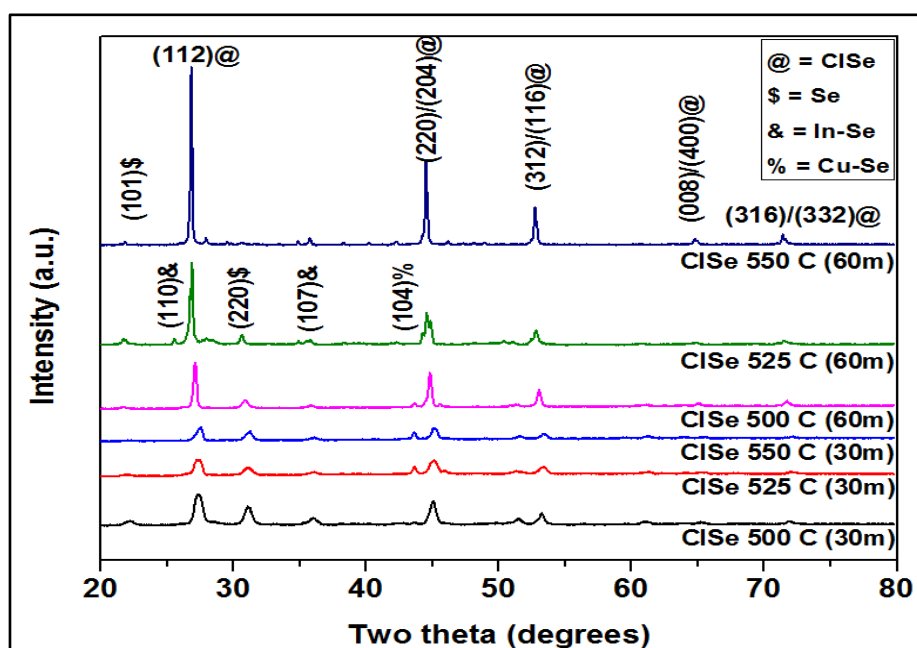


Fig. 4.8 XRD patterns of CISE thin films selenized at different temperatures (i.e., 500, 525, and 550°C) and times (i.e., 30 and 60 minutes)



Table 4.3 Structural parameters for CISE thin films selenized at different temperatures, and times

Parameters	CISE		CISE		CISE	
	500°C	525°C	550°C	500°C	525°C	550°C
	30 min	30 min	30 min	60 min	60 min	60 min
Two thetas (°)	27.32	27.29	27.49	27.09	26.83	26.80
FWHM (Rad)	0.014	0.0091	0.0086	0.0066	0.0067	0.0052
Crystallite size (nm)	13 ± 1	16 ± 2	17 ± 2	22 ± 2	21 ± 1	27 ± 1
Strain (ε) (Rad)	0.01425	0.00932	0.00881	0.00676	0.00695	0.00539
Dislocation density (δ) (lines/nm <sup>2</sup> )	0.00637	0.00406	0.00363	0.00214	0.00220	0.00133

Afterward, Raman spectroscopy of CISE thin films selenized at different temperatures (i.e., 500, 525, and 550°C) and times (i.e., 30 and 60 minutes) is shown in Fig. 4.9. Here, the most intense peak at Raman shift of 170 cm<sup>-1</sup> is related to the A<sub>1</sub> mode of CISE thin films, which is due to the motion of Se atoms with Cu and In atoms [14, 16–18]. Besides the A<sub>1</sub> mode peak, other peaks located at Raman shift of 205 and 227 cm<sup>-1</sup> are related B<sub>2</sub>/E mode of CISE thin films, showing good agreement with lattice modes of the chalcopyrite crystal structure of the CISE [16, 18]. The peak at around Raman shift of 130 cm<sup>-1</sup> corresponds to the B<sub>1</sub> phase of CISE thin films that conveys the vibration of Cu-In bonds [16]. There is a presence of another peak at Raman shift of 150 cm<sup>-1</sup> for CISE thin films selenized at low temperatures and times that resembles the vibrational mode of the Cu-poor ordered vacancy compound, indicating a low crystalline quality of the CISE thin films [17]. This result demonstrates that there is not sufficient temperature and time for the transformation of binary compounds into ternary CISE compound material. Hence, the selenization temperature of 550°C for 60 minutes is preferred for getting high crystalline quality CISE films.

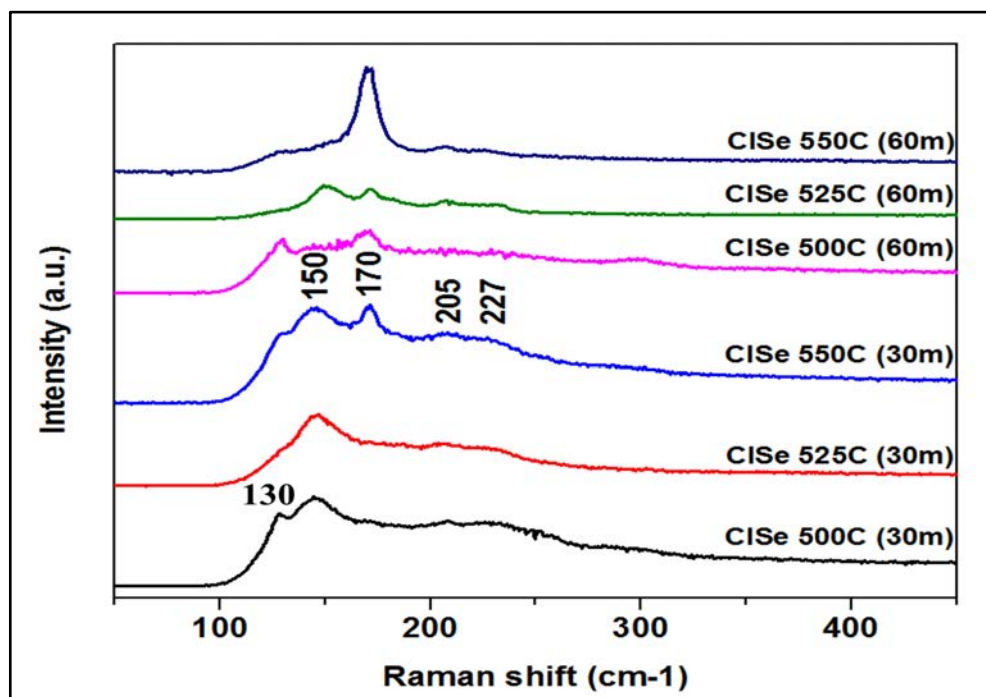


Fig. 4.9 Raman spectroscopy of CISE thin films selenized at different temperatures (i.e., 500, 525, and 550°C) and times (i.e., 30 and 60 minutes)

#### 4.2.1.2 Morphological properties of CISE thin films

Fig. 4.10 displays the SEM images of the CISE thin films at different temperatures (500, 525, and 550°C) and times (i.e., 30 and 60 minutes). The morphology of CISE thin films consists of small and large particles spread around the film surface. Here, the grain size of the CISE thin films is composed of smaller ( $\sim 100$  nm) and larger particles ( $\sim 1$   $\mu$ m). This result showed that the grain size of the CISE thin films is comparatively larger than the grain size of the precursor layer. The grain size enhancement is due to the recrystallization phenomenon through the transition of films from the Cu-poor phase to the Cu-rich phase. This recrystallization phenomenon minimizes the number of grain boundaries and the recombination centers. The compact and larger particles of the CISE thin films are seen when the selenization temperatures and times increase to a higher value. The grain size enhancement is due to the diffusion of atoms across the grain boundaries. From the images, the grains are surrounded by the small shrub-like structure that might be selenium atoms present on the surface after selenization of the CISE films. The voids between the grains are formed due to the consumption of the Cu-Se phase through interaction with the In-Se phase, forming ternary CISE phase [19, 20]. The large and compact grains observed for the CISE sample selenized at 550°C for 60 minutes can provide high solar cell performance.

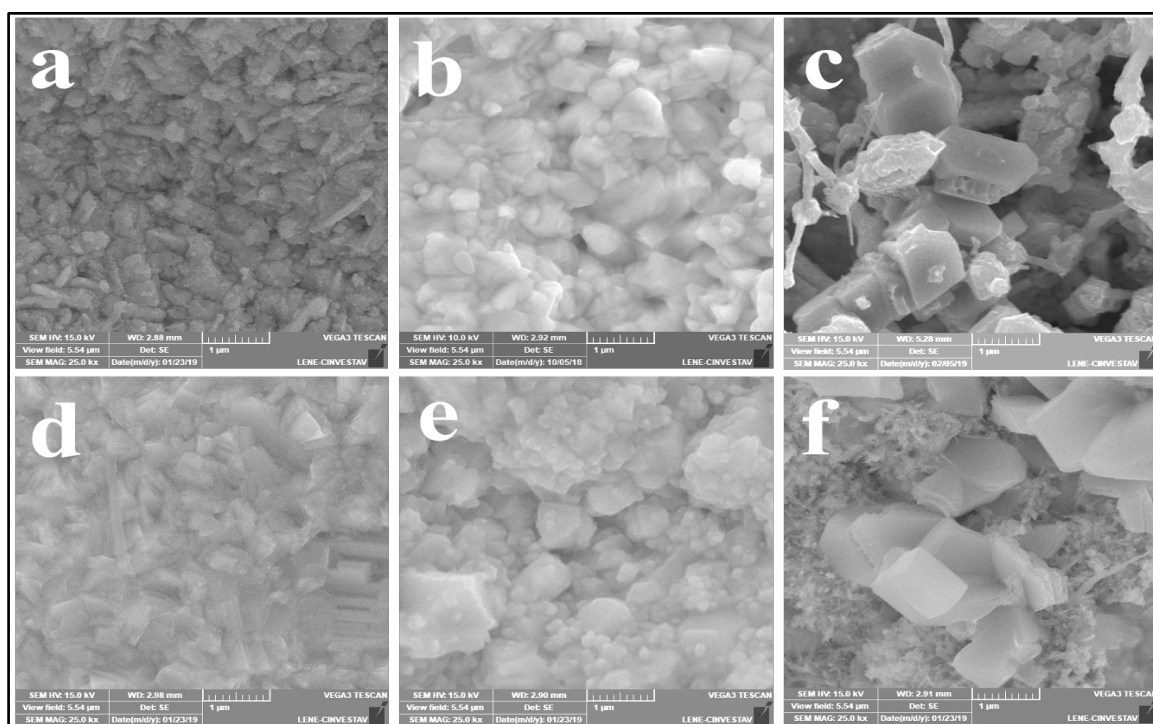


Fig. 4.10 SEM images of CISe thin films selenized at different temperatures and times a) 500°C 30 minutes, b) 525°C 30 minutes, c) 550°C 30 minutes, d) 500°C 60 minutes, e) 525°C 60 minutes, f) 550 °C 60 minutes

#### 4.2.1.3 Compositional analysis of CISe thin films

The phase of CISe ( $\alpha$ -,  $\beta$ -,  $\gamma$ - phase, etc.), types of defects (vacancies, antisite, interstitial), types of semiconductor (p-type or n-type), etc., are dependent on the elemental composition of CISe [21–23]. The slightly poor copper content (i.e., Cu/In)  $\sim$  0.85 to 0.95) and excess selenium content (i.e., Se/(Cu+In)  $>$  1) in the CISe thin film can provide the better CISe solar cell performance [12, 21]. The EDS data are taken from 10 different random points of CISe thin films deposited at different temperatures and times. The details of the atomic compositions of CISe selenized at different temperatures and times are presented in Table 4.4. The EDS spectrum of the CISe thin films selenized at the temperature of 550°C for 60 minutes is displayed in Fig. 4.11. The compositional analysis demonstrates that the copper content of the CISe thin films increases as the selenization temperature and time rise. The result showed the formation of slightly Cu-poor and In-rich with a stoichiometrically content of selenium, which is the required properties of the CISe absorber layer for high solar cell performance. Although selenium content in the film is reduced with an increase in

selenization temperature and time, the CISE thin films still contain higher selenium composition than other elements.

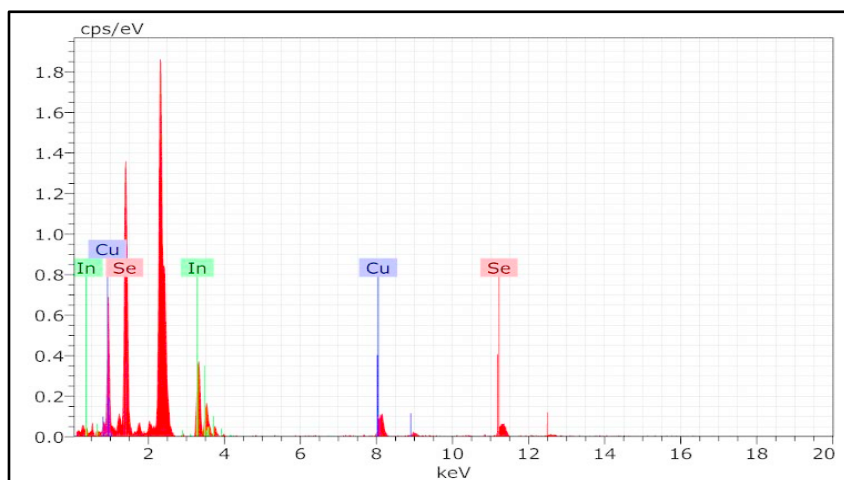


Fig. 4.11 EDS spectrum of selenized CISE thin films (at 550°C for 60 minutes)

Table 4.4 Compositional analysis for CISE thin films selenized at different temperatures, and times

Parameters	Samples	CISE 500°C 30 min	CISE 525°C 30 min	CISE 550°C 30 min	CISE 500°C 60 min	CISE 525°C 60 min	CISE 550°C 60 min
Copper (at. %)		19	20.5	19.5	20.5	22	23.5
Indium (at. %)		26	25.5	27	25	25.5	24.5
Selenium (at. %)		55	54	53.5	54.5	52.5	52
Cu/In		0.731	0.803	0.722	0.820	0.863	0.959
Se/(Cu+In)		1.222	1.174	1.151	1.197	1.105	1.083

#### 4.2.2 Effect of first stage temperatures

This study aims to optimize the first stage temperature for CISE thin film deposition by keeping the second and third stage temperature at 500°C. The first stage substrate temperatures for CISE thin films are varied from 300 to 340°C with the step of 20°C. The CISE thin films were selenized at the temperature of 550°C for 60 minutes. The basic characterizations such as XRD, Raman spectroscopy, SEM, EDS, AFM, and electrical properties were carried out for CISE thin films deposited at three different first-stage temperatures.

#### 4.2.2.1 Structural properties of CISE thin films

The XRD patterns of CISE thin films deposited at different first-stage substrate temperatures of 300, 320, and 340°C are shown in Fig. 4.12. It is observed that all the CISE thin films exhibited a preferential orientation of the (112) plane. The presence of the crystallographic planes such as (112), (204)/(220), (312)/(116), (008)/(400), and (316)/(332) prove the chalcopyrite crystal structure of CISE [12–18]. Those peaks' different intensities and orientations also confirm the polycrystalline nature of deposited CISE thin films [24, 25]. The international center for diffraction data (ICDD) PDF number 01-070-3358 verifies the polycrystalline and chalcopyrite natures of CISE thin films. The other planes, namely (121), (104) and (107), are related to InSe and CuSe binary phases, respectively. The CuSe phase in the CISE thin films can enhance the grain size of the film through the recrystallization phenomenon [26]. The structural parameters, such as crystallite size, strain, and dislocation density, of the CISE thin films deposited at different first-stage temperatures are presented in Table 4.5. A better crystallinity is observed for the CISE samples deposited at the first-stage temperature of 320°C than other samples. The low quality of the precursor layer at low first stage temperature (i.e., 300°C) and lower Se content in the precursor layer at high first stage temperature (i.e., 340°C) may impact the crystallinity of the final CISE.

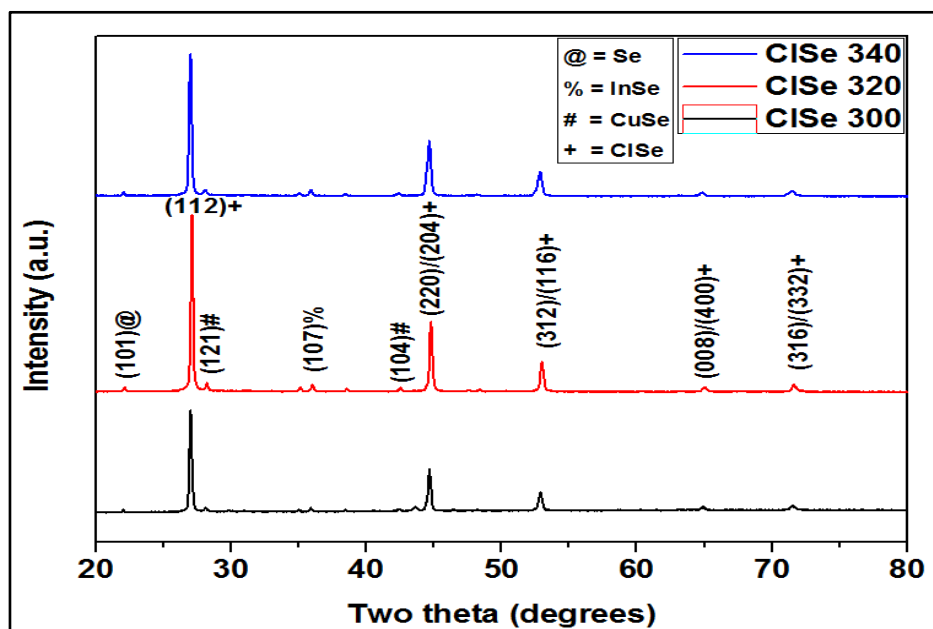


Fig. 4.12 XRD patterns of CISE thin films deposited at different first stage substrate temperatures of 300, 320, and 340°C

Table 4.5 Structural parameters for CISE thin films deposited at different first stage substrate temperatures

Samples Parameters	CISE 300	CISE 320	CISE 340
Two thetas (°)	26.99	27.12	27.00
FWHM (Rad)	0.0087	0.0058	0.0081
Crystallite size (nm)	$16 \pm 1$	$25 \pm 1$	$18 \pm 1$
Strain ( $\epsilon$ ) (Rad)	0.0091	0.0061	0.0084
Dislocation density ( $\delta$ ) (lines/nm <sup>2</sup> )	0.0037	0.0016	0.0032

The Raman spectra of CISE thin films deposited at different first-stage temperature is displayed in Fig. 4.13. The strongest peak at Raman shift of  $170 \text{ cm}^{-1}$  from the results corresponds to the  $A_1$  vibrational mode of CISE thin films, which is related to the characteristics of the chalcopyrite CISE phase [27–29]. The formation of  $A_1$  vibrational mode of CISE is due to the motion of Se atoms with Cu and In atoms [14, 16–18]. The other peaks corresponding to the  $B_2/E$  mode of CISE thin films (i.e., Raman shift at around  $205$  and  $227 \text{ cm}^{-1}$ ), ordered defect compound phase (i.e., Raman shift at around  $150 \text{ cm}^{-1}$ ), and  $\text{Cu}_x\text{Se}$  phase (i.e., Raman shift at around  $260 \text{ cm}^{-1}$ ) are negligible, forming the pure phase of the ternary CISE phase [17, 27]. The intensity, Raman shift, and FWHM value of the peak related to the  $A_1$  mode increase with a rise in the first stage temperature of the hybrid deposition method. The FWHM values for CISE thin films deposited at first stage substrate temperatures, namely  $300$ ,  $320$ , and  $340^\circ\text{C}$ , are  $7.93$ ,  $10.32$ , and  $11.22 \text{ cm}^{-1}$ , respectively. Hence, the selenization temperature of  $550^\circ\text{C}$  for 60 minutes is preferred for getting high crystalline quality CISE films. The observed results suggest that the CISE thin film deposited at  $320^\circ\text{C}$  is considered an optimal first-stage substrate temperature.

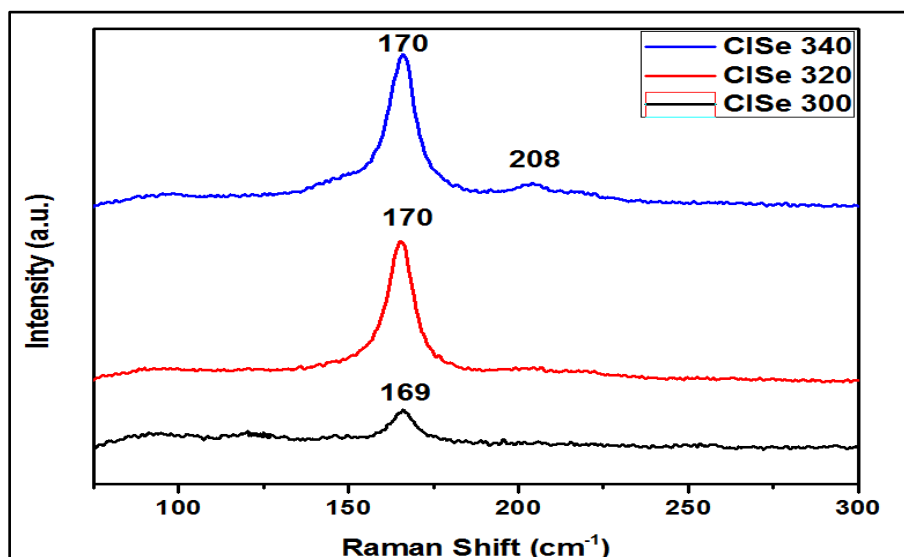


Fig. 4.13 Raman spectroscopy of CISE thin films deposited at three different first stage substrate temperatures of 300, 320, and 340°C

#### 4.2.2.2 Morphological properties of CISE thin films

The SEM images of the CISE thin films deposited at different first-stage substrate temperatures (i.e., 300, 320, and 340°C) are shown in Fig. 4.14. The morphology of CISE thin films is composed of smaller and larger particles spread around the film surface. The grain size of the CISE thin films from the micrographs ranges from 0.1 to 1  $\mu\text{m}$ , showing a comparatively larger grain size of the final CISE absorber layer than the  $\text{In}_2\text{Se}_3$  precursor layer. The recrystallization phenomenon obtained from the Cu-poor phase to the Cu-rich phase after the 2<sup>nd</sup> stage deposition diffuses the atoms across the grain boundaries and finally improves the size of the grains. There are some voids seen in the films. The Cu-Se binary compound are involved in a chemical reaction with In-Se binary compound forming ternary CISE compound, resulting in the formation of voids between the grains [19, 20]. A higher number of larger grains are seen for the CISE sample deposited at the first-stage temperature of 320°C, indicating a suitable condition for CISE absorber layer deposition.

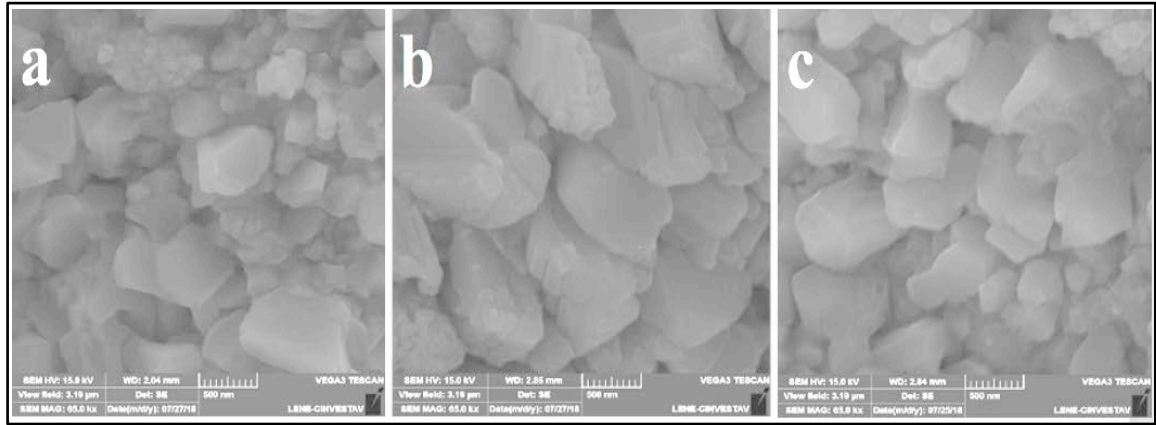


Fig. 4.14 SEM images of CISE thin films deposited at different first stage substrate temperatures a) 300 °C, b) 320 °C, and c) 340 °C

#### 4.2.2.3 Compositional analysis of CISE thin films

As stated before, elemental compositions of the CISE can vary its phase ( $\alpha$ -,  $\beta$ -,  $\gamma$ - phase, etc.), types of defects (vacancies, antisite, interstitial), semiconductor types [21–23]. The better solar cell performance is normally found at slightly copper poor composition (i.e.,  $\text{Cu/In} \sim 0.85$  to  $0.95$ ) and higher selenium composition (i.e.,  $\text{Se}/(\text{Cu}+\text{In}) > 1$ ) for CISE absorber layer [12, 21]. The average atomic compositions of ternary CISE, acquired from 10 different random points of CISE thin films deposited at different first stage temperatures, are determined by EDS measurement (presented in Table 4.6). Fig. 4.15 shows the schematic of the EDS spectrum and EDS mapping of CISE thin films deposited at the first-stage substrate temperature of 320°C. It is seen from the result that all the CISE thin films contain Cu-poor and In-rich with a high content of selenium, confirming the formation of  $\alpha$ -CISE phase (stable phase than other phases). Although selenium content in the film is reduced with an increase in selenization temperature and time, the CISE thin films still contain higher selenium composition than other elements. The atomic composition of Cu, In, and Se are varied by a little margin. All the CISE samples are suitable for using CISE thin-film solar cell as an absorber layer from the EDS result.



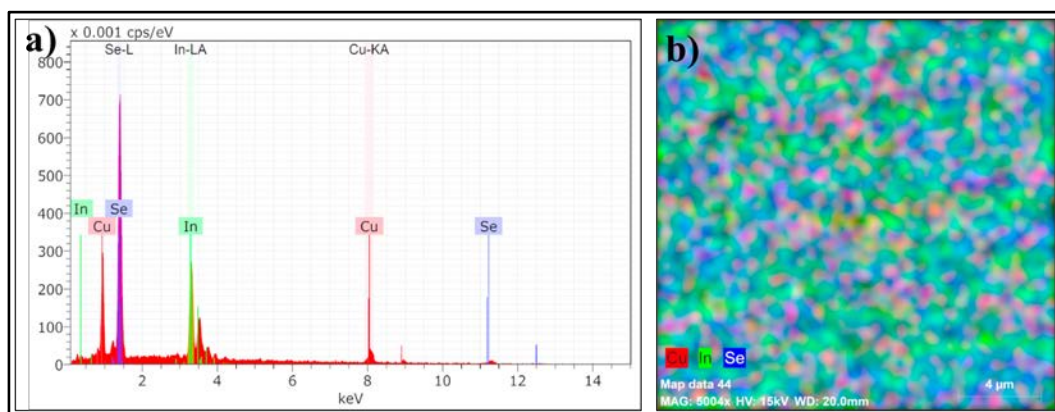


Fig. 4.15 Schematic of the a) EDS spectrum and b) EDS mapping of CISE thin films deposited at first stage substrate temperature of 320 °C

Table 4.6 Compositional analysis for CISE thin films deposited at different first stage substrate temperatures

Samples	CISE 300	CISE 320	CISE 340
Parameters			
Copper (at. %)	20.35	20.66	20.88
Indium (at. %)	23.28	23.15	22.98
Selenium (at. %)	56.37	56.19	56.14
Cu/In	0.874	0.892	0.908
Se/(Cu+In)	1.292	1.282	1.279

#### 4.2.2.4 Topographical analysis of CISE thin films

Fig. 4.16 displays the 2D AFM micrographs (inserted with 3D AFM micrographs) of CISE thin films deposited at different first stage temperatures of 300, 320, and 340°C. Uniformly distributed grains with irregular shapes (especially round and tetragonal shapes) and size (ranging from 100 to 1200 nm) are seen from the topography of CISE thin films. The average grain size, average roughness, skewness, and kurtosis of CISE thin films deposited at three different substrate temperatures are presented in Table 4.7. It is observed from the result that the average grain size and average roughness of the CISE thin films increase with a rise in first stage temperature, indicating that the kinetic energy is not sufficient for coalescence of the grains at a low first stage substrate temperature [12]. The grain sizes for CISE thin films obtained from the AFM measurement are consistent with grain sizes observed from SEM analysis. However, the higher value of roughness for CISE thin films deposited at high first stage substrate temperature may negatively affect the absorption process of incident photons and then the CISE solar cell performance. The small negative skewness value for CISE thin

films (except CISE at 340°C) confirmed the symmetrical height distribution of the grains. The kurtosis values (less than 3) for all CISE thin films confirmed more valleys than peaks in the film's surface [3].

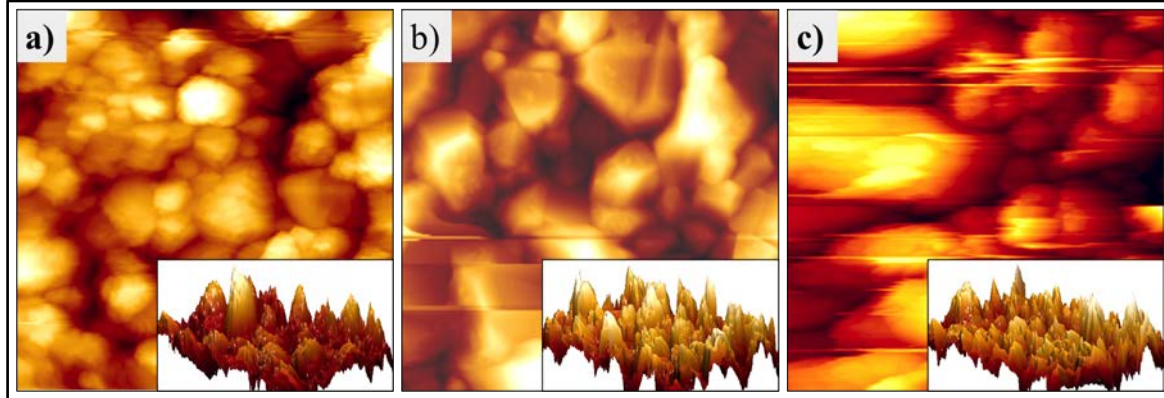


Fig. 4.16 AFM images of CISE thin films deposited at different first stage substrate temperatures a) 300 °C, b) 320 °C, and c) 340 °C

Table 4.7 Topographical parameters for CISE thin films deposited at different first stage substrate temperatures

Samples	CISE 300	CISE 320	CISE 340
Parameters			
Average grain size (nm)	744	885	1057
Average roughness (nm)	152	258	450
Skewness ( $S_{sk}$ )	-0.0309	-0.00923	-0.116
Kurtosis ( $S_{ka}$ )	2.388	2.595	2.972

#### 4.2.2.5 Electrical properties of CISE thin films

The electrical properties of CISE thin films were carried out by the Hall-van der Pauw method with a magnetic field of 0.55 T, determining the resistivity, mobility, carrier concentration, and type of semiconductor. These electrical properties play a vital role in CISE TFSC performance. These electrical properties are mainly dependent on the deposition methods, crystallinity, morphology, grain size, elemental compositions and their chemistry of thin films [12, 15, 30, 31]. The CISE material could be either p-type or n-type depending mainly on the copper ratio (Cu/In) and selenium ratio (Se/(Cu+In)) [30, 31]. The p-type semiconducting nature is formed when CISE thin films contain a copper ratio less than unity and excess selenium content. The CISE thin film with a copper ratio greater than unity and

selenium deficiency can provide an n-type semiconductor. The data of resistivity, mobility, carrier concentration, and hall Coefficient for CISE thin films grown at three different first-stage temperatures are inserted in Table 4.8. All the CISE samples have the average thickness of around 3.5  $\mu\text{m}$ . The resistivity, mobility, and carrier concentration of the CISE thin films, deposited at three different substrate temperatures 300, 320, and 340°C, varied from 20 to 11  $\Omega\text{cm}$ , 4.4 to 6.5  $\text{cm}^2/\text{Vs}$ , and  $7.1 \times 10^{16}$  to  $7.7 \times 10^{16} \text{ cm}^{-3}$ , respectively. The resistivity of CISE thin films decreases with an increase in the first stage temperatures is due to the reduced defects or enhancement in particle size. This result indicates better semiconducting behavior at higher first-stage temperatures. The positive values of Hall coefficient also confirmed the formation of p-type semiconductors, which is also in good agreement with elemental compositions of CISE thin films.

Table 4.8 Electrical parameters for CISE thin films deposited at different first stage substrate temperatures

Parameters \ Samples	CISE 300	CISE 320	CISE 340
Resistivity ( $\Omega\text{cm}$ )	20	16	11
Mobility ( $\text{cm}^2/\text{Vs}$ )	4.4	5.3	6.5
Carrier concentration ( $\text{cm}^{-3}$ )	7.1E16	7.3E16	7.7E16
Hall coefficient ( $\text{cm}^3\text{C}^{-1}$ )	140.84	136.98	129.87

### 4.3 Growth of the CIGSe absorber layer

The main objective of this research work is to find the best deposition condition of the CIGSe absorber layer for the CIGSe TFSC. The CIGSe thin films are also deposited by the hybrid deposition method. After optimizing the best selenization conditions for CI(G)Se thin films, the various first stage temperatures ranging from 300 to 340°C are studied. The CIGSe thin films are characterized to compare the material properties of CIGSe thin films before selenization and after selenization. The basic characterizations, such as XRD, Raman spectroscopy, SEM, EDS, AFM, and electrical properties, for the CIGSe thin films before and after selenization, are described following.

#### 4.3.1 Structural properties of CIGSe thin films

Fig. 4.17 exhibits the XRD pattern for CIGSe thin films at different first-stage substrate temperatures of 320, 330, and 340 °C (having common 2<sup>nd</sup> and 3<sup>rd</sup> stage temperatures of 500°C) before and after selenization. In both cases, the CIGSe thin films indicated a preferential orientation of the plane (112) plane, which is related to the chalcopyrite crystal structure. The different intensities and orientations of crystallographic planes (i.e., (112), (204)/(220), (312)/(116), (008)/(400), and (316)/(332)) for all samples confirms the formation of polycrystalline nature of CIGSe [32–38]. The secondary phases such as Cu<sub>2</sub>Se, Se, and (In,Ga)<sub>2</sub>Se<sub>3</sub> are seen for CIGSe thin films before selenization. However, the CIGSe thin films showed very few secondary phases after selenization. These secondary phases are involved in the chemical reaction during the selenization process, obtaining only intense peaks of the CIGSe thin films. The ICDD PDF number of 083-3359 {with lattice constants,  $a = 5.6959 \text{ \AA}$  and  $c = 11.3362 \text{ \AA}$  and  $c/a = 1.99$ } verified the chalcopyrite crystal structure of CIGSe thin films. The CuSe phase is also present inside the CIGSe thin films that can improve the grain size of the film through the recrystallization phenomenon [26]. The structural parameters, such as crystallite size, strain, and dislocation density, of CIGSe thin films before and after selenization at different first stage temperatures are calculated and demonstrated in Table 4.9. It is found from the table that the crystalline quality of CIGSe thin films increases after the selenization process. The CIGSe thin film deposited at first stage temperature of 320°C showed high crystalline nature than other samples, suggesting the optimal substrate temperature value for first layer deposition. The low-quality precursor layer at lower first stage temperature (i.e., 300°C) and lower Se content inside the precursor layer at higher first stage temperature (i.e., 340°C) could degrade the crystalline properties and crystallite sizes of the final CIGSe thin film.

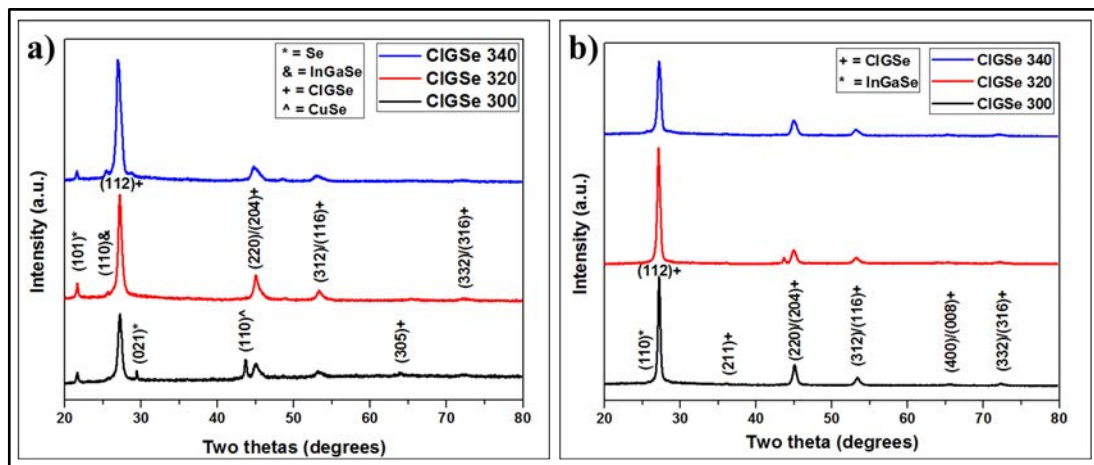


Fig. 4.17 XRD patterns of CIGSe thin films deposited at three different first stage substrate temperatures a) before selenization, and b) after selenization

Table 4.9 Structural parameters for CIGSe thin films before and after selenization at different first stage substrate temperatures

Parameters Samples	2 $\theta$ (degrees)	FWHM (Rad)	Crystallite Size (nm)	Strain (Rad)	Dislocation density (lines/nm <sup>2</sup> )
CIGSe 300 before Se	27.20	0.0218	12 $\pm$ 1	0.00324	0.00647
CIGSe 320 before Se	27.18	0.0189	14 $\pm$ 1	0.00288	0.00502
CIGSe 340 before Se	26.95	0.0172	13 $\pm$ 1	0.00335	0.00581
CIGSe 300 after Se	27.16	0.0135	19 $\pm$ 1	0.00210	0.00265
CIGSe 320 after Se	27.11	0.0127	20 $\pm$ 1	0.00209	0.00254
CIGSe 340 after Se	27.17	0.0142	19 $\pm$ 1	0.00218	0.00288

Next, Raman spectroscopy of the CIGSe thin films before and after selenization is shown in Fig. 4.18. The Raman spectra for CIGSe thin films reveal an intense  $A_1$  vibrational mode (around 170  $\text{cm}^{-1}$  for  $\text{CuInSe}_2$  and 185  $\text{cm}^{-1}$  for  $\text{CuGaSe}_2$ ) located in the range from 170 to 176  $\text{cm}^{-1}$ , which is due to symmetric vibration of Se atoms with Cu, In, and Ga atoms [39–42]. This result proves the formation of the chalcopyrite structure of CIGSe. Since there are no other peaks near to  $A_1$  mode of CIGSe, confirming the formation of poly-crystalline and stable CIGSe phase. The pure quaternary phase of CIGSe is found because the other peaks matching the  $B_2/E$  mode of CIGSe thin films, ODC phase, and  $\text{Cu}_x\text{Se}$  phase are insignificant. The position of the  $A_1$  mode peak in Raman spectra is shifted from lower value (i.e., around 170  $\text{cm}^{-1}$ ) to higher value (i.e., approximately 175  $\text{cm}^{-1}$ ) after selenization. This increment might be due to the change in the elemental composition (especially copper and gallium) of the CIGSe thin films after selenization. There is various literature that  $A_1$  mode phonon peak depends on the composition of elements of the CIGSe thin films [39, 40, 43]. This single-mode behavior of the  $A_1$  mode of CIGSe is consistent with various literature [37, 39–43].

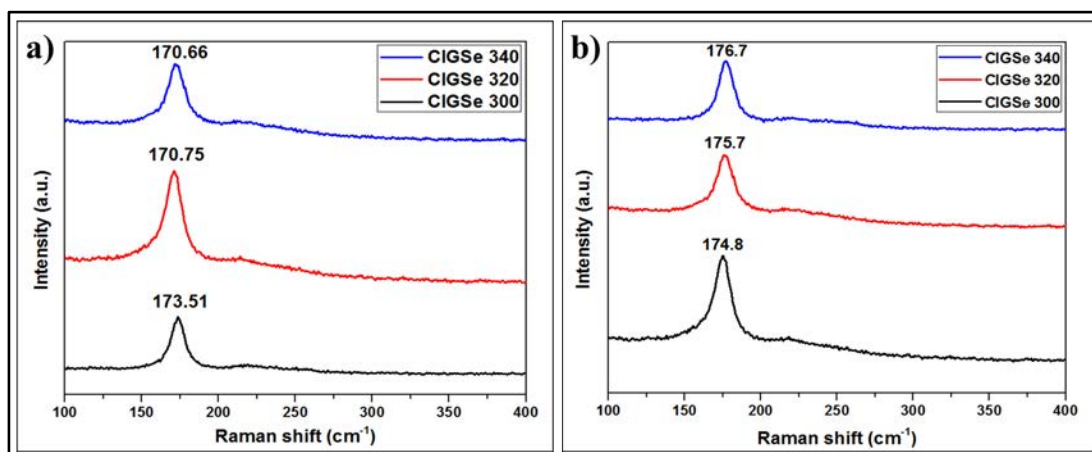


Fig. 4.18 Raman spectroscopy of CIGSe thin films deposited at three different first stage substrate temperatures a) before selenization, and b) after selenization

### 4.3.2 Morphological properties of CIGSe thin films

Fig. 4.19 displays the SEM image of the CIGSe absorber layer before and after selenization at different first stage temperatures of 320, 330, 340°C. The SEM micrograph reveals the smooth and small grain size of CIGSe thin films composed of both smaller (~100 nm) and larger particles (~500 nm). The morphology of CIGSe thin film also depends on the elemental composition (particularly with copper and gallium) of the film [26, 43, 44]. The grain size of the CIGSe films increases after selenization. This increment of grain size might be due to uniform distribution of elements inside the film that forms the solid-liquid copper selenide phases. As mentioned earlier, the grain size of CIGSe thin film improved after 2<sup>nd</sup> stage deposition through the recrystallization phenomenon obtained from the Cu-poor phase to the Cu-rich phase. The recrystallization phenomenon diffuses the atoms across the grain boundaries and enhances the grain size. The voids in CIGSe thin films are seen from the SEM micrograph. These voids are formed due to the interdiffusion of Cu-Se binary compounds, which are involved in chemical reactions with Ga-Se and In-Se compounds, resulting in the formation of ternary and quaternary compounds [19, 20]. The uniform and larger grains are found for the CIGSe samples deposited at 320°C than other conditions, showing suitable deposition conditions for using in solar cells as an absorber layer.

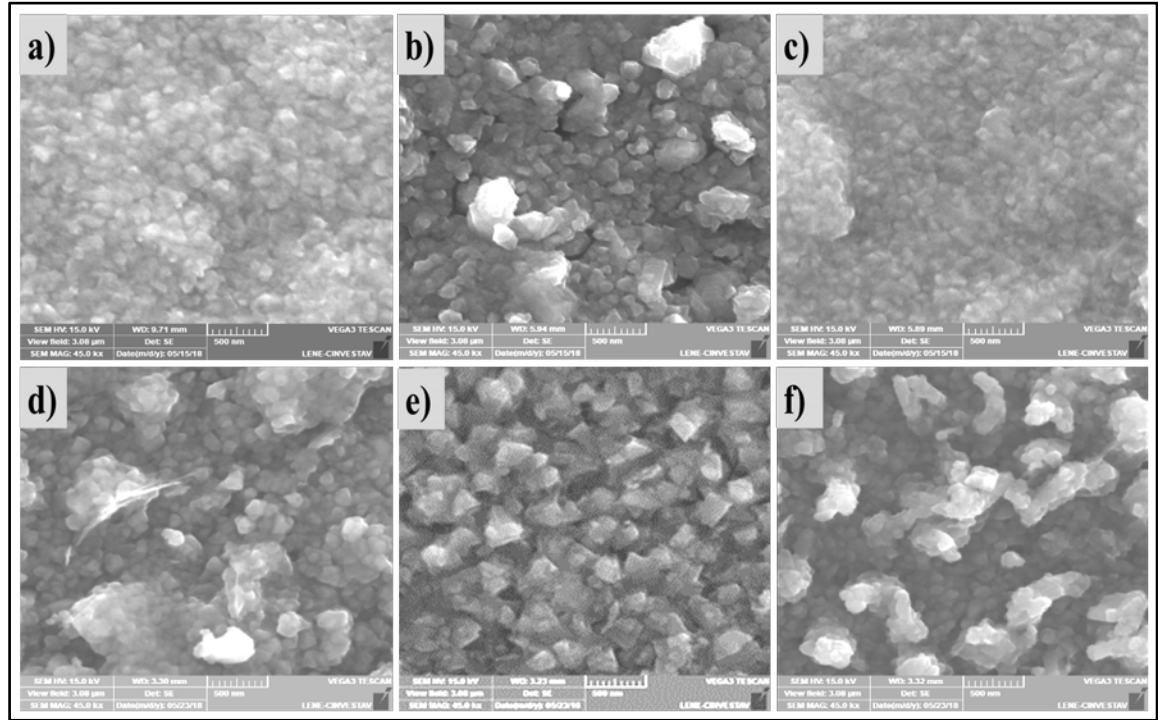


Fig. 4.19 SEM images of the CIGSe thin films a), b), and c) before selenization, d), e), and f) after selenization at three different first stage substrate temperatures of 300, 320, and 340°C, respectively

#### 4.3.3 Compositional analysis of CIGSe thin films

The phase, defects and semiconductor types of the CIGSe material depend on the elemental compositions of the quaternary CIGSe [21–23, 32, 45, 46]. For achieving high efficiency of the CIGSe TFSC, the copper content (i.e.,  $\text{Cu}/(\text{In}+\text{Ga})$ ), gallium content (i.e.,  $\text{Ga}/(\text{In}+\text{Ga})$ ), and selenium content (i.e.,  $\text{Se}/(\text{Cu}+\text{In}+\text{Ga})$ ) in CIGSe thin film could be around 0.85 to 0.95, around 0.1 to 0.3 and greater than 1, respectively [12, 21, 47, 48]. The average atomic compositions of quaternary CIGSe are identified by EDS measurement, which is taken from 10 different random points of CIGSe thin films before and after selenization presented in Table 4.10. The schematic diagram of the EDS spectrums (inserted with EDS mapping) of CIGSe thin films before and after selenization is shown in Fig. 4.20. From the results, the copper content in film increases, and gallium content decreases after selenization of CIGSe thin films. The higher selenium content in the film is observed after selenization than before selenization. The  $\alpha$ -CIGSe phase can be seen for the samples that have performed selenization, showing that selenization is needed to get high-quality CIGSe thin films. Therefore, The CIGSe samples after selenization can utilize in CIGSe TFSC as an absorber layer due to their suitable elemental compositions.



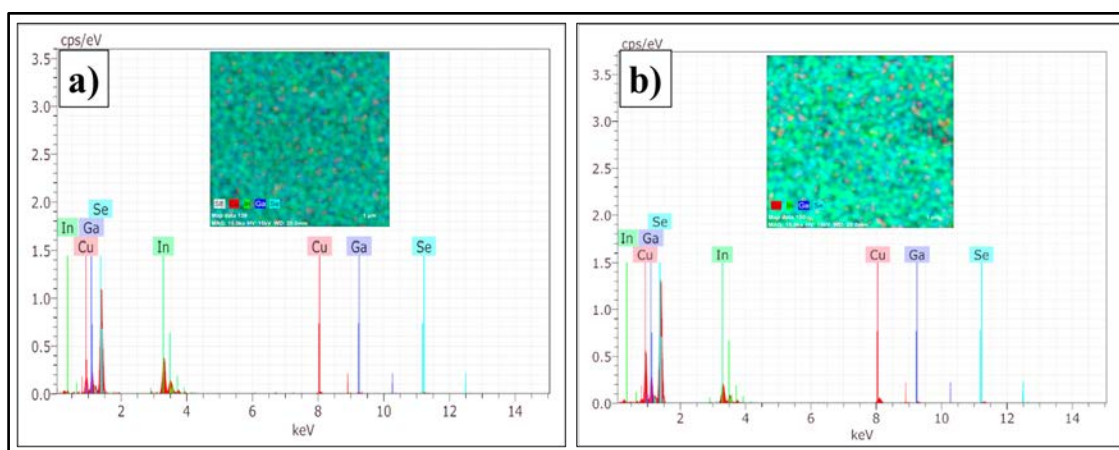


Fig. 4.20 Schematic of the EDS spectrum (inserted with EDS mapping) of the CIGSe thin films a) before selenization, b) after selenization

Table 4.10 Compositional analysis for CIGSe thin films before and after selenization at different first stage substrate temperatures

Elements Samples	Copper (at. %)	Indium (at. %)	Gallium (at. %)	Selenium (at. %)	Ga / (In+Ga)	(Cu) / (In+Ga)	Se / (Cu+In+Ga)
CIGSe 300 before Se	23	14	15	48	0.51	0.8	0.923
CIGSe 320 before Se	22	13	13.5	51.5	0.50	0.83	1.062
CIGSe 340 before Se	20.5	13.5	13	53	0.49	0.77	1.127
CIGSe 300 after Se	21	14.7	9	55.3	0.37	0.88	1.237
CIGSe 320 after Se	21.3	13	10.3	55.4	0.44	0.87	1.242
CIGSe 340 after Se	22	15	8.4	54.6	0.36	0.94	1.202

#### 4.3.4 Topographical analysis of CIGSe thin films

The qualitative (i.e., surface morphology as well as topography) and quantitative (i.e., grain size, roughness, skewness, and kurtosis) information for CIGSe thin films before and after selenization at three different first stage temperatures were analyzed from AFM measurement. Fig. 4.21 shows the 2D AFM images inserted with 3D AFM images of CIGSe thin films before and after selenization deposited at three different first-stage substrate temperatures of 300, 320, and 340°C, respectively. The parameters, such as average grain size, average roughness, root mean square (RMS) roughness, skewness, and kurtosis, of CIGSe thin films calculated from the convolution of the cantilever tip and surface of the CIGSe thin films and demonstrated in Table 4.11. From the AFM images, the CIGSe thin films are composed of laminar structure grains with irregular shapes and sizes ranging from



0.1 to 1  $\mu\text{m}$ . The grains are also uniformly distributed throughout the area. The parameters, namely average grain size, RMS roughness, and average roughness, are higher for CIGSe thin films after selenization than before selenization. The increment of those parameters for CIGSe thin films after selenization might be due to the greater segregation of elements in the CIGSe thin films compared to elemental segregation before selenization [14]. The grain sizes for CIGSe thin films obtained from the AFM measurement are consistent with grain sizes found from SEM analysis. The CIGSe thin films grown after selenization contain higher roughness than CIGSe samples before selenization, which can reduce the absorption of sunlight by increasing the reflection of sunlight from the film surface [14]. However, the rough surface of the CIGSe thin film can be eliminated through surface treatment with various chemicals. The symmetrical height distribution of grains is generalized from positive and small values (near to zero) of skewness for CIGSe thin films before and after selenization. The kurtosis values (greater than 3) for CIGSe thin films proved more peaks than valleys in the film's surface [3].

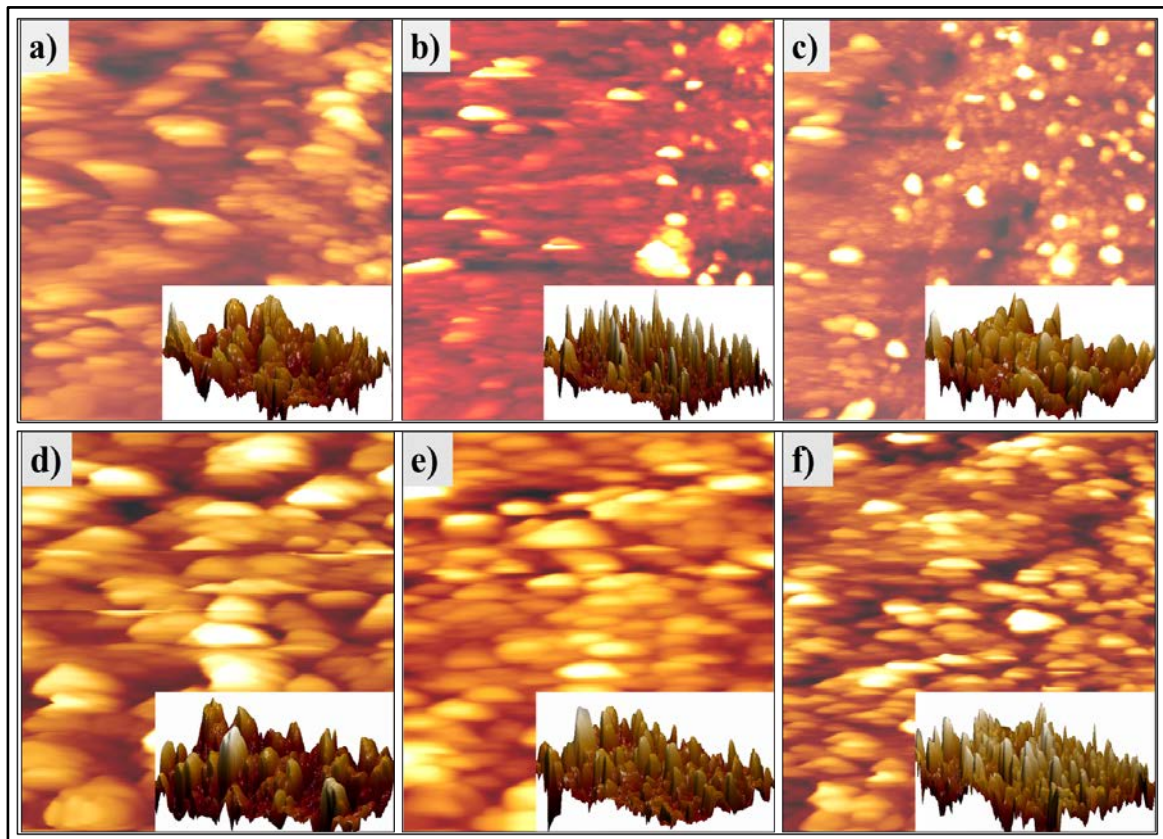


Fig. 4.21 AFM images of the CIGSe thin films a), b), and c) before selenization, d), e), and f) after selenization at three different first stage substrate temperatures of 300, 320, and 340°C, respectively

Table 4.11 Topographical parameters for CIGSe thin films before and after selenization at different first stage substrate temperatures

Properties Samples	Average grain size (nm)	RMS roughness (nm)	Average roughness (nm)	Skewness (S <sub>sk</sub> )	Kurtosis (S <sub>ka</sub> )
CIGSe 300 before Se	400	50.28	39.01	0.160	3.668
CIGSe 320 before Se	490	85.78	61.61	0.974	4.243
CIGSe 340 before Se	461	91.45	61.89	0.441	5.140
CIGSe 300 after Se	558	129.01	101.39	0.0238	3.188
CIGSe 320 after Se	565	105.93	79.81	0.0980	3.794
CIGSe 340 after Se	555	95.93	75.64	0.471	4.508

#### 4.3.5 Electrical properties of CIGSe thin films

The electrical properties of CIGSe thin films were estimated by the Hall-van der Pauw method with a magnetic field of 0.55 T. The electrical properties are mainly dependent on the deposition methods, crystallinity, morphology, grain size, elemental composition, and the chemistry of thin films that can affect the CIGSe solar cell parameters [12, 15, 30, 31]. These electrical properties, especially resistivity and carrier concentration, vary with the elemental composition of the CIGSe thin films. The CIGSe can be either p-type or n-type semiconductor, which depends on the copper ratio ( $\text{Cu}/(\text{In}+\text{Ga})$ ), gallium ratio ( $\text{Ga}/(\text{In}+\text{Ga})$ ), and selenium ratio ( $\text{Se}/(\text{Cu}+\text{In}+\text{Ga})$ ) [30, 31]. The copper ratio less than unity and selenium ratio greater than unity can form a p-type semiconductor. In contrast, the n-type semiconductor can observe in the reverse case (i.e., Cu-rich and selenium deficiency). Here, the electrical properties of CIGSe thin films grown after selenization are only studied because it was difficult to analyze the electrical properties of CIGSe thin films deposited before selenization. The data of resistivity, mobility, carrier concentration and hall Coefficient for CIGSe thin films after selenization deposited at three different first-stage temperatures are presented in Table 4.12. It is seen from the results that the lowest resistivity of  $8.95 \text{ } \Omega\text{cm}$  and the highest carrier concentration of  $8.3 \times 10^{16} \text{ cm}^{-3}$  are observed for the CIGSe samples deposited at  $320^\circ\text{C}$  after selenization. This result can be due to the higher gallium content in CIGSe 320 than other samples, which enhances the material properties of the CIGSe thin films [31, 37, 49]. The positive Hall coefficient values proved the formation of the p-type semiconductor. This outcome is consistent with the elemental compositions of the CIGSe thin films.

Table 4.12 Electrical properties for CIGSe thin films before and after selenization at different first stage substrate temperatures

Parameters Samples	Resistivity ( $\Omega$ cm)	Mobility ( $\text{cm}^2\text{V}^{-1}\text{s}^{-1}$ )	Hall coefficient ( $\text{cm}^3\text{C}^{-1}$ )	Carrier Concentration ( $\text{cm}^{-3}$ )
CIGSe 300 after Se	21.70	6.90	148.62	4.2E16
CIGSe 320 after Se	8.95	8.37	75.21	8.3E16
CIGSe 340 after Se	18.00	13.87	249.68	2.5E16

#### 4.4 Summary

The  $\text{In}_2\text{Se}_3$ , CIGSe and CIGSe thin films were successfully deposited and optimized the suitable deposition conditions. Preferential orientation of (006) from the XRD results, more than 60 at% of selenium content, Raman peaks at  $150\text{ cm}^{-1}$ , and bandgap of around 2 eV for  $\text{In}_2\text{Se}_3$  thin films confirmed the formation of the  $\gamma\text{-In}_2\text{Se}_3$  phase. The crystallinity of  $\text{In}_2\text{Se}_3$  thin films was enhanced when the substrate temperature increased from 300 to  $340^\circ\text{C}$ . The uniform, smooth, compact, and irregular grains for all  $\text{In}_2\text{Se}_3$  thin films are also observed in SEM and AFM studies. All the  $\text{In}_2\text{Se}_3$  samples can be used for the synthesis of the CI(G)Se thin films. For CI(G)Se thin films, the preferential orientation of (112) from XRD results and  $A_1$  vibrational phonon modes in the range of  $170$  to  $176\text{ cm}^{-1}$  from Raman spectra verified the polycrystalline and chalcopyrite structure of CI(G)Se thin films. The crystalline quality of CI(G)Se thin films is improved with an increase in selenization temperature and selenization time. The slightly Cu-poor composition and excess selenium content in the CI(G)Se thin films are observed from EDS analysis, which is the required composition for the formation of the most stable phase (i.e.,  $\alpha$ -phase phase). The compact and larger grains (greater than  $1\text{ }\mu\text{m}$  of grain size) with irregular shapes are seen from SEM and AFM analysis. These larger grains can reduce the grain boundaries where recombination of generated charge carriers occurs and improve the device performance. Hall effect analysis proved the p-type conductivity for deposited CI(G)Se thin films. The carrier concentrations of the CI(G)Se thin films are found in the range of  $10^{16}$  to  $10^{17}\text{ cm}^{-3}$ . After analyzing these properties, the selenization temperature of  $550^\circ\text{C}$  for 60 minutes and the first-stage temperature of  $320^\circ\text{C}$  are the best deposition conditions for CI(G)Se thin film by the hybrid deposition method.

#### References:

- [1] A. Ashok, G. Regmi, and S. Velumani, "Growth of  $\text{In}_2\text{Se}_3$  Thin Films Prepared by

- the Pneumatic Spray Pyrolysis Method for Thin Film Solar Cells Applications,” 2020 17th Int. Conf. Electr. Eng. Comput. Sci. Autom. Control. CCE 2020, pp. 2–7, 2020.
- [2] H. T. El-Shair and A. E. Bekheet, “Effect of Heat Treatment on The Optical Properties of  $\text{In}_2\text{Se}_3$  Thin Films,” *J. Phys. D. Appl. Phys.*, vol. 25, no. 7, pp. 1123–1130, 1992.
  - [3] D. Valencia, J. Conde, A. Ashok, and S. Velumani, “Optimization of  $\text{Cu}(\text{In}, \text{Ga})\text{Se}_2$  (CIGSe) thin film solar cells parameters through numerical simulation and experimental study,” *Sol. Energy*, 2021.
  - [4] D. Perednis and L. J. Gauckler, “Thin film deposition using spray pyrolysis,” *J. Electroceramics*, vol. 14, no. 2, pp. 103–111, 2005.
  - [5] C. H. De Groot and J. S. Moodera, “Growth and characterization of a novel  $\text{In}_2\text{Se}_3$  structure,” *J. Appl. Phys.*, vol. 89, no. 8, pp. 4336–4340, 2001.
  - [6] A. Chaiken et al., “Structural and electronic properties of amorphous and polycrystalline  $\text{In}_2\text{Se}_3$  films,” *J. Appl. Phys.*, vol. 94, no. 4, pp. 2390–2397, 2003.
  - [7] R. Panda, R. Naik, and N. C. Mishra, “Low-temperature growth of  $\gamma$  phase in thermally deposited  $\text{In}_2\text{Se}_3$  thin films,” *Phase Transitions*, vol. 91, no. 8, pp. 862–871, 2018.
  - [8] J. Weszka, P. Daniel, A. Burian, A. M. Burian, and A. T. Nguyen, “Raman scattering in  $\text{In}_2\text{Se}_3$  and  $\text{InSe}_2$  amorphous films,” *J. Non. Cryst. Solids*, vol. 265, no. 1, pp. 98–104, 2000.
  - [9] P. Reyes-Figueroa et al., “Structural properties of  $\text{In}_2\text{Se}_3$  precursor layers deposited by spray pyrolysis and physical vapor deposition for  $\text{CuInSe}_2$  thin-film solar cell applications,” *Thin Solid Films*, vol. 587, pp. 112–116, 2015.
  - [10] F. Hergert, S. Jost, R. Hock, and M. Purwins, “A crystallographic description of experimentally identified formation reactions of  $\text{Cu}(\text{In}, \text{Ga})\text{Se}_2$ ,” *J. Solid State Chem.*, vol. 179, no. 8, pp. 2394–2415, 2006.
  - [11] N. M. Shah, J. R. Ray, V. A. Kheraj, M. S. Desai, C. J. Panchal, and Bharti Rehani, “Structural, optical, and electrical properties of flash-evaporated copper indium diselenide thin films,” *J. Mater. Sci.*, vol. 44, no. 1, pp. 316–322, 2009.
  - [12] N. M. Shah, C. J. Panchal, V. A. Kheraj, J. R. Ray, and M. S. Desai, “Growth, structural and optical properties of copper indium diselenide thin films deposited by thermal evaporation method,” *Sol. Energy*, vol. 83, no. 5, pp. 753–760, 2009.
  - [13] S. Agilan, D. Mangalaraj, S. K. Narayandass, G. Mohan Rao, and S. Velumani, “Structure and temperature dependence of conduction mechanisms in hot wall

deposited CuInSe<sub>2</sub> thin films and effect of back contact layer in CuInSe<sub>2</sub> based solar cells,” *Vacuum*, vol. 84, no. 10, pp. 1220–1225, 2010.

- [14] G. Regmi and S. Velumani, “Impact of selenization temperature on the performance of sequentially evaporated CuInSe<sub>2</sub> thin film solar cells,” *Mater. Sci. Semicond. Process.*, vol. 137, no. May 2021, p. 106215, 2022.
- [15] H. M. Pathan and C. D. Lokhande, “Chemical deposition and characterization of copper indium diselenide (CISE) thin films,” *Appl. Surf. Sci.*, vol. 245, no. 1–4, pp. 328–334, 2005.
- [16] M. H. Valdés and M. Vázquez, “Pulsed electrodeposition of p-type CuInSe<sub>2</sub> thin films,” *Electrochim. Acta*, vol. 56, no. 19, pp. 6866–6873, 2011.
- [17] K. Abderrafi et al., “Epitaxial CuInSe<sub>2</sub> thin films grown by molecular beam epitaxy and migration enhanced epitaxy,” *J. Cryst. Growth*, vol. 475, pp. 300–306, 2017.
- [18] H. Tanino, T. Maeda, H. Fujikake, H. Nakanishi, S. Endo, and T. Irie, “Raman spectra of CuInSe<sub>2</sub>,” *Phys. Rev. B*, vol. 45, no. 23, pp. 13323–13330, 1992.
- [19] C. Lei, A. Rockett, I. M. Robertson, W. N. Shafarman, and M. Beck, “Void formation and surface energies in Cu(InGa)Se<sub>2</sub>,” *J. Appl. Phys.*, vol. 100, no. 7, 2006.
- [20] M. GREEN et al., “Solar cell efficiency tables (version 40),” *Ieee Trans Fuzzy Syst*, vol. 20, no. 6, pp. 1114–1129, 2012.
- [21] P. I. R. Figueroa, “Deposition and characterization of Cu(In<sub>1-x</sub>Ga<sub>x</sub>)Se<sub>2</sub> films by multiple deposition techniques,” CINVESTAV-IPN, 2016.
- [22] H. Marko et al., “Influence of Cu off-stoichiometry on wide band gap CIGSe solar cells,” *Thin Solid Films*, vol. 519, no. 21, pp. 7228–7231, 2011.
- [23] J. Bin Shi et al., “Effect of Cu/In ratio on properties of CuInSe<sub>2</sub> thin films prepared by selenization of Cu-In layers,” *Cryst. Res. Technol.*, vol. 48, no. 2, pp. 94–99, 2013.
- [24] H. Guo et al., “Electrodeposited CuInSe<sub>2</sub> counter electrodes for efficient and stable quantum dot-sensitized solar cells,” *Ceram. Int.*, vol. 44, no. 13, pp. 16092–16098, 2018.
- [25] J. Bin Shi, Y. C. Chen, C. J. Chen, and P. F. Wu, “Optical properties and synthesis of CuInSe<sub>2</sub> thin films by selenization of Cu/In layers,” *Cryst. Res. Technol.*, vol. 47, no. 2, pp. 183–186, 2012.
- [26] M. Nishitani, T. Negami, and T. Wada, “Composition monitoring method in CuInSe<sub>2</sub> thin film preparation,” *Thin Solid Films*, vol. 258, no. 1–2, pp. 313–316, 1995.
- [27] E. Dutková et al., “Mechanochemically synthesized nanocrystalline ternary CuInSe<sub>2</sub>

- chalcogenide semiconductor,” *Mater. Lett.*, vol. 173, pp. 182–186, 2016.
- [28] T. Schmid, N. Schafer, and D. Abou-Ras, “Raman microspectroscopy provides access to compositional and microstructural details of polycrystalline materials,” *Spectrosc. Eur.*, vol. 28, no. 5, pp. 16–20, 2016.
  - [29] C. Rincón and F. J. Ramírez, “Lattice vibrations of CuInSe<sub>2</sub> and CuGaSe<sub>2</sub> by Raman microspectrometry,” *J. Appl. Phys.*, vol. 72, no. 9, pp. 4321–4324, 1992.
  - [30] B. M. Palve, C. V. Jagtap, V. S. Kadam, C. D. Lokhande, and H. M. Pathan, “Chemically deposited CuInSe<sub>2</sub> thin films and their photovoltaic properties: A review,” *Eng. Sci.*, vol. 12, pp. 52–78, 2020.
  - [31] B. J. Babu, S. Velumani, A. Morales-Acevedo, and R. Asomoza, “Properties of CuInGaSe thin films prepared by chemical spray pyrolysis,” *Progr. Abstr. B. - 2010 7th Int. Conf. Electr. Eng. Comput. Sci. Autom. Control. CCE 2010*, no. September, pp. 582–586, 2010.
  - [32] C. Adel, B. M. Fethi, and B. Brahim, “Optical and electrical characterization of CIGS thin films grown by electrodeposition route,” *Optik (Stuttg.)*, vol. 127, no. 8, pp. 4118–4122, 2016.
  - [33] H. Rodriguez-Alvarez et al., “Recrystallization of Cu(In,Ga)Se<sub>2</sub> thin films studied by X-ray diffraction,” *Acta Mater.*, vol. 61, no. 12, pp. 4347–4353, Jul. 2013.
  - [34] D. Zhao et al., “Solution-deposited pure selenide CIGSe solar cells from elemental Cu, In, Ga, and Se,” *J. Mater. Chem. A*, vol. 3, no. 38, pp. 19263–19267, 2015.
  - [35] L. Zhang, F. F. Liu, F. Y. Li, Q. He, B. Z. Li, and C. J. Li, “Structural, optical and electrical properties of low-temperature deposition Cu(In<sub>x</sub>Ga<sub>1-x</sub>)Se<sub>2</sub> thin films,” *Sol. Energy Mater. Sol. Cells*, vol. 99, pp. 356–361, 2012.
  - [36] S. Velumani, B. J. Babu, B. Vidhya, P. Reyes, A. Angeles, and R. Asomoza, “Preparation, deposition of Cu(In<sub>1-x</sub>Ga<sub>x</sub>)Se<sub>2</sub> nanopowder thin films by non-vacuum processes and its characterization,” *Conf. Rec. IEEE Photovolt. Spec. Conf.*, no. June, pp. 000440–000445, 2011.
  - [37] M. Latha, R. Aruna-Devi, S. Velumani, B. Murali, J. Santoyo-Salazar, and F. De Moure-Flores, “Solution based synthesis of Cu(In,Ga)Se<sub>2</sub> microcrystals and thin films,” *RSC Adv.*, vol. 9, no. 60, pp. 35197–35208, 2019.
  - [38] B. J. Babu, B. Egaas, and S. Velumani, “Selenization of CIS and CIGS layers deposited by chemical spray pyrolysis,” *J. Mater. Sci. Mater. Electron.*, vol. 29, no. 18, pp. 15369–15375, 2018.

- [39] Y. M. Shin, D. H. Shin, J. H. Kim, and B. T. Ahn, "Effect of Na doping using Na<sub>2</sub>S on the structure and photovoltaic properties of CIGS solar cells," *Curr. Appl. Phys.*, vol. 11, no. 1 SUPPL., pp. S59–S64, 2011.
- [40] M. Beres, K. M. Yu, J. Syzdek, and S. S. Mao, "Improvement in the electronic quality of pulsed laser deposited CuIn<sub>0.7</sub>Ga<sub>0.3</sub>Se<sub>2</sub> thin films via post-deposition elemental sulfur annealing process," *Thin Solid Films*, vol. 608, pp. 50–56, 2016.
- [41] Z. Jehl et al., "Insights on the influence of surface roughness on photovoltaic properties of state of the art copper indium gallium diselenide thin films solar cells," *J. Appl. Phys.*, vol. 111, no. 11, 2012.
- [42] S. S. Schmidt et al., "Adjusting the Ga grading during fast atmospheric processing of Cu(In,Ga)Se<sub>2</sub> solar cell absorber layers using elemental selenium vapor," *Prog. Photovoltaics Res. Appl.*, vol. 25, no. 5, pp. 341–357, 2017.
- [43] H. Search, C. Journals, A. Contact, M. Iopscience, and I. P. Address, "Properties of Cu(In , Ga)Se<sub>2</sub> Thin Films Prepared by Chemical Spray Pyrolysis Properties of Cu(In , Ga)Se<sub>2</sub> Thin Films Prepared by Chemical Spray Pyrolysis," vol. 4997, 1999.
- [44] M. Ishii, K. Shibata, and H. Nozaki, "Anion distributions and phase transitions in CuS<sub>1-x</sub>Sex(x = 0-1) studied by raman spectroscopy," *Journal of Solid State Chemistry*, vol. 105, no. 2. pp. 504–511, 1993.
- [45] T. Nakada, H. Ohbo, M. Fukuda, and A. Kunioka, "Improved compositional flexibility of Cu(In,Ga)Se<sub>2</sub>-based thin film solar cells by sodium control technique," *Sol. Energy Mater. Sol. Cells*, vol. 49, no. 1–4, pp. 261–267, 1997.
- [46] V. S. P. and E. M. Shpilevsky, "Journal of Applied Spectroscopy, Vol. 77, No. 3, 2010," *J. Appl. Spectrosc.*, vol. 77, no. 3, pp. 335–342, 2010.
- [47] J. Bi et al., "Effect of Cu content in CIGSe absorber on MoSe<sub>2</sub> formation during post-selenization process," *Mater. Sci. Semicond. Process.*, vol. 121, no. November 2019, p. 105275, 2021.
- [48] P. Jackson, R. Wuerz, D. Hariskos, E. Lotter, W. Witte, and M. Powalla, "Effects of heavy alkali elements in Cu(In,Ga)Se<sub>2</sub> solar cells with efficiencies up to 22.6%," *Phys. Status Solidi - Rapid Res. Lett.*, vol. 10, no. 8, pp. 583–586, 2016.
- [49] B. J. Babu, S. Velumani, A. Kassiba, R. Asomoza, J. A. Chavez-Carvayar, and J. Yi, "Deposition and characterization of graded Cu(In<sub>1-x</sub>Ga<sub>x</sub>)Se<sub>2</sub> thin films by spray pyrolysis," *Mater. Chem. Phys.*, vol. 162, pp. 59–68, 2015.

## Chapter 5 Study on CdS buffer layer for CI(G)Se thin film solar cells

This chapter presents the introduction of the transition metal chalcogenides, possible growth methods for CdS thin films, and a detailed study of chemical bath deposition for the growth of CdS thin films including deposition mechanisms. The results and discussions of CdS thin films by a chemical bath deposition method deposited at different ammonia quantities, deposition temperatures and times are also illustrated. Finally, explains the summary of this study and optimizes the best CdS deposition conditions for solar cell application as a window layer.

### 5.1 Introduction

Transition metal chalcogenides, compounds consisting of chalcogens such as oxides, sulfides, selenides and tellurides, are important technological materials. Among those semiconductors, compound semiconductor of group II-VI such as ZnO, ZnS, ZnSe, ZnTe, CdO, CdS, CdSe, and CdTe have attracted much attention due to their potentials on various applications in optoelectronics, catalysis, gas sensors, optical filters, photodetectors, thin-film field effect transistors, semiconductor lasers, photo-electro-chemical cells, and photovoltaics [1–10]. With the exception of mercury compounds (semiconductor compounds such as HgSe and HgTe are semimetals), group II-VI semiconductors are direct bandgap materials with bandgap that ranges from 1.4 eV to 3.7 eV [10]. Metals of group IIB have two  $s^2$  electrons in the outer shell, while chalcogens have six  $s^2p^4$  electrons. Therefore, these compounds are typically characterized by the presence of four elongated electron clouds around each atom. These electron clouds are in the  $sp^3$  configuration, which is due to the hybridization of the  $s$ - and  $p$ -orbitals [11]. This leads that atoms are tetrahedrally coordinated where each atom is symmetrically surrounded by four nearest neighboring atoms of the other element. With this arrangement of atoms, group II-VI semiconductor compounds can satisfy two possible structures: zincblende (cubic) and wurtzite (hexagonal) crystal structures [10]. Group II metals have sufficiently high ionization potentials and do not give up their electrons but rather share them with neighboring electrons of chalcogens [11]. The stronger electronegativity of group VI chalcogens (i.e., electronegativity difference  $\sim 0.4$  to  $0.9$ ) causes the electron clouds to shift from group II metals to group VI chalcogens. As a result, the binding is partly ionic and partly covalent [11]. Ionic bonds are formed when



the valence electrons are detached from the metal and transferred to the chalcogens. While covalent bonds are formed upon equal distribution of valence electrons between the metal and the chalcogen. The cadmium sulfide (CdS) buffer layer is considered promising n-type material due to its function in band alignment, lattice matching, and surface cleaning, as well as forming a buried heterojunction via Cd doping of CIGSe absorber layer.

## **5.2 Deposition methods**

The CdS thin film material can be synthesized by a variety of fabrication techniques, divided into physical vapor deposition (PVD) and solution growth deposition techniques [12–16], such as sputtering, evaporation, molecular beam epitaxy, sol-gel, electrodeposition, screen printing, spin-coating, spray pyrolysis, metal organic chemical vapor deposition, successive ionic layer adsorption and reaction, close spaced sublimation, chemical bath deposition (CBD), etc. The advantages and disadvantages of using various thin film deposition methods and the main parameters that can affect the properties of films are given in literature [12–16]. Physical vapor deposition techniques typically operate at high temperatures and normally require higher capital costs. Solution growth deposition techniques offer opportunities to fabricate semiconductor compound material at lower temperatures and lower capital costs.

## **5.3 Chemical bath deposition method**

CBD is a purely chemical process, which has been intensively applied for the research and industrial deposition of CdS thin films on different substrates because of its simplicity, low process temperature ( $<100^{\circ}\text{C}$ ), scalability and reproducibility, high stability, commercial production, and high device efficiency [17]. The first CBD method was reported in 1984 by synthesizing lead sulfide for photoconductive detectors. The deposition of thin films in CBD occurs from aqueous solutions at low temperatures by a chemical reaction between dissolved precursors, with the help of a complexing agent (or ligand) [18]. CBD method has been attracted considerable attention as it does not require sophisticated instrumentation like vacuum system and other expensive equipment. The precursor materials are commonly available and inexpensive. Moreover, a large number of substrates can be coated in a single run of CBD deposition. The low temperature deposition avoids oxidation and corrosion of

metallic substrates. Formation of pin hole free, uniform and highly stoichiometric films are observed in CBD films since the basic building blocks are ions instead of atoms.

The metal precursors/salts used in CBD are expected to have moderate to high solubility in water, e.g., chlorides, iodides, acetates, nitrates, or sulfates. Chalcogenide sources such as thiourea, thiosulfate, or thioacetamide for sulfur, and selenourea, selenosulfate, or N,N-dimethylselenourea for selenium, while the dissociation of water itself provides oxygen in the form of OH<sup>-</sup> ions. Compounds such as ammonia, ethanolamine, ethylenediamine, methylamine, dimethylamine, triethanolamine, hydrazine, tartrate, citrate, cyanide, etc. are used as complexing agent for the formation of metal chalcogenides in CBD process. Group II-VI semiconductors, such as CdS, CdSe, CdO, HgS, HgSe, ZnS, ZnSe, and ZnO are synthesized extensively by CBD method [26–33].

In the CBD-CdS growth process, there is a slow release of cadmium ions and sulfur ions and then condensation of these ions on the substrate in an aqueous alkaline bath solution giving adherent and uniform CdS thin films. The nucleation and growth of thin films deposited using CBD method can be influenced by parameters such as types of precursor material, the concentration of precursor material, bath temperature, time of deposition, solubility equilibrium, pH of the solution, speed of stirrer, and nature of substrate [12]. In CBD-CdS growth process, ammonium hydroxide is the most used complexing agent, which reacts with cadmium ions from cadmium salts (i.e., cadmium chloride, cadmium iodide, cadmium sulfate, cadmium nitrate, cadmium acetate etc.) and forms cadmium tetraamine complex  $[\text{Cd}(\text{NH}_3)_4]^{2+}$ . The formation of cadmium tetraamine complex in the solution ensures the slow release of Cd<sup>2+</sup> ions and finally cadmium hydroxide (Cd(OH)<sub>2</sub>) will be formed. It is believed that Cd(OH)<sub>2</sub> acts as a catalyst for decomposition of thiourea (the S<sup>2-</sup> source). As a result, the formation CdS films occur through the chemical reaction between Cd(OH)<sub>2</sub> and sulfur ions. CBD-CdS give superior photovoltaic cells compared with the physical vapor deposition method, which is normally used on both CdTe and CIGSe photovoltaic cells [26]. Reynolds et al. first discovered the photovoltaic effect by using CdS thin films with copper contact while studying the properties of different rectifying contacts to CdS crystal in 1954 [27].

### 5.3.1 Deposition mechanisms

Various reaction steps are found at the substrate surface for thin film formation by CBD, which have a vital role in determining the film properties. Thin film deposition mechanism can be divided into two major processes such as the formation of needed film by ionic reactions involving free anions and the decomposition of metal complexes. These two mechanisms are mainly named as complex-decomposition ion-by-ion mechanism and complex-decomposition cluster-by-cluster mechanism [28]. These mechanisms for growth of films are described following.

#### 5.3.1.1 Ion by ion deposition

This mechanism is carried out by sequential reactions between the ions present in the solution. In this mechanism, Particles grow slowly to form a film through heterogeneous nucleation. In ion-by-ion nucleation, first cadmium ions and sulfur ions diffuse over the substrate which serve as a catalyst and facilitate the nucleation. These ions attach to the substrate and are then involved in chemical reactions. Finally, the nucleation grows as a result of the absorption of ions from the solution and CdS thin films are grown on the substrate as shown in Fig. 5.1. The growth of stable, dense, and well-adherent CdS films are normally found in ion-by-ion mechanism. When limiting reactant is used up then growth will start to slow down and eventually stop due to depletion of the reactant [29]. The possible chemical reaction for this mechanism is:

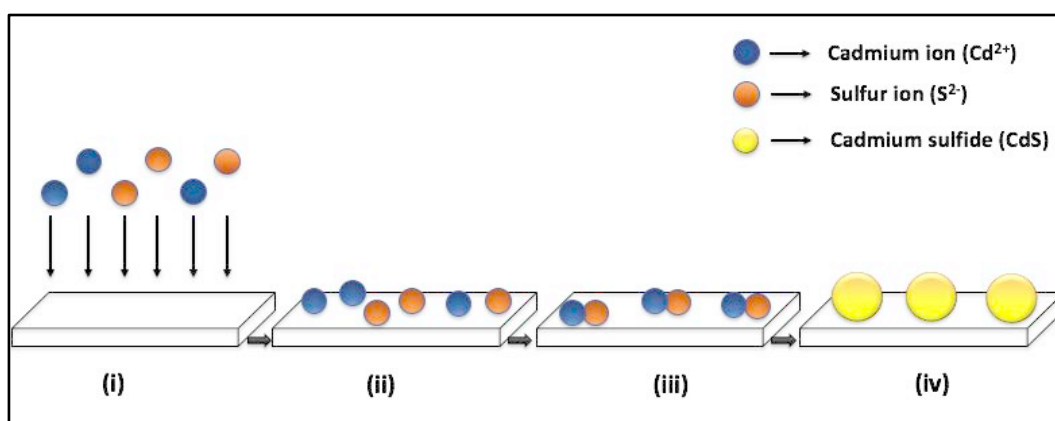


Fig. 5.1 Ion by ion mechanism for cadmium sulfide thin film formation on the substrate: i) diffusion of ions, ii) attach of ions on the substrate, iii) nucleation of the ions on the substrate forming CdS nuclei, iv) growth of the CdS film [30].

### 5.3.1.2 Cluster by cluster deposition

This mechanism is also known as nucleation by formation of metal hydroxides where the growth of stable films obtained through homogeneous nucleation. In cluster-by-cluster mechanism (see Fig. 5.2), metal hydroxide ( $\text{Cd}(\text{OH})_2$ ) colloidal particles first diffuse to the substrate and adhere to it. These metal hydroxide colloidal particles adsorbed onto the substrate react with free chalcogen ions ( $\text{S}^{2-}$ ) in the solution resulting in the displacement of hydroxide by the free ions. Such displacement reaction can occur both on the substrate and in the solution and continues until most of the hydroxide converts into metal-chalcogen ( $\text{CdS}$ ) compounds [31]. Cluster-by-cluster mechanism is dependent on a large difference between the solubility products of the hydroxide and chalcogenide of the required metal. There is a possibility on the process that it will change in the course of the deposition. As the metal is depleted from solution, the complex to metal ratio will increase and may pass the point where no solid hydroxide phase is present in the solution that can favor the ion-by-ion mechanism. The possible chemical reaction for this mechanism is:

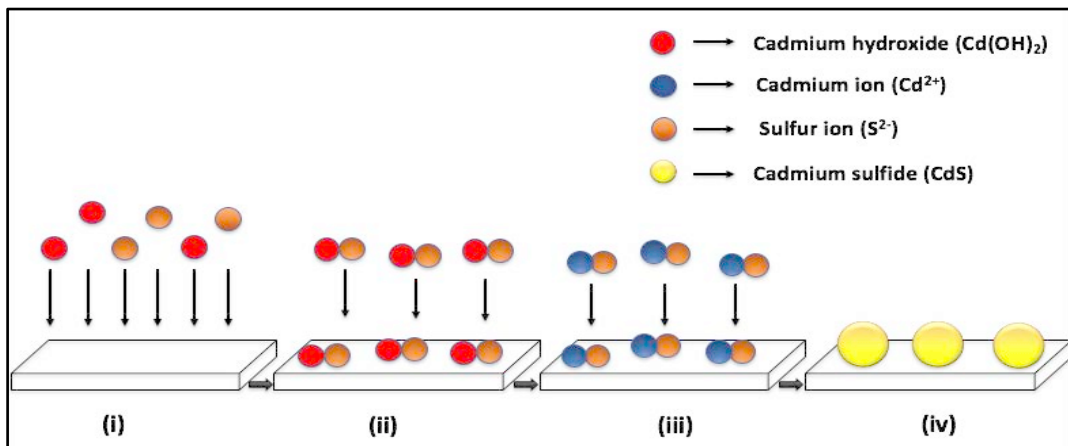


Fig. 5.2 Cluster by cluster mechanism for cadmium sulfide thin film formation on the substrate: i) diffusion of  $\text{Cd}(\text{OH})_2$  molecule and sulfur ions, ii) exchange reaction, iii) nucleation of the ions forming CdS nuclei, iv) growth of the CdS film [30].

### 5.3.2 Results and discussions

#### 5.3.2.1 Effect of ammonia

First of all, the ammonia concentration is fixed (i.e., 3M). Then, the CdS thin films are deposited at different proportions of ammonium hydroxide (i.e., from 1:1 to 5:1) compared to the quantity of cadmium acetate or thiourea, while bath temperature of 80°C and deposition time of 20 minutes are fixed. It is seen from the deposited samples that there is no deposition of films on the substrate at very low and high quantity of ammonia in the solution (i.e., the quantity of the ammonia to cadmium acetate ratio of 1:1 and 5:1). This outcome is due to the insufficient ammonia quantity in 1:1 condition that couldn't liberate the ions (mainly cadmium ions) into the solution and complete control of ions at very high quantity of ammonia (i.e., 5:1). Therefore, this research is only focused on the ammonia ratio from 2:1 to 4:1 to optimize the ammonia quantity for the deposition process.

XRD results (display in Fig. 5.3) revealed that the planes such as (100), (002), (101), and (110) are related to the hexagonal crystal structure of the CdS [32]. It is seen from the diffraction pattern that the peak intensity of the (002) plane for the samples deposited at ammonia ratio 2:1 and 3:1 was higher than the sample deposited at 4:1 condition. Since the deposited CdS films are very thin, the broad hump in the XRD pattern at 20 to 30° is related to the reflections of soda lime glass substrate. The diffraction line broadening occurs when a crystal is broken into smaller incoherent diffraction domains by dislocation arrays, stacking faults, or any other extended imperfection. Various factors, for example, instrument, specimen, lattice imperfection, etc., can broaden the diffraction line. Fig. 5.4 illustrates the SEM micrographs of the surfaces of the CdS films deposited at different ammonia proportions (i.e., 2:1, 3:1, and 4:1). The SEM micrographs exhibit that the film with sphere-like structure, compact, continuous, and smooth grains with well-defined grain boundaries with very few pinholes are found. Although thicker film deposition is found at ammonia proportion 3:1 than 2:1, both films showed analogous results from structure and morphology studies. Thus, constant ammonia proportion of 2:1 is chosen for further investigations such as deposition temperatures and time to get better quality of CdS thin films.

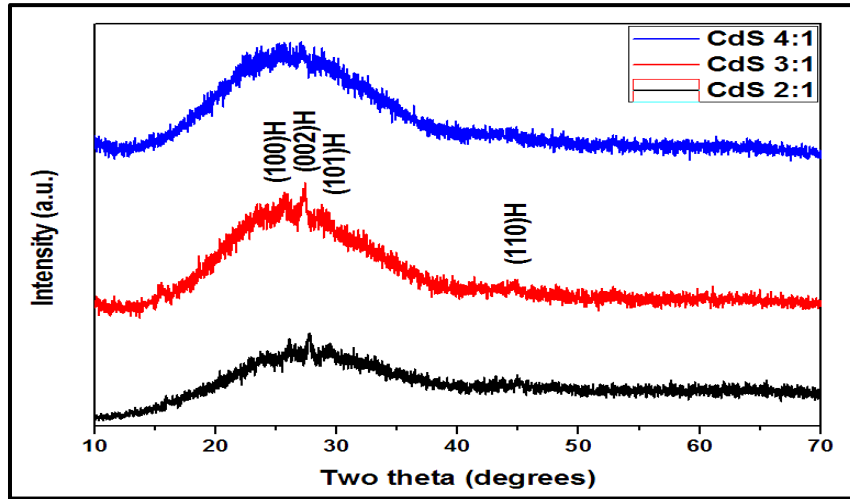


Fig. 5.3 XRD of CdS thin films deposited at various ammonia quantity (from 2:1 to 4:1)

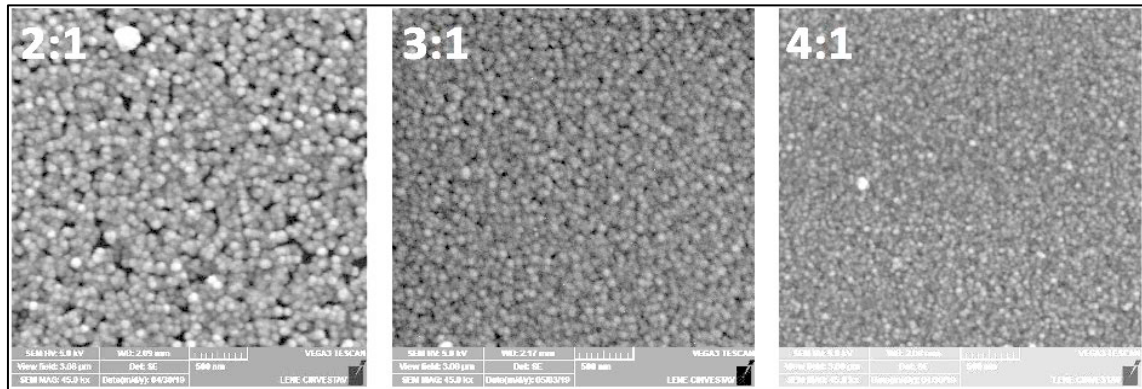


Fig. 5.4 SEM of CdS thin film deposited at different ammonia quantity (from 2:1 to 4:1)

### 5.3.2.2 Influence of temperatures and times

After optimizing the ammonia quantity, this research is focused on the deposition temperature and time for getting more quality of CdS thin film. First, the CdS films are deposited at various temperatures starting from 70 to 85°C with the step of 5°C. The better crystallinity and homogenous morphology are observed at higher deposition conditions (i.e., 80 and 85°C). This research focuses on the deposition temperature of 80°C due to the presence of airdrops inside the solution at 85°C which can affect the deposition of a film on the substrate. And Finally, the work is concentrated on the different deposition times (from 20 to 60 minutes with a step of 10 minutes) at a constant temperature of 80°C to get the best CdS samples for photovoltaic technology. The structural, morphological, compositional, topographical, optical, and electrical properties of CdS thin films deposited at various temperatures and times are studied together.

### 5.3.2.2.1 Growth rate

The growth mechanism of film in the CBD method involves mass transport of reactants, adsorption, surface diffusion, chemical reactions, nucleation and growth. The nucleation and growth rate of films also depend on the nature of energy applied for the formation of the film. The physical properties of thin films, such as the quantum size effect and film's color, rely on thickness. Fig. 5.5 displays the variation of the deposition rate of CdS thin films grown at different temperatures (constant time of 30 min) and at various times (constant bath temperature of 80°C). It is seen from the results that the growth rate of CdS thin films by the CBD method is enhanced with an increase in deposition temperatures and times. Increasing bath temperature improves the kinetics of particles in the solution and tends to have more thickness [33]. More new particles are deposited over the old deposited particles, forming the layer of particles with a rise in deposition time, leading to increase the film thickness [12]. The growth rate of the film can also be affected by the types of used substrates that provide nucleation sites on which the growing film can form. The higher amount of cadmium ions and sulfide ions concentrations inside the chemical bath are formed, as we increase to higher temperature and time of deposition. It is observed that the growth rate of the film enhances in higher deposition temperatures and times. As seen from the data, the minimum deposition rate was found around 1 nm/min for a lower value of deposition temperatures and times and more than 5 nm/min growth rate was observed at higher deposition temperatures and times.

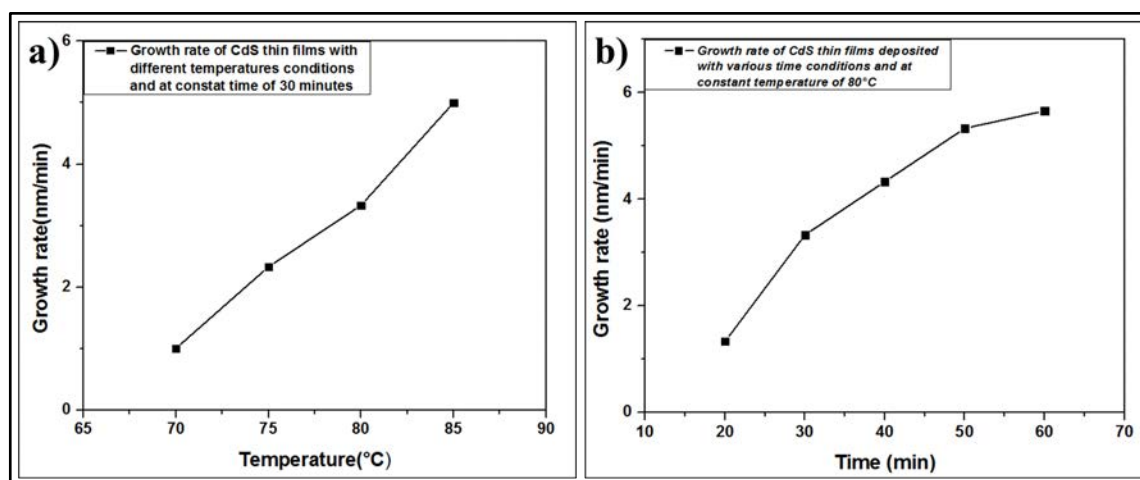


Fig. 5.5 Graphical representation of growth rate of CdS thin films deposited at different a) deposition temperatures (i.e., 70, 75, 80, 85°C) and b) deposition times (20, 30, 40, 50, 60 minutes)

### 5.3.2.2.2 Structural properties of CdS thin films

The preferred orientation CdS thin films is influenced by the source compound, nucleation process, and growth parameters of various deposition methods. In most of the research papers, XRD studies of physical vapor deposition methods revealed that deposited CdS thin films have dominant hexagonal structure and solution growth deposition methods have dominant hexagonal or dominant cubic or mixed (cubic + hexagonal) crystal structure [12]. Different growth methods for CdS thin films consist of varying nucleation and growth rate, which can differ the crystallinity of deposited CdS thin films [34]. For thin film solar cell, a buffer layer with hexagonal structure is preferred over the cubic one due to its stable nature, higher optical bandgap as well as mismatching lattice parameters [35].

XRD analysis is performed in the range of angle two-theta lying between 10 to 70° in order to find the crystallite size and also to study the structural properties of CdS thin films (see Fig. 5.6). In both cases, XRD results display the major reflection of (002) located at 2θ value of around 26.7° that correspond to the hexagonal crystal structure of CdS. The presence of minor reflections like (100), (101), (110), (103), and (112) are compatible with the hexagonal structure of CdS thin films [32][12]. The strong and sharp diffraction peaks of (002) plane increase with increasing deposition time and temperature; this is a consequence of thickness increasing due to the decomposition of reactants and the production of ions that shows the formation of well-crystallized films. The hexagonal system of lattice planes of CdS thin films were verified with the joint committee powder diffraction system (JCPDS PDF number: 01-074-9664 with lattice constants,  $a=4.1002\text{\AA}$ ,  $c=6.6568\text{\AA}$ , and  $c/a=1.62$  and inter-planer spacing ( $d$ )=  $3.3284\text{\AA}$ ) which is well matched with the calculated value. Table 5.2 presents the X-ray diffraction data of 2θ, full width half maximum (FWHM), crystallite size, strain, dislocation density, crystallite number per unit surface, inter-planer spacing, and lattice constants for various deposition time and temperature of CdS thin films. It is found that the intensity of the peaks increases and the width of peak decreases due to improved crystallinity with an increase in substrate temperature and deposition time (except at 60 min). And also, it is seen that 2θ, FWHM, strain, dislocation density value decreases in higher deposition temperatures as well as times. The decrease in strain due to the growth of film thickness demonstrates the reduction in the cohesive force between films and a substrate



material that represents the decrease in lattice imperfection and increase in the crystallite size.

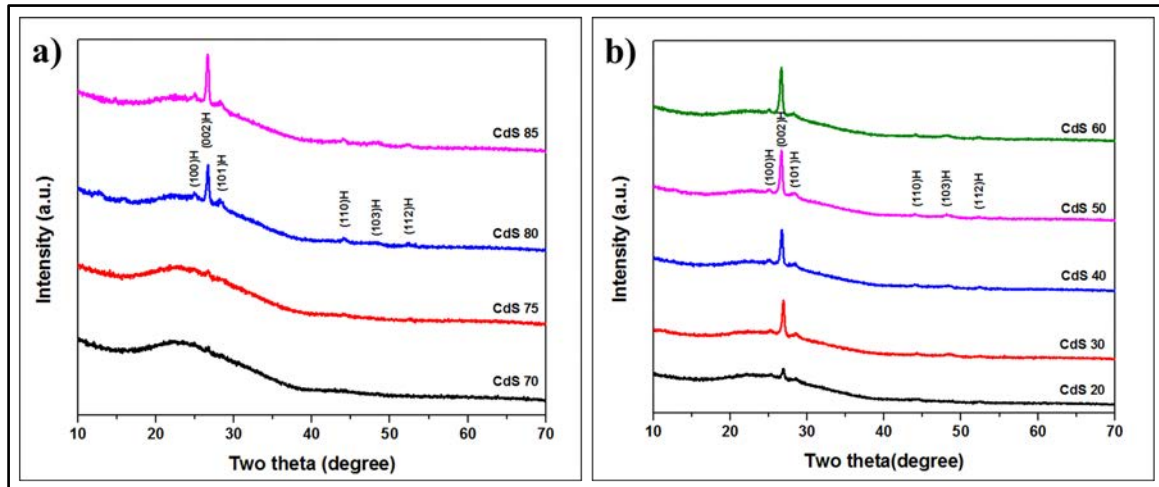


Fig. 5.6 XRD patterns of CdS thin films deposited at different a) deposition temperatures (i.e., 70, 75, 80, 85°C), and b) deposition times (i.e., 20, 30, 40, 50, 60 minutes)

Table 5.1 Calculated structural parameters of CdS thin films deposited different times and temperatures

Parameters Samples	2θ (degree)	FWHM ( $\times 10^{-3}$ Rad)	Crystallite Size (D) (nm)	Strain ( $\epsilon$ ) ( $\times 10^{-3}$ Rad)	Dislocation density ( $\delta$ ) ( $\times 10^{-3}$ lines/nm <sup>2</sup> )	N= $t/(D^3)$ ( $\times 10^{-3}$ nm <sup>-2</sup> )	Inter-planer spacing (d) (Å)	Lattice constants	
								c (Å)	a (Å)
CdS 70°C 30 min	26.70	6.8	$29 \pm 2$	7.09	1.21	1.26	3.336	6.672	4.44
CdS 75°C 30 min	26.69	6.6	$30 \pm 2$	6.88	1.15	2.73	3.337	6.675	4.45
CdS 80°C 30 min	26.76	5.3	$39 \pm 2$	5.53	0.68	1.40	3.329	6.658	4.44
CdS 85°C 30 min	26.64	4.8	$40 \pm 2$	5.01	0.64	2.42	3.343	6.687	4.45
CdS 80°C 20 min	26.92	5.7	$39 \pm 3$	5.94	0.67	0.69	3.310	6.620	4.43
CdS 80°C 30 min	26.76	5.3	$39 \pm 2$	5.53	0.68	1.40	3.329	6.658	4.44
CdS 80°C 40 min	26.70	4.9	$40 \pm 2$	5.11	0.63	2.04	3.336	6.672	4.25
CdS 80°C 50 min	26.64	4.7	$40 \pm 2$	4.90	0.61	2.42	3.343	6.687	4.46

CdS	80°C	26.62	5.4	$35 \pm 2$	5.63	0.82	4.00	3.346	6.692	4.46
	60 min									

Next, the Raman spectroscopy of CdS thin films deposited at different temperatures and times are shown in Fig. 5.7. From the results, the first order scattering of the longitudinal optical (1LO) phonon is observed at  $305 \text{ cm}^{-1}$ , and the second order scattering of longitudinal optical (2LO) phonon is found at  $605 \text{ cm}^{-1}$ . 1LO and 2LO peaks shifted to lower values in vacuum-based methods might be due to size effect or surface phonon mode effect and mechanical stress in the interface. The hexagonal wurtzite structure of CdS thin films corresponds to these two longitudinal optical phonons [36]. The variations in Raman shift and peak intensity depend mainly on the composition of elements, variation in crystallite size, as well as impurity present (i.e., oxygen incorporation into the lattice) inside the film [37]. Here, the intensity of the 1LO peak of CdS thin films increases at a higher value of deposition temperatures and times that signify the enhancement of the crystal structure of films. Similar results of Raman spectra can also be found in various scientific researches [38], [39].

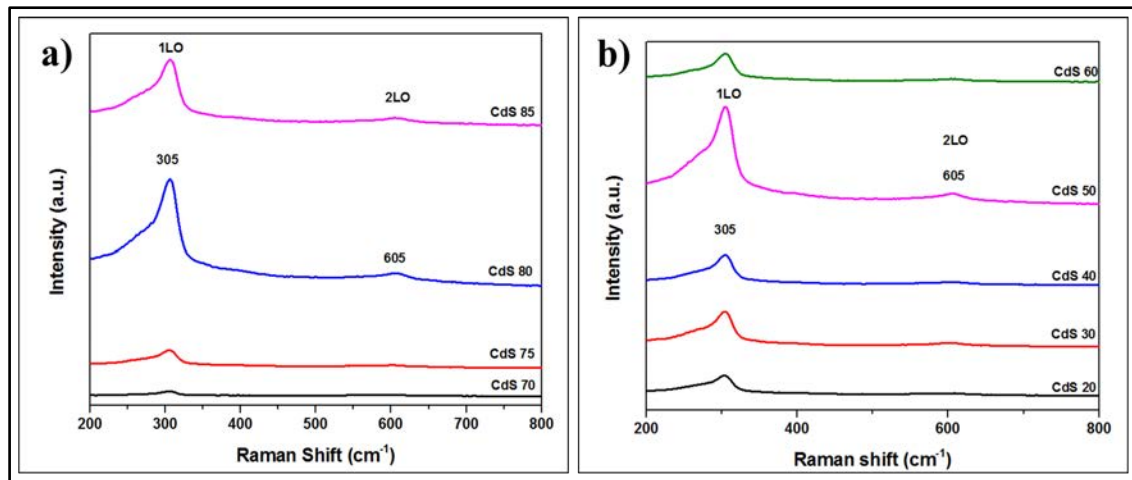


Fig. 5.7 Raman spectra of CdS thin films deposited at different a) deposition temperatures (i.e., 70, 75, 80, 85°C) and b) deposition times (i.e., 20, 30, 40, 50, 60 minutes)

#### 5.3.2.2.3 Morphological properties of CdS thin films

The hexagonal crystal structure films can grow with columnar structure along the c-axis perpendicular to the substrate, introducing fewer grain boundaries parallel to the junction that can restrict the flow of the photogenerated excess carriers to the grid [40]. The SEM

micrographs of CdS thin films prepared with various deposition temperatures and times are shown in Fig. 5.8, conforming the microstructure of thin films changes with different conditions. It is seen from the images that the particles have distinct features composed of a sphere-like structure with grain size distribution in a range of 10-20 nm. The samples deposited at lower temperatures and times show the non-uniform distribution of agglomerated particles with a large number of pinholes in them (see in Fig 5.8(a), 5.8(b), and 5.8(i)). Therefore, the CdS thin films grown at low deposition temperatures and times showed a larger number of defects (i.e., voids, dislocation density, etc.), which can reduce the crystallinity of the film (see Table 5.1). The continuous, dense, homogeneous films without cracks, smooth surfaces, fine spherical structures with fewer voids are observed at higher deposition temperatures and times, which is mainly due to the higher thickness of CdS than lower temperatures and times. The kinetics of film formation are enhanced by increasing the chemical reactions at higher deposition temperatures and the deposition of layers of new particles with an increase in deposition time, leading to a rise in the film thickness. The formation of spherical granules on the scanned image might be due to the spheroid structure of sulfur ions. The CdS thin films grown at a slow deposition rate led to the formation of a uniform film, fewer pinholes, and good adhesion to the substrate than deposition at a high rate [12].

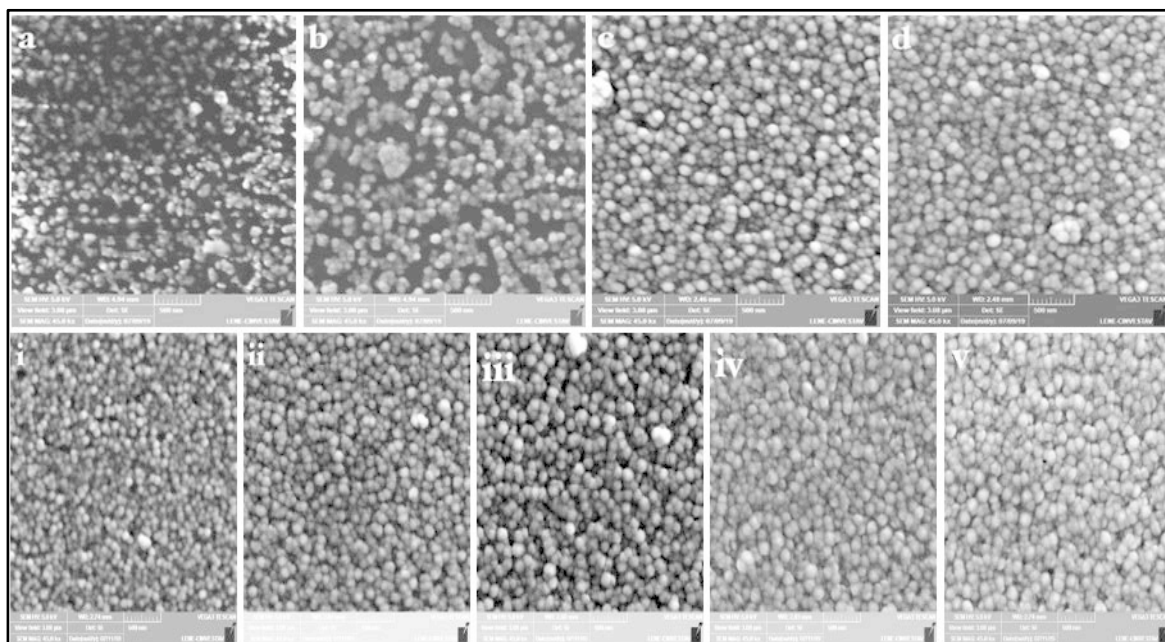


Fig. 5.8 SEM images of CdS thin films deposited at different a-d) deposition temperatures (i.e., 70, 75, 80, 85°C) and i-v) deposition times (i.e., 20, 30, 40, 50, 60 minutes)

### 5.3.2.2.4 Compositional analysis of CdS thin films

EDS analysis is performed on CBD-CdS thin films where the average atomic compositions of the films are taken from different random points of the samples. From Table 5.2, the cadmium concentration decreases from 67–50%, and sulfur concentrations increase from 33 to 50% with an increase in temperature and deposition time. The symmetric compositions of cadmium and sulfur atoms in the CdS thin films deposited at higher deposition temperatures and times are seen in the EDS results. It can infer from the XRD and SEM results that the symmetric compositions of elements can provide better crystallinity as well as morphology. The EDS spectrum verifies the presence of cadmium and sulfur atoms in the CdS thin films (see Fig. 5.9 (a)), and the distribution of cadmium and sulfur atoms in the film is displayed in EDS mapping shown in Fig. 5.9 (b).

Table 5.2 Compositional analysis of CdS thin films

Elements Sample	Cadmium (at. %)	Sulfur (at. %)	Cd/S
CdS 70°C 30 min	67	33	2.03
CdS 75°C 30 min	57	43	1.33
CdS 80°C 30 min	55	45	1.20
CdS 85°C 30 min	52	48	1.08
CdS 80°C 20 min	55	45	1.20
CdS 80°C 30 min	55	45	1.20
CdS 80°C 40 min	53	47	1.13
CdS 80°C 50 min	52	48	1.08
CdS 80°C 60 min	52	48	1.08

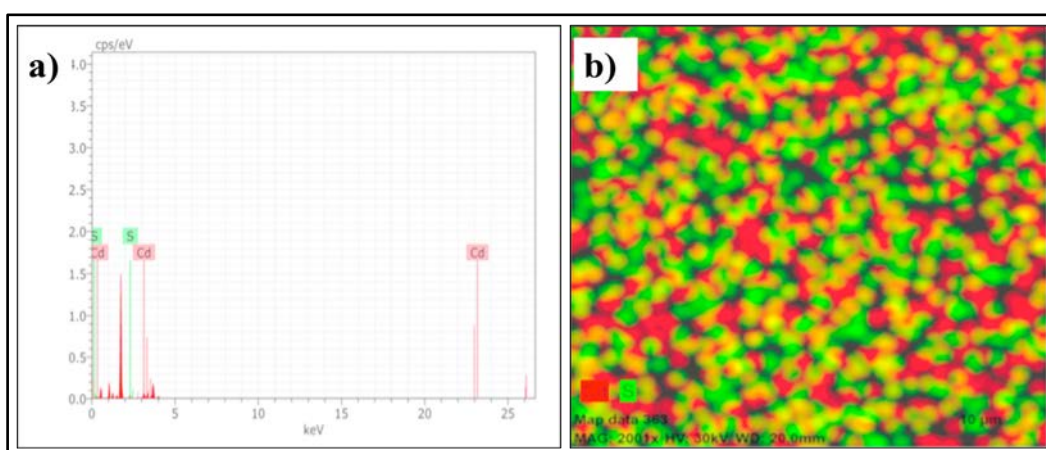


Fig. 5.9 Schematic of a) EDS spectrum and b) EDS Mapping of CdS thin films deposited at 80 °C for 30 min



### 5.3.2.2.5 Topographical analysis of CdS thin films

Topographical analysis on the CdS thin films has been done by using atomic force microscopy (AFM) where the image can be studied through the convolution of the tip of the cantilever and the samples. The non-contact AFM operation mode is used to analyze the surface of the samples [41]. It is observed, from Fig. 5.10, that the particles are uniformly distributed on the surface of the film and also the surfaces are composed of nano-sized grains with an approximate size of 80 to 110 nm. In both conditions, CdS thin films are composed of spherical shaped particulate, very well-connected grains without crack that presents an inhomogeneous compact surface. The grains were grouped together to form large clusters like cauliflower with an average size of around 200 to 400 nm. The value of average grain size, average roughness, skewness, and kurtosis are shown in Table 5.3. The surface roughness of the films lay in the range of 6 to 15 nm, which signifies the formation of a uniform and smooth surface. Moreover, the grains are distributed homogeneously in the film. The value of skewness was positive as well as a small value (i.e., near to zero), which represents the surface has more peaks than valleys and the height distribution is near to symmetrical [42]. This information can also be verified by the data of kurtosis, which was greater than the value of 3.

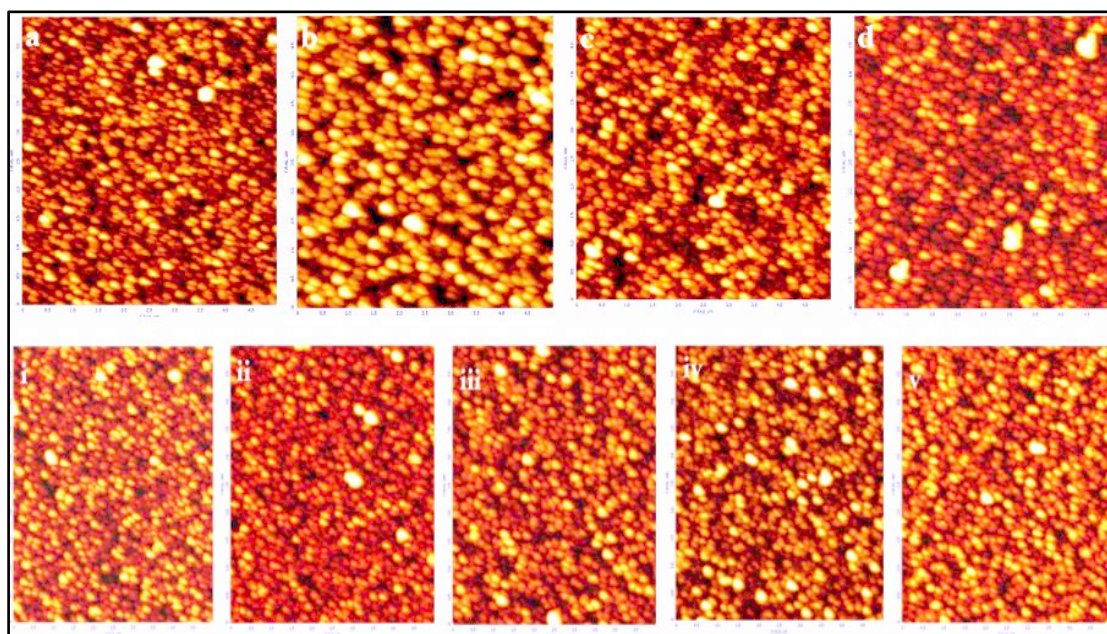


Fig. 5.10 AFM images (2D images with area of  $2 \times 2 \mu\text{m}^2$ ) of CdS thin films deposited at different deposition a-d) temperatures (i.e., 70, 75, 80, 85°C) and i-v) times (i.e., 20, 30, 40, 50, 60 minutes)

Table 5.3 Parameters such as average grain size, average roughness, RMS roughness, skewness, kurtosis calculated from AFM

Parameters Sample	Average grain size (nm)	Average Roughness (nm)	RMS Roughness (nm)	Skewness (S <sub>sk</sub> )	Kurtosis (S <sub>ka</sub> )
CdS 70°C 30 min	80	8	9.86	0.084	3.31
CdS 75°C 30 min	111	14	10.39	0.031	3.49
CdS 80°C 30 min	95	7.48	9.32	0.308	2.95
CdS 85°C 30 min	95	7.41	9.48	0.407	3.95
CdS 80°C 20 min	89	6.9	8.7	0.022	3.16
CdS 80°C 30 min	95	7.48	9.32	0.308	2.95
CdS 80°C 40 min	95	8.7	11.05	0.111	3.46
CdS 80°C 50 min	90	7.17	9.14	0.147	3.30
CdS 80°C 60 min	88	6.4	8.04	0.036	3.19

### 5.3.2.2.6 Optical properties of CdS thin films

The transmittance of the CdS thin films deposited at various temperatures and times are shown in Fig. 5.11, where the data are studied in the range of wavelength from 300 to 900 nm. It is seen that the deposited thin films transmit the light more than 75% in the visible region. These results infer that large numbers of photons will pass to the absorber layer in thin film solar cells. These photons can be absorbed in an absorber layer of thin film solar cells, generating large numbers of charge carriers and, finally, improving solar cell performance. The transmittance of photons at higher deposition temperatures and times is comparatively lower than that of photons at lower deposition temperatures and times. This decrement of transmittance at higher conditions is due to the high thickness of CdS thin films.

The bandgap of CdS thin films is the minimum energy required to excite an electron from a lower energy level (i.e., valence band) to a higher energy level (i.e., conduction band). The CdS bandgap can be calculated by extrapolating the straight-line part of plot  $(\alpha h\nu)^2$  versus photon energy ( $h\nu$ ) to the energy axis (i.e.,  $(\alpha h\nu)^2 = 0$ ) [12]. It is seen from Tauc plot (inserted in the Fig. 5.11) that the value of  $E_g$  for CdS films prepared at different temperatures and times varies from 2.65 to 2.52 eV and 2.49 to 2.62 eV with increasing order,

respectively. These observed bandgaps of CdS thin films resemble the bandgap of the hexagonal phase, which is more stable than the cubic phase of the CdS.

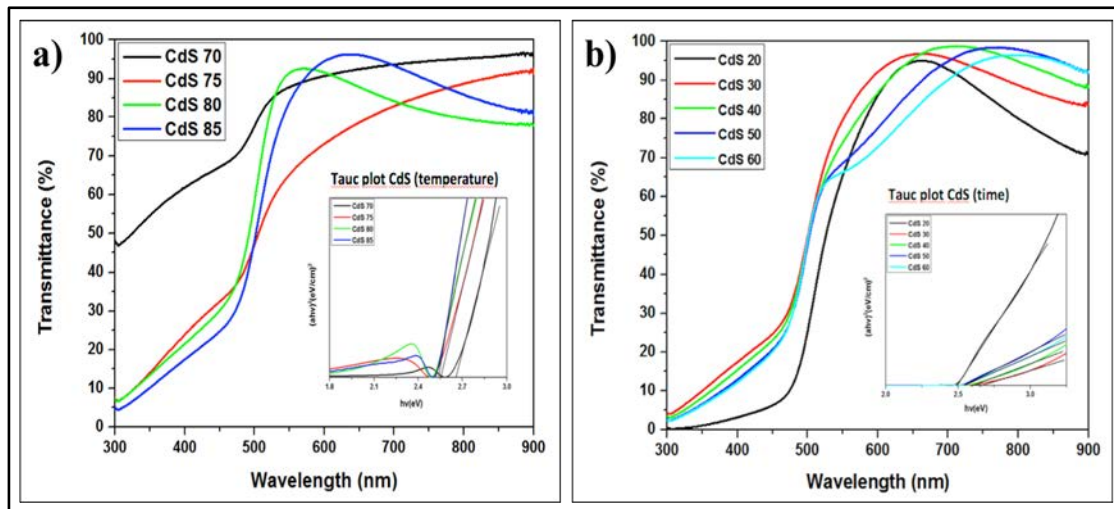


Fig. 5.11 Transmittance of CdS thin films (inserted with bandgap energy diagram) deposited at different a) deposition temperatures (i.e., 70, 75, 80, 85°C) and b) deposition times (i.e., 20, 30, 40, 50, 60 minutes)

The photoluminescence (PL) of the CdS thin films is also studied. The PL studies can analyze the effect of impurities, defect centers, and recombination of surface states on the quality of deposited thin films. Furthermore, information involving different energy states that lies between valence and conduction bands that are responsible for radiative recombination due to cadmium and/or sulfur defects are also achieved by PL studies. Fig. 5.12a shows the PL spectra of CdS thin films deposited with various temperatures from 70 to 85°C at a constant time of 30 min, and Fig. 5.12b displays the PL spectra of CdS thin films at different times from 20 to 60 min, while deposition temperature is kept the constant value of 80°C. For both deposition temperatures and time, there was one major peak ranging from 2.2 to 2.6 eV. The red emission (RE) band is located in the range of 1.7-1.86 eV energy level, which is due to cadmium interstitial (i.e., sulfur vacancies) [43]. The yellow emission (YE) band, situated in the range of 2.04-2.11 eV, arises from cadmium vacancies ( $I_{cd}-V_{cd}$ ) defects [44]. The energy level lies between 2.40 and 2.60 eV in PL spectra is known as a green emission (GE) band. This GE band is attributed to sulfur interstitial, which is related to deep trap/surface trap emission where electronic transitions occur from the conduction band to an acceptor level [44]. The peaks became narrower at higher deposition temperatures and times, which showed better crystallinity of the CdS thin films at higher deposition conditions than in lower deposition conditions. This increment of crystallinity with a rise in

deposition temperatures and times is due to the homogenous distribution of cadmium and sulfur atoms. In addition, there are several peaks located at 2.43, 2.47, and 2.58 eV ascribed to bound exciton for a mixture of cubic and hexagonal phases of CdS thin films [12]. The PL intensity of the peaks decreases with an increase in the deposition temperatures and times, which is due to a decrease in the defect density of elements (i.e., forming symmetrical compositions of cadmium and sulfur atoms) [45], [46]. The higher PL intensity of films may increase the recombination sites, impurities as well as the non-homogenous distribution of atoms.

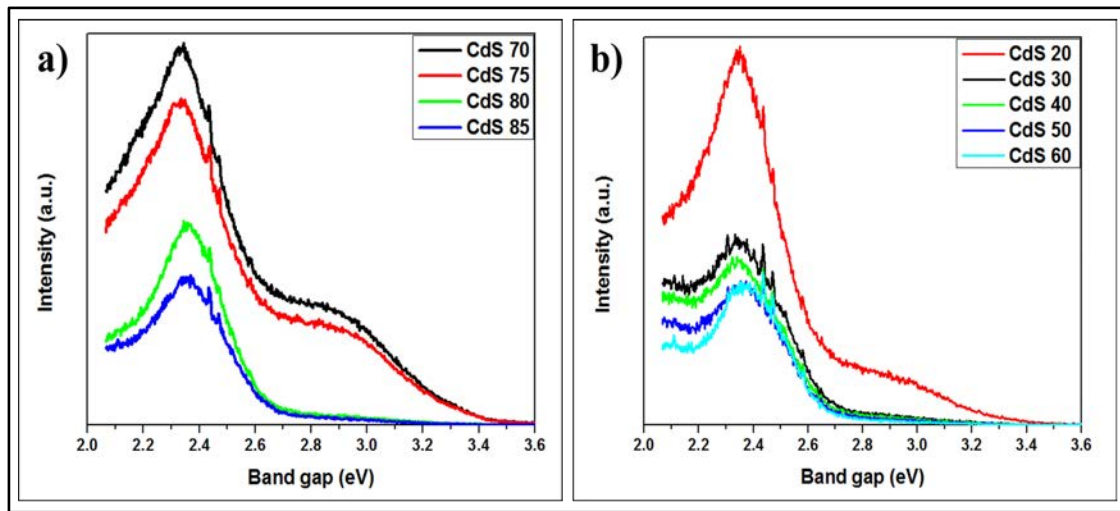


Fig. 5.12 The PL spectra of CdS thin films deposited at different a) deposition temperatures (i.e., 70, 75, 80, 85°C) and b) deposition times (i.e., 20, 30, 40, 50, 60 minutes)

#### 5.3.2.2.7 Electrical properties of CdS thin films

Conductivity, the degree of conduction of electricity, of the CdS thin films was estimated from the reciprocal of resistivity measurements. The electrical parameters like Hall coefficient, conductivity, mobility, and carrier concentration of CdS thin films are shown in Table 5.4. The deposited films at higher temperatures have higher conductivity, which may be due to the increased thickness of films (i.e., few numbers of pinholes) where distributions of ions are uniform. The increase in carrier concentrations of material may be due to bandgap narrowing, increase in grain sizes of film, and decrease in grain boundaries density and dislocations density [47]. The CdS thin films deposited at temperatures lower than 75°C showed more resistive nature due to the presence of many pinholes in the films (seen in SEM and AFM images). Therefore, it was not possible to measure the electrical parameters of the



CdS thin films through the Hall-van der Pauw. The n-type conducting nature of CdS thin films is verified by the negative values of the Hall coefficient. The carrier concentration, which is the number of charge carriers per unit volume, of the CdS semiconductor can be enhanced by doping impurities (i.e., Na, K, etc.) or/ and homogenous distribution of cadmium and sulfur atoms in the film [48], [49]. The CdS material is normally used as a buffer layer in thin film solar cells. The high carrier concentration of the CdS buffer layer can increase the space charge region in the absorber layer, where the generated charge carriers are separated. As a result, it improves the collection of generated charge carriers and improves solar cell performance. The electron mobility, carrier concentration, and conductivity of CdS thin films lie in the range of 6 to 116  $\text{cm}^2\text{V}^{-1}\text{s}^{-1}$ ,  $4.5 \times 10^{14}$  to  $8.3 \times 10^{16} \text{ cm}^{-3}$ , and  $6.63 \times 10^{-3}$  to  $8.00 \times 10^{-2} \Omega^{-1}\text{cm}^{-1}$ , respectively.

Table 5.4 Electrical properties of CdS thin films prepared by CBD method

Parameters Samples	Hall coefficient ( $\text{cm}^3\text{C}^{-1}$ )	Conductivity ( $\Omega^{-1}\text{cm}^{-1}$ )	Mobility ( $\text{cm}^2\text{V}^{-1}\text{s}^{-1}$ )	Carrier concentration ( $\text{cm}^{-3}$ )
CdS 70°C 30 min	-	-	-	-
CdS 75°C 30 min	-	-	-	-
CdS 80°C 30 min	-329	5.16E-2	-17	1.9E16
CdS 85°C 30 min	-75	8.00E-2	-6	8.3E16
CdS 80°C 20 min	-13888	8.35E-3	-116	4.5E14
CdS 80°C 30 min	-329	5.16E-2	-17	1.9E16
CdS 80°C 40 min	-868	3.57E-2	-31	7.2E15
CdS 80 °C 50 min	-11160	6.63E-3	-74	5.6E14
CdS 80°C 60 min	-625	2.56E-2	-16	1.0E16

## 5.4 Summary

The CdS thin films were successfully synthesized over SLG substrates with different deposition parameters. It was observed from the results that the growth of the film mainly depended on the deposition parameters such as concentration and quantity of ammonia, deposition temperature, and time. From XRD results, a hexagonal crystal structure with a preferential orientation along (002) with a crystallite size varied from 20-40 nm was found. The appearance of the first LO at  $305 \text{ cm}^{-1}$  and the second LO at  $605 \text{ cm}^{-1}$  from Raman spectroscopy verified the formation of hexagonal structure of CdS thin films. Uniform, smooth, dense film with fewer pinholes, spherical grains were observed from the SEM

analysis. The homogenous compositions of cadmium and sulfur atoms were observed for CdS thin films deposited at higher temperatures and times. RMS roughness, as determined by AFM measurements, of the CdS films were seen in the range of 5-11 nm showing grains are compact and uniformly distributed. The transmittance value of deposited CdS thin films started to increase after 500 nm and demonstrated more than 75% of transmittance in the visible spectrum. The optical bandgaps of CBD-CdS thin films are varied from 2.5 to 2.65 eV, which was near to the bandgap of CdS material with hexagonal structure (i.e., 2.58 eV). From PL spectra, the energy level lay in between 2.4 to 2.6 eV, confirming the presence of the GE band, which is attributed to sulfur interstitial. The PL peak intensity was decreased with an increase in deposition temperature and time, revealing that the number of impurities, defect centers, and recombination of surface states decreased. Hall effect studies depicted that CdS thin films with n-type nature have the carrier concentration found in the range of  $10^{14}$  to  $10^{16}$  cm<sup>-3</sup>. By comparing the material properties of all the CdS samples, the CdS thin film deposited at a temperature of 80°C for 30 minutes showed the most suitable deposition condition. Therefore, these deposited CdS materials by chemical bath deposition method can be used in the photovoltaic applications.

## References:

- [1] S. Yang, S. Khelifi, J. de Wild, B. Vermang, and J. Lauwaert, "Investigation of recombination mechanisms in Cu(In,Ga)Se<sub>2</sub> solar cells using numerical modelling," Sol. Energy, vol. 228, no. April, pp. 464–473, 2021.
- [2] J. Schrier, D. O. Demchenko, L. W. Wang, and A. P. Alivisatos, "Optical properties of ZnO/ZnS and ZnO/ZnTe heterostructures for photovoltaic applications," Nano Lett., vol. 7, no. 8, pp. 2377–2382, 2007.
- [3] S. J. Jiao et al., "ZnO p-n junction light-emitting diodes fabricated on sapphire substrates," Appl. Phys. Lett., vol. 88, no. 3, pp. 1–3, 2006.
- [4] J. Jie, W. Zhang, I. Bello, C. S. Lee, and S. T. Lee, "One-dimensional II-VI nanostructures: Synthesis, properties and optoelectronic applications," Nano Today, vol. 5, no. 4, pp. 313–336, 2010.
- [5] A. Dandia, V. Parewa, and K. S. Rathore, "Synthesis and characterization of CdS and Mn doped CdS nanoparticles and their catalytic application for chemoselective synthesis of benzimidazoles and benzothiazoles in aqueous medium," Catal.

Commun., vol. 28, pp. 90–94, 2012.

- [6] N. Zhu, A. Zhang, P. He, and Y. Fang, “Cadmium sulfide nanocluster-based electrochemical stripping detection of DNA hybridization,” *Analyst*, vol. 128, no. 3, pp. 260–264, 2003.
- [7] S. D. Naik, S. K. Apte, R. S. Sonawane, U. P. Mulik, and B. B. Kale, “Nanostructured CdS/CdSSe glass composite for photonic application,” *Pramana - J. Phys.*, vol. 65, no. 4 SPEC. ISS., pp. 707–712, 2005.
- [8] R. Agarwal, C. J. Barrelet, and C. M. Lieber, “Lasing in single cadmium sulfide nanowire optical cavities,” *Nano Lett.*, vol. 5, no. 5, pp. 917–920, 2005.
- [9] J. B. Seon, S. Lee, J. M. Kim, and H. D. Jeong, “Spin-coated CdS thin films for n-channel thin film transistors,” *Chem. Mater.*, vol. 21, no. 4, pp. 604–611, 2009.
- [10] N. Perspectives, *Handbook of Chalcogen Chemistry, new perspectives in sulfur, selenium and tellurium*. 2007.
- [11] E. V. S. N. K. Abrikosov, V. F. Bankina, L. V. Poretskaya, L. E. Shelimova, *Semiconducting II-VI, IV-VI, V-VI Compounds*. 1969.
- [12] A. Ashok, G. Regmi, and S. Velumani, “Comparative studies of CdS thin films by chemical bath deposition techniques as a buffer layer for solar cell applications,” *J. Mater. Sci. Mater. Electron.*, vol. 31, pp. 7499–7518, 2020.
- [13] G. Pérez-Hernández et al., “A comparative study of CdS thin films deposited by different techniques,” *Thin Solid Films*, vol. 535, no. 1, pp. 154–157, 2013.
- [14] B. S. Moon, J. H. Lee, and H. Jung, “Comparative studies of the properties of CdS films deposited on different substrates by R.F. sputtering,” *Thin Solid Films*, vol. 511–512, pp. 299–303, 2006.
- [15] J. Patel, F. Mighri, A. Ajji, D. Tiwari, and T. K. Chaudhuri, “Spin-coating deposition of PbS and CdS thin films for solar cell application,” *Appl. Phys. A Mater. Sci. Process.*, vol. 117, no. 4, pp. 1791–1799, 2014.
- [16] J. Nishino, S. Chatani, Y. Uotani, and Y. Nosaka, “Electrodeposition method for controlled formation of CdS films from aqueous solutions,” *J. Electroanal. Chem.*, vol. 473, no. 1, pp. 217–222, 1999.
- [17] P. K. Nair et al., “Semiconductor thin films by chemical bath deposition for solar energy related applications,” *Sol. Energy Mater. Sol. Cells*, vol. 52, no. 3–4, pp. 313–344, 1998.
- [18] H. Khallaf, I. O. Oladeji, and L. Chow, “Optimization of chemical bath deposited CdS

- thin films using nitrilotriacetic acid as a complexing agent,” *Thin Solid Films*, vol. 516, no. 18, pp. 5967–5973, 2008.
- [19] A. Slonopas et al., “Growth mechanisms and their effects on the opto-electrical properties of CdS thin films prepared by chemical bath deposition,” *Mater. Sci. Semicond. Process.*, vol. 52, pp. 24–31, 2016.
  - [20] Y. Zhao, Z. Yan, J. Liu, and A. Wei, “Synthesis and characterization of CdSe nanocrystalline thin films deposited by chemical bath deposition,” *Mater. Sci. Semicond. Process.*, vol. 16, no. 6, pp. 1592–1598, 2013.
  - [21] B. A. Ezekoye, V. A. Ezekoye, P. O. Offor, and S. C. Utazi, “Synthesis, structural and optical characterizations of cadmium oxide (CdO) thin films by chemical bath deposition (CBD) technique,” *Int. J. Phys. Sci.*, vol. 8, no. 31, pp. 1597–1601, 2013.
  - [22] R. S. Patil, T. P. Gujar, C. D. Lokhande, R. S. Mane, and S. H. Han, “Photoelectrochemical studies of chemically deposited nanocrystalline p-type HgS thin films,” *Sol. Energy*, vol. 81, no. 5, pp. 648–652, 2007.
  - [23] P. P. Hankare, V. M. Bhuse, K. M. Garadkar, S. D. Delekar, and I. S. Mulla, “Chemical deposition of cubic CdSe and HgSe thin films and their characterization,” *Semicond. Sci. Technol.*, vol. 19, no. 1, pp. 70–75, 2004.
  - [24] P. Roy, J. R. Ota, and S. K. Srivastava, “Crystalline ZnS thin films by chemical bath deposition method and its characterization,” *Thin Solid Films*, vol. 515, no. 4, pp. 1912–1917, 2006.
  - [25] S. D. Hutagalung and S. C. Loo, “Zinc selenide (ZnSe) nanoparticles prepared by sol-gel method,” 2007 7th IEEE Int. Conf. Nanotechnol. - IEEE-NANO 2007, Proc., pp. 930–933, 2007.
  - [26] J. B. Chu et al., “Nanostructured ZnO thin films by chemical bath deposition in basic aqueous ammonia solutions for photovoltaic applications,” *Appl. Phys. A Mater. Sci. Process.*, vol. 95, no. 3, pp. 849–855, 2009.
  - [27] M. A. Biondi, “Optical and infrared absorption of copper at 4.2A°K,” *Phys. Rev.*, vol. 96, no. 2, pp. 534–535, 1954.
  - [28] S. Gorer and G. Hodes, “Quantum size effects in the study of chemical solution deposition mechanisms of semiconductor films,” *J. Phys. Chem.*, vol. 98, no. 20, pp. 5338–5346, 1994.
  - [29] S. M. H. Al-jawad and H. K. J. Alogili, “Growth Kinetics of Chemically Deposited CdO Thin films,” vol. 27, no. 11, pp. 2335–2344, 2009.

- [30] H. Moualkia, S. Hariech, M. S. Aida, N. Attaf, and E. L. Laifa, "Growth and physical properties of CdS thin films prepared by chemical bath deposition," *J. Phys. D. Appl. Phys.*, vol. 42, no. 13, 2009.
- [31] S. M. Pawar, B. S. Pawar, J. H. Kim, O. S. Joo, and C. D. Lokhande, "Recent status of chemical bath deposited metal chalcogenide and metal oxide thin films," *Curr. Appl. Phys.*, vol. 11, no. 2, pp. 117–161, 2011.
- [32] D. Abou-Ras, G. Kostorz, A. Romeo, D. Rudmann, and A. N. Tiwari, "Structural and chemical investigations of CBD- and PVD-CdS buffer layers and interfaces in Cu(In,Ga)Se<sub>2</sub>-based thin film solar cells," *Thin Solid Films*, vol. 480–481, pp. 118–123, 2005.
- [33] N. G. Dhere, D. L. Waterhouse, K. B. Sundaram, O. Melendez, N. R. Parikh, and B. Patnaik, "Studies on chemical bath deposited cadmium sulphide films by buffer solution technique," *J. Mater. Sci. Mater. Electron.*, vol. 6, no. 1, pp. 52–59, 1995.
- [34] F. Lisco et al., "The structural properties of CdS deposited by chemical bath deposition and pulsed direct current magnetron sputtering," *Thin Solid Films*, vol. 582, pp. 323–327, 2015.
- [35] K. Subba Ramaiah, R. D. Pilkington, A. E. Hill, R. D. Tomlinson, and A. K. Bhatnagar, "Structural and optical investigations on CdS thin films grown by chemical bath technique," *Mater. Chem. Phys.*, vol. 68, no. 1–3, pp. 22–30, 2001.
- [36] J. H. Kwon, J. S. Ahn, and H. Yang, "Chemical bath deposition of CdS channel layer for fabrication of low temperature-processed thin-film-transistors," *Curr. Appl. Phys.*, vol. 13, no. 1, pp. 84–89, 2013.
- [37] S. Aksay, M. Polat, T. Özer, S. Köse, and G. Gürbüz, "Investigations on structural, vibrational, morphological and optical properties of CdS and CdS/Co films by ultrasonic spray pyrolysis," *Appl. Surf. Sci.*, vol. 257, no. 23, pp. 10072–10077, 2011.
- [38] S. Rajpal and V. Bandyopadhyay, "Structural and optical properties of CdS thin film grown by chemical bath deposition," *J. Nano- Electron. Phys.*, vol. 5, no. 3, 2013.
- [39] J. Trajić et al., "Raman spectroscopy of optical properties in cds thin films," *Sci. Sinter.*, vol. 47, no. 2, pp. 145–152, 2015.
- [40] M. A. Martínez, C. Guillén, and J. Herrero, "Morphological and structural studies of CBD-CdS thin films by microscopy and diffraction techniques," *Appl. Surf. Sci.*, vol. 136, no. 1–2, pp. 8–16, 1998.
- [41] M. C. Baykul and A. Balcioglu, "AFM and SEM studies of CdS thin films produced

- by an ultrasonic spray pyrolysis method,” *Microelectron. Eng.*, vol. 51, pp. 703–713, 2000.
- [42] Y. Al-Douri and U. Hashim, “Chalcogenide nanostructures: Topography, synthesis, properties, and applications,” *J. Renew. Sustain. Energy*, vol. 6, no. 1, 2014.
  - [43] P. S. Suryavanshi and C. J. Panchal, “Investigation of urbach energy of CdS thin films as buffer layer for CIGS thin film solar cell,” *J. Nano- Electron. Phys.*, vol. 10, no. 2, pp. 5–9, 2018.
  - [44] R. S. Yadav, P. Mishra, R. Mishra, M. Kumar, and A. C. Pandey, “Histidine functionalised biocompatible CdS quantum dots synthesised by sonochemical method,” *J. Exp. Nanosci.*, vol. 5, no. 4, pp. 348–356, 2010.
  - [45] F. Gemain, I. C. Robin, S. Renet, and S. Bernardi, “Photoluminescence studies of CdS layers for solar cells,” *Phys. Status Solidi Curr. Top. Solid State Phys.*, vol. 9, no. 8–9, pp. 1740–1743, 2012.
  - [46] J. Aguilar-Hernández et al., “Photoluminescence and structural properties of cadmium sulphide thin films grown by different techniques,” *Semicond. Sci. Technol.*, vol. 18, no. 2, pp. 111–114, 2003.
  - [47] M. Cao, Y. Sun, J. Wu, X. Chen, and N. Dai, “Effects of cadmium salts on the structure, morphology and optical properties of acidic chemical bath deposited CdS thin films,” *J. Alloys Compd.*, vol. 508, no. 2, pp. 297–300, 2010.
  - [48] S. A. Al Kuhaimi, “Influence of preparation technique on the structural, optical and electrical properties of polycrystalline CdS films,” *Vacuum*, vol. 51, no. 3, pp. 349–355, 1998.
  - [49] J. P. Enríquez and X. Mathew, “Influence of the thickness on structural, optical and electrical properties of chemical bath deposited CdS thin films,” *Sol. Energy Mater. Sol. Cells*, vol. 76, no. 3, pp. 313–322, 2003.

## **Chapter 6 Simulation study on CI(G)Se thin film solar cells**

SCAPS software has remained one of the favored simulators to analyze the device performance and optimize the parameters for high-efficiency solar cells. The basic introduction of SCAPS software is described in the section 1.3.1. A systematic investigation is needed to optimize the solar cell structure because the optimization process in experimental work is complex, costly, and time-consuming. This chapter presents the simulation results of CISE, CIGSe, and CIGSe bilayer TFSCs. The parameters of different layers used in CISE, CIGSe, and CIGSe bilayer TFSCs are presented in the section 3.2. The influence of the thickness and carrier concentration of each material used in TFSC on the solar cell performance is primarily analyzed and optimized to get high PCE. Our experimental results are also examined through this simulation and introduced in this chapter. Finally, the effect of defects in various layers (i.e., mainly in the absorber layer, in the buffer layer, and at the interface), ambient temperatures, and parasitic resistances on the solar cell parameters are studied for all CI(G)Se TFSCs.

### **6.1 Study on CISE thin film solar cells**

In this section, the thickness and carrier concentration of each layer used in CISE TFSC are graded and simulated. The output parameters, namely  $J_{sc}$ ,  $V_{oc}$ , FF, and PCE, for every graded condition are calculated from the SCAPS software. The CISE TFSC can optimize the best parameters to get high device performance by analyzing these parameters. A brief detail of the effect of thickness and carrier concentration of each layer used in CISE TFSC on the device performance is described following.

#### **6.1.1 Effect of thicknesses and carrier concentrations of CISE for CISE TFSC**

The thickness of the absorber layer is considered a vital parameter in solar cells because the quantity and quality of the material are directly related to the device's performance, material usage, and cost. The absorber layer thickness must be optimized for getting high PCE at a low thickness as much as possible. Here, the simulation study is carried out at a different thickness of the CISE absorber layer ranging from 1 to 10  $\mu\text{m}$  while other parameters are kept constant (see Table 6.1). Fig. 6.1 displays the J-V curve of CISE TFSC inserted with

the QE curve and the quantitative data of the solar cell parameters at different CISE thicknesses. From the results, all the solar cell parameters (i.e.,  $V_{oc}$ ,  $J_{sc}$ , FF, and PCE) are enhanced with a rise in CISE thickness. This increment is due to the collection of more photons in the absorber layer that generates more electron-hole pairs. Moreover, the photons having longer wavelengths may also absorb in a thicker absorber layer. The absorption of more photons improves the  $V_{oc}$  and  $J_{sc}$  of the solar cells and eventually increases the PCE of CISE TFSC [1–6]. At the low thickness of CISE, all the solar cell parameters are degraded, which may be due to the back-contact recombination. The back contact and depletion region are very close to each other at low CISE thickness. The chances of recombining generated charge carriers at back contact are high for the thin absorber layer, which declines the device performance [2, 6, 7]. This outcome is also confirmed from the inserted QE curve that the device performance is reduced at lower CISE thickness by increasing back-contact recombination and decreasing the absorption limit of CISE. Once the diffusion length of minority carriers is in the order of magnitude of the absorber layer thickness, the maximum number of photons is absorbed and collected. The PCE of the solar cells varies from 18.5 to 22% when the CISE thickness is changed from 1 to 10  $\mu\text{m}$ . These results are compatible with the previously published results [1, 8–12].

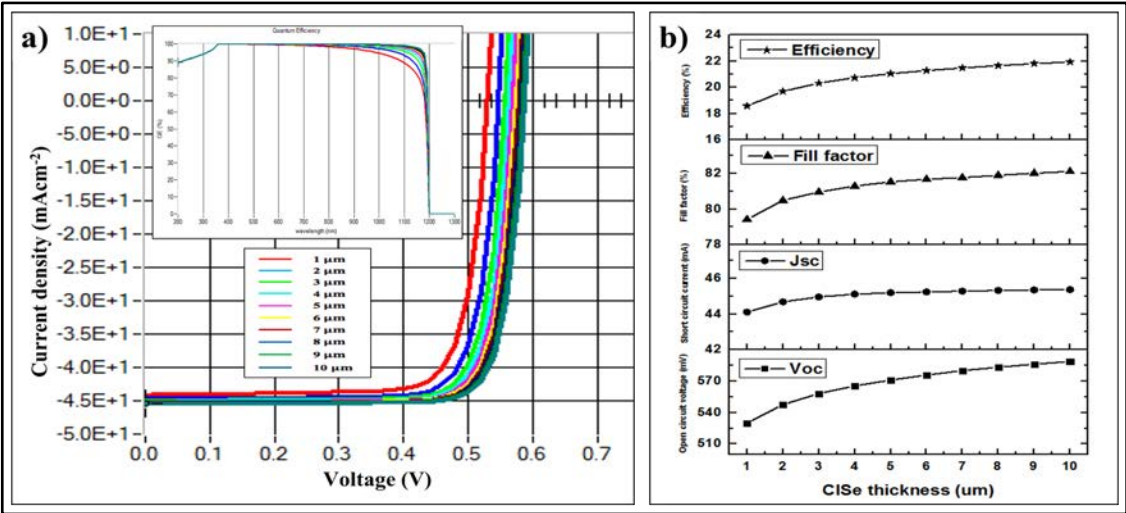


Fig. 6.1 Schematic of a) J-V curve of CISE TFSC inserted with QE curve, b) the solar cell parameter curve at different CISE thickness

Table 6.1 Parameters used in CISE TFSC at different CISE thicknesses

Materials	CISE	CdS	ZnO	ZnO:Al
Parameters				
Thickness (nm)	1000-10000	50	50	100



Bandgap (eV)	1.04	2.45	3.25	3.5
Donor density (cm <sup>-3</sup> )	0	1×10 <sup>17</sup>	1×10 <sup>17</sup>	1×10 <sup>17</sup>
Acceptor density (cm <sup>-3</sup> )	1×10 <sup>16</sup>	0	0	0

After studying the absorber layer thickness, the SCAPS software works on various carrier concentrations of the CISE absorber layer from 10<sup>14</sup> to 10<sup>18</sup> cm<sup>-3</sup>. The other parameters used in the SCAPS software are presented in Table 6.2. Fig. 6.2 displays the J-V curve of CISE TFSC inserted with the QE curve and the quantitative data of the solar cell parameters at different CISE carrier concentrations. The electric field intensity and width of the space charge region can be affected by the carrier concentration of the absorber layer. At higher carrier concentrations of the absorber layer, the semiconductive properties deteriorate and change into the metallic conductive state. This state elevates the recombination traps and centers in the film that impact the device's performance [7]. The  $V_{oc}$  is directly related to CISE carrier concentration (i.e.,  $V_{oc}$  rises from 439.3 to 696.4 mV with the increasing carrier concentration of CISE from 10<sup>14</sup> to 10<sup>18</sup> cm<sup>-3</sup>). The built-in electric field of solar cells improves with increasing carrier concentration of the CISE absorber layer, enhancing the  $V_{oc}$  value and then PCE of CISE [1, 6, 13–15]. The  $J_{sc}$  and FF parameters remain constant until the carrier concentration of 5×10<sup>16</sup> cm<sup>-3</sup> and reach the maximum PCE of 22.23%. At higher carrier concentration values than 5×10<sup>16</sup> cm<sup>-3</sup>, the  $J_{sc}$  and FF parameters are reduced by enhancing the recombination of photogenerated charge carriers. This degradation of the CISE TFSC performance through recombination losses at higher carrier concentrations of CISE is also verified by inserted QE curve. The defects in the solar cell enhance with an increase in the carrier concentration of CISE, which will further increase the recombination rate of charge carriers and finally, negatively affect the solar cell performance. The solar cell parameters such as  $J_{sc}$ , FF, and PCE values reduce from 45.19 to 31.95 mAcm<sup>-2</sup>, 81.53 to 31.77%, and 22.23 to 7.07%, respectively when CISE carrier concentration varies from 5×10<sup>16</sup> to 10<sup>18</sup> cm<sup>-3</sup>. These results are in good agreement with the various literature [14–19].

Table 6.2 Parameters used in CISE TFSC at different carrier concentrations of CISE

Materials Parameters	CISE	CdS	ZnO	ZnO:Al
Thickness (nm)	5000	50	50	100
Bandgap (eV)	1.04	2.45	3.25	3.5
Donor density (cm <sup>-3</sup> )	0	1×10 <sup>17</sup>	1×10 <sup>17</sup>	1×10 <sup>17</sup>

Acceptor density (cm <sup>-3</sup> )	$1 \times 10^{14}$ - $1 \times 10^{18}$	0	0	0
--------------------------------------	---	---	---	---

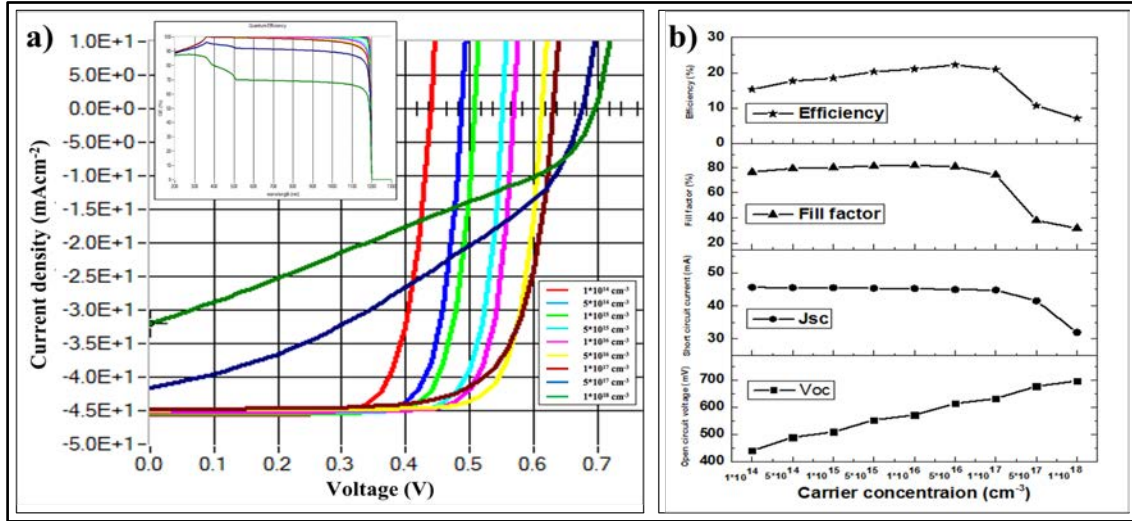


Fig. 6.2 Schematic of a) J-V curve of CISE TFSC inserted with QE curve, b) the solar cell parameter curve at different carrier concentration of CISE absorber layer

### 6.1.2 Influence of thicknesses and carrier concentrations of CdS for CISE TFSC

The primary function of the CdS buffer layer within the structure is to make the heterojunction and pass the photons to the absorber layer. Here, the device's performance is reviewed at a different thickness of CdS buffer layer varied from 20 nm to 100 nm (see Fig. 6.3). The other parameters are presented in Table 6.3. The PCE of CISE TFSC is slightly enhanced from 20.84 to 22.78% with a rise in the CdS thickness. The increment of device performance is mainly related to improving the CdS buffer layer's quality with an increase in the CdS thickness, which helps to reduce the defects and improve the solar cell performance [3, 16, 17]. But the CdS thickness greater than 100 nm may degrade the device's performance by absorbing photons in it. This absorption of photons in the CdS buffer layer will negatively impact the solar cell parameters. Besides, the series resistance of the CISE TFSC enhances at higher CdS thickness. The fill factor of the device is strongly affected by the series resistance. The shunt resistance of the device decreases at very thin CdS thin films (less than 30 nm) by providing an alternative path for generated charge carriers, which subsequently reduces the device performance [7]. Since this work studied up to 100 nm thickness of CdS, the effect of CdS thickness on the device performance is further explained in the simulation of experimental results. Several reported works of literature are closely consistent with these results [7, 8, 18–22].

Table 6.3 Parameters used in CISE TFSC at different CdS thicknesses

Materials	CISE	CdS	ZnO	ZnO:Al
Parameters				
Thickness (nm)	5000	20-100	50	100
Bandgap (eV)	1.04	2.45	3.25	3.5
Donor density (cm <sup>-3</sup> )	0	$1 \times 10^{17}$	$1 \times 10^{17}$	$1 \times 10^{17}$
Acceptor density (cm <sup>-3</sup> )	$5 \times 10^{16}$	0	0	0

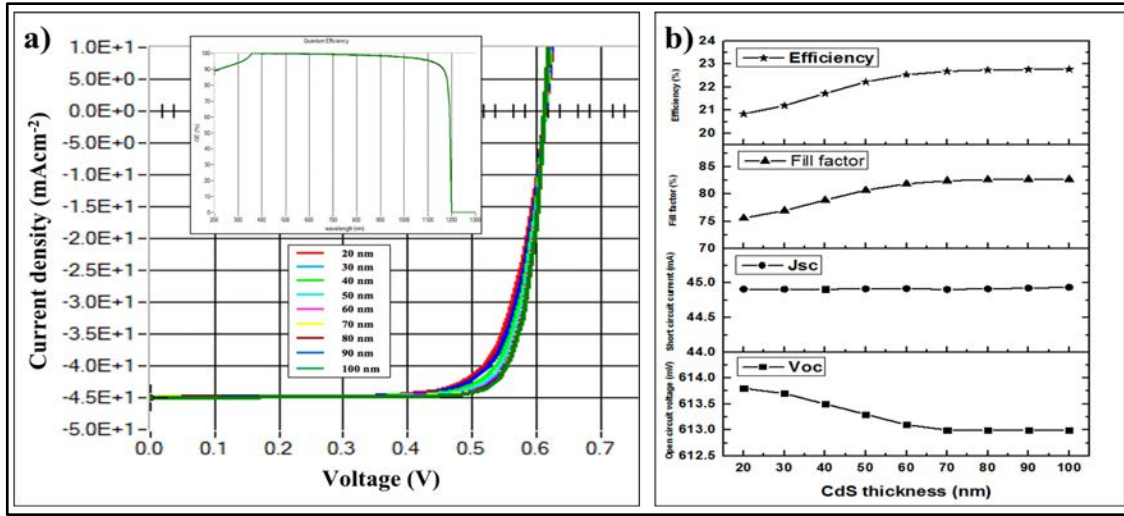


Fig. 6.3 Schematic of a) J-V curve of CISE TFSC inserted with QE curve, b) the solar cell parameter curve at different CdS thickness

Next, the simulation study is concentrated on the various carrier concentration of the CdS buffer layer (i.e., shallow uniform donor densities). The parameters used in CISE TFSC at various carrier concentrations of CdS are demonstrated in Table 6.4. Figure 6.4 shows the J-V curve of CISE TFSC inserted with the QE curve and the quantitative data of the solar cell parameters at different carrier concentrations of the CdS buffer layer. With an increase in carrier concentration of the CdS buffer layer, the collection of generated charge carriers may improve and consecutively favors the increase in the device performance. This increment in the collection of generated charge carriers is due to the enlargement of the space charge region into the absorber layer [5, 14]. When the carrier concentration of CdS increases from  $10^{14}$  to  $10^{19}$  cm<sup>-3</sup>, then the solar cell parameters are changed drastically. The  $V_{oc}$  and  $J_{sc}$  are slightly changed from 631.4 to 612.9 V and 44 to 45 mAcm<sup>-2</sup>, respectively. The parameter FF is enhanced from 35 to 82.67%, and consequently, PCE is increased from 9.83 to 22.81%. At higher carrier concentrations than  $10^{17}$  cm<sup>-3</sup>, the PCE of CISE TFSC became maximum

and remained unchanged. The lower device performance at a lower carrier concentration of CdS is due to the absorption of photons in CdS buffer layer instead of the absorber layer [23]. These results indicate that a higher carrier concentration of CdS than the carrier concentration of the absorber layer can provide better device performance. Similar results are found in previously reported literature [7, 14, 16, 18, 21].

Table 6.4 Parameters used in CISE TFSC at different carrier concentrations of CdS

Materials	CISE	CdS	ZnO	ZnO:Al
Thickness (nm)	5000	50	50	100
Bandgap (eV)	1.04	2.45	3.25	3.5
Donor density (cm <sup>-3</sup> )	0	$1 \times 10^{14}$ - $1 \times 10^{19}$	$1 \times 10^{17}$	$1 \times 10^{17}$
Acceptor density (cm <sup>-3</sup> )	$5 \times 10^{16}$	0	0	0

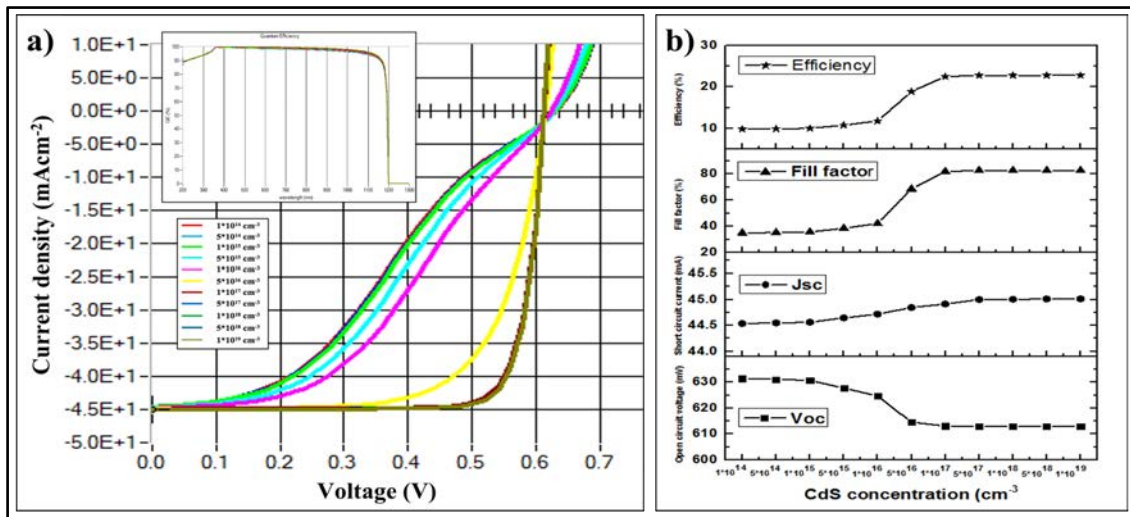


Fig. 6.4 Schematic of a) J-V curve of CISE TFSC inserted with QE curve, b) the solar cell parameter curve at different carrier concentration of CdS buffer layer

### 6.1.3 Analysis of thicknesses and carrier concentrations of ZnO for CISE TFSC

Afterward, the effect of thickness and carrier concentration of the ZnO window layer is analyzed (see Table 6.5). Fig. 6.5 displays the J-V curve of CISE TFSC inserted with the QE curve and the quantitative data of the solar cell parameters at different ZnO thicknesses varied from 20 to 100 nm. It is seen from the results that the solar cell parameters are not significantly affected by increasing the thickness of the ZnO window layer. Although there is no significant change in the cell performance parameters, a thick ZnO window layer can

negatively affect the device performance by absorbing the photons in it and by increasing the series resistance of the device [14, 17]. So, the thickness should be low with fewer defects for better device performance. The solar cell performance is also analyzed at various carrier concentrations of the ZnO window layer ranging from  $10^{14}$  to  $10^{20} \text{ cm}^{-3}$ , while other material parameters remain constant. Figure 6.6 presents the J-V curve of CISE TFSC inserted with the QE curve and the quantitative data of the solar cell parameters at different ZnO carrier concentrations. The results demonstrated that solar cell parameters are unchanged when the ZnO carrier concentration varies from lower to higher values. As the ZnO window layer is situated far from the p-n junction, the ZnO carrier concentration does not impact the space charge region width and then generated charge carriers. Although there is no effect of carrier concentrations of ZnO on the solar cell parameters, the low carrier concentrations of the ZnO window layer can absorb incident photons in it and reduce the solar cell parameters. Therefore, it is better to have a high carrier concentration of the ZnO in solar cells to improve the absorption of photons in the absorber layer.

Table 6.5 Parameters used in CISE TFSC at different thicknesses and carrier concentrations of ZnO

Materials	CISE	CdS	ZnO	ZnO:Al
Parameters				
Thickness (nm)	5000	50	20-100	100
Bandgap (eV)	1.04	2.45	3.25	3.5
Donor density ( $\text{cm}^{-3}$ )	0	$1 \times 10^{17}$	$1 \times 10^{14}$ - $1 \times 10^{20}$	$1 \times 10^{17}$
Acceptor density ( $\text{cm}^{-3}$ )	$5 \times 10^{16}$	0	0	0

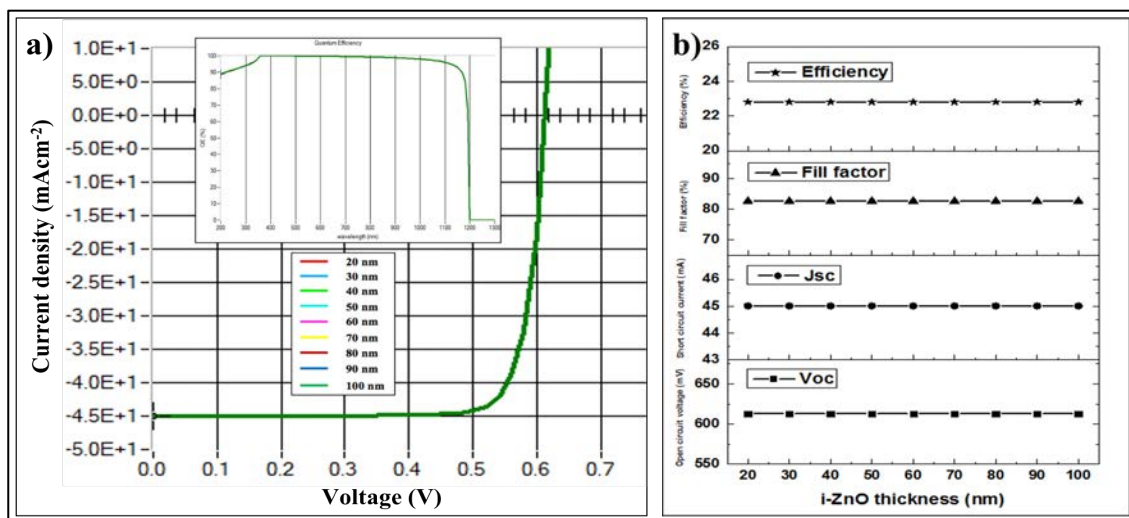


Fig. 6.5 Schematic of a) J-V curve of CISE TFSC inserted with QE curve, b) the solar cell parameter curve at different ZnO window layer thickness

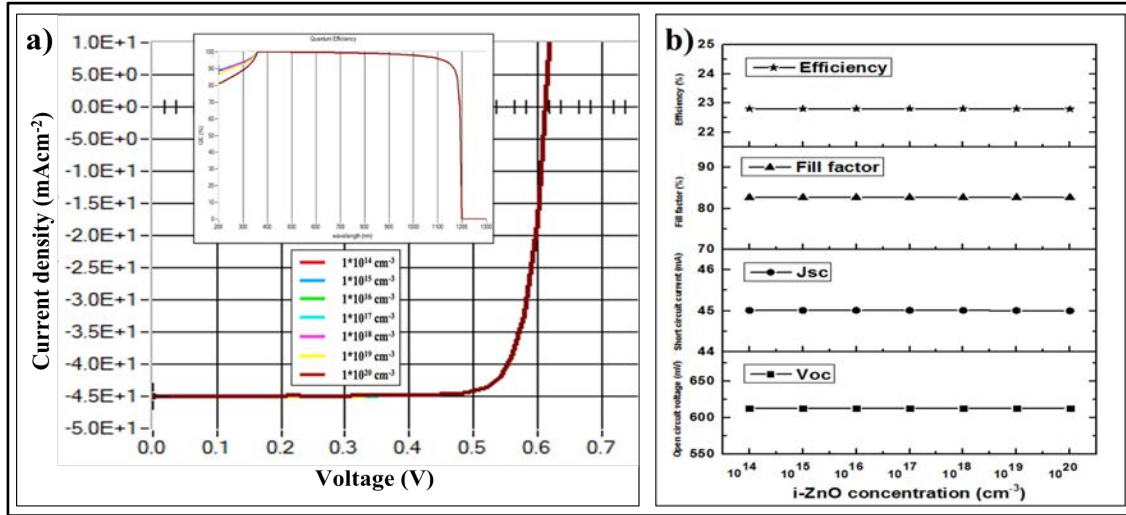


Fig. 6.6 Schematic of a) J-V curve of CISE TFSC inserted with QE curve, b) the solar cell parameter curve at different carrier concentration of ZnO window layer

#### 6.1.4 Effect of thicknesses and carrier concentrations of ZnO:Al for CISE TFSC

Finally, the solar cell performance is analyzed by varying the thicknesses and carrier concentrations of ZnO:Al TCO as presented in Table 6.6. Fig. 6.7 shows the J-V curve of CISE TFSC inserted with the QE curve and the quantitative data of the solar cell parameters at different ZnO:Al thicknesses. The thickness of the ZnO:Al TCO is graded from 50 to 350 nm. The  $J_{sc}$  value is slightly reduced with an increase in ZnO:Al thickness values while  $V_{oc}$  and FF are almost constant. The PCE of CISE TFSC is changed from 22.81 to 22.74 % when ZnO:Al thickness increases from 50 to 350 nm. The amount of the photons reaching the absorber layer can degrade at higher thickness of ZnO: Al by absorbing in it, leading to the loss of photons. The high ZnO:Al thickness may degrade the device performance by increasing the series resistance [17]. The lower thickness of 50 nm is preferred and considered the optimized conditions for CISE TFSC. Afterward, the effect of the ZnO:Al carrier concentration on the solar cell performance is also studied. Fig. 6.8 demonstrates the J-V curve of CISE TFSC inserted with the QE curve and the quantitative data of the solar cell parameters at different ZnO:Al carrier concentrations. The solar cell parameters have changed by a little margin with the increase in ZnO:Al carrier concentration. At lower carrier concentrations of ZnO:Al, more photons will be absorbed in ZnO:Al TCO layer and consecutively decreases the solar cell parameters. The PCE of CISE TFSC is enhanced from 22.78 to 22.81%, showing that increasing ZnO:Al carrier concentration may boost the collection of the generated charge carriers and improve the solar cell output parameters.



Table 6.6 Parameters used in CISE TFSC at different thicknesses and carrier concentrations of ZnO:Al

Materials	CISE	CdS	ZnO	ZnO:Al
Thickness (nm)	5000	50	50	50-350
Bandgap (eV)	1.04	2.45	3.25	3.5
Donor density (cm <sup>-3</sup> )	0	$1 \times 10^{17}$	$1 \times 10^{17}$	$1 \times 10^{14}$ - $1 \times 10^{21}$
Acceptor density (cm <sup>-3</sup> )	$5 \times 10^{16}$	0	0	0

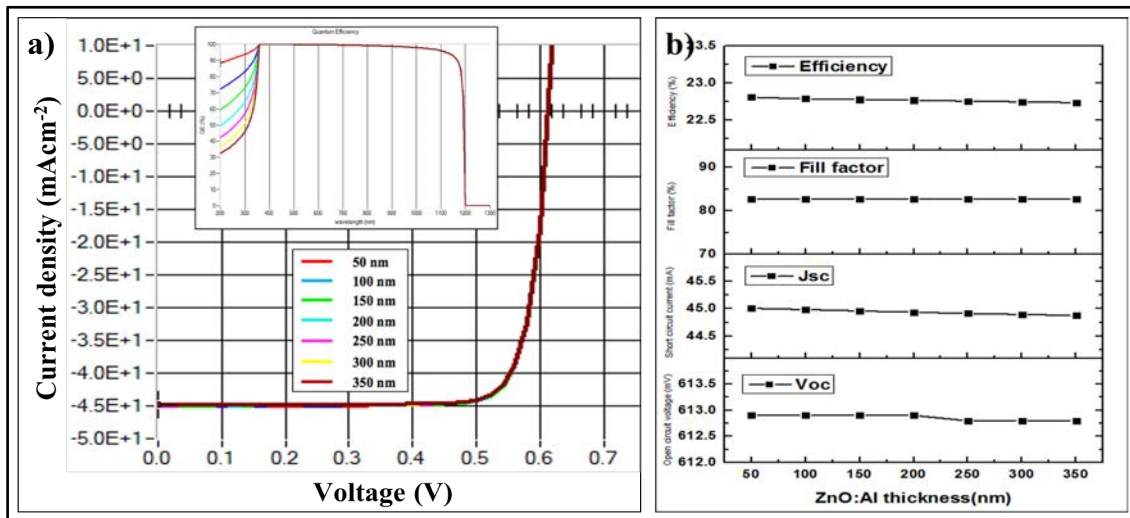


Fig. 6.7 Schematic of a) J-V curve of CISE TFSC inserted with QE curve, b) the solar cell parameter curve at different thickness of ZnO:Al TCO

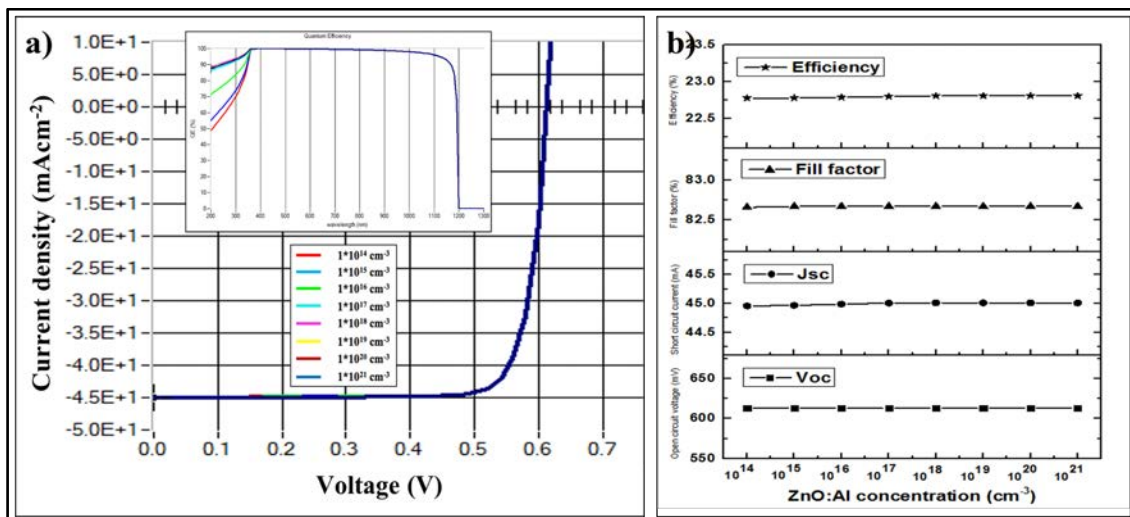


Fig. 6.8 Schematic of a) J-V curve of CISE TFSC inserted with QE curve, b) the solar cell parameter curve at different carrier concentration of ZnO:Al TCO

### 6.1.5 Optimized conditions for CISE TFSC

The material parameters, namely thickness and carrier concentration of each layer used in CISE TFSC, were analyzed and optimized for achieving high efficiency. Fig. 6.9 shows the J-V characteristics curve for high optimized efficiency CISE TFSC from simulation inserted with QE curve. The optimized thickness for CISE, CdS, ZnO, and ZnO:Al layers were 5  $\mu\text{m}$ , 50 nm, 50 nm, and 50 nm, respectively. Also, the optimum carrier concentration for CISE, CdS, ZnO, and ZnO:Al layers were respectively  $5 \times 10^{16}$ ,  $10^{17}$ ,  $10^{17}$ , and  $10^{17} \text{ cm}^{-3}$ . The optimized PCE of 22.81% from SCAPS software is comparable with the record efficiency (i.e., 22.9%) for CISE TFSC, showing that the optimal condition can get high device performance for CISE TFSC. The other optimized solar cell parameters such as  $V_{oc}$  of 612.9 mV,  $J_{sc}$  of  $45.01 \text{ mAcm}^{-2}$ , and FF of 82.67% are observed. The results obtained by varying the material parameters in SCAPS software are closely harmonious with the previously reported literature [1, 6, 11, 15, 24]. The slightly bending curve at two corners of the QE curve may be due to the front surface and back surface recombination [25]. Since the bandgap of CISE is 1.04 eV, the photons whose wavelength is smaller than 1200 nm have greater energy than the bandgap of CISE and can be absorbed in the CISE absorber layer.

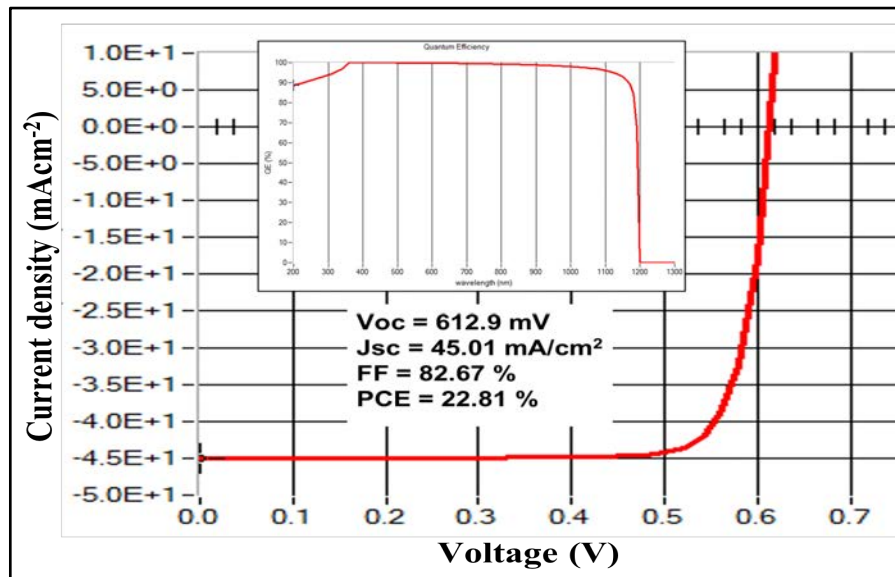


Fig. 6.9 Schematic of the J-V characteristics curve for optimized CISE TFSC inserted with QE curve

### 6.2 Study on CIGSe thin film solar cells



In this section, the thickness, bandgap (only for CIGSe) and carrier concentration of each layer employed in CIGSe TFSC are mainly graded and simulated. Similarly, the output solar cell parameters namely  $J_{sc}$ ,  $V_{oc}$ , FF, and PCE, for every graded condition are calculated from the SCAPS software. The CIGSe TFSC can optimize the best parameters to get high device performance by investigating these parameters. A brief detail of the effect of each layer's thickness and carrier concentration on the device performance is described following.

### 6.2.1 Effect of thicknesses, bandgaps, and carrier concentrations of CIGSe for CIGSe TFSC

Fig. 6.10 depicts the J-V curve of CIGSe TFSC (inserted with the QE curve) and the quantitative data of the solar cell parameters at different CIGSe thicknesses ranging from 1 to 10  $\mu\text{m}$ . The parameters of each layer used in CIGSe are presented in Table 6.7. It is seen that all the solar cell parameters (i.e.,  $V_{oc}$ ,  $J_{sc}$ , FF, and PCE) are increasing with an increase in CIGSe thickness. A large number of photons, along with photons having longer wavelengths, are absorbed in the absorber layer when the thickness of CIGSe rises. This absorption improves the generation of electron-hole pairs, which increases the collection of charge carriers and finally boosts the solar cell parameters [4, 7, 14, 15, 25]. The lower device performance at a low thickness of CIGSe may be due to the back-contact recombination. The back contact and depletion region are very close at low CIGSe thickness, enhancing the recombination of the generated charge carriers at the back contact. This outcome is also confirmed from the inserted QE curve that the CIGSe TFSC performance is dropped at lower CIGSe thickness by increasing back-contact recombination and decreasing the absorption limit of the CIGSe absorber layer. The solar cell performance at a higher thickness of CIGSe remains high and almost constant. As the thickness continues to be increasing a higher value, it may exceed the diffusion length of minority charge carriers. So, the absorption of sunlight outside of diffusion length can recombine before reaching the depletion region. When the CIGSe thickness increases from 1 to 10  $\mu\text{m}$ , the parameters, namely  $V_{oc}$ ,  $J_{sc}$ , FF, and PCE, are increased from 685.80 to 744.60 mV, 37.67 to 38.59  $\text{mAcm}^{-2}$ , 82.39 to 84.89%, and 21.29 to 24.39%, respectively. These results are consistent with various works of literature [12, 21, 25–28].

Table 6.7 Parameters used in CIGSe TFSC at different CIGSe thicknesses

Materials Parameters	CIGSe	CdS	ZnO	ZnO:Al
Thickness (nm)	1000-10000	50	50	100
Bandgap (eV)	1.2	2.45	3.25	3.5
Donor density (cm <sup>-3</sup> )	0	$1 \times 10^{17}$	$1 \times 10^{17}$	$1 \times 10^{17}$
Acceptor density (cm <sup>-3</sup> )	$1 \times 10^{16}$	0	0	0

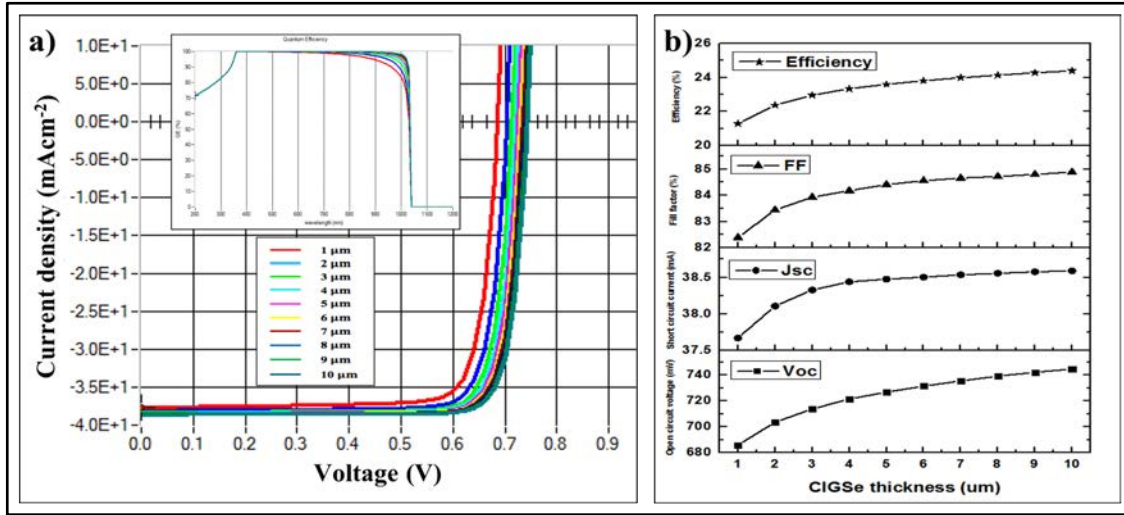


Fig. 6.10 Schematic of a) J-V curve of CIGSe TFSC inserted with QE curve, b) the solar cell parameter curve at different CIGSe thicknesses

Another property of the CIGSe absorber layer that can influence the device's performance is its bandgap. Due to the flexible bandgap of the CIGSe, the suitable bandgap can vary to obtain high device performance. The bandgap of CIGSe can be tuned depending on the gallium content in the film, where the CIGSe bandgap increases with the rise in gallium content. In this study, the bandgap of the CIGSe is varied from 1.0 eV to 1.7 eV for the optimization process while other parameters are kept constant (see Table 6.8). The J-V curve and the quantitative data of the solar cell parameters at different CIGSe bandgaps are shown in Fig. 6.11. As expected, the  $J_{sc}$  is become high at a lower CIGSe bandgap, and then it is degraded steadily with an increase in the CIGSe bandgap. The absorption of photons in the absorber layer at high CIGSe bandgap diminishes because only photons with higher energies than bandgap are absorbed [29, 30]. This result is also proved from the inserted QE curve that the absorption of photons having longer wavelength reduces with a rise in the CIGSe bandgap. On the other hand, the  $V_{oc}$  is enhanced when the CIGSe bandgap increases because  $V_{oc}$  directly relates to the bandgap (i.e., the maximum  $V_{oc}$  can be the ratio of bandgap and charge of the carriers). The  $J_{sc}$  value is degraded from 48.02 mAcm<sup>-2</sup> at 1.0 eV to 22.25

$\text{mAcm}^{-2}$  at 1.7 eV. And the  $V_{oc}$  value is increased from 532.50 to 1212.50 mV when the CIGSe bandgap increases from 1.0 to 1.7 eV. The PCE of CIGSe TFSC gradually increases with the CIGSe bandgap and found the optimum value at 1.4 eV. The PCE started to drop after the 1.4 eV bandgap of CIGSe, mainly reducing the  $J_{sc}$  value at a higher CIGSe bandgap. The PCE initially increases from 20.60 (for a bandgap of 1.0 eV) to 25.76% (for a bandgap of 1.4 eV) and then drops to 24.03% (for a bandgap of 1.7 eV). These outcomes are in good agreement with previously published results [4, 28, 29, 31, 32].

Table 6.8 Parameters used in CIGSe TFSC at different bandgaps of CIGSe

Materials Parameters	CIGSe	CdS	ZnO	ZnO:Al
Thickness (nm)	5000	50	50	100
Bandgap (eV)	1.0-1.7	2.45	3.25	3.5
Donor density ( $\text{cm}^{-3}$ )	0	$1 \times 10^{17}$	$1 \times 10^{17}$	$1 \times 10^{17}$
Acceptor density ( $\text{cm}^{-3}$ )	$1 \times 10^{16}$	0	0	0

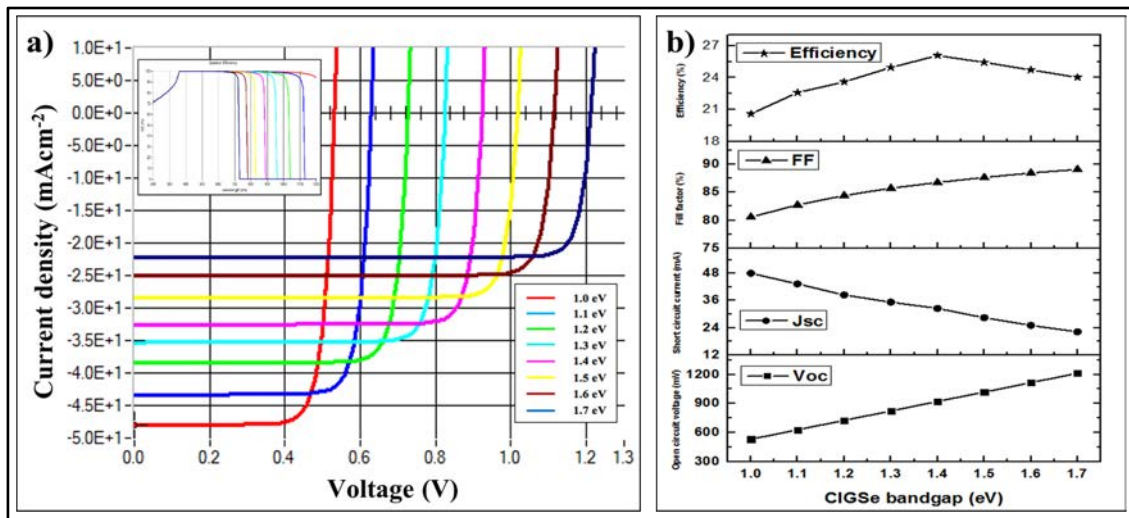


Fig. 6.11 Schematic of a) J-V curve of CIGSe TFSC inserted with QE curve, b) the solar cell parameter curve at different CIGSe bandgaps

Afterward, this study is concentrated on the various carrier concentrations of the CIGSe absorber layer ranging from  $1 \times 10^{14}$  to  $5 \times 10^{17} \text{ cm}^{-3}$ , while other parameters are kept constant (see Table 6.9). Understanding the effect of the carrier concentration on the device performance will be beneficial and crucial for optimizing the material parameters. Fig. 6.12 displays the J-V curve of the CIGSe TFSC inserted with the QE curve and the quantitative data of the solar cell output parameters at different CIGSe carrier concentrations. The carrier

concentration of the absorber layer primarily influences the electric field intensity and width of the space charge region. The semiconductive properties degrade and change into the metallic conductive state at higher carrier concentrations of the absorber layer [34], which elevates the recombination centers in the film and consequently affects the device performance. The carrier concentration of CIGSe leads to an increase the  $V_{oc}$ , which is increased from 792.20 to 1028.90 mV. This increment is due to the improvement of the built-in electric field with increasing carrier concentrations [7, 13, 33, 34]. The  $J_{sc}$  is slightly changed from 32.94 to 31.67  $\text{mAcm}^{-2}$  when the carrier concentration varies from  $1 \times 10^{14}$  to  $5 \times 10^{17} \text{ cm}^{-3}$ . The PCE of CIGSe initially enhanced and reached the maximum value of 26.82% at CIGSe carrier concentration of  $5 \times 10^{16} \text{ cm}^{-3}$  and then reduced to 15.42% (for carrier concentration of  $5 \times 10^{17} \text{ cm}^{-3}$ ). The recombination centers for the generated charge carriers enhance at higher carrier concentration, which is due to the deteriorating semiconducting properties of the CIGSe semiconductor [34]. The generated charge carriers undergo Coulombic interactions, which improves the recombination process. Hence, the solar cell performance degrades at higher carrier concentrations of the absorber layer. Similar trends in the results are found in different reported literature [14, 16, 17, 19, 21, 27, 33, 34].

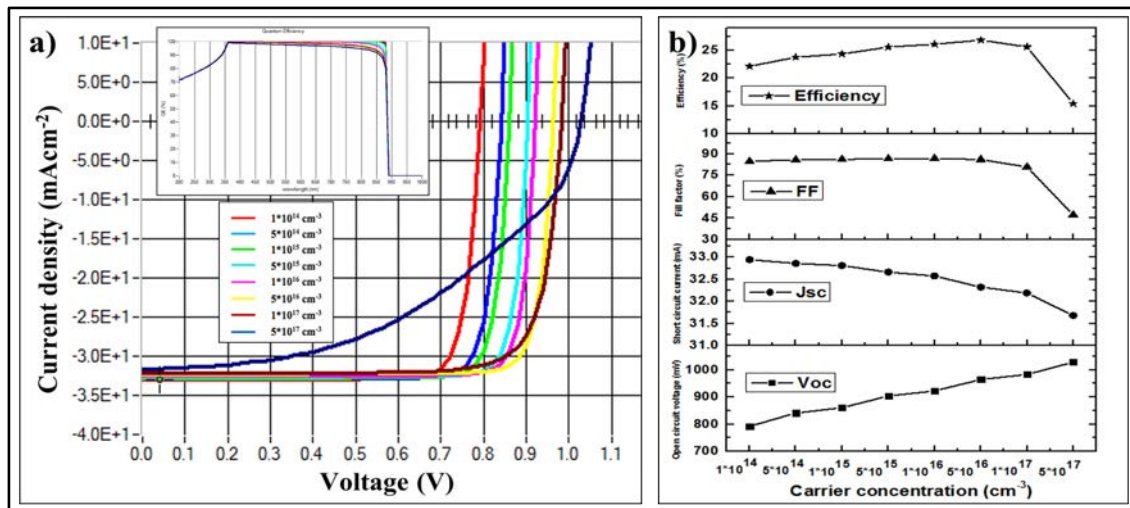


Fig. 6.12 Schematic of a) J-V curve of CIGSe TFSC inserted with QE curve, b) the solar cell parameter curve at different CIGSe carrier concentrations

Table 6.9 Parameters used in CIGSe TFSC at different carrier concentrations of CIGSe

Materials	CIGSe	CdS	ZnO	ZnO:Al
Parameters				
Thickness (nm)	5000	50	50	100

Bandgap (eV)	1.4	2.45	3.25	3.5
Donor density (cm <sup>-3</sup> )	0	1×10 <sup>17</sup>	1×10 <sup>17</sup>	1×10 <sup>17</sup>
Acceptor density (cm <sup>-3</sup> )	1×10 <sup>14</sup> -5×10 <sup>17</sup>	0	0	0

### 6.2.2 Analysis of thicknesses and carrier concentrations of CdS for CIGSe TFSC

Here, the effect of CdS thickness on the CIGSe solar cell performance is studied. Table 6.10 presents the parameters used in CIGSe TFSC at various CdS thicknesses. Fig. 6.13 shows the J-V curve (inserted with the QE curve) and the quantitative data of the solar cell parameters at different CdS thicknesses ranging from 20 to 100 nm. It is found that the PCE of CIGSe increased by a little margin from 25.82% (for 20 nm) to 27.26% (for 100 nm). The quality of CdS thin films improves with an increase in CdS thickness. However, the device performance may reduce at a very high thickness (greater than 100 nm) of the CdS buffer layer because most of the incident photons absorb in the CdS that can decrease the absorption of photons on the CIGSe absorber [24, 25]. The series resistance also increases at higher CdS thickness, which affects the FF of the solar cell. As a result, the device performance will reduce by recombining charge carriers in the CdS buffer layer. At a very low thickness of CdS (less than 30 nm), there will be many defects in the CdS buffer layer. These defects provide an alternative path for the generated charge carriers and reduce the solar cell parameters [7, 24]. The low thickness of CdS with fewer defects is suitable in solar cells. Since this work studied up to 100 nm thickness of CdS, the influence of CdS thickness on the solar cell parameters is described more in the simulation of experimental results. These results are consistent with the various literature [8, 14, 16, 20, 21, 35].

Table 6.10 Parameters used in CIGSe TFSC at different CdS thicknesses

Materials Parameters	CIGSe	CdS	ZnO	ZnO:Al
Thickness (nm)	5000	20-100	50	100
Bandgap (eV)	1.4	2.45	3.25	3.5
Donor density (cm <sup>-3</sup> )	0	1×10 <sup>17</sup>	1×10 <sup>17</sup>	1×10 <sup>17</sup>
Acceptor density (cm <sup>-3</sup> )	5×10 <sup>16</sup>	0	0	0

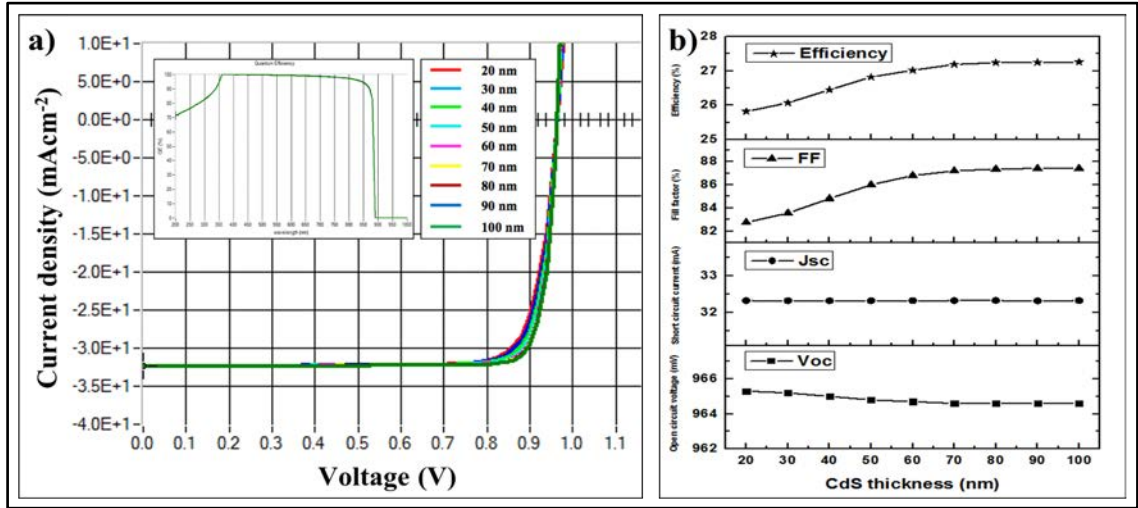


Fig. 6.13 Schematic of a) J-V curve of CIGSe TFSC inserted with QE curve, b) the solar cell parameter curve at different CdS thicknesses

Afterward, the effect of carrier concentrations of the CdS buffer layer on the device performance is investigated. The parameters used in CIGSe TFSC are shown in Table 6.11. The J-V curve of CIGSe TFSC inserted with the QE curve and the quantitative data of the solar cell parameters at different CdS carrier concentrations are displayed in Fig. 6.14. The carrier concentration of CdS is increased from  $10^{13}$  to  $10^{20}$  cm<sup>-3</sup>. All the solar cell parameters except  $V_{oc}$  are increased significantly with a rise in CdS carrier concentration. When carrier concentration of CdS varied from  $10^{13}$  to  $10^{20}$  cm<sup>-3</sup>, the  $J_{sc}$ , FF and PCE of CIGSe TFSC are enhanced from 7.57 to 32.40 mAcm<sup>-2</sup>, 67.49 to 87.35%, and 5.68 to 27.30%, respectively. The parameter  $V_{oc}$  is slightly changed from 1110.20 to 964.5 mV. As mentioned earlier, the collection of generated charge carriers may increase with a rise in carrier concentration of the CdS buffer layer. The space charge region will extend wider in the CIGSe absorber layer and can improve the collection of generated charge carriers and consecutively, enhances the device performance [5, 14]. The PCE of CIGSe TFSC is increased drastically (i.e., from 15.88 to 27.28%) when the carrier concentration increases from  $10^{16}$  to  $10^{17}$  cm<sup>-3</sup>, showing that the higher (or equal) carrier concentration of CdS compared to the carrier concentration of CIGSe absorber layer can increase the device performance. But the device performance can decrease at a lower carrier concentration of CdS by absorbing incident photons in CdS buffer layer rather than absorber layer [23]. From the QE curve, device performance reduction is due to recombination losses at low CdS carrier concentration. These outcomes are similar to several reported works of literature [7, 14, 16, 19, 21, 35].

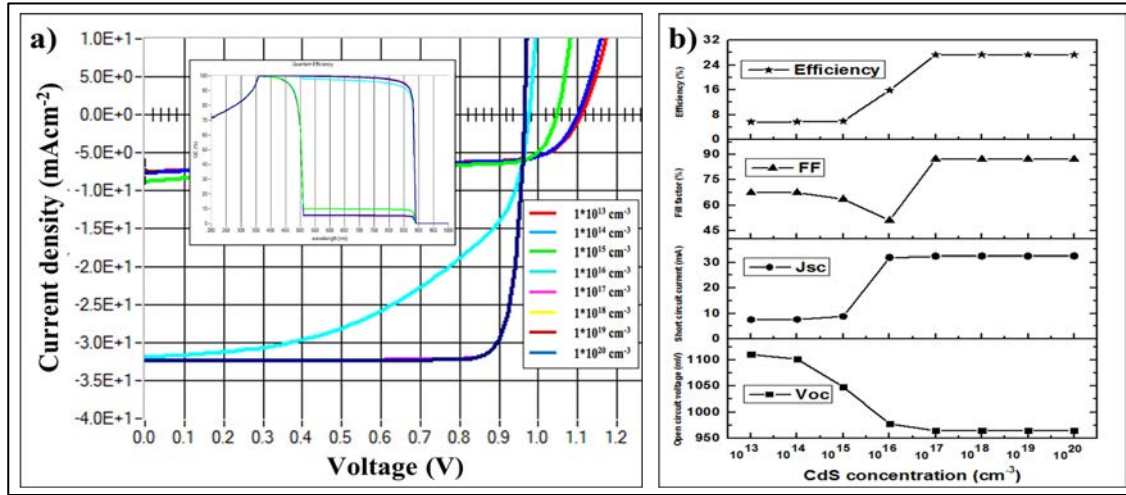


Fig. 6.14 Schematic of a) J-V curve of CIGSe TFSC inserted with QE curve, b) the solar cell parameter curve at different CdS carrier concentrations

Table 6.11 Parameters used in CIGSe TFSC at different carrier concentrations of CdS

Materials	CIGSe	CdS	ZnO	ZnO:Al
Thickness (nm)	5000	50	50	100
Bandgap (eV)	1.4	2.45	3.25	3.5
Donor density ( $\text{cm}^{-3}$ )	0	$1 \times 10^{13}$ - $1 \times 10^{20}$	$1 \times 10^{17}$	$1 \times 10^{17}$
Acceptor density ( $\text{cm}^{-3}$ )	$5 \times 10^{16}$	0	0	0

### 6.2.3 Influence of thicknesses and carrier concentrations of ZnO for CIGSe TFSC

After simulating the CIGSe absorber and CdS buffer layers, the effect of the various thicknesses and carrier concentrations of the ZnO window layer on the device performance is studied (see Table 6.12). Fig. 6.15 exhibits the J-V curve of CIGSe TFSC inserted with the QE curve and the quantitative data of the solar cell parameters at different ZnO thicknesses ranging from 20 to 80 nm. It is noticed from the results that the solar cell parameters are remained constant with an increase in the ZnO thickness. This outcome might be due to its high bandgap compared with the CdS buffer and CIGSe absorber layers, showing no effect on the generation and collection of charge carriers. But a very thick ZnO can absorb many photons, preventing the photons from reaching the absorber that can reduce the parameter  $J_{sc}$  and then minimize the device performance [14, 17]. Moreover, the series resistance of the solar cell also increases with an increase in the thickness of ZnO. At a very low thickness of ZnO (less than 30 nm), the shunt resistance of the device reduces by



providing an alternative path for generated charge carriers. Therefore, a low thickness of ZnO with fewer defects will be preferred for better device performance. Next, the simulation study was focused on the carrier concentrations of the ZnO. The ZnO carrier concentration is graded from  $10^{13}$  to  $10^{20} \text{ cm}^{-3}$  while other material parameters are kept constant (see Table 6.12). The J-V curve of CIGSe TFSC inserted with the QE curve and the quantitative data of the solar cell parameters at different ZnO carrier concentrations are presented in Fig. 6.16. It is found that the device performance remains constant when ZnO carrier concentration rises. But the low carrier concentrations of the ZnO window layer can absorb incident photons in it and can reduce the value of parameter  $J_{sc}$ . Hence, the high carrier concentration of the ZnO in solar cells is required to improve the absorption of photons in the absorber layer and then increase the PCE of solar cells.

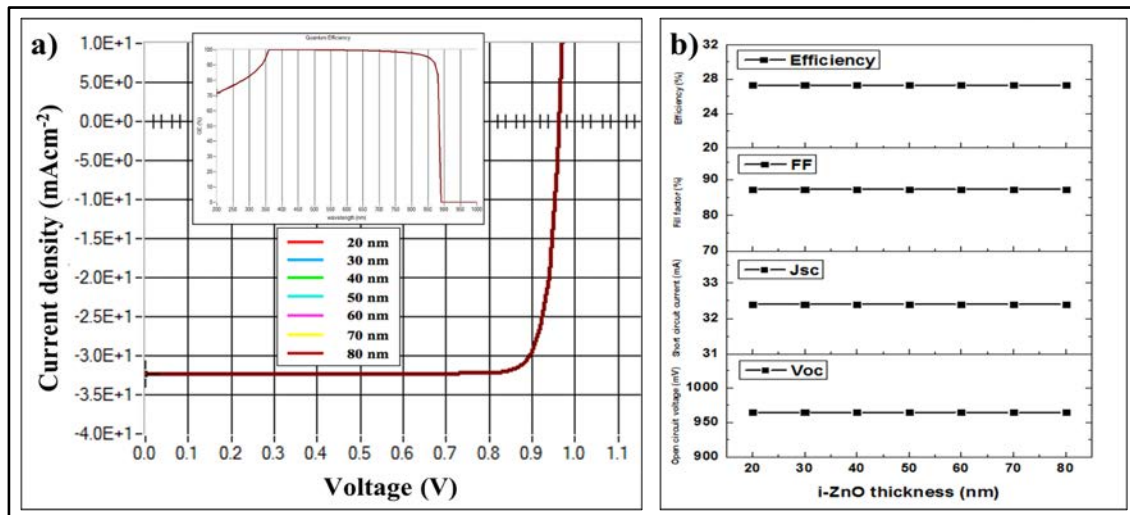


Fig. 6.15 Schematic of a) J-V curve of CIGSe TFSC inserted with QE curve, b) the solar cell parameter curve at different ZnO thicknesses

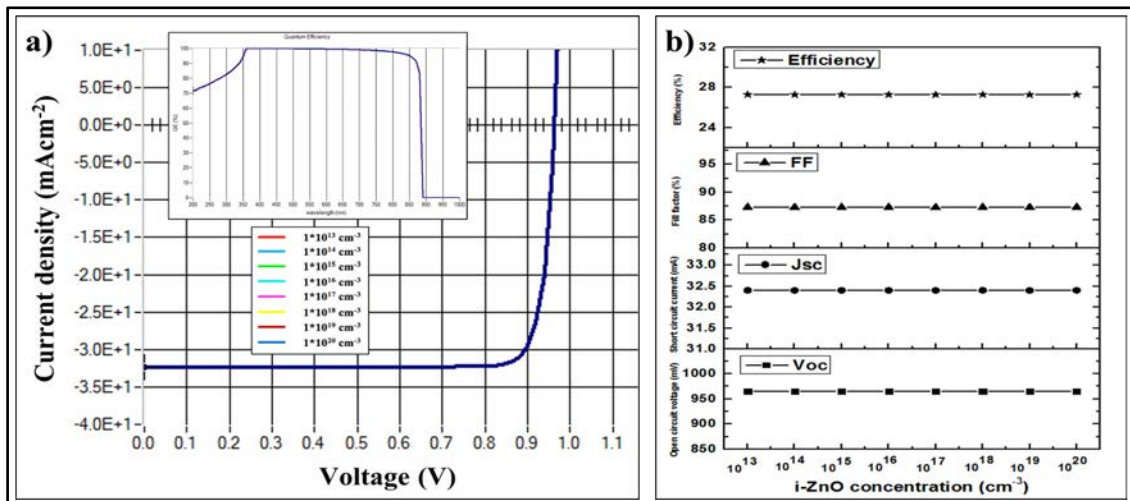




Fig. 6.16 Schematic of a) J-V curve of CIGSe TFSC inserted with QE curve, b) the solar cell parameter curve at different ZnO carrier concentrations

Table 6.12 Parameters used in CIGSe TFSC at different thicknesses and carrier concentrations of ZnO

Materials Parameters	CIGSe	CdS	ZnO	ZnO:Al
Thickness (nm)	5000	50	20-80	100
Bandgap (eV)	1.4	2.45	3.25	3.5
Donor density (cm <sup>-3</sup> )	0	$1 \times 10^{17}$	$1 \times 10^{13}$ - $1 \times 10^{20}$	$1 \times 10^{17}$
Acceptor density (cm <sup>-3</sup> )	$5 \times 10^{16}$	0	0	0

#### 6.2.4 Effect of thicknesses and carrier concentrations of ZnO:Al for CIGSe TFSC

This section analyzes solar cell performance at various thicknesses and carrier concentrations of ZnO:Al TCO. The parameters used in the SCAPS software for CIGSe TFSC are demonstrated in Table 6.13. The J-V curve of CIGSe TFSC inserted with the QE curve and the quantitative data of the solar cell parameters at different ZnO:Al thicknesses are depicted in Fig. 6.17. First, the ZnO:Al TCO thickness is varied from 50 to 400 nm. The  $J_{sc}$  and PCE are slightly degraded with increased thickness of ZnO:Al while  $V_{oc}$  and FF remained unchanged. The PCE of CIGSe TFSC is changed from 27.32 to 27.19% when ZnO:Al thickness rises from 50 to 400 nm. The number of the photons reaching the absorber layer can reduce at higher ZnO:Al thickness by absorbing in it, leading to the loss of photons that can reduce the generation of electron-hole pairs. The series resistance of the device may also increase with a rise in ZnO:Al thickness that degrades the FF and the device performance [17]. Hence, the low ZnO:Al thickness with fewer defects is preferred in CIGSe TFSC. Finally, the CIGSe TFSC performance is simulated at different carrier concentrations of ZnO:Al TCO. Fig. 6.18 depicts the J-V curve of CIGSe TFSC inserted with the QE curve and the quantitative data of the solar cell parameters at various ZnO:Al carrier concentrations. The ZnO:Al carrier concentration is changed from  $10^{13}$  to  $10^{21}$  cm<sup>-3</sup>. The PCE of CIGSe TFSC is slightly changed from 27.26 to 27.32% once the carrier concentration of ZnO:Al is varied from  $10^{13}$  to  $10^{21}$  cm<sup>-3</sup>. At a lower carrier concentration of ZnO:Al, the incident photons can be absorbed in ZnO:Al layer rather than the absorber layer and decrease the collection of generated charge carriers. Therefore, higher carrier concentrations of ZnO:Al is suitable in the CIGSe TFSC to obtain high device performance.

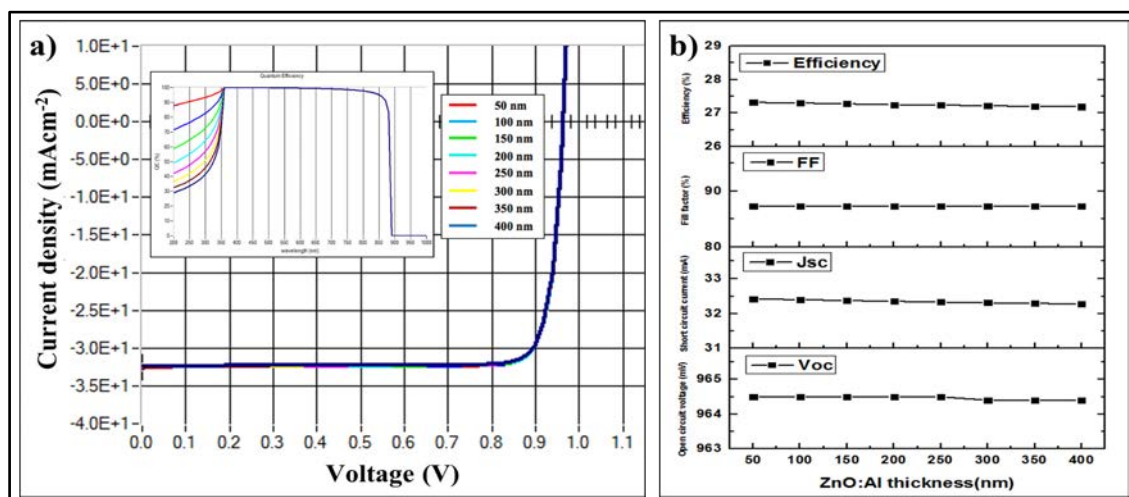


Fig. 6.17 Schematic of a) J-V curve of CIGSe TFSC inserted with QE curve, b) the solar cell parameter curve at different ZnO:Al thicknesses

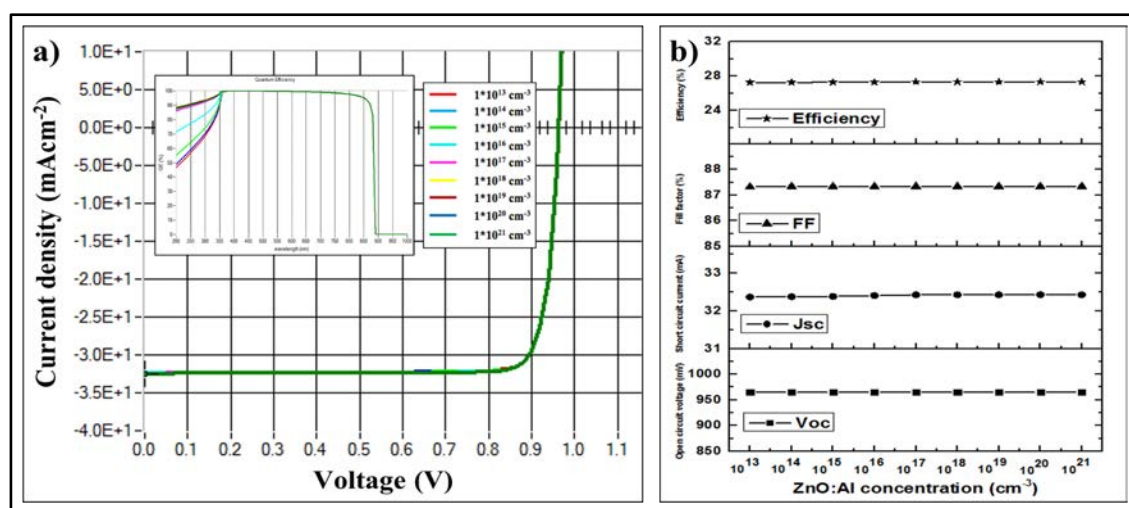


Fig. 6.18 Schematic of a) J-V curve of CIGSe TFSC inserted with QE curve, b) the solar cell parameter curve at different ZnO:Al carrier concentrations

Table 6.13 Parameters used in CIGSe TFSC at different thicknesses and carrier concentrations of ZnO:Al

Materials	CIGSe	CdS	ZnO	ZnO:Al
Thickness (nm)	1000-10000	20-100	20-80	50-400
Bandgap (eV)	1.0-1.7	2.45	3.25	3.5
Donor density (cm <sup>-3</sup> )	0	$1 \times 10^{13}$ - $1 \times 10^{20}$	$1 \times 10^{13}$ - $1 \times 10^{20}$	$1 \times 10^{13}$ - $1 \times 10^{21}$
Acceptor density (cm <sup>-3</sup> )	$1 \times 10^{14}$ - $5 \times 10^{17}$	0	0	0

## 6.2.5 Optimized conditions for CIGSe TFSC

The thickness and carrier concentration of each layer used in the CIGSe TFSC is simulated and optimized to reduce the material quantity as little as possible and get high CIGSe TFSC performance. The J-V characteristics curve for optimized CIGSe TFSC from SCAPS software inserted with QE curve is displayed in Fig. 6.19. The thickness of 5  $\mu\text{m}$  for CIGSe, 50 nm for CdS, 50 nm for ZnO, and 50 nm for ZnO: Al was optimized. The optimum bandgap of the CIGSe for getting maximum device performance was 1.4 eV. Similarly, the optimized carrier concentrations of CIGSe, CdS, ZnO, and ZnO: Al were  $5 \times 10^{16}$ ,  $1 \times 10^{17}$ ,  $1 \times 10^{17}$ ,  $1 \times 10^{17} \text{ cm}^{-3}$ , respectively. Using those optimized parameters of each layer, the PCE of 27.32% is observed for CIGSe TFSC. The optimized PCE from this simulation is greater than the record PCE (i.e., 23.35%) for CIGSe TFSC, showing that the optimum condition can have the potential to get high device performance. The respective  $V_{oc}$ ,  $J_{sc}$ , and FF values for the optimized condition were 964.5 mV,  $32.42 \text{ mAcm}^{-2}$ , and 87.34%. The slightly bend QE curve at two corners is related to front surface and back surface recombination [25]. Since the optimized bandgap of CIGSe was 1.4 eV, the photons having wavelengths lower than 885nm can be absorbed in the CIGSe absorber layer, which is also confirmed by the QE results.

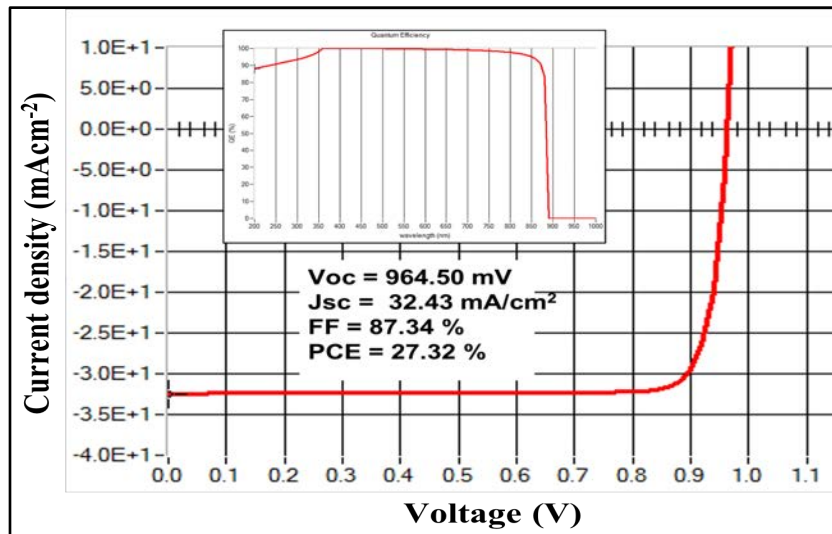


Fig. 6.19 Schematic of the J-V curve of optimized CIGSe TFSC inserted with QE curve

### 6.3 Study on CIGSe bilayer thin film solar cells

It is noticed that the production cost can be reduced by lessening the consumption of high-cost precursor materials or/and improving the device performance. A novel approach of using two absorber layers, namely CISE and CIGSe, is introduced in this investigation for

improving the device performance. The CIGSe absorber layer is coupled with the CdS buffer layer in the CIGSe bilayer TFSC and forms the CdS/CIGSe heterojunction. The CIGSe absorber layer is placed between the CIGSe absorber layer and back contact. Similarly, the material properties such as thicknesses and carrier concentrations of each layer used in CIGSe bilayer TFSC are simulated and optimized for achieving high device performance. The effect of material parameters on the CIGSe bilayer TFSC performance is briefly described below.

### 6.3.1 Influence of thicknesses and carrier concentrations of CIGSe for CIGSe bilayer TFSC

In this research, the effect of CIGSe thickness on the device performance is analyzed for optimizing the best condition. The thickness of the CIGSe is varied from 1 to 10  $\mu\text{m}$  while other parameters are kept constant (see Table 6.14). The J-V curve of CIGSe bilayer TFSC inserted with the QE curve and the quantitative data of the solar cell parameters at different CIGSe thicknesses are displayed in Fig. 6.20. All the solar cell parameters are remained constant with an increase in the CIGSe thickness. This outcome shows that the thickness of the absorber layer near to back contact does not affect the device's performance. However, the use of a high thickness of CIGSe can increase the device cost, which can prevent the CI(G)Se TFSC from commercialization. Hence, the low CIGSe thickness will be preferred in CIGSe bilayer TFSC.

Table 6.14 Parameters used in CIGSe bilayer TFSC at different CIGSe thicknesses

Materials Parameters	CIGSe	CIGSe	CdS	ZnO	ZnO:Al
Thickness (nm)	1000-9000	1000	50	50	100
Bandgap (eV)	1.04	1.2	2.45	3.25	3.5
Donor density ( $\text{cm}^{-3}$ )	0	0	$1 \times 10^{17}$	$1 \times 10^{17}$	$1 \times 10^{17}$
Acceptor density ( $\text{cm}^{-3}$ )	$1 \times 10^{16}$	$1 \times 10^{16}$	0	0	0

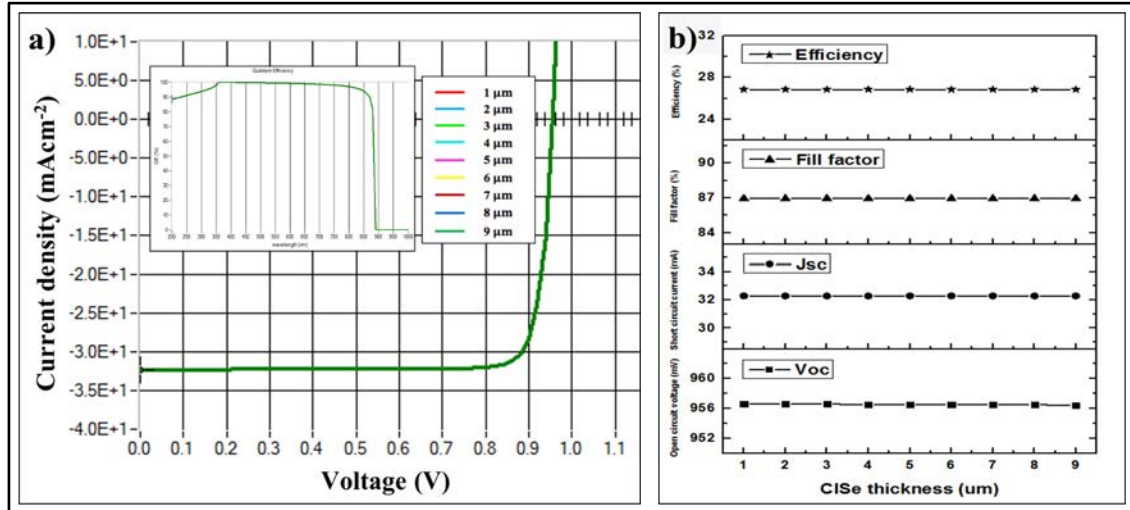


Fig. 6.20 Schematic of a) J-V curve of CIGSe bilayer TFSC inserted with QE curve, b) the solar cell parameter curve at different CIGSe thicknesses

Here, the simulation of the carrier concentration of CIGSe is carried out. The CIGSe carrier concentration is changed from  $10^{13}$  to  $10^{20} \text{ cm}^{-3}$ , while other parameters are kept constant (see Table 6.15). The J-V curve of CIGSe bilayer TFSC inserted with the QE curve and the quantitative data of the solar cell parameters at different carrier concentrations of CIGSe are displayed in Fig. 6.21. All the solar cell parameters except  $J_{sc}$  slightly improve with a rise in CIGSe carrier concentration. The  $V_{oc}$  depends directly on the magnitude of the carrier concentration [13]. The semiconductive properties degrade and change into the metallic conductive state at higher carrier concentrations of the absorber layer [34]. Since the CIGSe absorber layer is connected to the back-contact side, this metallic state at high carrier concentration can reduce the recombination centers and then can improve solar cell parameters. The PCE of the CIGSe bilayer TFSC changes from 26.26% (for  $10^{13} \text{ cm}^{-3}$ ) to 27.12% (for  $10^{20} \text{ cm}^{-3}$ ). The device performance is changed with a little margin after the CIGSe carrier concentration of  $10^{18} \text{ cm}^{-3}$ . It is inferred that using high CIGSe carrier concentration can improve the device's performance.

Table 6.15 Parameters used in CIGSe bilayer TFSC at different carrier concentrations of CIGSe

Materials	CIGSe	CIGSe	CdS	ZnO	ZnO:Al
Parameters					
Thickness (nm)	1000	1000	50	50	100
Bandgap (eV)	1.04	1.2	2.45	3.25	3.5
Donor density ( $\text{cm}^{-3}$ )	0	0	$1 \times 10^{17}$	$1 \times 10^{17}$	$1 \times 10^{17}$
Acceptor density ( $\text{cm}^{-3}$ )	$1 \times 10^{13}$ - $1 \times 10^{20}$	$1 \times 10^{16}$	0	0	0

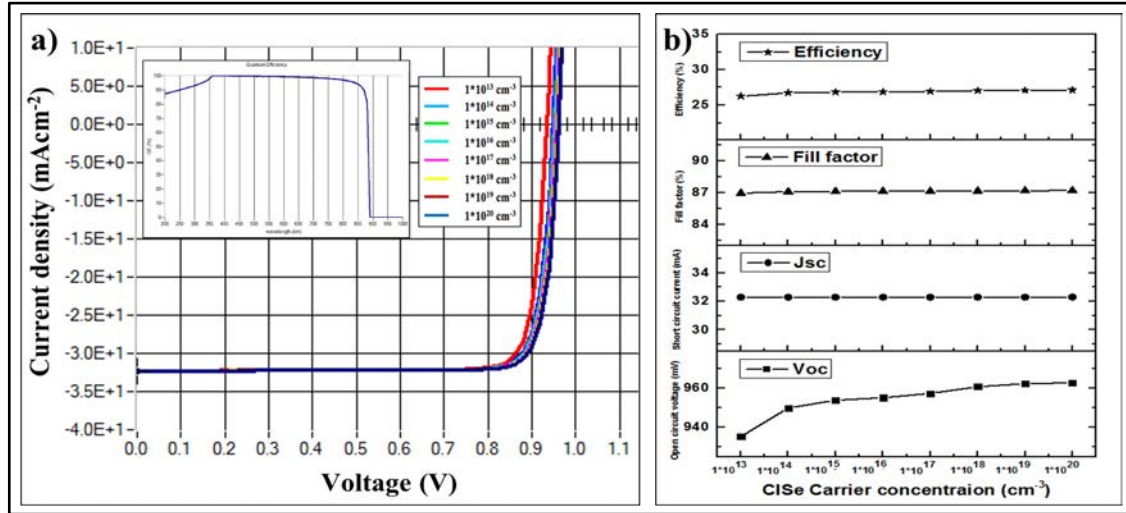


Fig. 6.21 Schematic of a) J-V curve of CIGSe bilayer TFSC inserted with QE curve, b) the solar cell parameter curve at different CIGSe carrier concentrations

### 6.3.2 Effect of thicknesses, bandgaps, and carrier concentrations of CIGSe for CIGSe bilayer TFSC

The second absorber layer used in the CIGSe bilayer TFSC is the CIGSe absorber layer placed between the CIGSe absorber layer and the CdS buffer layer. The p-type CIGSe and n-type CdS are sandwiched and form the p-n junction for CIGSe bilayer TFSC. As the thickness of CIGSe can relate to the device's performance and cost, it should be optimized. Here, the influence of the CIGSe thickness on the performance of the CIGSe bilayer TFSC is simulated. The CIGSe thickness is varied from 1 to 9  $\mu\text{m}$ , while other parameters kept constant (see Table 6.16). Fig. 6.22 shows the J-V curve and the quantitative data of the solar cell parameters for CIGSe bilayer TFSC at different CIGSe thicknesses. It is observed from the results that all the solar cell parameters (i.e.,  $V_{oc}$ ,  $J_{sc}$ , FF, and PCE) increased with a rise in CIGSe thickness. More photons along with photons having longer wavelengths are absorbed in high CIGSe thickness [12, 14, 37]. So, the generation of electron-hole pairs increases that improves the current collection of the solar cell and the device performance. Although device performance improves by absorbing extra photons at a higher thickness, it can raise the device cost and subsequently prevent the solar cell from commercialization. The solar cell parameters are reduced at very low CIGSe thickness due to the decrease in the absorption of photons in the absorber layer and the recombination of the generated charge carriers at back contact. Hence, the thickness of the CIGSe absorber layer should be properly optimized for the CIGSe bilayer TFSC. The solar cell parameters, namely  $V_{oc}$ ,  $J_{sc}$ , FF, and

PCE, are respectively changed from 911.90 to 976.60 mV, 29.15 to 32.64 mAc<sup>m-2</sup>, 84.56 to 87.61%, and 22.48 to 27.94% when the CIGSe thickness increases from 1 to 9  $\mu\text{m}$ . These results are in good agreement with various literature [4, 7, 12, 15, 20, 28].

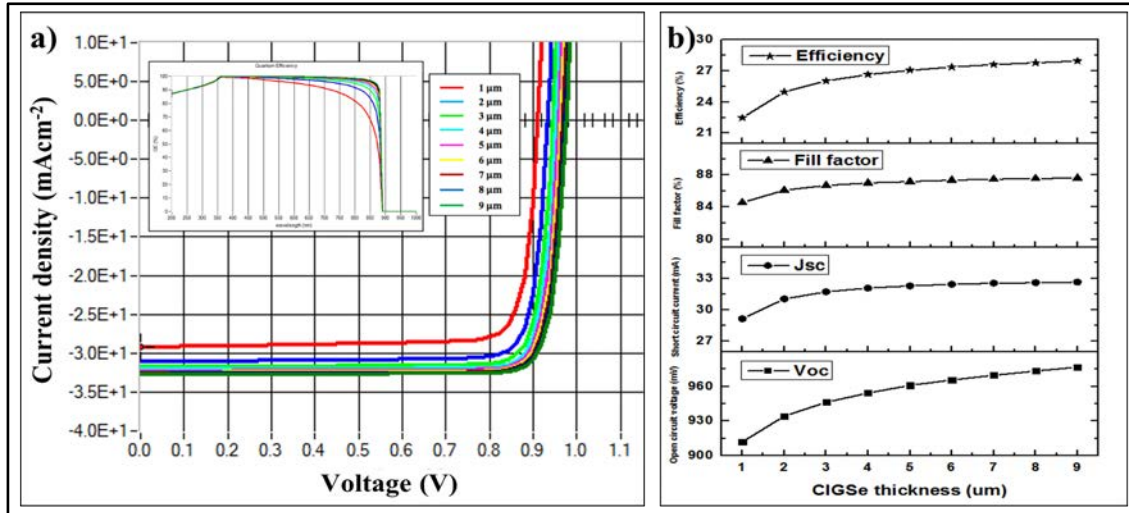


Fig. 6.22 Schematic of a) J-V curve of CIGSe bilayer TFSC inserted with QE curve, b) the solar cell parameter curve at different CIGSe thicknesses

Table 6.16 Parameters used in CIGSe bilayer TFSC at different CIGSe thicknesses

Materials	CiSe	CIGSe	CdS	ZnO	ZnO:Al
Thickness (nm)	1000	1000-9000	50	50	100
Bandgap (eV)	1.04	1.2	2.45	3.25	3.5
Donor density (cm <sup>-3</sup> )	0	0	$1 \times 10^{17}$	$1 \times 10^{17}$	$1 \times 10^{17}$
Acceptor density (cm <sup>-3</sup> )	$1 \times 10^{18}$	$1 \times 10^{16}$	0	0	0

The CIGSe bandgap is flexible depending on the gallium content in the film. The variation of solar cell parameters at different bandgaps of the CIGSe ranging from 1.1 to 1.7 eV is simulated in this section while other parameters are kept constant (see Table 6.17). Fig. 6.23 displays the J-V curve of CIGSe bilayer TFSC inserted with the QE curve and the quantitative data of the solar cell parameters at different CIGSe bandgaps. With an increase in the CIGSe bandgap, the absorption of photons on the absorber layer reduces and consequently drops the J<sub>sc</sub> value from 43.46 to 22.13 mAc<sup>m-2</sup> [30], [31]. On the contrary, the V<sub>oc</sub> directly correlates to the bandgap (i.e., the maximum V<sub>oc</sub> can be the ratio of bandgap and charge of the carriers) [4, 31], which is increased from 698.90 to 1073.40 mV with a rise in the CIGSe bandgap from 1.1 to 1.7 eV. The FF of CIGSe bilayer TFSC is also



increased at higher bandgap values of CIGSe. The PCE of CIGSe bilayer TFSC first increases and then reaches an optimum value of 27.98% at 1.4 eV of the CIGSe bandgap and then starts to fall (i.e., 21% of PCE at 1.7 eV). The lower value of PCE at the higher CIGSe bandgap is mainly due to the high reduction of the  $J_{sc}$  value. This result is also verified from the inserted QE curve that the absorption of longer wavelength photons decreases with a rise in the CIGSe bandgap. The variation of solar cell parameters at different CIGSe bandgaps is in good agreement with various literature [4, 21, 27, 29, 31, 32].

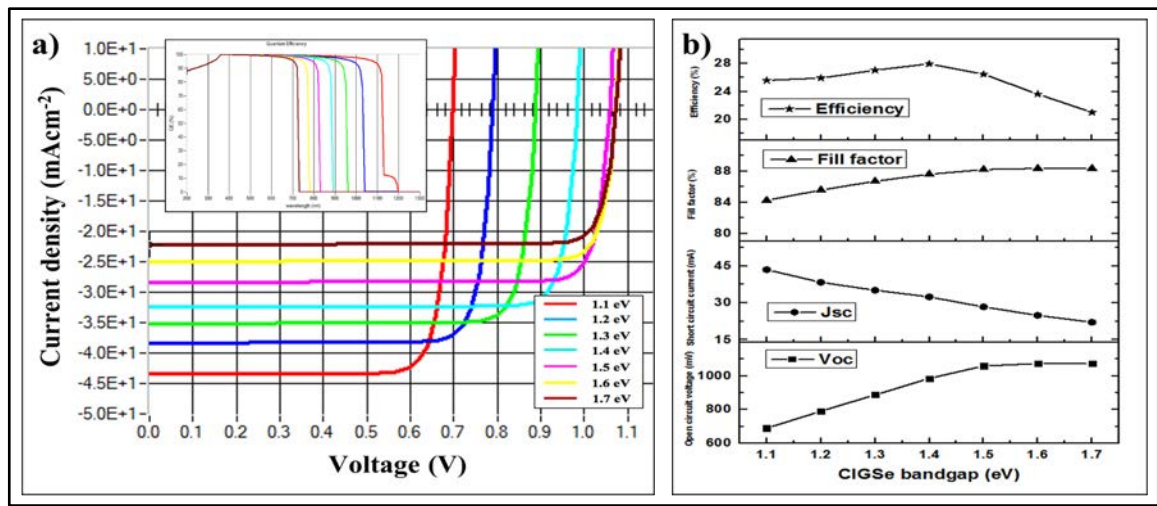


Fig. 6.23 Schematic of a) J-V curve of CIGSe bilayer TFSC inserted with QE curve, b) the solar cell parameter curve at different CIGSe bandgaps

Table 6.17 Parameters used in CIGSe bilayer TFSC at different bandgaps of CIGSe

Materials	CiSe	CIGSe	CdS	ZnO	ZnO:Al
Thickness (nm)	1000	5000	50	50	100
Bandgap (eV)	1.04	1.1-1.7	2.45	3.25	3.5
Donor density ( $\text{cm}^{-3}$ )	0	0	$1 \times 10^{17}$	$1 \times 10^{17}$	$1 \times 10^{17}$
Acceptor density ( $\text{cm}^{-3}$ )	$1 \times 10^{18}$	$1 \times 10^{16}$	0	0	0

Here, the influence of the CIGSe carrier concentration ranging from  $10^{13}$  to  $10^{20} \text{ cm}^{-3}$  on the solar cell parameters is simulated. Table 6.18 presents the parameters used in the SCAPS software for the CIGSe bilayer TFSC. Fig. 6.24 shows the J-V curve of CIGSe bilayer TFSC inserted with the QE curve and the quantitative data of the solar cell parameters at different carrier concentrations of the CIGSe absorber layer. The semiconductive properties weaken with an increase in the carrier concentration of the CIGSe. At higher CIGSe carrier concentration, the semiconductor may change into the metallic conductive state by losing its



semiconducting property [34], [38]. This metallic state promotes the recombination centers in the device, which reduces the device performance at higher CIGSe carrier concentrations. Increasing CIGSe carrier concentration from  $10^{13}$  to  $10^{20} \text{ cm}^{-3}$  enhances the  $V_{oc}$  from 683.10 to 1170.90 mV by improving the built-in electric field [13]. On the other hand, the  $J_{sc}$  is decreased from 41.43 to 11.86  $\text{mAcm}^{-2}$ . The width of the space charge region reduces with increasing CIGSe carrier concentration, which increases the recombination centers for the generated charge carriers [34]. So, the  $J_{sc}$  and FF are affected and reduced with a rise in CIGSe carrier concentration. The PCE of the CIGSe bilayer TFSC initially increased from 21.71 to 27.62% when the CIGSe carrier concentration changed from  $10^{13}$  to  $10^{17} \text{ cm}^{-3}$ . After that, PCE started to decrease and reach 8.83% at a CIGSe carrier concentration of  $10^{20} \text{ cm}^{-3}$ . This degradation of the device performance at higher CIGSe carrier concentration is mainly Coulombic interactions of charge carriers that enhance the recombination of generated charge carriers [7]. The QE result also confirms that the CIGSe bilayer TFSC performance degrades through recombination losses at a very high carrier concentration of CIGSe. These results are consistent with various published results [14, 27, 33–35].

Table 6.18 Parameters used in CIGSe bilayer TFSC at different carrier concentrations of CIGSe

Materials	CISE	CIGSe	CdS	ZnO	ZnO:Al
Parameters					
Thickness (nm)	1000	5000	50	50	100
Bandgap (eV)	1.04	1.4	2.45	3.25	3.5
Donor density ( $\text{cm}^{-3}$ )	0	0	$1 \times 10^{17}$	$1 \times 10^{17}$	$1 \times 10^{17}$
Acceptor density ( $\text{cm}^{-3}$ )	$1 \times 10^{18}$	$1 \times 10^{13}$ – $1 \times 10^{20}$	0	0	0

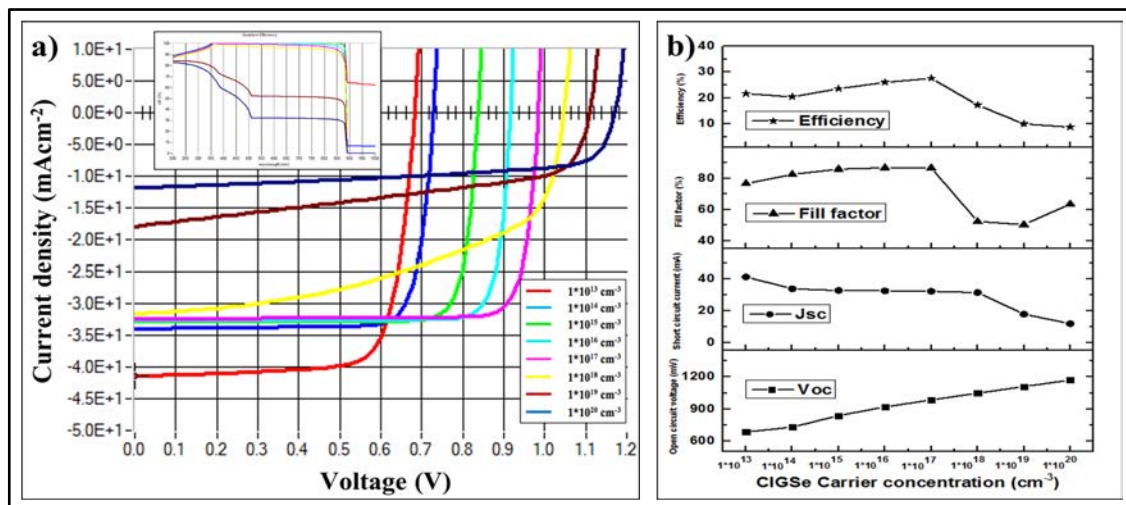


Fig. 6.24 Schematic of a) J-V curve of CIGSe bilayer TFSC inserted with QE curve, b) the solar cell parameter curve at different CIGSe carrier concentrations

### 6.3.3 Analysis of thicknesses, and carrier concentrations of CdS for CIGSe bilayer TFSC

Next, the performance of the CIGSe bilayer TFSC was simulated at different thicknesses of the CdS buffer layer. The parameters of each layer used in the CIGSe bilayer are displayed in Table 6.19. The J-V curve of CIGSe bilayer TFSC inserted with the QE curve and the quantitative data of the solar cell parameters at different CdS thicknesses ranging from 20 to 90 nm are presented in Fig. 6.25. It is found from the results that the solar cell parameters of the CIGSe bilayer TFSC are slightly changed with a rise in CdS thickness. The high performance at higher CdS thickness might be due to the improvements in the CdS material quality. The better quality of the CdS buffer layer can degrade the defects and then reduce the recombination centers for generated charge carriers. However, the device performance may reduce at a very high CdS thickness by absorbing photons and increasing the series resistance of the device [24, 25]. The shunt resistance of the solar cell decreases at very low CdS thickness by providing an alternative path for the generated charge carriers [24]. Therefore, the CdS thickness should be low with fewer defects for getting the high performance of solar cells. The effect of CdS thickness on the device performance of CI(G)Se TFSC is further explained in the simulation of experimental results. Various literature is consistent with these results [7, 9, 14, 21].

Table 6.19 Parameters used in CIGSe bilayer TFSC at different CdS thicknesses

Materials Parameters	CISE	CIGSe	CdS	ZnO	ZnO:Al
Thickness (nm)	1000	5000	20-90	50	100
Bandgap (eV)	1.04	1.4	2.45	3.25	3.5
Donor density (cm <sup>-3</sup> )	0	0	$1 \times 10^{17}$	$1 \times 10^{17}$	$1 \times 10^{17}$
Acceptor density (cm <sup>-3</sup> )	$1 \times 10^{18}$	$1 \times 10^{17}$	0	0	0

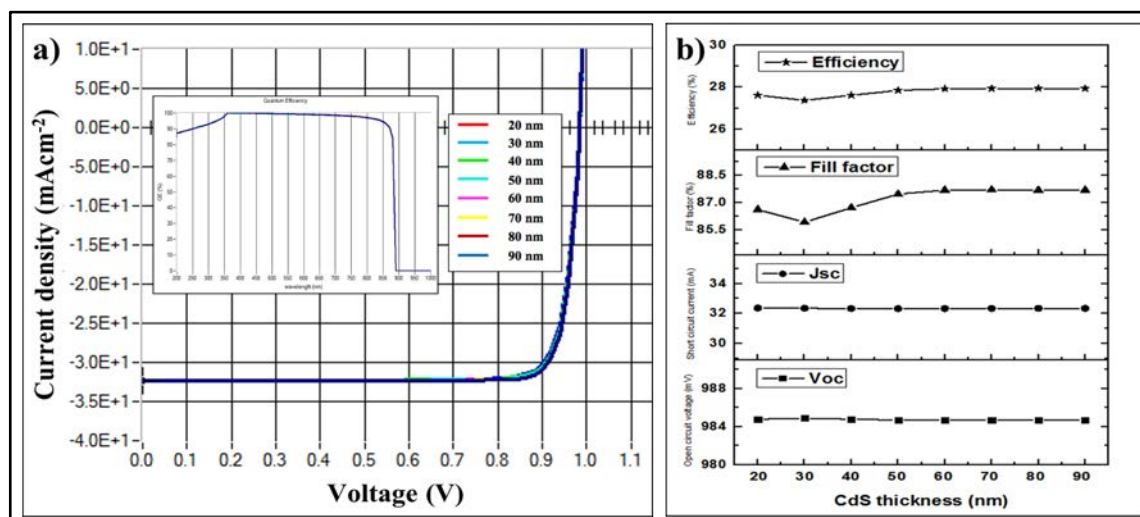


Fig. 6.25 Schematic of a) J-V curve of CIGSe bilayer TFSC inserted with QE curve, b) the solar cell parameter curve at different CdS thicknesses

This study is focused on the variation of the CIGSe bilayer TFSC at various carrier concentrations (i.e., shallow uniform donor densities) of the CdS buffer layer, while other parameters are kept constant (see Table 6.20). Fig. 6.26 displays the J-V curve of CIGSe bilayer TFSC inserted with the QE curve and the quantitative data of the solar cell parameters at different CdS carrier concentrations. When the CdS carrier concentration is varied from  $10^{13}$  to  $10^{20}$  cm<sup>-3</sup>, the PCE of the CIGSe bilayer TFSC is enhanced from 14.61 to 27.98% by mainly improving the FF value. The  $J_{sc}$  of CIGSe bilayer TFSC remains constant with an increase in the carrier concentration of CdS. The FF increases from 45.53 to 87.64%, showing that the series resistance of CIGSe bilayer TFSC decreases with an increase in the carrier concentration of CdS. The parameters  $V_{oc}$  is slightly changed from 996.50 to 984.60 mV as the carrier concentration of CdS increases. When the CdS carrier concentration rises, the space charge region extends wider in the absorber layer that can improve the absorption of photons in the absorber layer [5, 14]. At a lower carrier concentration of CdS, the incident photons can absorb in it and reduce the device performance [23]. Although  $V_{oc}$  decreases with a rise in CdS carrier concentration, the PCE is elevated by increasing the FF of the CIGSe bilayer TFSC. The device performance was changed enormously when the CdS carrier concentration rose from  $10^{16}$  to  $10^{17}$  cm<sup>-3</sup> (i.e., from 17.09 to 27.93%). This increment of PCE may be due to the greater carrier concentration of the CdS than the carrier concentration of the CIGSe absorber layer, which minimizes the recombination of generated charge carriers [7]. Therefore, high CdS carrier concentration will be preferred for improving the device performance [7, 14, 19].

Table 6.20 Parameters used in CIGSe bilayer TFSC at different carrier concentrations of CdS

Materials	CIGSe	CdS	ZnO	ZnO:Al
Thickness (nm)	1000	5000	50	100
Bandgap (eV)	1.04	1.4	2.45	3.25
Donor density (cm <sup>-3</sup> )	0	0	$1 \times 10^{13}$ - $1 \times 10^{20}$	$1 \times 10^{17}$
Acceptor density (cm <sup>-3</sup> )	$1 \times 10^{18}$	$1 \times 10^{17}$	0	0

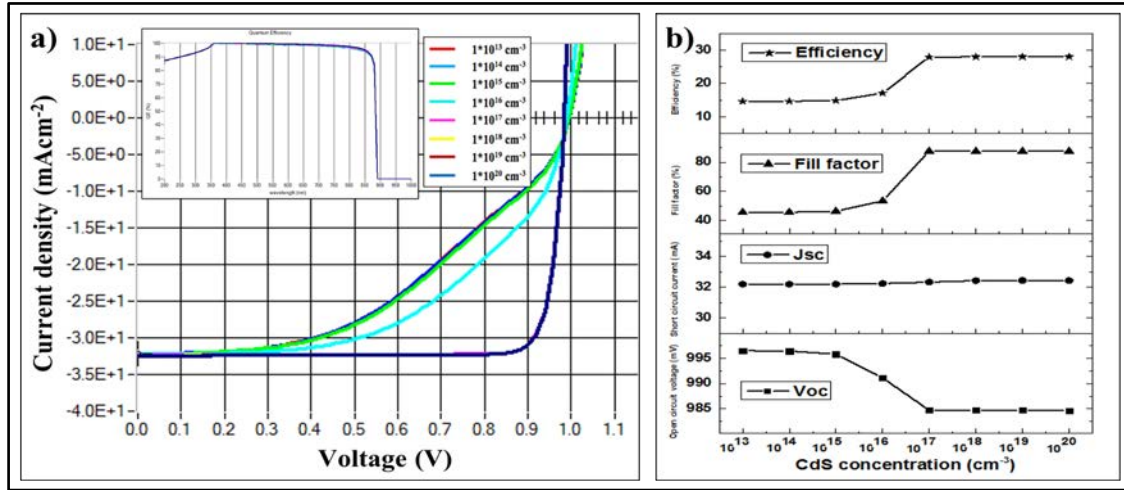


Fig. 6.26 Schematic of a) J-V curve of CIGSe bilayer TFSC inserted with QE curve, b) the solar cell parameter curve at different CdS concentrations

#### 6.3.4 Effect of thicknesses and carrier concentrations of ZnO for CIGSe bilayer TFSC

Next, the influence of different thicknesses and carrier concentrations of the ZnO window layer on the CIGSe bilayer TFSC performance is simulated. The parameters used in SCAPS software for CIGSe bilayer TFSC are presented in Table 6.21. Fig. 6.27 exhibits the J-V curve of CIGSe bilayer TFSC inserted with the QE curve and the quantitative data of the solar cell parameters at different ZnO thicknesses varying from 20 to 80 nm. It is found that the solar cell parameters of CIGSe bilayer TFSC are remained constant with an increase in the thickness of the ZnO. Although the solar cell parameters are not changing with the thickness of ZnO, the solar cell parameters may reduce at a higher ZnO thickness by absorbing incident photons in it and by increasing the series resistance of the device [14, 17]. At a very low ZnO thickness (less than 30 nm), the material contains more defects (i.e., pinholes) and provides an alternative path for generated charge carriers, and subsequently decreases the device performance. Therefore, a low thickness of ZnO with lower defects is

preferred in solar cells. The effect of the carrier concentrations of the ZnO on the CIGSe bilayer TFSC performance is then analyzed. Fig. 6.28 shows the J-V curve of the CIGSe bilayer TFSC inserted with the QE curve and the quantitative data of the solar cell parameters at different ZnO carrier concentrations ranging from  $10^{13}$  to  $10^{20} \text{ cm}^{-3}$ . The solar cell parameters are also unchanged when the carrier concentration of ZnO increases. Although there is no variation of the solar cell parameters by varying the carrier concentration of ZnO, the device performance may improve by reducing the recombination of minority charge carriers [14]. On the other hand, the low carrier concentrations of the ZnO window layer can absorb incident photons in it. This absorption of photons in ZnO can reduce the value of parameter  $J_{sc}$  and finally, decrease the device performance. Therefore, the high carrier concentration of the ZnO in solar cells is preferred in solar cells to improve solar cell parameters.

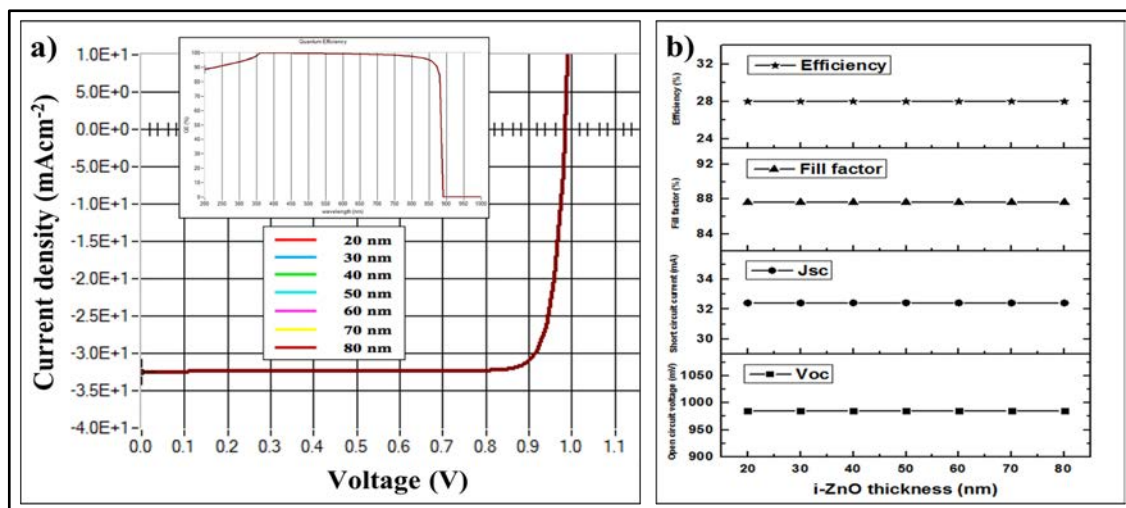


Fig. 6.27 Schematic of a) J-V curve of the CIGSe bilayer TFSC inserted with QE curve, b) the solar cell parameter curve at different ZnO thicknesses

Table 6.21 Parameters used in CIGSe bilayer TFSC at different thicknesses and carrier concentrations of ZnO

Materials	CiSe	CIGSe	CdS	ZnO	ZnO:Al
Parameters					
Thickness (nm)	1000	5000	50	20-80	100
Bandgap (eV)	1.04	1.4	2.45	3.25	3.5
Donor density ( $\text{cm}^{-3}$ )	0	0	$1 \times 10^{17}$	$1 \times 10^{13}$ - $1 \times 10^{20}$	$1 \times 10^{17}$
Acceptor density ( $\text{cm}^{-3}$ )	$1 \times 10^{18}$	$1 \times 10^{17}$	0	0	0

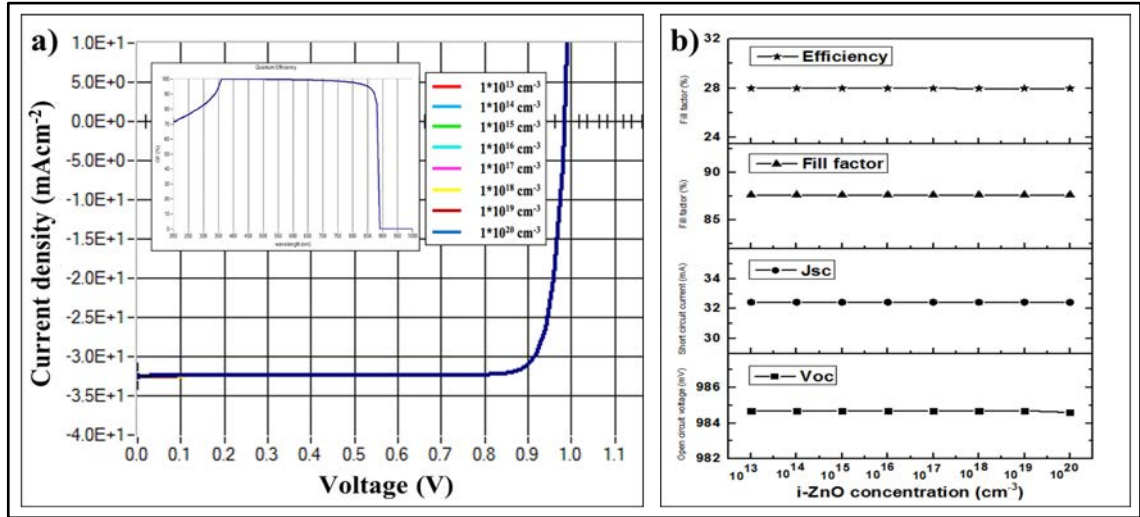


Fig. 6.28 Schematic of a) J-V curve of CIGSe bilayer TFSC inserted with QE curve, b) the solar cell parameter curve at different ZnO carrier concentrations

### 6.3.5 Influence of thicknesses and carrier concentrations of ZnO:Al for CIGSe bilayer TFSC

At last, the CIGSe bilayer TFSC performance is analyzed at diverse thicknesses and carrier concentrations of ZnO:Al TCO while other parameters are kept constant (see Table 6.22). The J-V curve of CIGSe bilayer TFSC inserted with the QE curve and the quantitative data of the solar cell parameters at different ZnO: Al thicknesses are shown in Fig. 6.29. The ZnO:Al TCO thickness is graded from 50 to 400 nm. It is observed from the results that the PCE of the CIGSe bilayer TFSC is slightly reduced from 27.99 to 27.19% when the thickness of ZnO:Al increases from 50 to 400 nm. This decrement of solar cell performance with a rise in ZnO:Al thickness may be due to the decrease in the absorption of photons in the absorber layer by absorbing incident photons in ZnO:Al layer and by increasing the series resistance of the device [17, 22]. Hence, the low thickness of the ZnO:Al layer is favored to get the high efficiency of CIGSe bilayer TFSC. Then, the numerical study is focused on different carrier concentrations of ZnO:Al TCO. The J-V curve of the CIGSe bilayer TFSC inserted with the QE curve and the quantitative data of the solar cell parameters at various ZnO:Al carrier concentrations are displayed in Fig. 6.30. When ZnO:Al carrier concentration is increased from  $10^{13}$  to  $10^{20}$   $\text{cm}^{-3}$ , the PCE of CIGSe bilayer TFSC is slightly improved from 27.92 to 27.99%. But the device performance can decrease at a lower carrier concentration of ZnO:Al by absorbing photons in it. Therefore, the higher carrier



concentration of ZnO:Al is suitable in CIGSe bilayer TFSC to increase the performance of the device.

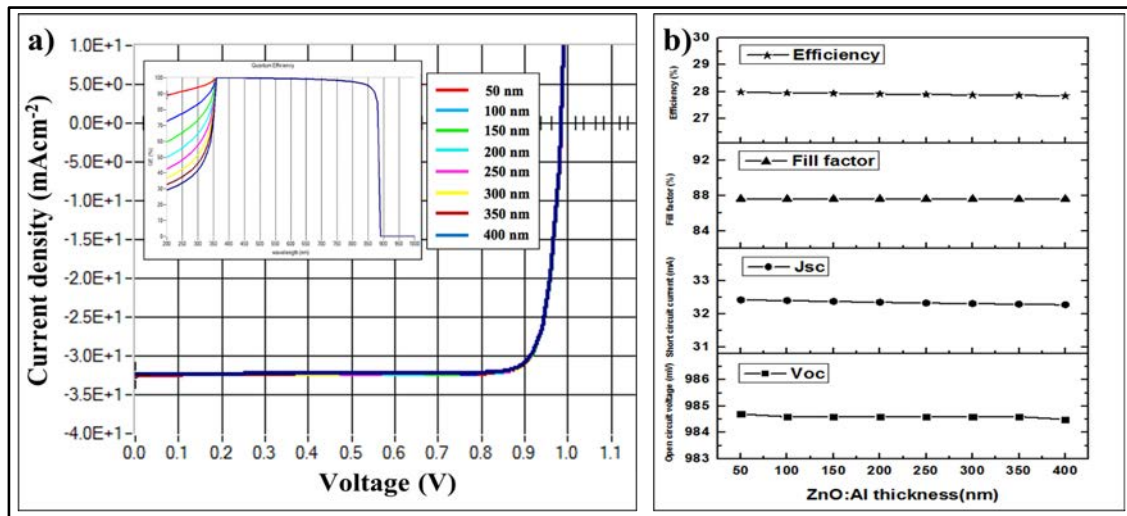


Fig. 6.29 Schematic of a) J-V curve of CIGSe bilayer TFSC inserted with QE curve, b) the solar cell parameter curve at different ZnO:Al thicknesses

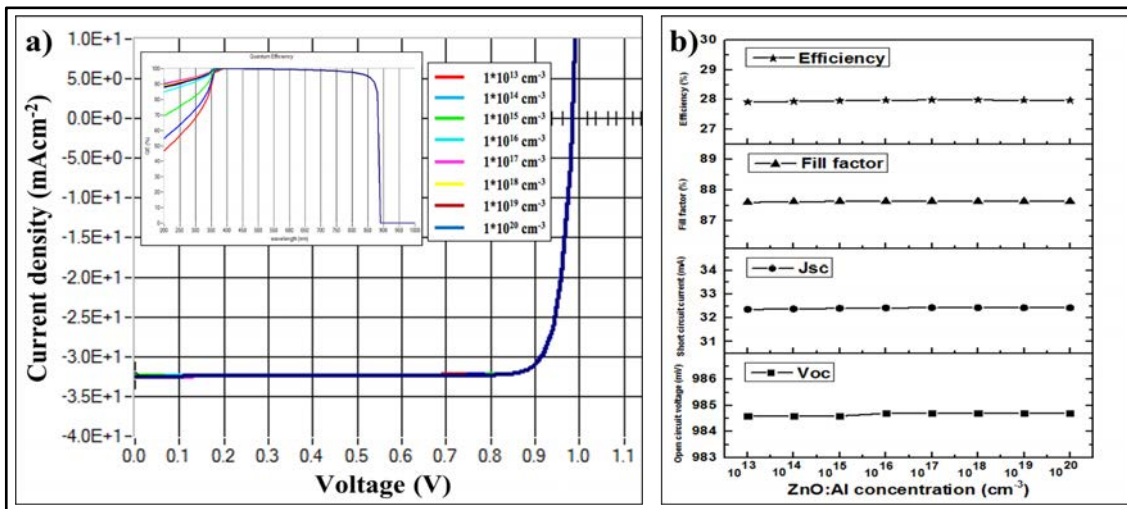


Fig. 6.30 Schematic of a) J-V curve of the CIGSe bilayer TFSC inserted with QE curve, b) the solar cell parameter curve at different ZnO:Al carrier concentrations

Table 6.22 Parameters used in CIGSe bilayer TFSC at different thicknesses and carrier concentrations of ZnO:Al

Materials	CISe	CIGSe	CdS	ZnO	ZnO:Al
Parameters					
Thickness (nm)	1000	5000	50	50	50-400
Bandgap (eV)	1.04	1.4	2.45	3.25	3.5
Donor density ( $\text{cm}^{-3}$ )	0	0	$1 \times 10^{17}$	$1 \times 10^{17}$	$1 \times 10^{13}$ - $1 \times 10^{20}$

Acceptor density (cm <sup>-3</sup> )	1×10 <sup>18</sup>	1×10 <sup>17</sup>	0	0	0
--------------------------------------	--------------------	--------------------	---	---	---

### 6.3.6 Optimized conditions for CIGSe bilayer TFSC

The material parameters such as thickness and carrier concentration of each layer used in the CIGSe bilayer TFSC are studied through SCAPS software and optimized for high CIGSe bilayer TFSC performance. Fig. 6.31 depicts the J-V characteristics curve for optimized CIGSe bilayer TFSC inserted with the QE curve. From the simulated results, the optimized thicknesses of CIGSe, CIGSe, CdS, ZnO, and ZnO:Al were 1  $\mu\text{m}$ , 5  $\mu\text{m}$ , 50 nm, 50 nm, 50 nm, respectively. The optimal bandgap of the CIGSe absorber layer for CIGSe bilayer TFSC was 1.4 eV. Also, the carrier concentration of  $10^{18} \text{ cm}^{-3}$  for CIGSe,  $10^{17} \text{ cm}^{-3}$  for CIGSe,  $10^{18} \text{ cm}^{-3}$  for CdS,  $10^{18} \text{ cm}^{-3}$  for ZnO, and  $10^{18} \text{ cm}^{-3}$  for ZnO:Al were optimized. The optimized PCE of 27.99% is noted for CIGSe bilayer TFSC by utilizing optimized material parameters of each layer used in CIGSe bilayer TFSC. This obtained PCE of CIGSe bilayer TFSC showed a higher value than the PCE of CIGSe TFSC, indicating that the use of two absorber layers has the potential to enhance greater device performance than using a single absorber layer. This improvement of PCE in CIGSe bilayer TFSC is due to an increase in the absorption of photons on the absorber layer. The  $V_{oc}$  of 984.7 mV,  $J_{sc}$  of  $32.43 \text{ mAcm}^{-2}$ , and FF of 87.64% are other optimized solar cell parameters for CIGSe bilayer TFSC. The slightly bend curves at two corners of the QE curve are related to front and back surface recombination [25]. Since the CIGSe bilayer includes CIGSe and CIGSe materials, the photons whose wavelength is greater than 900 nm will not absorb in the device.

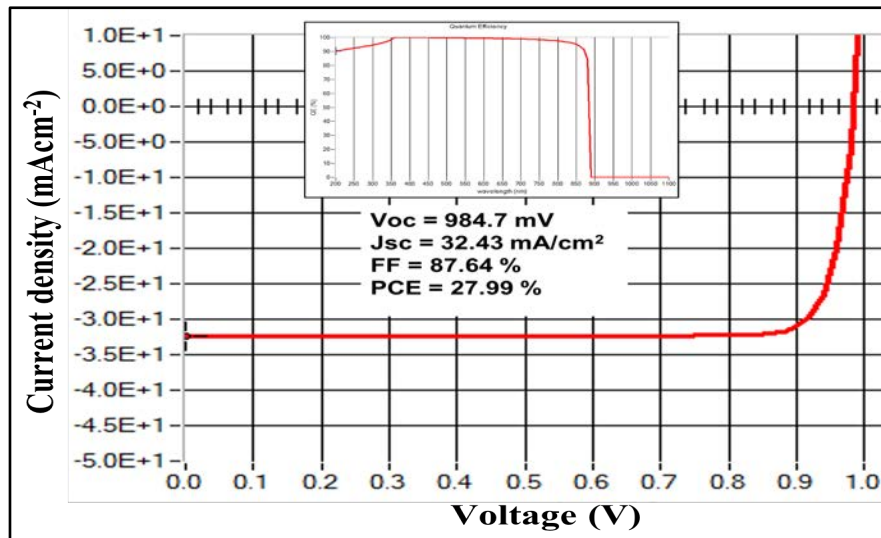


Fig. 6.31 Schematic of the J-V curve of the optimized CIGSe bilayer TFSC inserted with QE curve



## 6.4 Fitting experimental results in the simulation

### 6.4.1 Study on CISE thin film solar cells

This numerical study inserted the experimentally obtained parameters such as the thickness, bandgap, carrier concentration, and mobility of CISE and CdS thin films into the optimized CISE TFSC and then analyzed the solar cell performance. Fig. 6.32 displays the J-V curves of CISE TFSC and solar cell parameters after replacing the experimental parameters of the CISE absorber layer and the CdS buffer layer. The material properties of the CISE absorber layer grown by the hybrid deposition method and the material properties of CdS thin films deposited by the CBD method are presented in Table 6.23. Here, five different samples of CdS that are deposited at different deposition times are studied. After substituting the experimental parameters of CISE and CdS thin films into the optimized simulation results of CISE TFSC, the maximum PCE of 19.35% is obtained for CdS thin film grown at 80°C for 20 minutes, offering an excellent experimental condition to achieve the device's high performance. This obtained PCE is slightly lower than the optimized theoretical study (i.e., 22.81%).

All the solar cell parameters ( $J_{sc}$ , FF, and PCE) except  $V_{oc}$  are changed to lower values with increasing deposition time from 20 to 60 minutes for CdS thin films. This result showed that CdS thickness mainly affects the  $J_{sc}$  and FF but not on  $V_{oc}$ . Photons are absorbed far from the space charge region at a higher thickness of the CdS. The generated photons recombine before reaching the space charge region due to recombination centers found in thin film CdS that reduce the lifetime of the minority carriers. The  $J_{sc}$  value falls to a lower value at higher CdS thickness. Therefore, a thinner CdS buffer layer in CISE TFSC is preferred to enhance the optical absorption. The solar cell conversion efficiency also depends on the carrier concentration of the CdS buffer layer that affects the collection of photogenerated carriers by varying the space charge region. At a higher carrier concentration of the CdS buffer layer, the space charge region extends wider in the CISE absorber layer and helps to increase the collection of photogenerated charge carriers. The  $J_{sc}$ , FF, and PCE of CISE TFSC are varied from 43.24 to 28.42  $\text{mAcm}^{-2}$ , 70.83 to 20.66%, and 19.87 to 3.93%, with the increase in the CdS deposition time (i.e., thickness), respectively. The CdS sample deposited at 80°C for 60

min has the highest carrier concentration, lowest mobility, and thick thickness showing bad CdS experimental conditions for CISE TFSC as a buffer layer. It is seen from the QE curve that the photons whose wavelength is greater than 1150 nm are not absorbed in the solar cell. The simulation study using experimental parameters provides a concise interpretation of the effect of materials parameters on the CISE TFSC performance.

Table 6.23 Experimental results of CISE and CdS materials

Parameters Samples	Thickness (nm)	Bandgap (eV)	Mobility (cm <sup>2</sup> V <sup>-1</sup> s <sup>-1</sup> )	Carrier Concentration (cm <sup>-3</sup> )
CISE	3500	1.07	6.50	7.7×10 <sup>16</sup>
CdS 20	40	2.49	116	4.5E14
CdS 30	80	2.54	15	1.9E16
CdS 40	130	2.55	31	7.2E15
CdS 50	160	2.58	16	5.6E14
CdS 60	170	2.64	74	1.0E16

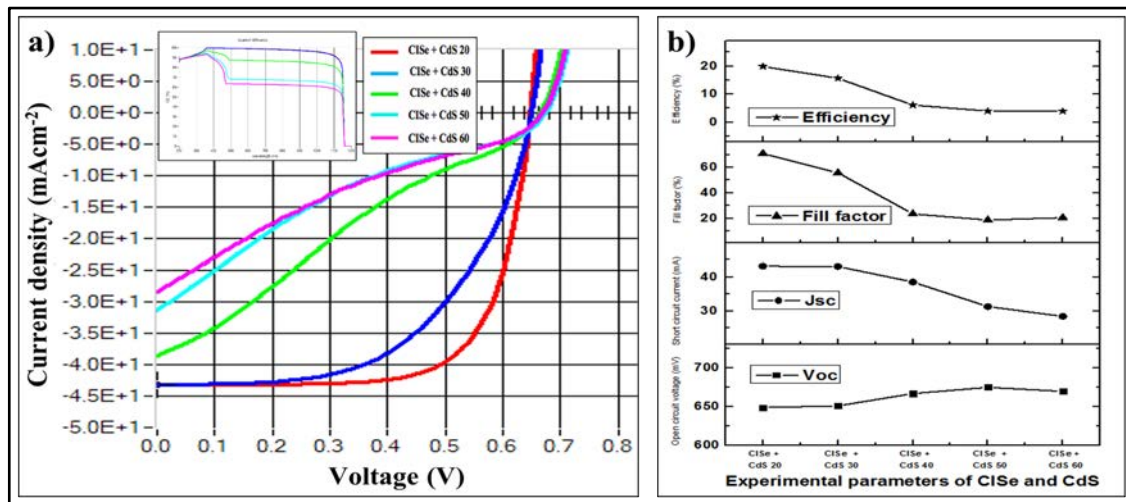


Fig. 6.32 Schematic of a) J-V curves of CISE TFSC b) solar cell parameter curve after analyzing the experimental results of CISE absorber layer and CdS buffer layer

#### 6.4.2 Analysis on CIGSe thin film solar cells

Here, the material parameters of CIGSe and CdS thin films, such as the thickness, bandgap, carrier concentration, and mobility, were replaced in the SCAPS software and then studied the variation in device performance. The J-V curves of the CIGSe TFSC and solar cell output parameters after replacing the experimental parameters of the CIGSe absorber layer and the CdS buffer layer are shown in Fig. 6.33. The experimental results of the CIGSe by hybrid

deposition method and the CdS by the chemical bath deposition method are summarized in Table 6.24. In this case, the experimental results of five different CdS are analyzed. After replacing the experimental properties of CIGSe and CdS thin films with the optimized condition, it is seen from the simulation results that the best solar cell performance ( $>23\%$  of PCE) is obtained for CdS thin films deposited at  $80^{\circ}\text{C}$  for 20 and 30 minutes. The obtained PCE for CIGSe TFSC from simulation after substituting the experimental parameters is compatible with high record efficiency of  $23.35\%$  for CIGSe TFSC, showing an excellent material parameter for achieving the high performance of solar cells.

The parameters FF and PCE of CIGSe TFSC are strongly affected by increasing growth time from 20 to 60 minutes for CdS thin films where the solar cell parameters  $J_{sc}$  and  $V_{oc}$  are slightly influenced. This outcome of reducing the PCE for CIGSe TFSC is due to the increasing thickness of the CdS buffer layer. At higher CdS thickness in solar cells, photons are absorbed far from the space charge region and recombined before collecting the generated charge carriers. The CdS buffer layer should be thinner as possible without defects to reduce the optical absorption in this layer and improve the device performance. The carrier concentration of the CdS thin films also affects the collection of photogenerated carriers. The carrier concentration of CdS thin films must be greater than the carrier concentration of the CIGSe absorber layer to get a better result. The solar cell parameters, namely  $V_{oc}$ ,  $J_{sc}$ , FF, and PCE, are varied from 768 to 789 mV, 37.82 to 37.24  $\text{mAcm}^{-2}$ , 81.93 to 33.66%, and 23.80 to 9.89% with an increase in the CdS thickness, respectively. The CdS sample deposited at  $80^{\circ}\text{C}$  for 20 min showed the best deposition condition for CIGSe TFSC as a buffer layer. The QE curve (see Fig. 6.33a) showed that the photons having wavelengths greater than 1000 nm will be absorbed in the CIGSe TFSC.

Table 6.24 Experimental results of CIGSe and CdS materials

Parameters Samples	Thickness (nm)	Bandgap (eV)	Mobility ( $\text{cm}^2\text{V}^{-1}\text{s}^{-1}$ )	Carrier Concentration ( $\text{cm}^{-3}$ )
CIGSe	3000	1.23	13.87	$2.5 \times 10^{16}$
CdS 20	40	2.49	116	$4.5\text{E}14$
CdS 30	80	2.54	15	$1.9\text{E}16$
CdS 40	130	2.55	31	$7.2\text{E}15$
CdS 50	160	2.58	16	$5.6\text{E}14$

CdS 60	170	2.64	74	1.0E16
--------	-----	------	----	--------

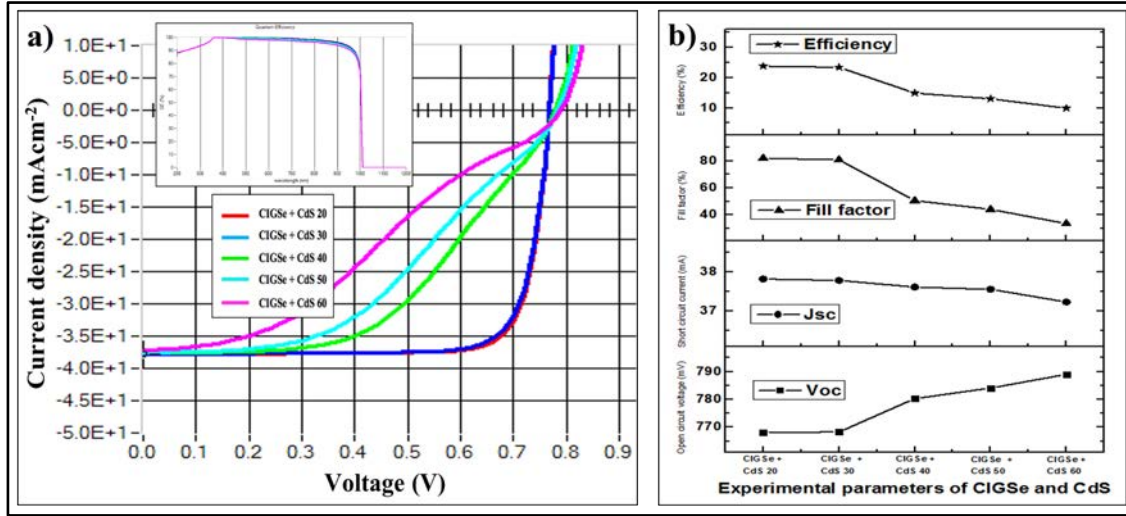


Fig. 6.33 Schematic of a) J-V curves of CIGSe TFSC b) solar cell parameter curve after analyzing the experimental results of CIGSe absorber layer and CdS buffer layer

#### 6.4.3 Study on CIGSe bilayer thin film solar cells

In this case, the material parameters, including the thickness, bandgap, carrier concentration, and mobility of CISE, CIGSe, and CdS thin films, are inserted into the simulation. The solar cell parameters are then analyzed to find the best condition. Fig. 6.34 presents the J-V curves of CIGSe bilayer TFSC and solar cell output parameters after replacing the experimental parameters of CISE, CIGSe, and CdS thin films. The experimental results of the CISE and CIGSe thin films by the hybrid deposition method, and the CdS thin films by the CBD method are demonstrated in Table 6.25. After replacing the experimental properties of CISE, CIGSe, and CdS thin films with the optimized condition, it is observed that the best CIGSe bilayer TFSC performance (>24 % of PCE) is found for CdS thin films deposited at 80°C for 20 and 30 minutes. The obtained PCE for CIGSe bilayer TFSC from the simulation study with experimental parameters is slightly greater than the high record efficiency of 23.35% for CIGSe based TFSC. This result shows that the solar cell performance can be improved using the two absorber layers.

The solar cell parameters such as  $J_{sc}$ , FF, and PCE for CIGSe bilayer TFSC are declined with rising deposition time from 20 to 60 minutes for CdS thin films, while  $V_{oc}$  is slightly increased. This increment of  $V_{oc}$  for CIGSe bilayer TFSC is due to the enhancement of the

bandgap range of the absorber layer. Although the  $V_{oc}$  of the solar cells is increased, the PCE of the CIGSe bilayer is decreased with increasing CdS deposition time (i.e., thickness). This decrement of PCE at higher thickness might be due to the absorption of photons in the CdS buffer layer rather than the absorber layer. The series resistance can also increase with an increase in the CdS thickness that can reduce the device's performance. Therefore, the PCE of CIGSe bilayer TFSC for CdS thin films deposited at lower times (20 and 30 minutes) showed better results than other samples. The carrier concentration of CdS thin films is another parameter that can affect the collection of photogenerated carriers. A lower carrier concentration of CdS may reduce the solar cell parameters by absorbing photons in it [23]. Hence, the carrier concentration of CdS thin films should be larger to have the best result. The solar cell parameters  $V_{oc}$ ,  $J_{sc}$ , FF, and PCE of CIGSe bilayer TFSC are changed from 779 to 795 mV, 38.21 to 37.87  $\text{mAcm}^{-2}$ , 82.70 to 37.34%, and 24.63 to 11.25% with a rise in the CdS deposition time from 20 to 60 minutes, respectively. The CdS sample deposited at 80°C for 20 min showed the best deposition condition for CIGSe bilayer TFSC that provides a maximum PCE of 24.63%. It is observed from the QE curve inserted in the J-V curve (see Fig. 6.34 a) of the CIGSe bilayer TFSC that the photons having wavelength values lower than 1000 nm can generate the charge carriers.

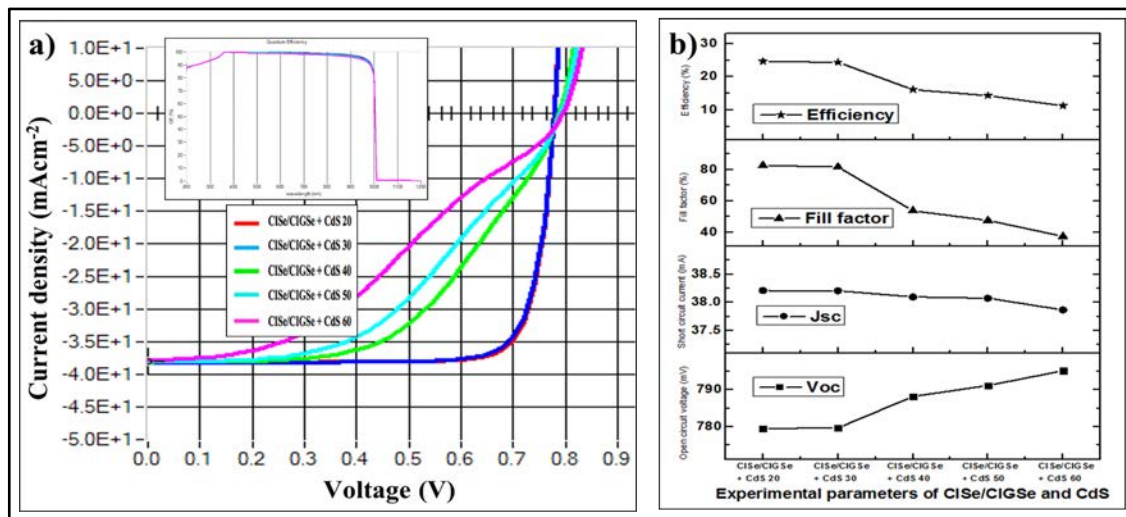


Fig. 6.34 Schematic of a) J-V curves of the CIGSe bilayer TFSC b) solar cell parameter curve after analyzing the experimental results of CIGSe, CIGSe, and CdS thin films

Table 6.25 Experimental results of CIGSe, CIGSe and CdS materials

Parameters Samples	Thickness (nm)	Bandgap (eV)	Mobility ( $\text{cm}^2\text{V}^{-1}\text{s}^{-1}$ )	Carrier Concentration ( $\text{cm}^{-3}$ )
CIGSe	3500	1.07	6.50	$7.7 \times 10^{16}$

CIGSe	3000	1.23	13.87	$2.5 \times 10^{16}$
CdS 20	40	2.49	116	4.5E14
CdS 30	80	2.54	15	1.9E16
CdS 40	130	2.55	31	7.2E15
CdS 50	160	2.58	16	5.6E14
CdS 60	170	2.64	74	1.0E16

## 6.5 Effect of the defects on the solar cell performance

The electrical properties of solar cell devices are strongly affected by the quality of semiconductor materials. Defects (i.e., some impurities, vacancies, interstitials, or clusters) in semiconductor materials are responsible for the recombination process that negatively affects the device performance. The recombination of the generated charge carriers can occur in a bulk layer, interface, or metal contacts. Here, Shockley-Read-Hall (SRH) recombination processes in the absorber layer, buffer layer, and their interface are studied. In semiconductors, the most common defects are either donor or acceptor defects. However, there exist defects with more than two different charge states called multivalent defects, whose algorithms are explained in [39]. The neutral defect, an idealization of a defect, contributes to the SRH recombination but not to the space charge region. In a neutral defect, it is possible to calculate electron and hole lifetimes without specifying a defect in the space charge region. The magnitude of diffusion length can explain the recombination process for minority charge carriers [40]. The diffusion length depends on the lifetime and consecutively the diffusion coefficient of charge carriers [41]. If the diffusion length of minority charge carriers is high value, then the recombination process will be low and improve the device performance [44, 48]. A better understanding of the defects in the device can help to improve the solar cell parameters. Here, the defect density and carrier capture cross-section (CCCS) are introduced and analyzed their effects on the solar cell parameters.

### 6.5.1 Defects in the absorber layer

The absorber layer is the most important in the solar cell because photons from the Sun absorb and electron-hole pairs generate in this layer. The defects in the absorber layer act as recombination centers and degrade the device performance very effectively. So, understanding how the defects affect the solar cell parameters can help to improve the

device's performance. Fig. 6.35a-c depicts the J-V curves (inserted with solar cell output parameters curve) of the CI(G)Se TFSC at different defect densities of the CI(G)Se absorber layers. It is noticed from Fig. 6.35a-c that all the four solar cell parameters are affected and reduced when the defect density of the CIGSe semiconductor rises. The defect density present in the absorber layer enhances the carrier's recombination centers that degrade the solar cell performance. This degradation of device performance with a rise in defect densities is mainly due to the recombination of minority charge carriers at the localized energy levels by creating an alternative path for generated charge carriers [37, 40–[43]. For CIGSe TFSC, the solar cell parameters, namely  $V_{oc}$ ,  $J_{sc}$ , FF and PCE, are dropped respectively from 612.9 to 305.5 mV, 45.01 to 25.77  $\text{mAcm}^{-2}$ , 82.67 to 54.91%, and 22.81 to 4.32% after increasing the defect density from  $10^{12}$  to  $10^{19} \text{ cm}^{-3}$ . The solar cell parameters, namely  $V_{oc}$ ,  $J_{sc}$ , FF, and PCE, are changed from 964.5 to 461.7 mV, 32.42 to 10.14  $\text{mAcm}^{-2}$ , 87.34 to 48.96% and 27.32 to 2.29%, respectively, when defect density of CIGSe absorber layer increased from  $10^{12}$  to  $10^{20} \text{ cm}^{-3}$  in the CIGSe TFSC. In CIGSe bilayer TFSC, the parameters  $V_{oc}$ ,  $J_{sc}$ , FF and PCE are reduced from 984.6 to 631.3 mV, from 32.42 to 20.81  $\text{mAcm}^{-2}$ , from 87.64 to 66.07%, and from 27.99 to 8.68%, respectively, with a rise in CIGSe defect density.

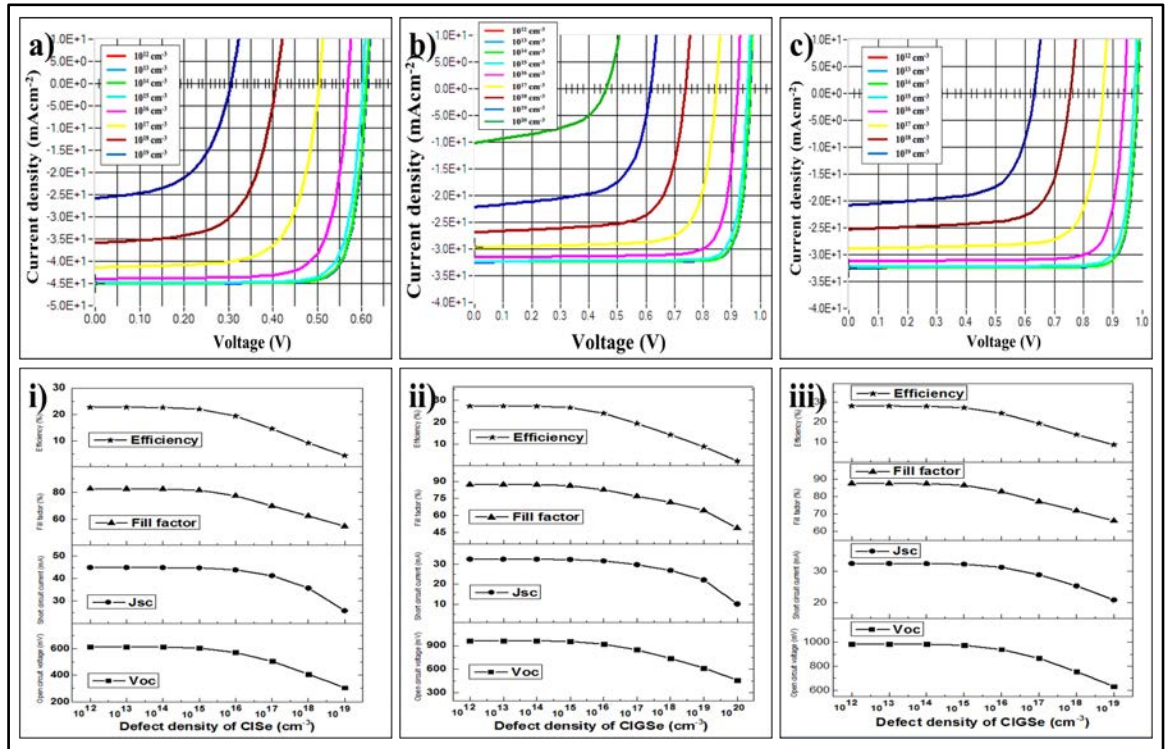


Fig. 6.35 J-V curves for a) CIGSe TFSC, b) CIGSe TFSC and c) CIGSe bilayer TFSC, and solar cell parameter curves for i) CIGSe TFSC, ii) CIGSe TFSC and c) CIGSe bilayer TFSC at different defect densities in absorber layer



The simulation study is then focused on the CCCS of the CISE absorber layer for CISE TFSC, the CIGSe absorber layer for CIGSe TFSC, and the CIGSe absorber layer for CIGSe bilayer TFSC. The J-V curves of CI(G)Se TFSC (inserted with a curve of solar cell parameters) at various CCCS of the absorber layers are shown in Fig. 6.35i-iii. The CCCS involves relaxation processes within the band, where a carrier will be captured at a defect center with a phonon ladder that dissipates its energy. The probability of recombining the free charge carriers enhances due to the Coulombic attraction between the trap and the charge carriers [37, 44]. The recombination process is also occurred through the multi-phonon process, which is strongly dependent on the depth of the trap [44, 45]. The solar cell parameters such as  $V_{oc}$ , FF, and PCE gradually decrease with an increase in the CCCS of the CISE absorber layer while  $J_{sc}$  remained almost constant. With an increase in CCCS of the absorber layers, the PCE of the CISE TFSC, CIGSe TFSC, and CIGSe bilayer TFSC is dropped from 22.81 to 22.09% (when CCCS of CISE is varied from  $10^{-18}$  to  $10^{-12}$   $\text{cm}^2$ ), 27.32 to 26.63% (when CCCS of CISE is varied from  $10^{-20}$  to  $10^{-12}$   $\text{cm}^2$ ), and 27.99 to 19.29% (when CCCS of CISE is varied from  $10^{-17}$  to  $10^{-10}$   $\text{cm}^2$ ), respectively. Hence, the defect density and the CCCS of the CISE absorber layer should be as low as possible in solar cells.

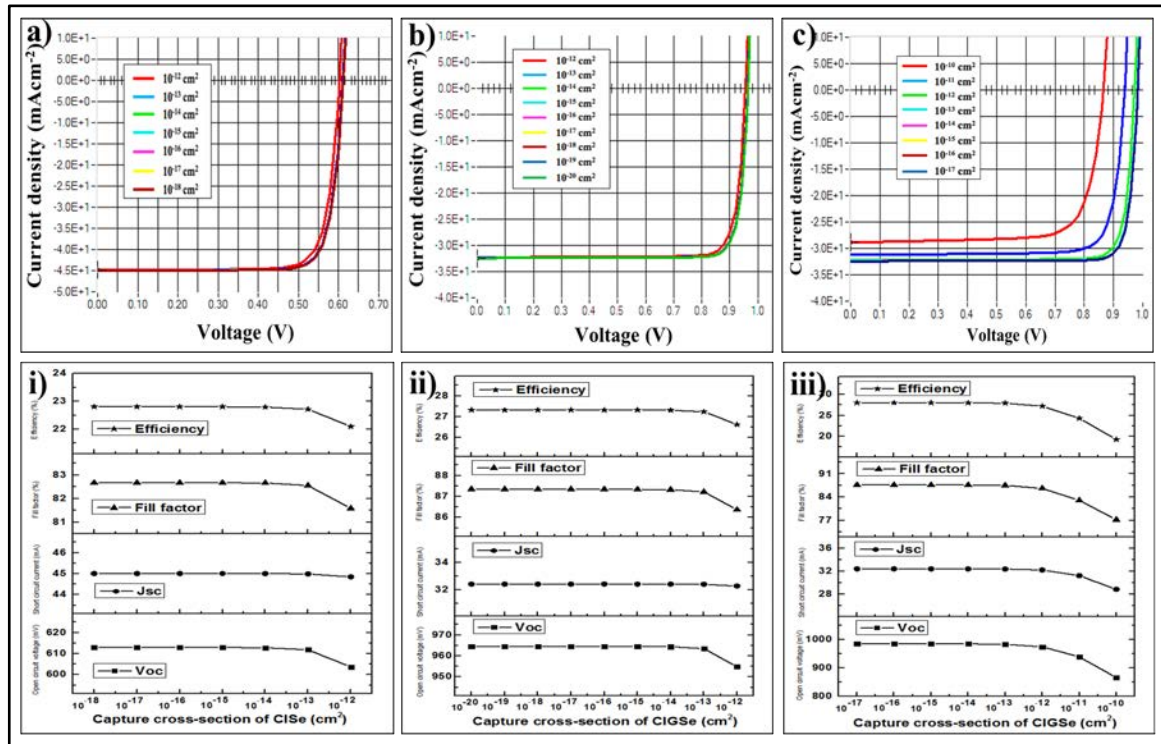


Fig. 6.36 J-V curves for a) CISE TFSC, b) CIGSe TFSC and c) CIGSe bilayer TFSC, and solar cell parameter curves for i) CISE TFSC, ii) CIGSe TFSC and c) CIGSe bilayer TFSC at different CCCS in absorber layer



### 6.5.2 Defects in the CdS buffer layer

Another essential layer in CI(G)Se TFSC is an n-type CdS semiconductor that forms a p-n junction with the p-type CISE absorber layer. So, the solar cell parameters can be influenced if the defects are present in the CdS buffer layer. The J-V curves inserted with the curve of solar cell output parameters of CI(G)Se TFSC at different defect densities of the CdS buffer layer are displayed in Fig. 6.36a-c. Here, the defect density of the CdS buffer layer is varied from  $10^{12}$  to  $10^{18}$   $\text{cm}^{-3}$  for CISE TFSC, from  $10^{12}$  to  $10^{19}$   $\text{cm}^{-3}$  for both the CIGSe TFSC and CIGSe bilayer TFSC. All solar cell parameters are decreased with an increase in defect density of the CdS buffer layer, which is primarily due to the presence of leakage current resulting from the recombination with the localized energy levels created by the defects [40–43]. The PCE of the CISE TFSC, CIGSe TFSC, and CIGSe bilayer TFSC are slightly decreased from 22.81 to 22.13%, from 27.32 to 25.11%, and 27.99 to 26.08%, respectively.

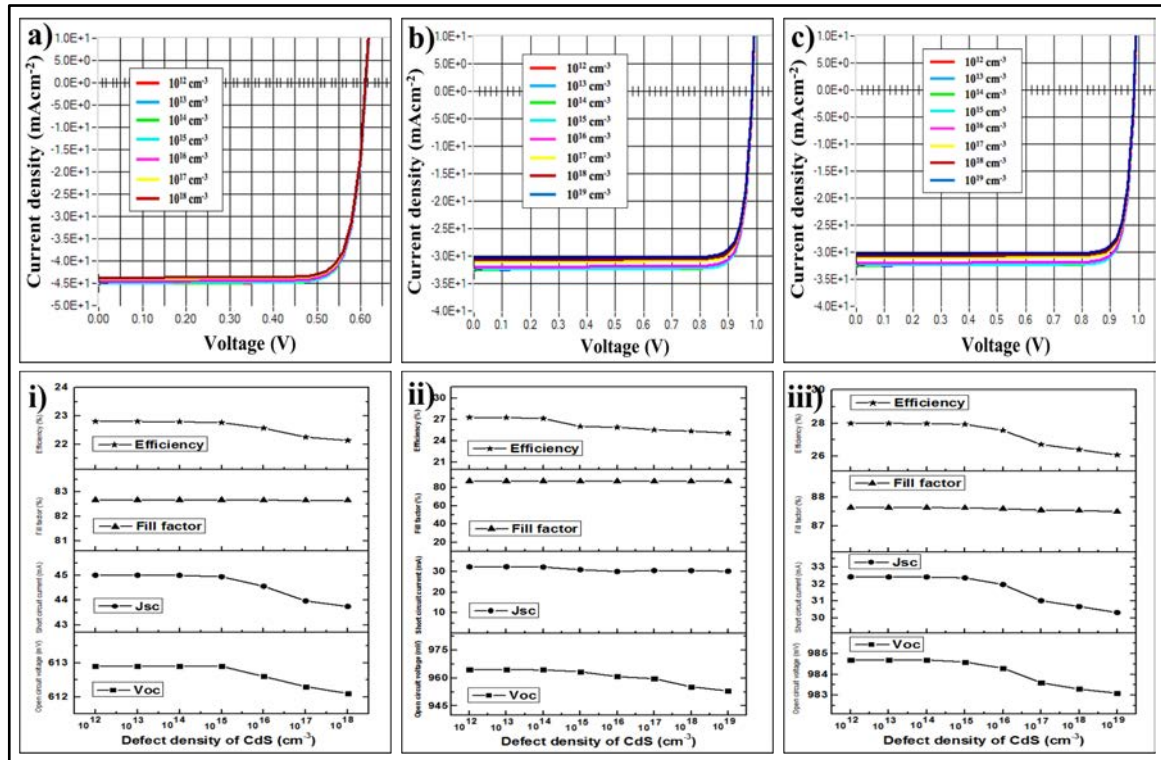


Fig. 6.37 J-V curves for a) CISE TFSC, b) CIGSe TFSC and c) CIGSe bilayer TFSC, and solar cell parameter curves for i) CISE TFSC, ii) CIGSe TFSC and c) CIGSe bilayer TFSC at different defect densities in CdS buffer layer

Subsequently, the study of the effect of the CCCS in the CdS for all CI(G)Se TFSC on the device performance is carried out as shown in Fig. 6.36i-iii. The CCCS of CdS is varied from  $10^{-18}$  to  $10^{-12}$  cm<sup>2</sup> for CISE TFSC, from  $10^{-19}$  to  $10^{-12}$  cm<sup>2</sup> for CIGSe TFSC, and from  $10^{-17}$  to  $10^{-10}$  cm<sup>2</sup> for CIGSe bilayer TFSC. Likewise, all the solar cell parameters are slightly degraded at higher CCCS in the CdS. The decrement of the solar cell parameters is due to the recombination of charge carriers through the Coulombic attraction of charge carriers [37, 44, 45]. The PCE of the CISE TFSC, CIGSe TFSC, and CIGSe bilayer TFSC is reduced from 22.81 to 22.77%, 27.32 to 26.05% and 27.99 to 26.72%, respectively. The generated charge carriers recombine when they have low diffusion length and finally, they don't contribute to the power generation [40]. Therefore, the defect density and CCCS in CdS for CI(G)Se TFSC must be lower values to get high performance of the device.

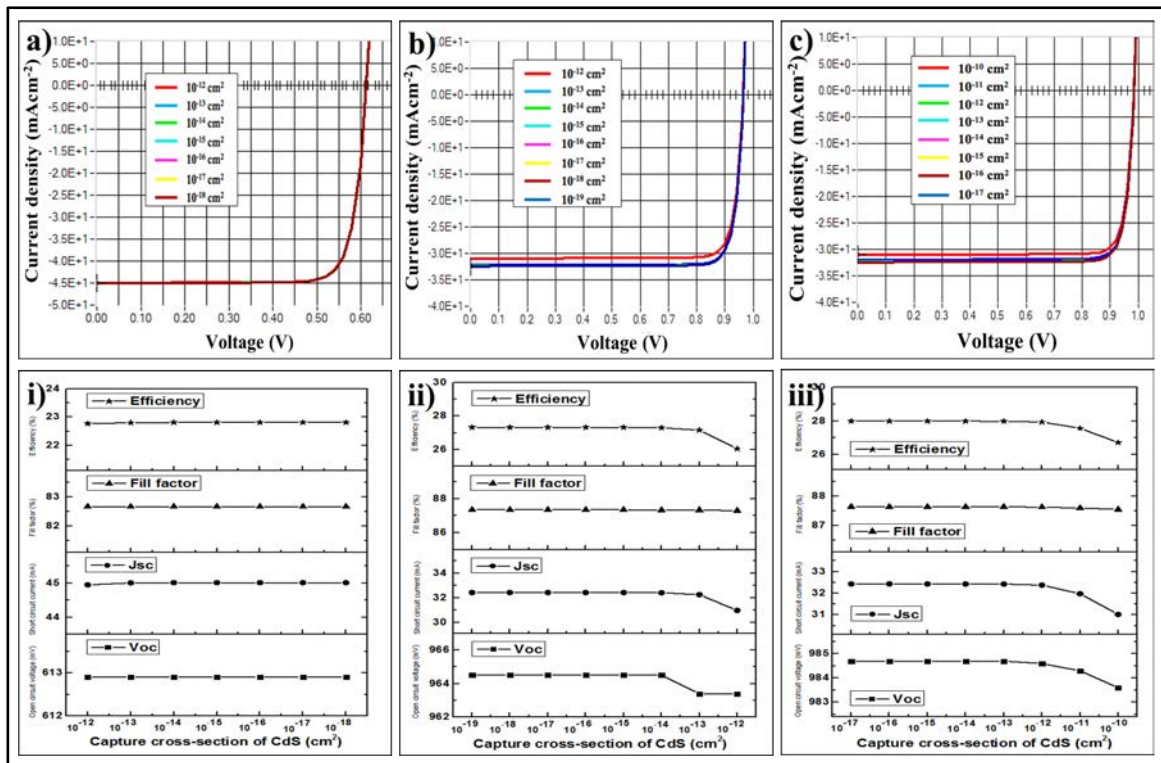


Fig. 6.38 J-V curves for a) CISE TFSC, b) CIGSe TFSC and c) CIGSe bilayer TFSC, and solar cell parameter curves for i) CISE TFSC, ii) CIGSe TFSC and c) CIGSe bilayer TFSC at different CCCS in CdS buffer layer

### 6.5.3 Defects at the interface

The definition of the defects at an interface is very similar to the defects in the bulk semiconductor. The Pauwels-Vanhoutte theory modeled the recombination at an interface, which extends the SRH theory [49]. In CI(G)Se TFSCs, the p-n junction is formed by

combining two different materials, normally the CdS buffer layer and CI(G)Se absorber layer. Since these two materials contain different physical and material properties, the interface between CdS and CI(G)Se absorber layers will contain recombination centers for generated charge carriers and affect the device performance [49]. This section analyzes the device performance with different defect densities and CCCS at the CdS/CISe interface for CISe TFSC, at the CdS/CIGSe interface for CIGSe TFSC, and at the CdS/CIGSe interface for CIGSe TFSC. Fig. 6.37a-c shows the J-V curves inserted with solar cell parameters curves at different defect densities in the CdS/CISe interface for CISe TFSC (varied from  $10^{11}$  to  $10^{16}$   $\text{cm}^{-3}$ ), in the CdS/CIGSe interface for CIGSe TFSC (varied from  $10^{11}$  to  $10^{16}$   $\text{cm}^{-3}$ ), and in the CdS/CIGSe interface of CIGSe bilayer TFSC (varied from  $10^{11}$  to  $10^{15}$   $\text{cm}^{-3}$ ). All four solar cell parameters of CI(G)Se TFSC are affected and reduced with an increase in defect densities at the interface. The PCE of CISe TFSC, CIGSe TFSC, and CIGSe bilayer TFSC is dropped from 22.81 to 1.08%, 27.32 to 1.99 %, and 27.99 to 2.43%, respectively. These results showed that the device performance is very sensitive to the defect density at the interface than at bulk semiconductors. Next, the effect of different CCCS in the interface of CI(G)Se TFSC on the solar cell parameters is studied (See Fig. 6.37i-iii). Here, the CCCS in the interface is varied from  $10^{-17}$  to  $10^{-11}$   $\text{cm}^2$  for CISe TFSC, from  $10^{-19}$  to  $10^{-12}$   $\text{cm}^2$  for CIGSe TFSC, and from  $10^{-17}$  to  $10^{-10}$   $\text{cm}^2$  for CIGSe bilayer TFSC. It is noticed that the solar cell parameters are decreased with a rise in the CCCS in the interface. This decrement of solar cell parameters at the interface is due to the increase in recombination centers for generated charge carriers. The respective PCE of CISe TFSC, CIGSe TFSC, and CIGSe bilayer TFSC is degraded from 22.81 to 20.60%, 27.32 to 24.56%, and 27.99 to 22.55%. Hence, defects at the interface should be negligible for attaining better performance.

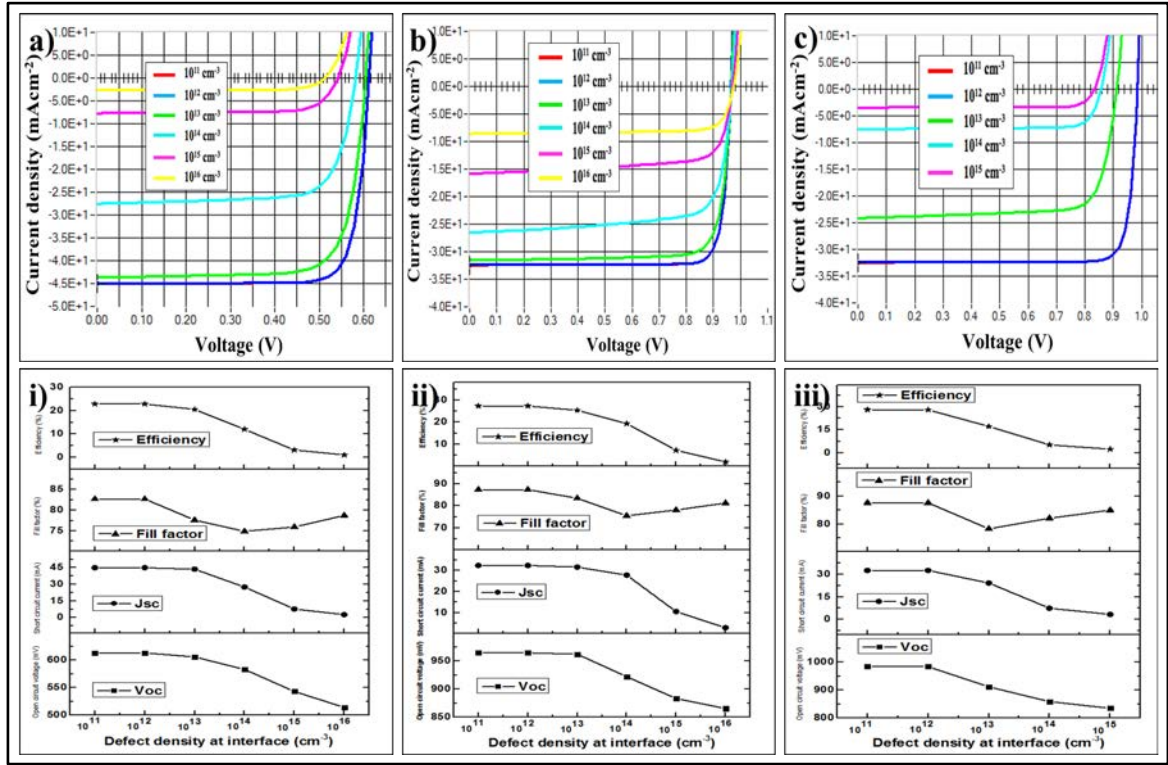


Fig. 6.39 J-V curves for a) CISE TFSC, b) CIGSe TFSC and c) CIGSe bilayer TFSC, and solar cell parameter curves for i) CISE TFSC, ii) CIGSe TFSC and c) CIGSe bilayer TFSC at different defect densities in the interface

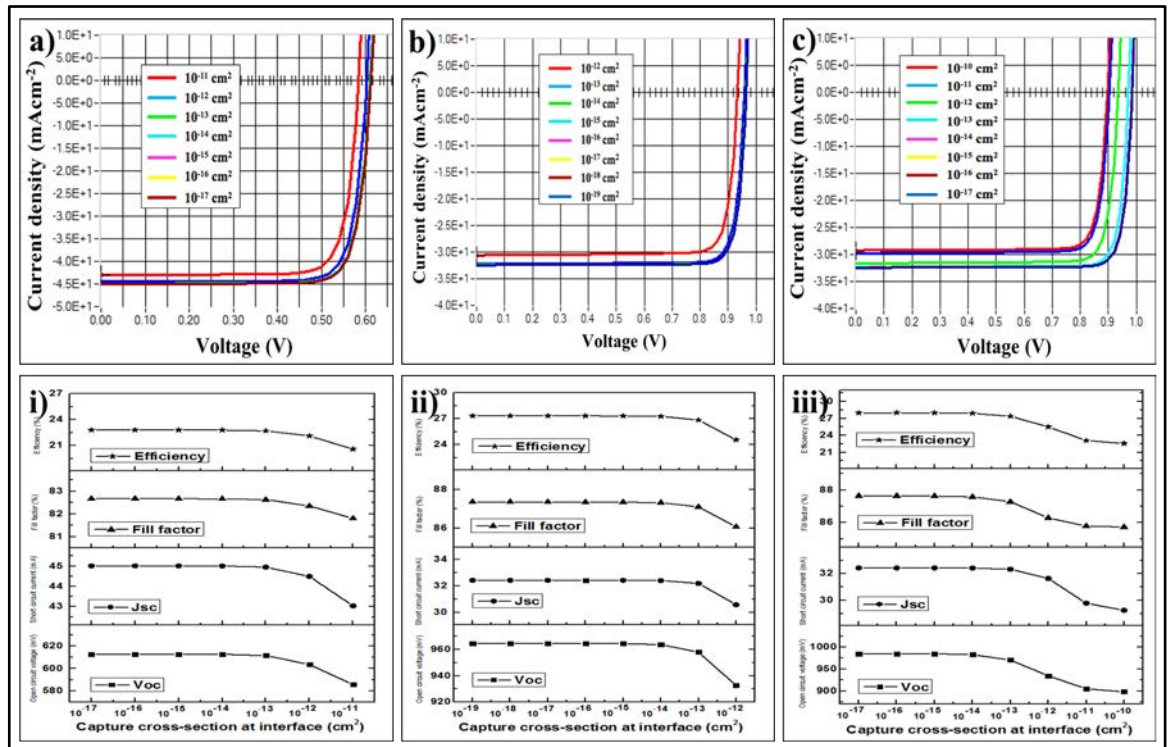


Fig. 6.40 J-V curves for a) CISE TFSC, b) CIGSe TFSC and c) CIGSe bilayer TFSC, and solar cell parameter curves for i) CISE TFSC, ii) CIGSe TFSC and c) CIGSe bilayer TFSC at different CCCS in the interface

## 6.6 Effect of ambient temperatures on the solar cell performance

The solar cell panels are generally installed outside. Since the part of the sun's energy contains thermal energy, it can increase the ambient temperature and cause the heating of solar cell devices. Solar cell devices are sensitive to the ambient temperature like all other semiconductor devices. The effect of ambient temperature on the solar cell parameters of CISE, CIGSe, and CIGSe bilayer TFSC is studied using SCAPS software. Fig. 6.38a-c depicts the J-V curves of CISE, CIGSe, and CIGSe bilayer TFSCs at different ambient temperatures ranging from 270 to 350 K, respectively. It is seen from Fig. 6.53 that all the solar cell parameters ( $V_{oc}$ , FF, PCE) except  $J_{sc}$  decrease when ambient temperature increases. The saturation current, an indication of the quality of solar cell, is strongly affected and rapidly increased with an increase in ambient temperature due to changes in the material properties such as intrinsic carrier concentration, bandgap, electron and hole mobilities [5, 8, 11, 26, 50]. Since the parameter  $V_{oc}$  is inversely proportional to the saturation current [5], the  $V_{oc}$  degrades with a rise in ambient temperature. The bandgap of semiconductors also becomes narrower with a rise in ambient temperature. The parameter  $V_{oc}$  is the ratio of bandgap and charge. Therefore,  $V_{oc}$  can reduce with a decrease in the bandgap of semiconductor and subsequently, reduce the solar cell performance [51]. At higher ambient temperatures, more photons have enough energy to create electron-hole pairs that help to increase the  $J_{sc}$  value [35]. The electrons in the solar cells become unstable by taking extra energy and recombining with the holes at higher ambient temperatures [7, 26]. Hence, these results implied that the solar cells provide better results in the lower ambient temperatures (i.e., cold region) than in the higher ambient temperatures (i.e., hot region). When ambient temperatures increase from 270 to 350 K, the efficiency reduces from 25.40 to 18.59%, 29.26 to 24.16%, and 29.81 to 24.76%, respectively, for CISE, CIGSe, and CIGSe bilayer TFSC. Therefore, understanding the effect of temperature on the solar cell device can guide to use of favorable materials in the solar cell.



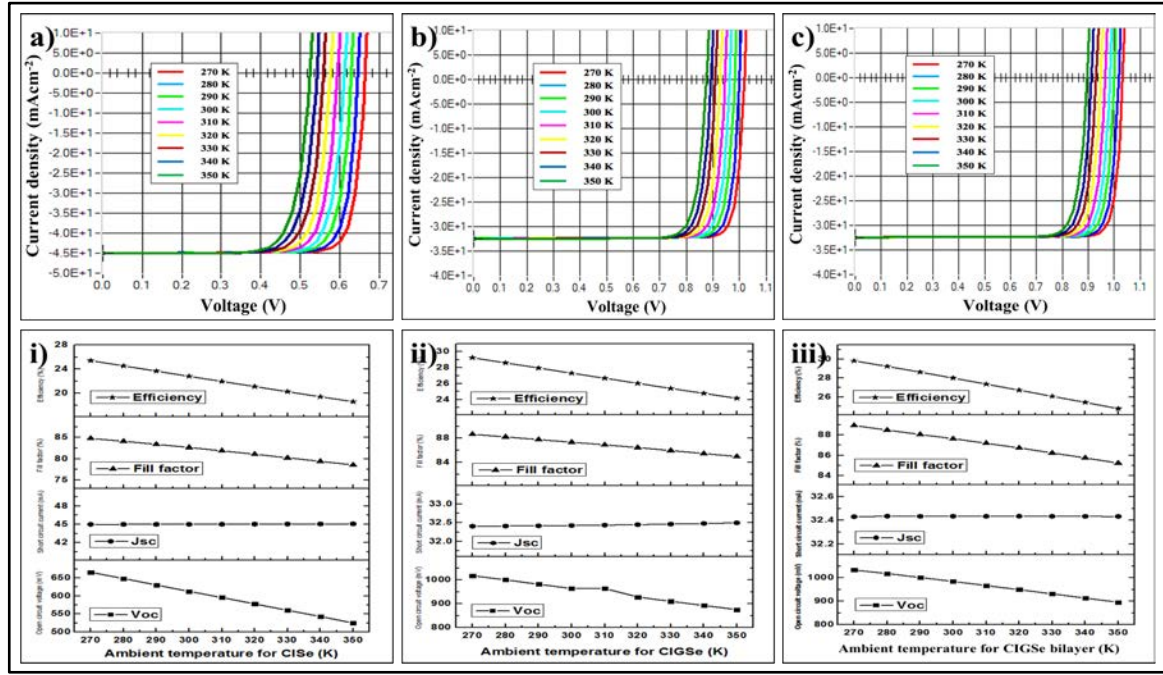


Fig. 6.41 J-V curves for a) CISE TFSC, b) CIGSe TFSC and c) CIGSe bilayer TFSC, and solar cell parameter curves for i) CISE TFSC, ii) CIGSe TFSC, and iii) CIGSe bilayer TFSC at different ambient temperatures

## 6.7 Influence of parasitic resistances on the solar cell performance

Resistive effects in photovoltaic technology reduce the efficiency of the solar cell by dissipating power within the resistances. The most common parasitic resistances are series resistance and shunt resistance. These parasitic resistances negatively affect the FF of the solar cell, which is mainly dependent on the solar cell's geometry (i.e., area) [5, 11, 26, 34, 53]. In this work, the effect of series and shunt resistances on the performance of CISE, CIGSe, and CIGSe bilayer TFSC are reviewed. The series resistance of solar cells involves the bulk resistance, metallic contact resistance and the resistance of the circuit of the terminal. Fig. 6.39a-c depicts the J-V curves of the CISE, CIGSe, and CIGSe bilayer TFSC inserted with solar cell parameters curve at different series resistances. The solar cell parameters are analyzed at different magnitudes of series resistance starting from 0 to  $35 \Omega\text{cm}^2$ , while the shunt resistance is fixed at  $10^6 \Omega\text{cm}^2$ . It can observe from the results that the solar cell parameters  $J_{sc}$ , FF, and PCE are strongly affected and degraded with increasing series resistances while  $V_{oc}$  remains constant. At higher series resistance, the drift transport of free charge carriers towards the electric contacts is hindered under the influence of the internal electric field [52]. The parameter  $J_{sc}$  values for CISE, CIGSe, and CIGSe bilayer TFSC are reduced from 45.01 to 17.17  $\text{mAcm}^{-2}$ , 32.42 to 26.31  $\text{mAcm}^{-2}$ , and 32.43 to 26.83

$\text{mAcm}^{-2}$ , respectively. Similarly, the FF values for CISE, CIGSe, and CIGSe bilayer TFSC are decreased from 82.67 to 14.08%, 87.34 to 21.01%, and 87.63 to 21.33%, respectively. This result shows that FF is strongly affected by the series resistance value. Finally, the PCE is declined from 22.81 to 2.03% (for CISE TFSC), 27.32 to 5.34% (for CIGSe TFSC) and 27.99 to 5.64% (for CIGSe bilayer TFSC).

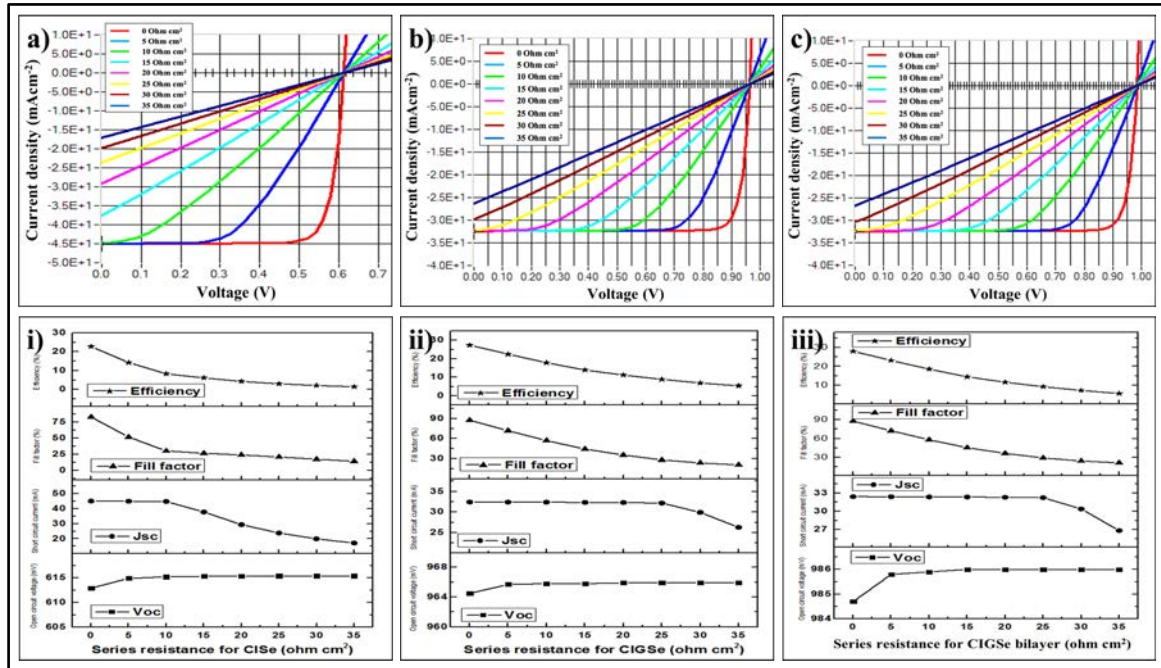


Fig. 6.42 J-V curves for a) CISE TFSC, b) CIGSe TFSC, and c) CIGSe bilayer TFSC, and solar cell parameter curves for i) CISE TFSC, ii) CIGSe TFSC and iii) CIGSe bilayer TFSC at different series resistances

Fig. 6.39i-iii shows the J-V curves of the CISE, CIGSe, and CIGSe bilayer TFSC inserted with solar cell parameters curve at different shunt resistances. The influence of shunt resistance on the solar cell parameters is analyzed. Here, the shunt resistance is varied from  $10^6$  to  $10^0 \Omega\text{cm}^2$ , while series resistance is kept at a constant value of  $0 \Omega\text{cm}^2$ . In this case, all the solar cell parameters  $V_{oc}$ , FF, and PCE except  $J_{sc}$  values are affected by decreasing shunt resistance of the solar cells. The significant change in the solar cell parameters started when shunt resistance values were less than  $10^2 \Omega\text{cm}^2$ . The simulation results showed that the  $V_{oc}$  value is intensely affected at a lower shunt resistance value, which is due to an increase in the recombination rate of the generated charge carriers [52]. The PCE for all TFSC found almost zero at a very low magnitude of shunt resistance (i.e.,  $10^0 \Omega\text{cm}^2$ ). Therefore, it is desirable to have the value of series resistance as low as possible and the

shunt resistance as high as possible [5, 26, 34]. It can infer from the results that both parasitic resistances strongly influence the FF and then PCE of the solar cells.

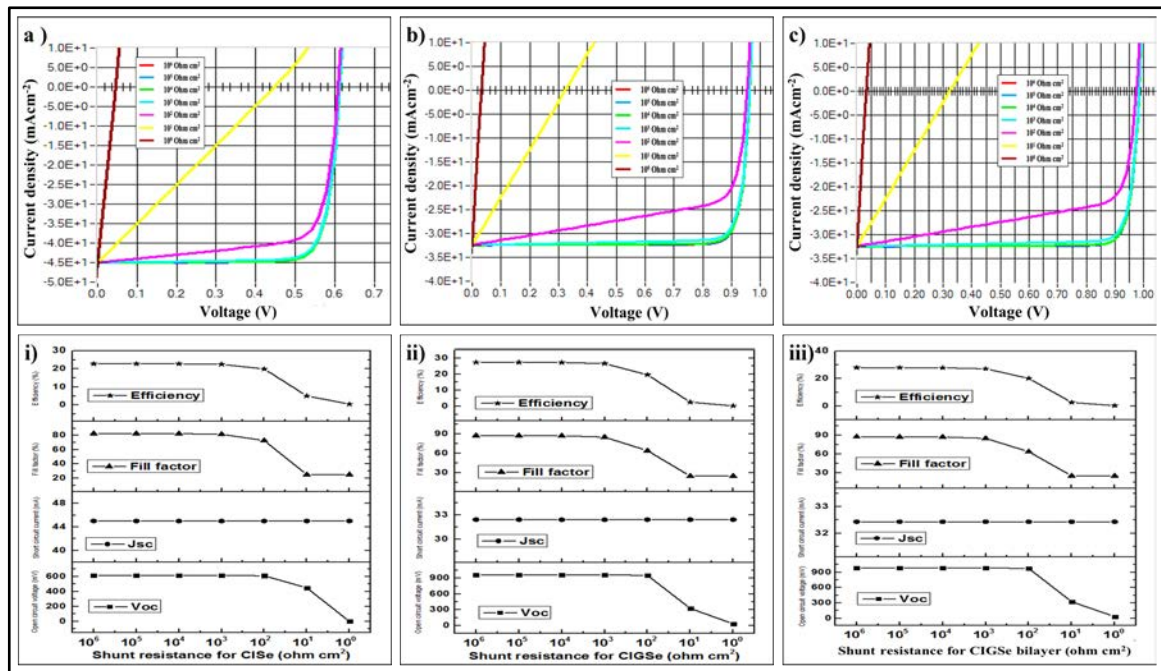


Fig. 6.43 J-V curves for a) CISE TFSC, b) CIGSe TFSC, and c) CIGSe bilayer TFSC, and solar cell parameter curves for i) CISE TFSC, ii) CIGSe TFSC and iii) CIGSe bilayer TFSC at different shunt resistances

## 6.8 Summary

The three different types of CI(G)Se TFSC, namely CISE, CIGSe and CIGSe bilayer, were effectively simulated through SCAPS software. It was observed from the results that the solar cell performance improves with an increase in thickness of the absorber layer by increasing the absorption of photons in the device. The absorber layer's carrier concentration in the range of  $5 \times 10^{16}$  to  $1 \times 10^{17} \text{ cm}^{-3}$  were suitable values for getting high results. A high carrier concentration of the absorber material can enhance the recombination centers for the generated charge carriers. The lower thickness of CdS with fewer material defects was favored for achieving high efficiency. A high CdS thickness can reduce the absorption of photons in the absorber layer by absorbing photons in it. The series resistance of the device may also increase with an increase in CdS thickness. The low carrier concentration of CdS can also absorb photons, which prevents the photons from reaching the absorber layer. After analyzing these results, the CI(G)Se TFSCs were optimized to obtain as high PCE as possible. The optimized PCE of 22.81, 27.32, and 27.99% were observed for CISE, CIGSe,



and CIGSe bilayer TFSCs, respectively. These results showed that the thin film solar cell using a CIGSe bilayer has the potential to get high device performance compared to a single absorber layer thin film solar cell, which is due to an increase in the absorption of photons by widening the bandgap of absorber material.

The experimental results of the CI(G)Se thin films and CdS thin films were also studied through SCAPS software. It is found from the simulation results that the device performance was decreased with an increase in CdS thickness. The maximum efficiency was noticed for CdS thin film deposited at 80°C for 20 minutes, which has a lower thickness than other deposition conditions. The presence of defects in the bulk semiconductor (mainly in the CdS buffer layer and CI(G)Se absorber layer) and at the interface can increase the recombination centers. This increment reduces the diffusion length of the generated charge carriers and finally, degrades the solar cell performance. The reverse saturation current was increased with an increase in ambient temperature, which reduces the  $V_{oc}$  of solar cells. Therefore, better solar cell performance is observed in a lower temperature than in a higher temperature. The fill factor of the solar cell was mainly influenced by parasitic resistances. The high device performance was detected at low values of series resistance through the drift transport of free charge carriers towards the electrodes and high values of shunt resistance by minimizing the recombination rate. Hence, this simulation study could be helpful for designing the experimental work.

## References:

- [1] A. K. Esman, G. L. Zykov, V. A. Potachits, and V. K. Kuleshov, "Simulation of thin-film solar cells with a CuInSe<sub>2</sub> chalcopyrite structure," *Energ. Proc. CIS High. Educ. Institutions Power Eng. Assoc.*, vol. 63, no. 1, pp. 5–13, 2020.
- [2] N. Amin, P. Chelvanathan, M. I. Hossain, and K. Sopian, "Numerical modelling of ultra thin Cu(In,Ga)Se<sub>2</sub> solar cells," *Energy Procedia*, vol. 15, no. 2011, pp. 291–298, 2012.
- [3] N. Khoshsirat and N. A. Md Yunus, "Numerical simulation of CIGS thin film solar cells using SCAPS-1D," *Proc. - 2013 IEEE Conf. Sustain. Util. Dev. Eng. Technol. IEEE CSUDET 2013*, no. September 2015, pp. 63–67, 2013.
- [4] N. Khoshsirat, N. A. Md Yunus, M. N. Hamidon, S. Shafie, and N. Amin, "Analysis of absorber layer properties effect on CIGS solar cell performance using SCAPS,"

- Optik (Stuttg.), vol. 126, no. 7–8, pp. 681–686, 2015.
- [5] S. R. I. Biplab, M. H. Ali, M. M. A. Moon, M. F. Pervez, M. F. Rahman, and J. Hossain, “Performance enhancement of CIGS-based solar cells by incorporating an ultrathin BaSi<sub>2</sub> BSF layer,” *J. Comput. Electron.*, vol. 19, no. 1, pp. 342–352, 2020.
  - [6] D. W. Houck, T. D. Siegler, and B. A. Korgel, “Predictive Modeling of CuInSe<sub>2</sub> Nanocrystal Photovoltaics: The Importance of Band Alignment and Carrier Diffusion,” *ACS Appl. Energy Mater.*, vol. 2, no. 2, pp. 1494–1504, 2019.
  - [7] M. W. Bouabdelli, F. Rogti, M. Maache, and A. Rabehi, “Performance enhancement of CIGS thin-film solar cell,” *Optik (Stuttg.)*, vol. 216, no. March, p. 164948, 2020.
  - [8] P. Chelvanathan, M. I. Hossain, and N. Amin, “Performance analysis of copper-indium-gallium-diselenide (CIGS) solar cells with various buffer layers by SCAPS,” *Curr. Appl. Phys.*, vol. 10, no. SUPPL. 3, pp. 387–391, 2010.
  - [9] A. Benmir and M. S. Aida, “Analytical modeling and simulation of CIGS solar cells,” *Energy Procedia*, vol. 36, pp. 618–627, 2013.
  - [10] M. Saadat, M. Moradi, and M. Zahedifar, “CIGS absorber layer with double grading Ga profile for highly efficient solar cells,” *Superlattices Microstruct.*, vol. 92, pp. 303–307, 2016.
  - [11] M. A. Ghebouli, B. Ghebouli, R. Larbi, T. Chihi, and M. Fatmi, “Effect of buffer nature, absorber layer thickness and temperature on the performance of CISSe based solar cells, using SCAPS-1D simulation program,” *Optik (Stuttg.)*, vol. 241, no. July 2020, p. 166203, 2021.
  - [12] R. N. Mohottige and S. P. Kalawila Vithanage, “Numerical simulation of a new device architecture for CIGS-based thin-film solar cells using 1D-SCAPS simulator,” *J. Photochem. Photobiol. A Chem.*, vol. 407, no. July 2020, p. 113079, 2021.
  - [13] R. A. Sinton and A. Cuevas, “Contactless determination of current-voltage characteristics and minority-carrier lifetimes in semiconductors from quasi-steady-state photoconductance data,” *Appl. Phys. Lett.*, vol. 69, no. 17, pp. 2510–2512, 1996.
  - [14] H. Heriche, Z. Rouabah, and N. Bouarissa, “High-efficiency CIGS solar cells with optimization of layers thickness and doping,” *Optik (Stuttg.)*, vol. 127, no. 24, pp. 11751–11757, 2016.
  - [15] M. A. Ashraf and I. Alam, “Numerical simulation of CIGS, CISSe and CZTS-based solar cells with In<sub>2</sub>S<sub>3</sub> as buffer layer and Au as back contact using SCAPS 1D,” *Eng. Res. Express*, vol. 2, no. 3, 2020.

- [16] T. Alzoubi and M. Moustafa, "Numerical optimization of absorber and CdS buffer layers in CIGS solar cells using SCAPS," *Int. J. Smart Grid Clean Energy*, vol. 8, no. 3, pp. 291–298, 2019.
- [17] S. Dabbabi, T. Ben Nasr, and N. Kamoun-Turki, "Parameters optimization of CIGS solar cell using 2D physical modeling," *Results Phys.*, vol. 7, pp. 4020–4024, 2017.
- [18] M. Sijanur, R. Robin, M. Mansoor, and M. Rasmi, "Numerical Modeling and Analysis of Ultra Thin Film Cu(In,Ga)Se<sub>2</sub> Solar Cell using SCAPS-1D," 2016.
- [19] Y. Osman, M. Fedawy, M. Abaza, and M. H. Aly, "Optimized CIGS based solar cell towards an efficient solar cell: impact of layers thickness and doping," *Opt. Quantum Electron.*, vol. 53, no. 5, pp. 1–16, 2021.
- [20] A. Benmir and M. S. Aida, "Analytical modeling and simulation of CIGS solar cells," *Energy Procedia*, vol. 36, pp. 618–627, 2013.
- [21] M. W. Bouabdelli, F. Rogti, M. Maache, and A. Rabehi, "Performance enhancement of CIGS thin-film solar cell," *Optik (Stuttg.)*, vol. 216, p. 164948, 2020.
- [22] M. Sijanur, R. Robin, M. Mansoor, and M. Rasmi, "Numerical Modeling and Analysis of Ultra Thin Film Cu ( In , Ga ) Se<sub>2</sub> Solar Cell using SCAPS-1D," 2016.
- [23] D. Rauh, A. Wagenpfahl, C. Deibel, and V. Dyakonov, "Relation of open circuit voltage to charge carrier density in organic bulk heterojunction solar cells," *Appl. Phys. Lett.*, vol. 98, no. 13, 2011.
- [24] H. Elfarrri and M. Bouachri, "Optimization of simulations of thickness layers , temperature and defect density of CIS based solar cells , with SCAPS-1D software , for photovoltaic application," *Chalcogenide Lett.*, 2021.
- [25] A. Rohatgi and P. Rai-Choudhury, "Research on the Basic Understanding of High Efficiency in Silicon Solar Cells," p. 127, 1984.
- [26] T. N. Fridolin, D. K. G. Maurel, G. W. Ejeh, T. T. Bénédicte, and N. J. Marie, "Highlighting some layers properties in performances optimization of CIGSe based solar cells: Case of Cu(In, Ga)Se–ZnS," *J. King Saud Univ. - Sci.*, vol. 31, no. 4, pp. 1404–1413, 2019.
- [27] H. Heriche, Z. Rouabah, and N. Bouarissa, "New ultra thin CIGS structure solar cells using SCAPS simulation program," *Int. J. Hydrogen Energy*, vol. 42, no. 15, pp. 9524–9532, 2017.
- [28] A. Bouich et al., "Experimental, theoretical, and numerical simulation of the performance of CuIn<sub>x</sub>Ga<sub>(1-x)</sub>Se<sub>2</sub>-based solar cells," *Optik (Stuttg.)*, vol. 183, no.

February, pp. 137–147, 2019.

- [29] S. Ouédraogo, F. Zougmore, and J. M. Ndjaka, “Numerical analysis of copper-indium-gallium-diselenide-based solar cells by SCAPS-1D,” *Int. J. Photoenergy*, vol. 2013, 2013.
- [30] A. Belghachi and N. Limam, “Effect of the absorber layer band-gap on CIGS solar cell,” *Chinese J. Phys.*, vol. 55, no. 4, pp. 1127–1134, 2017.
- [31] A. K. Daoudia, E. H. Youssef, and A. Benami, “Investigation of the effect of thickness, band gap and temperature on the efficiency of CIGS solar cells through SCAPS-1D,” *Int. J. Eng. Tech. Res.*, vol. 6, no. September 2018, p. 71, 2016.
- [32] M. Asaduzzaman, M. Hasan, and A. N. Bahar, “An investigation into the effects of band gap and doping concentration on Cu(In,Ga)Se<sub>2</sub> solar cell efficiency,” *Springerplus*, vol. 5, no. 1, 2016.
- [33] A. K. Daoudia, “Investigation of the effect of thickness, band gap and temperature on the efficiency of CIGS solar cells through SCAPS-1D,” *Int. J. Eng. Tech. Res.*, 2016.
- [34] M. A. Rahman, “Design and simulation of a high-performance Cd-free Cu<sub>2</sub>SnSe<sub>3</sub> solar cells with SnS electron-blocking hole transport layer and TiO<sub>2</sub> electron transport layer by SCAPS-1D,” *SN Appl. Sci.*, vol. 3, no. 2, pp. 1–15, 2021.
- [35] M. Al-Hattab, L. Moudou, M. Khenfouch, O. Bajjou, Y. Chrafi, and K. Rahmani, “Numerical simulation of a new heterostructure CIGS/GaSe solar cell system using SCAPS-1D software,” *Sol. Energy*, vol. 227, no. September, pp. 13–22, 2021.
- [36] N. Khoshsirat and N. A. Md Yunus, “Numerical simulation of CIGS thin film solar cells using SCAPS-1D,” *Proc. - 2013 IEEE Conf. Sustain. Util. Dev. Eng. Technol. IEEE CSUDET 2013*, pp. 63–67, 2013.
- [37] M. Mostefaoui, H. Mazari, S. Khelifi, A. Bouraiou, and R. Dabou, “Simulation of High Efficiency CIGS Solar Cells with SCAPS-1D Software,” *Energy Procedia*, vol. 74, pp. 736–744, 2015.
- [38] M. Al-Hattab, L. Moudou, M. Khenfouch, O. Bajjou, Y. Chrafi, and K. Rahmani, “Numerical simulation of a new heterostructure CIGS/GaSe solar cell system using SCAPS-1D software,” *Sol. Energy*, vol. 227, no. September, pp. 13–22, 2021.
- [39] K. Decock, S. Khelifi, and M. Burgelman, “Modelling multivalent defects in thin film solar cells,” *Thin Solid Films*, vol. 519, no. 21, pp. 7481–7484, 2011.
- [40] S. J. Heise, V. Gerliz, M. S. Hammer, J. Ohland, J. Keller, and I. Hammer-Riedel, “Light-induced changes in the minority carrier diffusion length of Cu(In,Ga)Se<sub>2</sub>

- absorber material,” *Sol. Energy Mater. Sol. Cells*, vol. 163, no. November 2016, pp. 270–276, 2017.
- [41] N. E. I. Boukourt and S. Patané, “Single junction-based thin-film CIGS solar cells optimization with efficiencies approaching 24.5 %,” *Optik (Stuttg.)*, vol. 218, no. July, 2020.
  - [42] D. Niane, A. K. Ehemba, S. Cissé, O. Diagne, and M. Dieng, “Influence of the Doping Rate of the CIGSe Layer on the Recombination-generation Mechanisms with 25 nm Incorporation of a KF Layer on a CIGSe Solar Cell,” vol. 6, no. 1, pp. 30–34, 2018.
  - [43] J. V. Marc Burgelman, Koen Decock, Alex Niemegeers, “SCAPS manual,” *SCAPS Man.*, no. December, 2016.
  - [44] S. Yang, S. Khelifi, J. de Wild, B. Vermang, and J. Lauwaert, “Investigation of recombination mechanisms in Cu(In,Ga)Se<sub>2</sub> solar cells using numerical modelling,” *Sol. Energy*, vol. 228, no. September, pp. 464–473, 2021.
  - [45] S. Siebentritt U. Rau, *Wide-Gap Chalcopyrites*. 2015.
  - [46] S. Oladapo, B. M. SOUCASE, and B. AKA, “Numerical Simulation And Performance Optimization Of Cu(In,Ga)Se<sub>2</sub> Solar Cells,” *IOSR J. Appl. Phys.*, vol. 08, no. 04, pp. 01–11, 2016.
  - [47] A. Khadir, “Simulation of effects of defects and layers thickness on the performance of CIGS solar cells,” *Acta Phys. Pol. A*, vol. 137, no. 6, pp. 1128–1134, 2020.
  - [48] B. Das, I. Aguilera, U. Rau, and T. Kirchartz, “What is a deep defect? Combining Shockley-Read-Hall statistics with multiphonon recombination theory,” *Phys. Rev. Mater.*, vol. 4, no. 2, pp. 1–14, 2020.
  - [49] H. J. Pauwels and G. Vanhoutte, “The influence of interface state and energy barriers on the efficiency of heterojunction solar cells,” *J. Phys. D. Appl. Phys.*, vol. 11, no. 5, pp. 649–667, 1978.
  - [50] M. K. Sobayel et al., “Efficiency enhancement of CIGS solar cell by cubic silicon carbide as prospective buffer layer,” *Sol. Energy*, vol. 224, no. May, pp. 271–278, 2021.
  - [51] Sadanand and D. K. Dwivedi, “Modeling of CZTSSe solar photovoltaic cell for window layer optimization,” *Optik (Stuttg.)*, vol. 222, no. August, p. 165407, 2020.
  - [52] F. F. Muhammad et al., “Employment of single-diode model to elucidate the variations in photovoltaic parameters under different electrical and thermal conditions,” *PLoS One*, vol. 12, no. 8, 2017.

## Chapter 7 Conclusions

### 7.1 General conclusions

The objective of this research work was to study the deposition of CI(G)Se by the hybrid deposition method and deposition of CdS by the chemical bath deposition method. A SCAPS software was used to study the effect of material properties on the performance of CI(G)Se TFSC and to theoretically optimize the best properties of each layer used in CI(G)Se TFSC.

In this study, the CI(G)Se thin films were successfully synthesized by the hybrid deposition method. The first stage substrate temperatures, selenization temperatures and times were mainly studied because these parameters could influence the structural, morphological, compositional and electrical properties of the deposited thin films. The formation of the  $\gamma$ - $\text{In}_2\text{Se}_3$  phase was confirmed by the characteristic peak of (006) from XRD results, Raman shift at  $150\text{ cm}^{-1}$ , high selenium content (i.e.,  $> 60\text{at}\%$ ) from EDS analysis, and about 2 eV bandgap from optical results. The obtained  $\text{In}_2\text{Se}_3$  thin films can be used as a precursor layer for the preparation of CI(G)Se thin films. The XRD results of CI(G)Se thin films showed a preferential orientation of (112), confirming the formation of chalcopyrite crystal structure. From Raman spectra of CI(G)Se thin films, the  $A_1$  vibrational mode in the range of  $170$  to  $176\text{ cm}^{-1}$  for CI(G)Se thin films verified the poly-crystalline and chalcopyrite crystal structure of CI(G)Se. The uniform, well-connected, and irregular-shaped grains for CI(G)Se thin films were observed from SEM and AFM results. The electrical properties of CI(G)Se thin films confirmed the formation of p-type semiconducting nature. After studying these results, the first stage substrate temperature of  $320^\circ\text{C}$  and the selenization temperature of  $550^\circ\text{C}$  for 60 minutes were the best deposition conditions for CI(G)Se thin films. Moreover. The CdS thin films were grown by the chemical bath deposition method at various ammonia quantities, deposition temperatures and deposition times. The characteristic peak (002) and other minor peaks from XRD results, and the Raman shift of the 1LO at  $305\text{ cm}^{-1}$  and the 2LO at  $605\text{ cm}^{-1}$  verified the formation of the hexagonal crystal structure. Uniform, smooth, compact, dense film and spherical grains were found from morphological properties. The observed bandgaps in the range of 2.5 to 2.65 eV for CdS thin films were also related to the hexagonal crystal structure. Hall effect studies confirmed the n-type nature of CdS material having the carrier concentration in the range of  $10^{14}$  to  $10^{16}\text{ cm}^{-3}$ . By careful analysis, the

CdS thin film deposited at a temperature of 80°C for 30 minutes showed the most suitable condition to use in the CI(G)Se TFSCs as a buffer layer.

The material properties such as thickness and carrier concentration of semiconductors used in the CI(G)Se TFSCs were simulated through SCAPS software. The performance of CI(G)Se was increased with an increase in the CI(G)Se thickness. The better results were observed in the range from  $10^{16}$  to  $10^{17}$  cm<sup>-3</sup> of CI(G)Se carrier concentration. The CdS thickness of 50 nm and CdS carrier concentration greater than  $10^{17}$  cm<sup>-3</sup> were suitable for obtaining high results. The optimized PCE of 22.81, 27.32, and 27.99% were found for CISE, CIGSe, and CIGSe bilayer TFSCs, respectively. After analyzing the experimental results, the maximum PCE of 19.87, 23.80, and 24.63% were achieved for CISE, CIGSe, and CIGSe bilayer TFSC, respectively. But it is difficult to obtain similar efficiency experimentally because the effect of impurities (i.e., oxides, selenides, etc.) is not considered in the simulation study. The presence of defects in semiconductors or/and at an interface can negatively affect the device performance by increasing the recombination centers, which can reduce the solar cell performance. It was seen that the solar cell can obtain higher PCE in a low ambient temperature than in a high ambient temperature by increasing the  $V_{oc}$  with a decrease in ambient temperature. The high device performance was observed at a very high shunt resistance and a very low series resistance. Therefore, the theoretical study is promising for modeling solar cells and can be helpful for designing experimental work that can save material resources as well as research time.

## 7.2 Future perspectives

In this study, the deposition parameters of the hybrid deposition method for CI(G)Se thin films and the chemical bath deposition method for CdS thin films were optimized by analyzing their material properties. Moreover, the material parameters of each layer used in CI(G)Se TFSC are analyzed and optimized through theoretical study. This simulation study can help to understand the effect of material properties on the device performance and finally, can provide an idea for designing the experimental activities. Further studies are needed in the future to enhance the presented results. We need to:

1. Optimize the substrate temperatures of the 2<sup>nd</sup> and 3<sup>rd</sup> stages of the hybrid deposition method to improve further quality of CI(G)Se thin films.
2. Study on the optimization of Mo, i-ZnO, and ZnO:Al layers to fabricate the complete CI(G)Se TFSCs.
3. Investigate the effect of alkali elements present in the CI(G)Se TFSCs on their performance and optimize the best condition (i.e., name of alkali elements, its quantity, and incorporation process into solar cells).
4. Study on different Cd-free buffer layers such as In<sub>2</sub>S<sub>3</sub>, ZnS, etc. to obtain more environment-friendly CI(G)Se TFSCs.
5. Standardize the equipment for large area and large-scale production of solar cell.

### **7.3 Research publications and conference activities**

#### **7.3.1 Journal publications**

1. A. Ashok, G. Regmi, A. Romero-Nuñez, M. Solis-López, S. Velumani, H. Castaneda, Comparative Studies of CdS Thin Films by Chemical Bath Deposition Techniques as a Buffer Layer for Solar Cell Applications, *Journal of Materials Science: Materials in Electronics* (2020), 31, pp. 7499-7518, <https://doi.org/10.1007/s10854-020-03024-3>.
2. G. Regmi, A. Ashok, P. Chawla, P. Semalti, S. Velumani, Perspectives of Chalcopyrite based CIGSe Thin film Solar cell - A Review, Accepted in *Journal of Materials Science: Materials in Electronics* (2020), <https://doi.org/10.1007/s10854-020-03338-2>.
3. D. Valencia, J. Conde, A. Ashok, C. A. Meza-Avendaño, H. Vilchis, S. Velumani, Optimization of Cu(In, Ga)Se<sub>2</sub> (CIGSe) Thin Film Solar Cells Parameters Through Numerical Simulation and Experimental Study, *Solar Energy*, Vol. 224, August 2021, Pages 298-308, <https://doi.org/10.1016/j.solener.2021.05.075>.

#### **7.3.2 Conference publications**

1. A. Ashok, G. Regmi, S. Velumani, D. Valencia, J. Conde, H. Castaneda, Numerical optimization of materials properties for high-efficiency CIGSe thin film solar cells



- using SCAPS-1D simulator, 2021 18th International Conference on Electrical Engineering, Computing Science and Automatic Control (CCE). Mexico City, Mexico. November 10-12, 2021, DOI: 10.1109/CCE53527.2021.9632878.
2. D. Valencia, J. Conde, A. Ashok, S. Velumani, Numerical Study of the recombination profiles in CIGSe thin film solar cells through Silvaco Atlas simulator after using experimental parameters, 2021 18th International Conference on Electrical Engineering, Computing Science and Automatic Control (CCE). Mexico City, Mexico. November 10-12, 2021, DOI: 10.1109/CCE53527.2021.9633066.
  3. A. Ashok, G. Regmi, S. Velumani, Growth of  $\text{In}_2\text{Se}_3$  Thin Films Prepared by the Pneumatic Spray Pyrolysis Method for Thin Film Solar Cells Applications, 2020 17th International Conference on Electrical Engineering, Computing Science and Automatic Control (CCE). Mexico City, Mexico. November 11-13, 2020, DOI: 10.1109/CCE50788.2020.9299133.
  4. G. Regmi, A. Ashok, S. Velumani, Large Area ( $10 \times 10 \text{ cm}^2$ ) production of CdS Buffer Layer for Solar Cells by Chemical Bath Method, 2020 17th International Conference on Electrical Engineering, Computing Science and Automatic Control (CCE). Mexico City, Mexico. November 11-13, 2020, DOI: 10.1109/CCE50788.2020.9299158.
  5. A. Ashok, G. Regmi, S. Velumani, Characterizations of a Selenized  $\text{Cu}(\text{In}_{1-x}\text{Ga}_x)\text{Se}_2$  Thin Film Absorber Layer Fabricated By a Three- Stage Hybrid Method, 2018 15th International Conference on Electrical Engineering, Computing Science and Automatic Control (CCE), 2018, DOI: 10.1109/ICEEE.2018.8533902.
  6. G. Regmi, A. Ashok, S. Velumani, Structural, Morphological, Topographical, and Electrical Properties of Selenized Stacked CIGSe Layers by Evaporation Technique, 2018 15th International Conference on Electrical Engineering, Computing Science and Automatic Control (CCE), DOI: 10.1109/ICEEE.2018.8533910.

### **7.3.3 Patent publication**

1. Proceso híbrido de tres etapas para formar películas absorbedoras en celdas de película delgada CIS y CIGS ("Three-stage hybrid process to form absorbent films in CIS and CIGS thin film cells") presentada el 20 de marzo del 2020 y a la que le correspondió el no. De solicitud MX/a/2020/003232.

### 7.3.4 Conference activities

1. A. Ashok, G. Regmi, S. Velumani, Numerical optimization of materials properties for high-efficiency CISE thin film solar cells using SCAPS-1D simulator (Oral presentation in CCE 2021, México)
2. A. Ashok, G. Regmi, S. Velumani, Study of CISE thin films deposited by the novel hybrid deposition method and SCAPS-1D simulation for CISE thin film solar cells (Poster presentation in IMRC 2021, México).
3. A. Ashok, G. Regmi, S. Velumani, Study on the effect of annealing treatment on properties of cadmium sulfide thin films grown by a chemical bath deposition process (Oral presentation in IMRC 2021, México).
4. A. Ashok, G. Regmi, S. Velumani, Growth of  $\text{In}_2\text{Se}_3$  Thin Films Prepared by the Pneumatic Spray Pyrolysis Method for Thin Film Solar Cells Applications (Oral presentation in CCE 2020, México)
5. A. Ashok, G. Regmi, S. Velumani, Growth of the  $\text{CuInSe}_2$  Thin Film Photovoltaic Material deposited by the Novel Hybrid Deposition Method (Poster presentation on SIMPEST 2020, UNAM, México)
6. A. Ashok, G. Regmi, S. Velumani, Growth and Characterization of CdS Thin Films by Chemical Bath Deposition for Thin Film Solar Cell Applications (Oral presentation in IMRC 2019, México).
7. A. Ashok, G. Regmi, S. Velumani, Deposition and Characterization of CIGS Absorber Layer Obtained by Hybrid Deposition Process for Photovoltaic Applications (Poster presentation in Segundo Coloquio de Semiconductores, Aplicaciones y Tendencias, 2019 CINVESTAV-IPN, México).
8. A. Ashok, G. Regmi, S. Velumani, Deposition and Characterization of  $\text{In}_2\text{Se}_3$  Precursor Layers by Pneumatic Spray Pyrolysis for CIS/CIGS Thin Film Solar Cell Applications (Poster presentation in IMRC 2019, México).
9. A. Ashok, G. Regmi, S. Velumani, Deposition and characterization of CIGS Absorber layer obtained by Hybrid deposition process for photovoltaic applications (Poster presentation in CCSI 2019 conducted by CeMIESOL at Cuernavaca, Morelos and won Second position).

10. A. Ashok, G. Regmi, S. Velumani, Fabrication and Characterizations of a  $\text{CuInSe}_2$  Thin Film Deposited by a Three-stages Hybrid (3SH) Method (Oral presentation in IMRC 2018, México).
11. A. Ashok, G. Regmi, S. Velumani, Characterizations of a selenized CIGSe thin film absorber layer fabricated by a Three-stage Hybrid Method (Oral presentation in CCE 2018, México).
12. G. Regmi, A. Ashok, S. Velumani, Synthesis and characterization of CdS thin film as a buffer layer for CIGSe based solar cell, (Poster presentation in IMRC 2018, México).
13. G. Regmi, A. Ashok, S. Velumani, Growth of stacked CIGSe thin film absorber layer by thermal evaporation process, (Oral presentation in IMRC 2019, México).
14. D. Valencia, A. Ashok, J. Conde, S. Velumani, Numerical simulation study of CIGS solar cells obtained by the hybrid process (3SH), (Poster presentation in IMRC 2019, México).
15. G. Regmi, A. Ashok, S. Velumani, Intrinsic and Al-doped ZnO thin films using radio frequency magnetron sputtering as window layer in CIGSe solar cell, (Poster presentation in IMRC 2021, México).
16. D. Valencia, A. Ashok, J. Conde, S. Velumani, Optimization of  $\text{Cu(In,Ga)Se}_2$  (CIGSe) thin film solar cell parameters through numerical simulation and experimental study, (Poster presentation in IMRC 2021, México).
17. J. Conde, A. Ashok, D. Valencia, S. Velumani, Optimization of parameters by means 2D and 3D simulations and experimental study: a review of different kind of solar cells (Oral presentation in IMRC 2021, México).